Unclassified **NEA/RWM/CLAYCLUB(2013)1**

Organisation de Coopération et de Développement Économiques
Organisation for Economic Co-operation and Development **28-May-2013**

English - Or. English

NUCLEAR ENERGY AGENCY
RADIOACTIVE WASTE MANAGEMENT COMMITTEE

Cancels & replaces the same document of 24 May 2013

Integration Group for the Safety Case (IGSC)

CLAY CHARACTERISATION FROM NANOSCOPIC TO MICROSCOPIC RESOLUTION

NEA CLAY CLUB Workshop Proceedings

Karlsruhe, Germany
6-8 September 2011

Update of the title of the document on the official OLIS cover page.

For any additional information, please contact Mr. Hiroomi AOKI at hiroomi.aoki@oecd.org.

JT03340363

NEA/RWM/CLAYCLUB(2013)1
Unclassified

English - Or. English

FOREWORD

A wide spectrum of argillaceous media are being considered in Nuclear Energy Agency (NEA) member countries as potential host rocks for the final, safe disposal of radioactive waste, and/or as major constituent of repository systems in which wastes will be emplaced. In this context, the NEA established the Working Group on the "Characterisation, the Understanding and the Performance of Argillaceous Rocks as Repository Host Formations" in 1990, informally known as the "Clay Club". The Clay Club examines various argillaceous rocks that are being considered for the underground disposal of radioactive waste, ranging from soft clays to indurated shales.

Very generally speaking, these clay rocks are composed of fine-grained minerals showing pore sizes from < 2nm (micropores) up to > 50nm (macropores). The water flow, solute transport and mechanical properties are largely determined by this microstructure, the spatial arrangement of the minerals and the chemical pore water composition. Examples include anion accessible ("geochemical") porosity and macroscopic membrane effects (chemical osmosis, hyperfiltration), geomechanical properties and the characteristics of two-phase flow properties (relevant for gas transport). At the current level of knowledge, there is a strong need to improve the nanoscale description of the phenomena observed at a more macroscopic scale. However, based on the scale of individual clay-minerals and pore sizes, for most of the imaging techniques this resolution is a clear challenge.

The workshop, hosted by the Institute for Nuclear Waste Disposal (INE), Karlsruhe Institute of Technology (KIT) in the Akademiehotel Karlsruhe (Germany) from the 6th to the 8th of September 2011, was intended to give, inter alia, a discussion platform on:

- The current state-of-the-art of different spectro- microscopic methods
- New developments addressing the above mentioned knowledge gaps in clays.
- The perception of the interplay between geometry and electrostatics of experimentalists and molecular / Monte Carlo modeling groups providing valuable information on a lattice (1 clay surface; Å-scale).

This workshop was sponsored by the Federal Ministry of Economy and Technology (BMWi, Germany).

Bundesministerium
für Wirtschaft
und Technologie

TABLE OF CONTENTS

EXPECTATIONS, OPEN QUESTIONS TO BE ADDRESSED IN THE WORKSHOP WITHIN THE CONTEXT OF A DEEP GEOLOGICAL REPOSITORY IN CLAY FORMATIONS

(Summary of the introductory presentation given by Patrick Landais, ANDRA;
Chair of the NEA Clay Club)

Concerning radioactive waste disposal in geological formations a growing consensus in the world can be observed that deep geological disposal is the most appropriate solution for the long-term management of spent fuel and long-lived wastes (especially high level wastes). This consensus is based on the scientific work over several decades to develop technical solutions for deep geological repositories and to assess their long term safety over long time periods (up to 1 Million year). In many countries (such as i.a. Belgium, Germany, France, Japan, Switzerland, United Kingdom) deep argillaceous formations are considered as potential host rock for radioactive waste disposal. In other countries favoring crystalline host rock formations (such as e.g. Sweden, Finland) clay-based materials (e.g. bentonite) are proposed as the geotechnical barrier of the multi-barrier system for a deep geological repository.

Precise knowledge of the clay properties in the various domains concerned by the construction feasibility, the exploitation phase of the repository facilities, as well as the long term evolution of the waste and of its environment is therefore of crucial importance in assessing the performance and the safety of the various radioactive waste disposal concepts. The knowledge to be acquired on clays as such goes well beyond solely the field of disposal of radioactive waste. For both, clay formations or bentonites in engineered barriers, the characterization in a continuous way from the nanometer to the micrometer, of their internal structure and the study of the associated physico-chemical phenomena is a fundamental issue. It aims for explaining:

- The “Initial state” of the clays, in particular for the clay formations: the nature of the mechanical, hydraulic and geochemical processes, in a broad sense, and the way these processes were involved during the geological history of these formations,
- The fundamental processes involved by physico-chemical or hydraulic stresses, related to the evolution of the repository at the macroscopic scale.

Some major (macroscopic) objectives of Research & Development (R&D) work can be pointed out. For an appropriate characterization of the 3D poral and mineral organization of the clay rocks at the infra-millimeter scale (a) the characterization and the modeling of the elementary HMC (hydrological-mechanical-chemical) mechanisms and the transfer of gas involved at very small scales and (b) the establishment of a link between the elementary HMC mechanisms and the fluid transfer is needed. Here, examples on the atomistic scale looking in detail on the structuring of water molecules at the clay mineral surface or the cation complexation at the clay mineral surface have improved clearly our knowledge.

Clay Rocks are a complex material in terms of *mineralogical composition* constituting of variable proportions of clay minerals and mainly carbonates/ tectosilicates and *microstructural organization* with variations of pore sizes and minerals from some nanometers to several tens of microns. The spatial arrangement of these minerals controls the distribution and the nature of the water (free, bound, interlayer) and of the solutes within the clay-rich rocks and consequently the reactivity under repository conditions. Therefore, the nano- to mesoscopic microstructure given by the mineralogy, the porosity and the pore size distribution and also microstructural variations on the formation scale due to sedimentary processes will determine the transport processes (anion exclusion, surface diffusion and water structuration) and transport properties (permeability, diffusion coefficients, ion concentrations) on the small and large scale (basin). Similarly, mechanical and gas transport properties are closely related to this microstructure and can be described with this approach (see Figure 1).

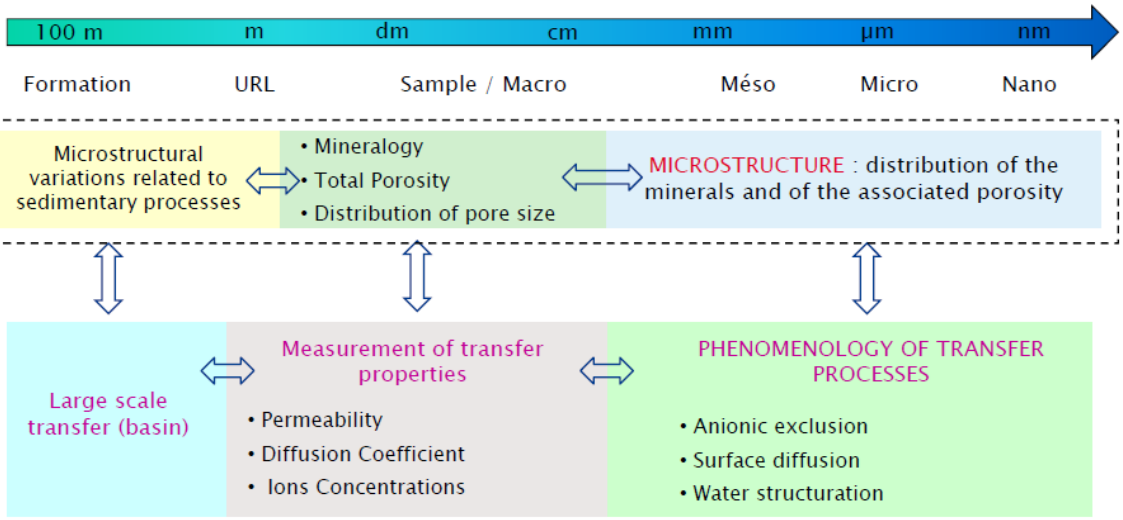

Figure 1. The multi-scale approach connecting mineralogy, porosity and transport properties.

Consequently, the choice of the characterization scale and relevant modeling is of first importance in the approaches leading to the establishment of the models of representation. Various research works pointed to experimental difficulties in quantifying the microstructure of the clay rocks at scales smaller than a micrometer, because of technical/instrumental limitations. This lack of knowledge at small scales does not allow to fully connect all the Thermal-hydrological-mechanical-chemical (THMC) mechanisms and to integrate them into an up-scaling approach.

There already exist conceptual models and experimental approaches to describe the microstructure of argillaceous formations in terms of porosity and texture (see Figure 2). Here, examples on the undisturbed Callovo-Oxfordian (COx) argillite are given:

- **Sample scale.** Variability investigations on the decimetre to centimetre scale on COx rock slices typically with a thickness of approx. 1cm by radiography and thin sections by optical microscopy have revealed a clear positive correlation of clay content and sample homogeneity showing highest heterogeneity in samples with carbonate rich zones and calcified zones having up to 65% carbonate content.
- **Mineral scale.** Investigating samples on the mineral scale by SEM- BSE/EDX with a resolution of 0.3µm and by X-Ray Microtomography under a voxel resolution of 0.7µm revealed a simplified 2D and 3D distribution of carbonates, tectosilicates, heavy minerals and the not further resolvable matrix. This information can furthermore resolved by microprobe (EPMA) analysis to obtain data beside the argillaceous matrix on calcite, quartz, dolomite, feldspar, pyrite, siderite and muscovite.
- **Pore scale.** As shown schematically in Figure 2 different types of pores have to be considered in argillaceous rocks with a) intergranular pores ranging from 50-100nm as observed in SEM and FIB-tomography and b) clay sheet stacks with interlayer pores considerably smaller that can be resolved by TEM having a resolution of 1-10nm.

Differences in bulk material properties (mass transfer) observed for anion and cation diffusion can be directly explained by molecular scale interactions (anion exclusion, surface diffusion) and/or directly linked to the geometry and poral network of the rock as in the case of the difference between horizontal effective diffusion coefficient ($D_{e,h}$) and vertical effective diffusion coefficient ($D_{e,v}$) with $D_{e,h}/D_{e,v} = 2$.

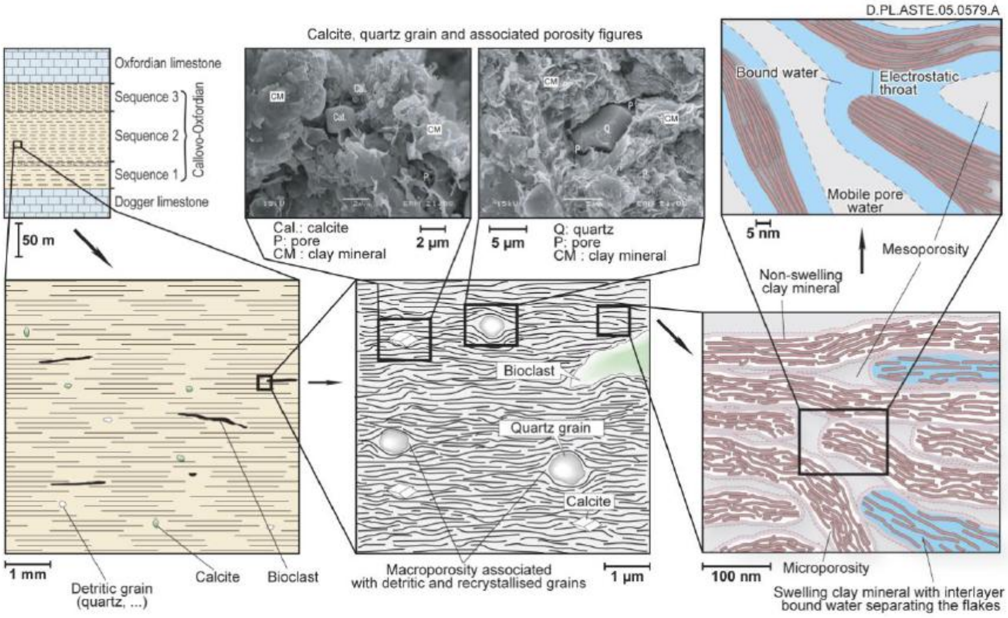

Figure 2. Conceptual model of the porosity scales to be considered within the Callovo-Oxfordian argillite (COX).

Another example is the issue of heat transfer properties, which has shown to be strongly influenced by the petrofabric and specifically by the distribution and content of heat conducting minerals (quartz, calcite). Here, in the bedding plane the thermal resistivity is weak, whereas perpendicular to the bedding plane the resistivity shows significant variability due to the clay mineral content and the porosity of the material.

Beside the characterization of the undisturbed clay rock an additional complexity is given by the processes involved during the evolution of a deep geological repository. Here, examples are given on a) the understanding of the long-term evolution of the EDZ, b) alteration processes at the interface between clay and engineered material and c) the complex interactions at the different interfaces in a high level waste cell.

a) The hydraulic properties of fractures created during the excavation of the repository infrastructure depend on their aperture (width). Those properties evolve as a function of the applied stress but also of the potential fractures self-sealing due to the swelling properties of the clay minerals. In the vicinity of seals and plugs the progressive re-saturation of the repository will be associated with the swelling of the clay minerals and the sealing of the fractures. If the bentonite plug is in contact with the geological formation its swelling pressure will increase the stress on the fractures.

b) In the framework of the iron (canister)-clay interaction the identification of corrosion rates, the corrosion reaction products and therefore the process understanding will lead to an adequate design (thickness) of the steel containers.

c) In a high level waste cell usually three type of materials have to be considered, namely the waste glass containing the radionuclides, the iron (steel) as canister material and the argillite/bentonite and it's contact with the steel canister. A temperature gradient will evolve from the glass to the argillite (host rock) whereas the penetration of water will progress from the far-field. Processes like glass dissolution and radionuclide release, the interaction with corrosion steel products and their interaction with mineralogical transformations of the argillite are of THMC (thermo-hydro-mechanical-chemical) type and occur on small to very small scales.

Overall, these three examples above highlight that a more precise and detailed description on the nano- to microscale is needed for the progressive optimization of the repository architecture and components.

In the following, questions and objectives to be addressed during the workshop on undisturbed argillaceous rocks concerning the characterization of the poral and mineral 3D network geometry at the infra-millimeter scales are highlighted.

- What is the spatial distribution and the morphology of pores?
- How are they organized with regard to minerals?
- What are the surfaces of interaction between minerals and pores?
- How get organized minerals at small scales?
- What is the morphology of the contacts between minerals?
- Are non-clay minerals in inclusion within a clay phase?
- Do carbonates constitute a skeleton?

Further objectives and questions in mechanical disturbed could include the following:

- Determination of the mechanical damage as a function e.g. of the type of mechanical discharge, deviatoric stress (in compression or in extension)
- In the case of a thermal load, in what pores is the dilatation of the water located? Is there a redistribution of the proportions of the various types of water? How is the pressure of the water on minerals reorganized? Where and how the porosity redistributed?
- Where are the deformations located? (Micro- fissuring of non-clay minerals and\or the clay phase, detachment between clay and non-clay minerals, sliding, dilatance of clay minerals)
- Is there an evolution of the nature of the water in the zones where deformations is located?

In chemical disturbed systems a focus is on precipitation and dissolution processes and their influence on transport/mass transfer parameters and the following questions inter alia can be raised:

- How and where in a 3D porous structure take the processes of dissolution-precipitation in saturated conditions and in non-saturated conditions to place?
- What pores are involved in the transport of solutions?
- Is there a partial or total accessibility of all the minerals to aggressive solutions?

  Beside the number of questions raised above the workshop was primarily intended to give an overview of currently available techniques as listed in the glossary using different incident beams, e.g. x-rays, neutrons, ions and electrons.

In the oral presentations by the invites speakers of the workshop the experts in the field/ technique are encouraged to give information on technical questions as e.g.:

Instrumental limitations? The Beam/probe technology specific resolution limits, incident energy and invasive/destructive or non-invasive/non-destructive method, sensor technology and detection limits.

How are images obtained? Addressing issues like sample collection and preparation/ preservation of samples (so called "Environmental" imaging by preservation of water content and textural information), image acquisition, and signal processing/signal mapping/ signal reconstruction as well as the elementary representative volume analysed.

What kind of information is collected? Here differentiation should be made between physical parameters (e.g. temperature, thermal conductivity, and magnetism), chemical parameters (e.g. composition, crystal structure), textural parameters (e.g. porosity, orientation, surface, relief) and the potential monitoring of property changes (spatial, temporal resolution, real time analysis). Furthermore, information on qualitative or quantitative results and the potential way to obtain quantitative data by combining different techniques on the same sample or the combination of microscopic and spectroscopic techniques should be given.

Patrick Landais ended his presentation with some concluding remarks/observations highlighting the importance of micro- to nano focusing techniques:

- Radioactive waste disposal offer a wide range of questions connected to various research areas
- Clay minerals and clay rocks still need to be studied in detail in order to provide robust models for the evaluation of the processes occurring during the evolution of an underground disposal
- Issues related to thermo-hydro-mechanical-chemical (THMC) processes are central when evaluating the safety of an underground repository
- Nano or microscopic resolution techniques provide new insights for the understanding of clay minerals reactivity
- Some phenomena, the description and understanding of which require micro-nano approaches, still constitutes major issues for the demonstration of the safety and the dimensioning of repository components.

SYNOPSIS SESSION –I "CHEMICAL INFORMATION UNDER HIGH SPATIAL RESOLUTION"

High spatial resolution in this research field is a prerequisite for a better understanding of governing processes, as individual clay particles are very small in dimension (clay size fraction typically defined as < 2µm). The phenomena that have been looked at under this resolution are narrow alteration zones either due to relatively short term laboratory experiments compared to the repository evolution time scale and/or due to the low reaction rates observed for clay minerals at ambient temperature. Another challenge in the field of chemical information to be extracted from compacted clay systems is that mostly the research is focused on the potential contaminants released from the repository near-field, which will be in the trace element concentration and analytical systems have to be tuned to increase the sensitivity under this high spatial resolution. Therefore, chemical information in form of element maps or correlation maps were shown on the initial clay material composition and its heterogeneities (e.g. phase assemblages), the water composition, sorption and migration effects of trace elements, reaction products of geochemical perturbation/alteration and the surface speciation/binding environment of the radionuclides or their chemical homologues.

Overall, six invited presentation were given in this session plus additional poster presentations. Beside this, a number of presentations in the other sessions showed a great overlap presenting also chemical data under high spatial resolution. All these oral contributions have shown the progress in this field focusing on the current resolution limits set by the physics and instrumentation available (C. Jacobsen, APS), the micro-focusing instrumentation available at the Karlsruhe Institute of Technology (KIT) synchrotron light source ANKA (J. Göttlicher, KIT-ISS), the application of nanoSIMS to retrieve elemental/isotope maps on complex organo-mineral structures (C. Höschen, TU München), the application of a multi-method approach to obtain nano- to microscopic 3D information on compacted clays (M.A. Denecke, KIT-INE) and the formation of secondary clay phases during glass corrosion and the speciation of trace elements as cerium (E. Curti, PSI-LES). In addition, C. Jacobsen (APS) gave a talk on post-processing methods as principle component analysis (PCA) combined with cluster analysis nowadays available to resolve spectral difference in heterogeneous samples discussing the strength and limitations of this approach.

In general, the presentations could be grouped by the applied methods in destructive techniques as nanoSIMS or laser ablation (LA-ICP-MS) and non-destructive methods (µXRF, µXANES, µEXAFS, µFTIR, (S)TEM-EDS and NMR). The progress made over the last couple of years compared to previous published work can be summarized as follows: (a) the progress in increasing the spatial resolution and sensitivity of methods/instrumentation gives possibilities to make surface analysis at atomic scale,
(b) these developments can be used for a better description and understanding of phenomena/processes as neo-formed mineral phases and their effect on element mobility/retention and
(c) the developments in post processing methods and computer power available combining different chemical information in form of e.g. cross correlations opens new ways of data interpretation and/or modeling.

In conclusion, the workshop has shown that chemical data is one of the *"pieces in the puzzle"* that is and has to be linked to physical data to understand processes as transport, clogging, self-sealing or deformation. Furthermore, in most of the applications shown having in mind the limitations of each analytical method the use of complementary analytical techniques has be proven to be most successful. The interest in the chemical evolution over time might however constrains the application of techniques to non-destructive methods. However, the combination of destructive and non-destructive methods is sometimes needed to obtain full quantitative information. It has also to be stated clearly, that the resolution reached so far is sometimes not sufficient enough to clearly discriminate phenomena such as sorption and co-precipitation.

There are also some critical points that have to be addressed in the near future, these are *inter alia*:

1) The very critical steps of sample selection (representativity), sample preparation and preservation prior to chemical analysis are not always properly documented and seem to be sometimes the secret of the researcher. This has to be optimized to avoid artefacts and finally miss- or over-interpretation of data.

2) Is there a way to follow or could be proposed as a kind of guideline for data segmentation, noise filtering and post-processing in form of correlation/distribution together with a criteria catalog to rank the techniques available for clay systems to optimize the scientific output?

3) Foster the communication between the experimentalists and the modelers to clarify what kind of data is needed and available at different scales (element distribution, chemical formula, binding environment).

There are no extended abstracts submitted for the presentations of C. Jacobsen (APS, Northwestern University) entitled:

"Application of PCA and cluster analysis to heterogeneous samples: strength and weaknesses" and

"Current resolution limits and future directions: Achievements & challenges".

However, the presentations as well as the analysis software can be downloaded from the following link:

http://xrm.phys.northwestern.edu/~jacobsen/clay_club/

SYNOPSIS SESSION –II "PORE STRUCTURE AND CONNECTIVITY"

In the second session in total four invited talks were given by the lecturers Guillaume Desbois (RWTH Aachen, Germany), Dimitri Prêt (HYDRASA, Poitiers, France), Lukas Keller (EMPA, Dübendorf, Switzerland) and Cino Viggiani (UJF Grenoble, France). Beside this oral presentations research results were also shown in a number of poster presentations.

Key aspects of this session were

(a) the sample preparation requirements for artefact-free microstructural characterization via freezing, high pressure freezing and impregnation protocols,

(b) the representative area/volume to be studied and

(c) the combination of analytical techniques used complementary to obtain data on the 3D mineral fabric at different scales and to build a 3D pore network model.

Several methods were discussed to examine the pores and pore size distribution in clays including *inter alia* BIB-SEM, µCT and TEM nano tomography (nT). Progress was made over the last couple of years in continuous pore size distribution analysis determined by FIB- nT, and it could be shown to be in good agreement to models based on N_2 adsorption isotherms. Furthermore, the TEM results presented in the workshop suggests that this technique resolves approx. 50 vol. % of the total pore space corresponding to the pore space characterized by pore radii ~>2nm in contrast to X-ray tomography, where only ~1 vol. % (under a voxel size of 2.6µm) of the pore space is resolved (see Keller & Holzer for details). The correlation with independent methods like N_2-adsorption isotherms or Hg intrusion porosimetry is a common approach, but techniques as NMR cryoporometry presented by Istvan Furó (session III) offer capabilities to be tested for compacted clay systems [1,2], although issues like salinity effects and the interaction of water at mineral surfaces effecting the pore size distribution results have to be discussed. There are still a number of challenges starting from e.g. the specimen preparation, the image analysis algorithm that need to be specially designed to perform automatic pore segmentation, the handling of very large data amounts obtained by the tomographic techniques to very fundamental questions as *"at which scale(s) is the* ***interesting physics*** *for damage and deformation in clay rocks taking place?"*. However, the presentations have shown that there is a rapid progress both in instrumentation and model development that will help to characterize pore structure and connectivity in compacted clays and claystones.

References

[1] P.A.C. Gane, C.J. Ridgway, E. Lehtinen, R. Valiullin, I. Furó, J. Schoelkopf, H. Paulapuro, J. Daicic, Comparison of NMR Cryoporometry, Mercury Intrusion Porosimetry, and DSC Thermoporosimetry in Characterizing Pore Size Distributions of Compressed Finely Ground Calcium Carbonate Structures, Ind. Eng. Chem. Res., 43 (2004) 7920-7927.

[2] S.-Y. Ryu, D.S. Kim, J.-D. Jeon, S.-Y. Kwak, Pore Size Distribution Analysis of Mesoporous TiO2 Spheres by 1H Nuclear Magnetic Resonance (NMR) Cryoporometry, The Journal of Physical Chemistry C, 114 (2010) 17440-17445.

SYNOPSIS SESSION III & IV “WATER AND ION MOBILITY, UP-SCALING AND IMPLEMENTATION IN MODEL APPROACHES”

In the agenda of the workshop Session III was entitled *“Water and ion mobility”* and Session IV *“Up-scaling and implementation in model approaches”.* However, the overlap of these two sessions especially concerning scale issues was substantial so that it was decided to merge the contributions of these two sessions for the proceedings volume. The sessions included presentations from István Furó (KTH) on the application of MRI and NMR cryo-porometry on clay systems, the effect of organics on the adsorption and mobility of metal cations in clay systems from both the experimental and molecular modeling approach given by A. Kalinichev (SUBATECH), the migration of colloids and stable isotopes of water in clay-rich aquitards presented by J. Hendry (Univ. of Saskatchewan), and the Cs migration in Opalinus Clay revealed by tomography and neutron radiography by Daniel Grolimund (PSI). F. Juranyi (PSI) gave a presentation on the linkage of water diffusion in compacted clays at two different time scales, namely tracer through diffusion experiments and quasi-elastic neutron scattering (QENS) and B. Rotenberg (UPMC, PESCA, Paris) gave an overview on how current nano-microscopic knowledge is implemented in modeling approaches..

The range of scales we are interested in starts at molecular scale (1-3Å) to crystal scale (3Å-2nm) over particle scale with 2-200nm dimension to the particle/macro-aggregate scale with 0.2-1500µm (see for example Fig. 45). Methods available to study the particle scale concerning pore structure and connectivity which determines water mobility are under dry conditions N_2 adsorption and Hg intrusion, whereas under the hydrated state methods like X-Ray tomography and X-ray and neutron scattering are available. Going down in size molecular modeling, x-ray and neutron diffraction modeling and water adsorption gravimetry are *inter alia* available.

Because the oral presentation by István Furó (KTH), Jim Hendry (Univ. of Saskatchewan) and Daniel Grolimund (PSI) are not presented as extended abstracts in this proceedings volume, short summaries are given here:

István Furó focused on two analytical techniques, namely Magnetic Resonance Imaging (MRI) and Nuclear Magnetic Resonance (NMR) cryo-porometry. The application of these methods in clay systems was done in the context of clay swelling/gel formation phenomena to measure solid content in highly hydrated systems via proton-NMR [1]. MRI is a quantitative method, however the spatial resolution is at best ~10µm. The application in compacted clay systems has to be tested, as the signal might be too low for accurate results above 6-10 vol% water content. Furthermore, MRI offers the direct quantitative determination of diffusion coefficients time resolved and cation exchange processes in the gel layer. Via NMR cryo-porometry a direct measurement of pore size distribution below 2-3nm is possible, offering a method besides BET to give information of pore neck sizes and applicability of Pareto’s law.

Jim Hendry (Univ. of Saskatchewan) gave a presentation on mobility of colloids, whereas the migration is controlled by sizes of the colloid and pores. An approach was made to determine indirectly pore throat diameters (i.e., constrictions between larger pores) through colloid diffusion experiments on the example of clay till. Natural DOC found showed an average size of 2.2-2.4nm, and a mean D_a = 1.9x10-10 m^2/s. Additional experiments using sodium poly(styrene sulphonate) polymers and Suwannee River FA/HA confirmed this cutoff of 2-2.5nm. This data was compared to mercury intrusion porosimetry showing high porosity (31%) and broad pore size distribution between 3-1000nm and X-Ray tomography identifying highly connected porosity (resolution ~2µm) giving no direct argument for the size constrictions observed in the colloid migrations studies in such an open, highly connected system.

Daniel Grolimund (PSI) focused on the question: *“Why is chemical information under high spatial resolution needed?”* and showed in a couple of examples the importance of domain boundaries/interfaces being the key for reactions. These interfaces are characterized by steep gradients in

composition and chemical potentials, and information on the local molecular structure is needed to understand the surface speciation. X-ray microscopy nowadays gives maximum resolutions of 10-50nm in optimized experimental conditions and element concentrations, but routinely for heterogeneous environmental samples 1-10µm are obtained. In his presentation a multi method approach on Cs diffusion in Opalinus Clay was chosen, starting from quantitative imaging of Cs profiles by cross-correlating X-Ray fluorescence maps to lower resolution LA-ICP-MS data and cross-correlating the results. Furthermore, element selective tomography performing tomography directly at an element absorption edge was used to overcome low contrast gradients for segmentation. Additional information was gathered by neutron imaging on water mobility and diffusion at a resolution of ~15µm.
Finally all this information obtained on classical tomography (structural properties), µXRF, µXRD, µLA-ICP-MS, chemical tomography (chemical properties), neutron studies (fluid properties) and macroscopic in-diffusion results were used for random walk simulations on this realistic porous media (Opalinus Clay) and comparison with chemical tomography. It turned out that the simulated diffusion lengths are systematically longer than experimentally observed which might give hint to effects of non-linear sorption that are focus of new experiments.

There are resolution limits to the methods presented in session II (e.g. BIB-SEM) on pore characterization as e.g. the clay matrix characterization being only possible under a limited clay induration and pore throats being on the limit of resolution. These pore throats however are very important for as macroscopic phenomena observed. One methological approach to bridge the gap between the molecular/crystal scale and the particle/macro-aggregate scale (FIB-SEM) is to use complementary techniques as cryo-NMR, N_2 and water ad-/desorption and TEM. An issue that has not always been explicitly addressed within this workshop is: *"How are the results obtained on the µm- to nm resolution related to macroscopic phenomena or could be taken as a reasoning for the "interesting physics"observed?".* More explicitly, can we give strong scientific arguments on the µm-nm scale for observations made on:
a) ***chemistry/coupled phenomena*** as anion exclusion, chemical osmosis or hyperfiltration and clay swelling properties,
b) ***hydraulics*** as validity of Darcy's law, threshold gradients, gas entry pressure, gas migration pathways and filtration of colloids and
c) ***rock mechanics*** as strength parameters and strain localization.
The presentations on molecular modeling by B. Rotenberg (UPMC, PESCA) and A. Kalinichev (SUBATECH) have shown that laminar flow across a pore in clay could be reproduced and the possibility is given to look at membrane properties of clays. There seems to be an unexploited potential to bridge the scale gaps and to obtain mechanistic process understanding at the scale of these "interesting physics" and the particle flow code (PFC) modeling has to be applied to rock mechanics, see also [2,3].
Beside technical aspects discussed within these sessions it became clear that currently research institution dependent approaches exists for sample preparation and preservation lacking a standardized procedure and in addition "institutional" codes are used for post-processing data as segmentation and image reprocessing. Here, improvements in the future could lead to a type of standardized protocol, which would reduce uncertainties related to the aspects mentioned above.

[1] Dvinskikh, S. V. and Furó, I., 2009. Magnetic resonance imaging and nuclear magnetic resonance investigations of bentonite systems. SKB Technical report TR-09-27. Svensk Kärnbränslehantering AB, Stockholm, Sweden.

[2] J. Yoon, Application of experimental design and optimization to PFC model calibration in uniaxial compression simulation, International Journal of Rock Mechanics and Mining Sciences, 44 (2007) 871-889.

[3] C. O’Sullivan, Particle-Based Discrete Element Modeling: Geomechanics Perspective, International Journal of Geomechanics, 11 (2011) 449-464.

CONCLUSIONS

For both, clay formations or compacted bentonites in engineered barriers, the characterization in a continuous way from the nanometer to the micrometer, of their internal structure and the study of the associated physico-chemical phenomena is a fundamental issue.

On one side the workshop has shown a variety of experimental techniques such as, e.g., neutron diffraction; µ-XAFS; nanoSIMS, TEM, AFM, nano-XCT; etc., will yield new and fundamental insights into physical/chemical processes acting on the solid phase on a microscopic scale, i.e., down to the scale of the molecular level.

There are some critical points that have to be addressed in the near future, these are *inter alia*:

- Beside technical aspects and limitations discussed within these sessions it became clear that currently research institution dependent approaches exists for sample preparation and preservation lacking a standardized procedure and in addition, “institutional” codes are used for post-processing data as segmentation and image reprocessing. The very critical steps of sample selection (representativity), sample preparation and preservation prior to chemical analysis are not always properly documented and seem to be sometimes the secret of the researcher. This has to be optimized to avoid artefacts and finally miss- or over-interpretation of data. Here, improvements in the future could lead to a type of standardized protocol for compacted clay materials, which would reduce uncertainties related to the aspects mentioned above.
- In the same manner, guidelines for data segmentation, noise filtering and post-processing in form of correlation/distribution together with a criteria catalog to rank the techniques available for clay systems would optimize the scientific output.

The workshop has clearly fostered the communication between the experimentalists and the modelers and this has to be continued to clarify what kind of data is needed and available at different scales (element distribution, chemical formula, binding environment).

On the other side – as an example – molecular modeling techniques will allow to elucidate on an atomic scale the mechanisms of radionuclide sorption onto clay minerals and to explore the migration behavior of solutes through compacted clays. All these new methods will result in an improved system understanding and help to further reduce conservatisms in transport models. Furthermore, approaches have been demonstrated throughout this workshop how it might be possible to upscale these microscopic results to scales in space and time relevant in performance assessments.

In conclusion, the workshop has shown that for most of the applications having in mind the limitations of each analytical method the use of complementary analytical techniques has be proven to be most successful. The interest in the chemical evolution over time might however constrains the application of techniques to non-destructive methods. However, the combination of destructive and non-destructive methods is sometimes needed to obtain full quantitative information. It has also to be stated clearly, that the resolution reached so far is sometimes not sufficient enough to clearly discriminate phenomena such as sorption and co-precipitation, but there is rapid instrumental development that might overcome this problem in the near future.

APPENDIX A – ABSTRACTS OF PRESENTATION

SESSION –I "CHEMICAL INFORMATION UNDER HIGH SPATIAL RESOLUTION"

Glass Corrosion and Secondary Clay Mineral Formation: The Fate of Ni and Ce as Revealed by μ-XRF/XAS Techniques

Enzo Curti[1*], Rainer Dähn[1], Marika Vespa[1,3], Daniel Grolimund[2] and Camelia N. Borca[2]

[1] Laboratory for Waste Management, Paul Scherrer Institut, Villigen (CH)
[2] Swiss Light Source, Villigen (CH)
[3]present affiliation: Nagra, Wettingen (CH)

* Corresponding author: enzo.curti@psi.ch

Abstract

In the present study, Ni (representing the activation products ^{59}Ni / ^{63}Ni) and Ce (a surrogate of Pu) were investigated in a simulated nuclear waste glass after aqueous alteration during 12 years at 90 ^{o}C and pH ~ 9.6, using X-ray spectroscopic techniques at μm resolution. Particular focus was put on the redistribution of these elements in the secondary Mg-clays formed during the alteration process and on their atomic/redox speciation.

Na-Mg μ-XRF maps and the STEM-EDS data revealed consistently that the core regions of the glass fragments are intact and compositionally homogeneous, whereas rims and interstitial spaces are depleted in Na and enriched in secondary Mg-smectites, formed as secondary products during the leaching process. The μ-XANES spectra collected at the Mg K-edge in the altered regions show three sharp resonances distinctive for Mg occupying undistorted octahedral positions, as expected in 2:1 clay minerals and other Mg-silicates. In contrast, the μ-XANES spectra collected in the core zones of the glass fragments lack this resonance pattern and are identical to the spectra measured on the pristine (unleached) glass.

The μ-EXAFS spectra collected at the Ni K-edge showed that Ni associated to the Mg-clay has a coordination environment and interatomic distances consistent with Ni adsorbed on or incorporated into clay minerals. The spectroscopic signature is completely different from that of Ni in the non-altered regions of the glass.

μ-XRF maps integrating the signals from Ce^{III}, Ce^{IV} and total Ce were prepared using a special technique based on the fluorescence contrast of the two mentioned redox species at different beam energies. They revealed that Ce, dominantly present as oxidized species (Ce^{IV}) in the original glass, was partly reduced during the aqueous corrosion process and re-precipitated a few tens of μm away as Ce^{III} in the interstitial spaces between the glass particles filled with the secondary Mg-clay. μ-XANES spectra collected at locations representative of both altered and non-altered glass domains were compared with appropriate Ce^{III} and Ce^{IV} compounds, confirming the findings obtained by the redox mapping.

The present study allowed us to shed light on the fate of radionuclides (or analogues thereof) after their dissolution from the waste glass matrix and to image chemical reactions at the microscopic scale. In particular, it was shown that considerable fractions of Ni and Ce were adsorbed on or coprecipitated almost *in-situ* with secondary Mg-clays formed during the glass alteration process. The

immobilization of cerium was found to be triggered by a reductive co-precipitation or adsorption mechanism, probably mediated by Fe(0) from the steel vessel used in the experiments. Thus, our experiment supports the common assumption that steel canisters will provide a reducing environment in the near-field of a nuclear waste repository. Low solubility implies a limited mobility of redox-sensitive nuclides and therefore lower doses in the safety case.

Introduction

Reprocessing and vitrification is a strategy followed by many countries for the safe disposal of high-level radioactive waste (HLW) originating from nuclear power plants (*Witherspoon and Bodvarsson (2006)*). In Switzerland, about 1/3 of the activity produced by the five currently operating reactors will be disposed of as vitrified waste in a deep underground repository planned to be hosted in clay-rich formations, whereas the remaining 2/3 will be disposed of as spent fuel (*Nagra (2002)*).

In safety assessments, radionuclides are assumed to be released congruently from the dissolving glass up to element-specific solubility limits, which depend on parameters such as the concentration of complexing ligands, ionic strength, pH and Eh. Because many long-lived fission products (^{79}Se, ^{129}I, ^{99}Tc, ^{126}Sn) and actinides ($^{233-238}$U, $^{238-242}$Pu and ^{237}Np) are redox-sensitive, their solubility will strongly depend on the oxidation potential of the pore water in contact with the vitrified waste. In general, the solubility and thus the mobility of such nuclides are very low under reducing conditions.

The oxidation potential is therefore a critical parameter in safety assessment calculations for radioactive waste repositories. In many countries, the environment of underground repositories is designed to provide strongly reducing conditions. This is achieved by selecting a sufficient depth to avoid contact with atmospheric oxygen and by encapsulating the waste within steel/copper canisters. Under such conditions, redox sensitive radionuclides (mostly occurring in the oxidized form within the glass matrix) should be converted to the sparingly soluble reduced species once they are released from the waste, resulting in small concentrations and slow transport rates.

In the present study, we focus on the fate of Ni (representing the activation products ^{59}Ni / ^{63}Ni) and Ce (a surrogate of Pu) in a simulated (i.e. non-radioactive) nuclear waste glass after prolonged aqueous corrosion (12 years at 90 ^{o}C and pH ~ 9.6) in a stainless steel reaction vessel. The investigated borosilicate glass is one of two reference formulations for reprocessed high-level radioactive waste in Switzerland (*Curti et al. (2006)*). It is an Mg-rich borosilicate glass, denoted “MW” (Magnox Waste) since it is derived from reprocessing of waste originating from now obsolete “Magnox” reactors, which used Mg as cladding material. The main aims of our investigation were: (a) to study the mobility of Ni and Ce at the micrometer scale after dissolution from the glass matrix, (b) to correlate the redistribution of the mentioned elements with secondary phases, notably with secondary Mg-clay identified as the main product of glass alteration, (c) to provide atomic-scale information on the coordination environment of Ni throughout the sample, (d) to identify and characterize possible redox reactions involving Ce$^{III/IV}$, (e) to infer, from the obtained information, possible consequences for the fate of ^{59,63}Ni and Pu under repository conditions.

1. Methods and data analysis

1.1 Techniques used

The techniques employed were: (a) micro X-ray fluorescence (μ-XRF), which allowed us to map on the 1-10 μm scale the distribution of key elements (Na, Mg, Ni, Ce), as well as the redox species Ce^{III} and Ce^{IV}; (b) micro X-ray absorption near edge structure (μ-XANES) from which characteristic features typical of the coordination environment of Mg/Ni and the oxidation state of Ce in the glass sample could be unraveled; and (c) micro extended X-ray absorption fine structure (μ-EXAFS), from which coordination number and interatomic distances around Ni atoms could be determined. The X-ray spectroscopy measurements were performed at beamline 10.3.2 (ALS, Berkeley) and at the LUCIA, MicroXAS and SuperXAS beamlines (SLS, Villigen). These data were complemented by X-ray diffraction (XRD) and scanning transmission electron microscopy coupled with energy dispersive analysis (STEM-EDS), making information at the nanometer scale accessible.

1.2 Leaching Experiments and sample preparation

The MW glass sample was crushed, sieved and the fraction <160 μm was collected. The sieved fraction was then washed with ethanol in an ultrasonic bath, decanted and dried at room temperature. Leaching experiments were carried out statically in quintuplet in 600 ml distilled water within airtight stainless steel vessels thermostated at 90 °C. At corrosion times of 5.7 and 12.2 years, single experiments were interrupted to collect altered glass for the spectroscopic investigations. The wet glass was separated from the aqueous solution and stored at 100% humidity in a refrigerator (T = 0-10 °C). Prior to use for spectroscopic investigations, the altered glass was rapidly washed with distilled water to remove the interstitial solution and dried in the oven at 40 °C for 24 h. During the alteration process, the glass grains and the corrosion products coalesced to form a mm-thick crust on top of the loose powder. The crust was cut transversally, embedded in epoxy resin and prepared as 30 μm-thick polished thin section for optical microscopy and X-ray spectroscopy. The nominal composition of the non-altered MW glass is as follows (in wt %): SiO_2=46.7, B_2O_3=16.0, Na_2O=8.5, Al_2O_3=6.6, MgO=5.9, Li_2O=3.9, REE_2O_3=3.4, Fe_2O_3=3.1, MoO_2=1.4, ZrO_2=1.4, Cs_2O=1.1, Cr_2O_3=0.6, BaO=0.5, NiO=0.4, minor oxides =0.5.

Commercial $Ce^{IV}O_2$ and hydrated $Ce^{III}_2(SO_4)_3$ from Aldrich® diluted with boron nitride were used without further treatment as reference compounds in order to characterize the two oxidation states of Ce in the glass samples.

1.3 Redox mapping of $Ce^{III/IV}$

In the case of cerium, the redox-sensitivity relies on the shift to higher energy of the white line (from 5725.9 eV to 5729.6 eV) upon oxidation of Ce^{III} to Ce^{IV} and the appearance of an additional resonance at 5737.8 eV in Ce^{IV} compounds, which is absent in Ce^{III} compounds (Figure 1). The different energy positions and amplitudes of the white lines at the Ce-L_{III} edge give rise to differences in the normalized absorbances of Ce^{III} and Ce^{IV}. The differences are largest at two specific X-ray incident energies, where the normalized absorbance of Ce^{IV} exceeds that of Ce^{III} by a maximum amount, and vice versa. The contrast in the absorbance of Ce^{III} and Ce^{IV} translates to a contrast in the emitted fluorescence intensity, which can be used to map the distribution of the two species at the spatial resolution given

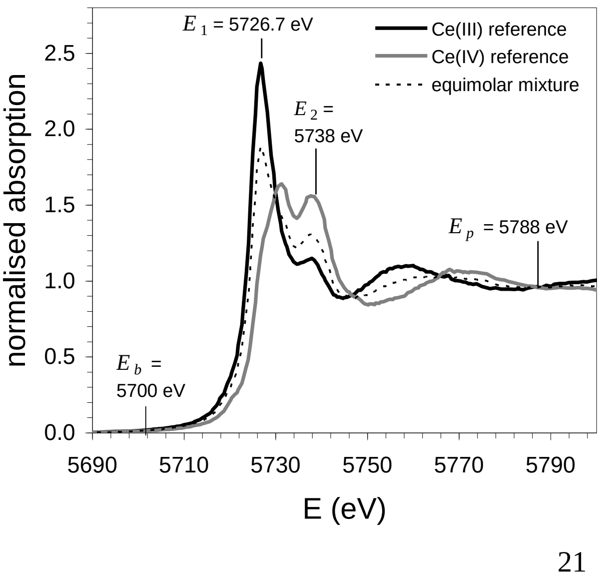

Figure 1. Experimental XANES spectra of $Ce^{III}_2(SO_4)_3$ and $Ce^{IV}O_2$, respectively, as well as of their equimolar mixture (50%-50%). These spectra were used to calibrate the Ce^{III}/Ce^{IV} distribution model. E_b is the beam energy used for background subtraction, E_1 and E_2 are the energies of maximum intensity contrast between Ce^{III}/Ce^{IV} and E_p is a selected energy of zero contrast used to map the total Ce concentration. μ-XRF maps were recorded at the 4 indicated X-ray energies over a common sample area in order to compute Ce^{III}, Ce^{IV} and Ce(total) distribution maps.

by the X-ray beam size. *Takahashi et al. (2002; 2007)* developed and applied a quantitative method to determine the Ce^{III}/Ce^{IV} ratios in natural rock samples based on the calibration of suitable reference compounds. The same method was applied to the investigated altered MW glass sample. Details on the implementation of the method can be found in *Curti et al. (accepted)*.

2. Results

2.1 STEM-EDS

In a preliminary STEM-EDS study (*Curti et al, (2006)*), the altered zone was found to consist dominantly of Mg-rich clay that envelope and partly cement the glass grains (Figure 2). Based on semi-quantitative analyses and conventional XRD, the clay was identified to have a smectitic composition close to montmorillonite, hectorite or saponite.

2.2 Mg-Na µ-XRF map, Ni-Mg µ-XANES

The combined µ-XRF map of the Mg-K_α and Na-K_α signals from the MW glass altered in water during 12 years (Figure 3a) reveals the granular structure of the glass powder and provides insights into the nature of the alteration process. The or-

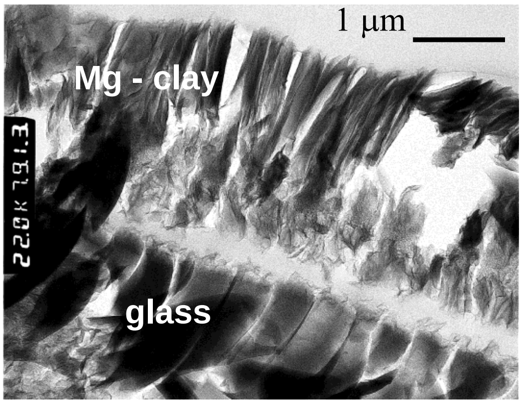

Figure 2. STEM image of the altered MW glass, showing the secondary Mg-clay minerals precipitated on its surface.

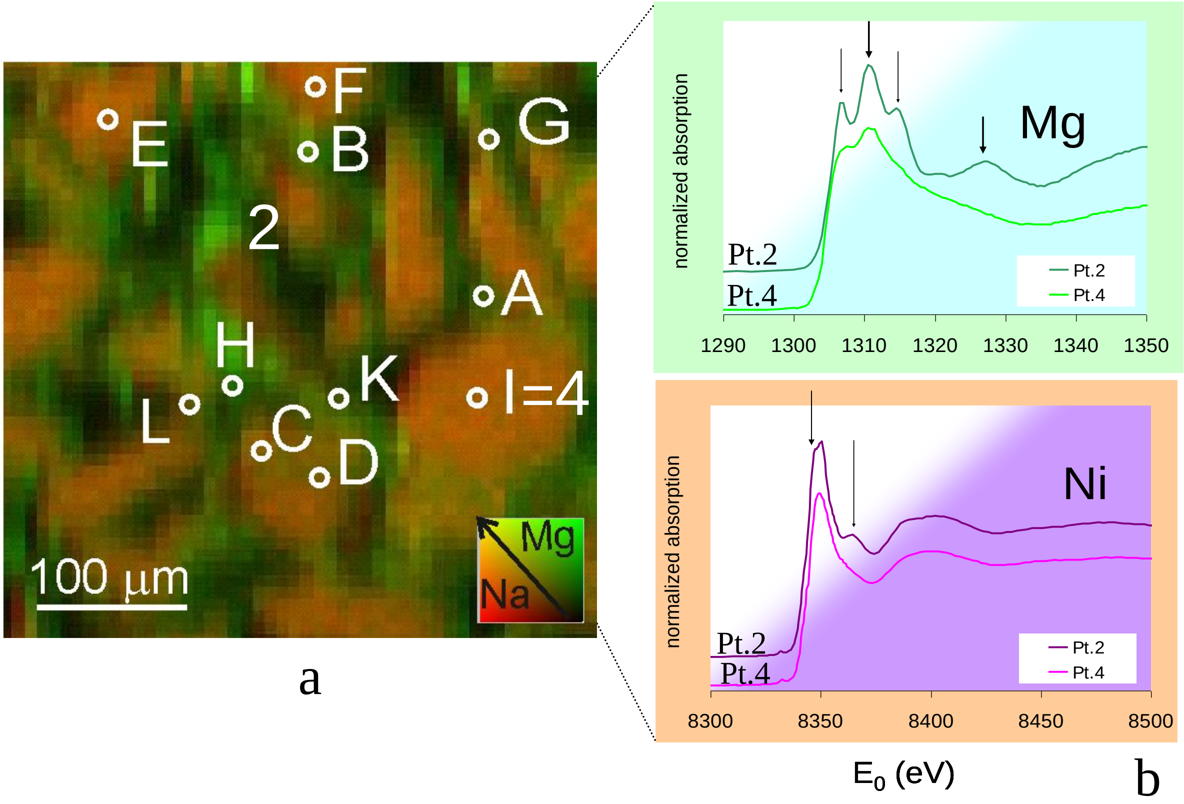

Figure 3 Mg-Na µ-XRF map and correlation with Mg-K and Ni-K spectra at the indicated locations, from Curti et al. (2009)

colored areas at the periphery of the glass fragments (partially filling the interstitial space) are Mg-rich and Na-depleted. Since Na and other alkalis are rapidly leached out during the aqueous alteration of silicate glasses via alkali-proton exchange (*Wicks et al., (1993)*), the interface between orange and green areas marks the reaction front of the glass corrosion reaction. Thus, the orange areas represent pristine glass apparently unaffected by the corrosion process, whereas the green-colored areas represent altered regions.

The Mg-K and Ni-K μ-XANES spectra recorded at the two locations indicated in the map are shown in Figure 3b. At location #4, which is representative of apparently intact glass, both spectra are "smooth" and resemble the Mg and Ni spectra recorded for the pristine (non-leached) MW glass, indicating that that the coordination environment of Mg and Ni were not affected by the aqueous corrosion process at that location. In contrast, both spectra recorded at spot #2 (Mg-rich, representative of altered glass) have features typical of clay minerals. Specifically, the resonances indicated with the arrows are multiple scattering effects typical of crystalline Mg-silicates (including Mg-clay minerals). Analogous spectroscopic features, typical of Ni associated to ordered clay minerals, are found in the Ni-K spectrum, suggesting a "clay-like" Ni environment.

A fit of the Ni-K edge μ-EXAFS spectrum collected at spot #2 (Figure 4) yielded interatomic distances and coordination numbers consistent with Ni either substituted into the bulk lattice of a 2:1 clay mineral (as solid solution), or adsorbed on edge sites of the clay surface (Table 1). No evidence was found for the formation of a Ni-rich phase, since Ni-Ni backscattering pairs could be excluded in the EXAFS analysis (*Curti et al. (2009)*).

Table 1. Results of a 3-shell fit of μ-EXAFS data collected at the Ni K-edge at location #2.

	N	R [Å]	σ^2 [Å^2]
Ni-O	5.3 ± 0.3	2.05 ± 0.01	0.006
Ni-Mg	3.1 ± 1.6	3.08 ± 0.03	0.008
Ni-Si	4.5 ± 1.6	3.26 ± 0.02	0.008

$\Delta E_0 = 2.8 \pm 1.7$ eV; S_0= *0.85;* R-factor = 0.020; reduced χ^2=6.26

N = coordination number, R = interatomic distance , σ^2 = Debye-Waller factors (fixed),
ΔE_0 = energy shift, S_0 = amplitude reduction factor

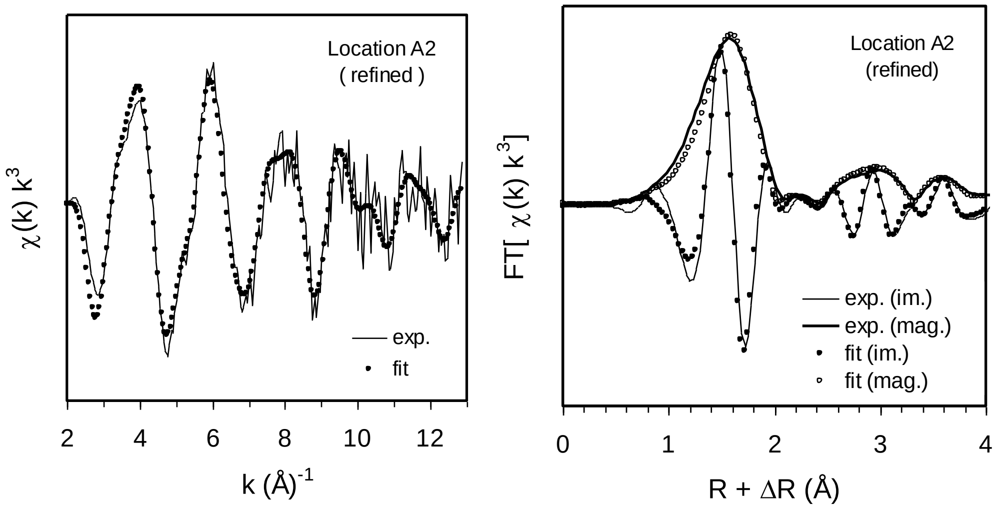

Figure 4. Fits of the Fourier transformed (FT) Ni K-edge μ-EXAFS spectra collected at spot #2, using the talc structure as starting model. Left: k^3 weighted normalized spectra; right: magnitude and imaginary part of FT, uncorrected for phase shift.

Figure 5a shows the spatial distribution and concentrations of Ce^{III}, Ce^{IV} and total Ce over the same sample area shown in Figure 3a. In this map, two color ranges (red-yellow and blue-cyan) sharply separate regions where Ce^{III}, respectively Ce^{IV} predominate. The total Ce concentration increases with the brightness of either color. According to the calibration made with the spectra of the two reference compounds $Ce^{III}_2(SO_4)_3$ and $Ce^{IV}_2O_4$, theoretically red-yellow areas refer to regions with $Ce^{III} > 50\%$ and blue-cyan areas to regions with $Ce^{IV} > 50\%$ i.e., the lines delimiting the two color ranges should be contours of equal Ce^{III} and Ce^{IV} concentration.

The comparison of the Mg-Na map with the Ce map readily shows that Ce^{IV} dominates in the non-altered core regions of the glass fragments, whereas the reduced Ce^{III} form prevails in the peripheral and interstitial regions rich in secondary clay. These results are confirmed by the µ-XANES spectra collected at representative locations (Figure 5b). The spectrum most closely matching that of $Ce^{IV}O_2$ was collected at the center of the largest glass shard (spot I) whereas spectra collected in peripheral or interstitial (Mg-rich) zones (spots A, B, C) bear more resemblance with the spectrum of $Ce^{III}_2(SO_4)_3$. Note that even spot I must contain some Ce^{III}, as evidenced by the negative shift of the first white line compared to the spectrum of $Ce^{IV}O_2$. The fact that the XANES spectrum recorded on a pristine, non-altered sample of the MW glass (thick broken line, Figure 5b) is identical to that of spot I is a clear indication for the presence of a native Ce^{III} component in the original glass.

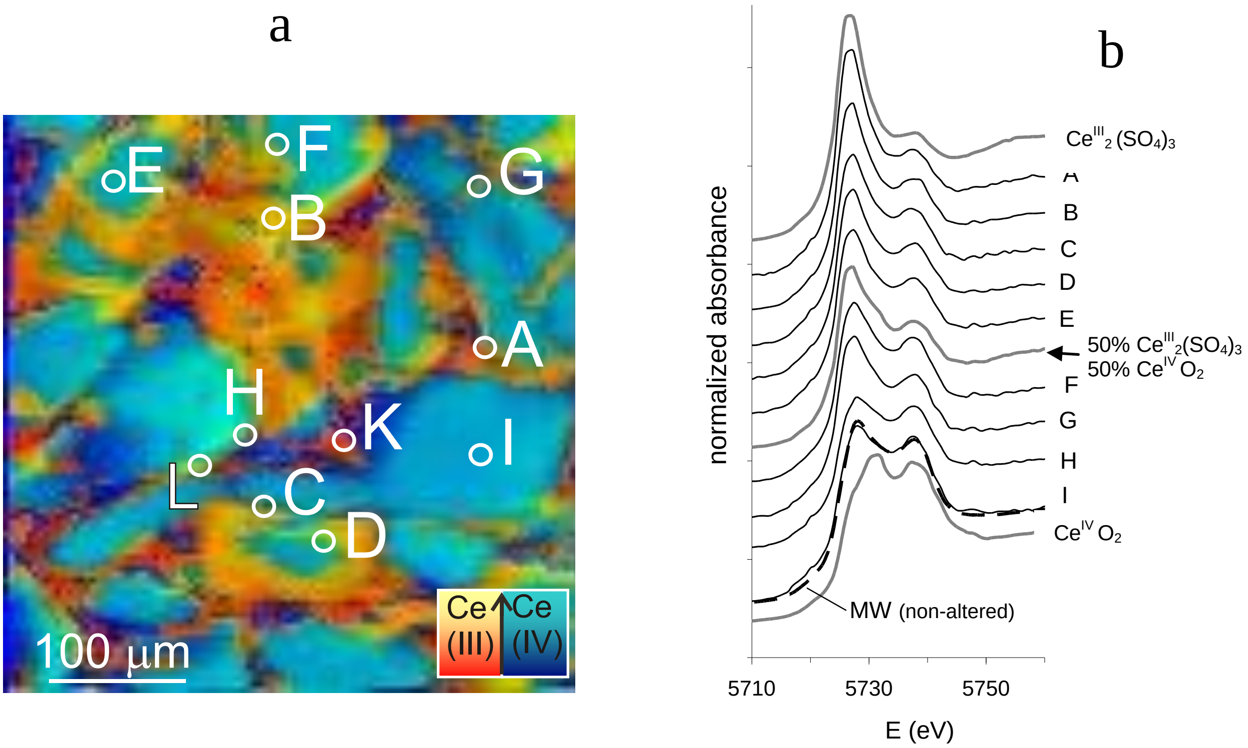

Figure 5. Combined map showing the distribution of Ce^{III} , Ce^{IV} and Ce(total) over the same sample area shown in the Na-Mg map (Figure 3a). (b) µ-XANES spectra measured at the locations indicated in the map on the left, compared with the XANES spectra of reference compounds and non-altered MW glass.

Summary and Conclusions

In this contribution, we present the results of X-ray spectroscopic investigations carried out at micrometric resolution on a simulated nuclear waste glass (MW) subject to aqueous alteration at 90 ^{o}C during more than 12 years. The alteration of such glasses is a geochemically complex process involving dissolution and partial re-precipitation, almost in situ, of minor elements such as Ni and Ce, which simulate radionuclides (^{59,63}Ni and Pu, respectively) occurring in real nuclear waste.
Detailed μ-XAS/XRF analyses, in combination with other techniques (XRD, STEM-EDS), allowed us to determine that Ni released from the glass is partly immobilized in Mg-rich smectites precipitated during the aqueous alteration of the MW glass, either through substitution in octahedral sites of the clay mineral lattice (as true solid solution), or adsorbed on edge surface sites. The Ce released from the glass was also found to be trapped as trace element in the secondary clay via reduction of Ce^{IV} to the less soluble Ce^{III}. The reducing agent was probably Fe(0) dissolved from the reaction vessel. This reaction suggest that Pu released from vitrified waste in a deep underground repository may also be stabilized to its sparingly soluble trivalent state via reduction by Fe(0) supplied from the steel canister. In both cases, no specific concentrated (Ni or Ce) phase was formed during the glass alteration process. Our study evidences the important role of clay minerals as alteration products of silicate glasses and host phases for radionuclides released from nuclear waste.

Acknowledgements

We are grateful to M. Marcus and S. Fakra (ALS, Berkeley) for their invaluable assistance during beamtimes and for providing the software used to create the chemical maps shown in this paper. F. Farges (National Museum of Natural History, Paris), M. Janousch (SLS, LUCIA beamline) and D. Kunz (Paul Scherrer Institut) are greatefully acknowledged for their precious support and help during data collection campaigns. Many thanks are due to J.L. Crovisier, A.M. Karpoff and G. Morvan (University of Strasbourg) for careful sample preparation and the collection of STEM-EDS data.

References

Curti E., Crovisier J. L., Karpoff A. M. and Morvan G. (2006). Long-term corrosion of two nuclear waste reference glasses (MW and SON68): a kinetic and mineral alteration study. Appl. Geochem. 21, 1152–1168.

Curti E., Dähn R., Farges F. and Vespa M. (2009). Na, Mg, Ni and Cs distribution and speciation after long-term alteration of a simulated nuclear waste glass: A micro-XAS/XRF/XRD and wet chemical study. Geochim. Cosmochim. Acta 73, 2283–2298.

Curti E., Grolimund D. and Borca C. (accepted). A micro-XAS/XRF and thermodynamic study of CeIII/IV speciation after long-term aqueous alteration of simulated nuclear waste glass: relevance for predicting Pu behaviour? Appl. Geochem.

Nagra (2002) Project Opalinus Clay - Safety Report, Technical Report NTB 02-05, Nagra, Wettingen, Switzerland

Takahashi Y., Sakami H. and Nomura M. (2002). Determination of the oxidation state of cerium in rocks by Ce LIII-edge X-ray absorption near-edge structure spectroscopy. Anal. Chim. Acta 468, 345–354.

Takahashi Y., Manceau A., Geoffroy N., Marcus M.A. and Usui A. (2007). Chemical and structural control of the partitioning of Co, Ce, and Pb in marine ferromanganese oxides. Geochim. Cosmochim. Acta 71, 984-1008.

Wicks G.G., Lodding A.R. and Molecke M.A. (1993). Aqueous alteration of nuclear waste glasses and metal package components. MRS Bull. XVIII(9), 32-39.

Witherspoon P.A. and Bodvarsson G.S. (2006). Geological Challenges in Radioactive Waste Isolation – Fourth Worldwide Review. LBNL-59808, Lawrence Berkeley National Laboratory and University of California, Berkeley, U.S.A., 295 p.

3D Chemical Information in Clays Using Synchrotron Techniques

Melissa A. Denecke[*], Thorsten Schäfer

Karlsruhe Institute of Technology, Institute for Nuclear Waste Disposal (D)

[*] Corresponding author: email address

Abstract

In this presentation, two examples exploiting these advantages of using focused beams and especially X-rays for understanding actinide geochemistry in heterogeneous, natural geological media (sediment and granite), necessary for establishment of reliable predictive models required for designing safe nuclear disposal concepts and assessing associated potential long-term hazards. Combining spectroscopic results from focused IR radiation and X-rays in both the hard and soft (C 1s) regimes in the first example reveals the speciation of U in U-rich argillaceous sediment to be a nanoparticulate tetravalent UO_2-like phase, which is associated with light elements and organic material. This allows a tentative hypothesis for U immobilization in the sediment involving the organic material associated with the clay. The second example specifically deals with characterizing an immobile actinide (Np) species in a granite column following a tracer experiment. These results will be presented orally and are not found in the abstract below; information can be found in (Denecke et al. 2009, 2011). The talk will conclude with an outlook of the exciting opportunities offered by emerging X-ray sources such as the new PETRAIII facility at the Deutsches Elektronen-Synchrotron (DESY).

Introduction

The goal of geochemical speciation investigations related to deep geological nuclear waste disposal often is to identify and characterize the long term determinant behavior of actinide transport in geological media, requisite to establishing reliable prognoses of proposed repository sites. Because these studies involve natural systems with inherent heterogeneity (multi-component systems), spatially resolved speciation techniques are essential. Focused X-ay techniques are becoming an increasingly used tool. The advantage of using X-rays is their high penetration capability and that in situ investigations are possible due to elimination of a vacuum requirement, thereby avoiding invasive sample preparation. The advantage of using a focused beam is that small volumes can be probed. This is not only important for studying heterogeneous samples but also applicable for sample environments with limited space, and to reduce the amount of activity in an experiment for radiological safety reasons (ALARA principle).

Investigations of actinide geological transport in the context of nuclear waste disposal are especially challenging, as an accurate prognosis demands process understanding over an immense time domain. One strategy for meeting this challenge is through investigation of geological natural analogs, which mimic repository geochemical and geological conditions on a geological time scale. Knowledge gained from natural analogs can be used to span the long time scales in a top down approach for predicting repository radiological safety. In order to reliably predict evolution on very long time scales, knowledge of the primary reactions and processes determinant in the fate of radionuclides released into the environment (e.g., sorption, precipitation, solid solution formation reactions) is required, often under non-equilibrium conditions. To this end, as well as for site specific characterization method development, we investigate actinide transport in column tracer studies, which are models simulating actinide release (plume). The following discussion is divided according to these two major investigative themes. Recent, new results obtained on natural U-rich argillaceous sediment high in organic matter are presented in detail. A short summary of results from investigations of granite column following a radionuclide trace investigation are then presented. These examples should lend an impression of the information available from such spatially resolved investigations. The ultimate goal of these studies is to advance development of thermodynamic/kinetic descriptions used for modeling/prediction of actinide transport processes at varying spatial and temporal scales, with a reliable estimate of uncertainty.

Natural analog from the Permian Lodève Basin in France

Recently we have performed spatially resolved -ray fluorescence and X-ray absorption fine structure investigations with a micrometer-scale resolution (µ-XRF and µ-XAFS, comprised of the near ionization threshold energy region, XANES, and the extended energy region, EXAFS) on two uranium-rich clay samples originating from Autunian shales in the Permian Lodève Basin (France), provided by CREGU (Centre de Recherche sur la Géologie des Matières Premières Minerals et Energétiques). This argillaceous formation is a natural U deposit (or mineralization) associated with organic matter (bitumen) (Marignac et al. 1999, Mathis et al. 1990). The goal of this study is to determine the U oxidation state in the sample and to ascertain if any correlation between the U distribution and that of other elements present in the organic-rich fine-grained pelites exists, which might give us insight into the mechanism of U immobilization through either adsorption/co-precipitation with iron hydroxides and/or clay minerals. To this end, we use focused radiation in the X-ray, the soft X-ray and the infrared (IR) regimes in scanning mode to obtain spatially resolved information in the heterogeneous samples.

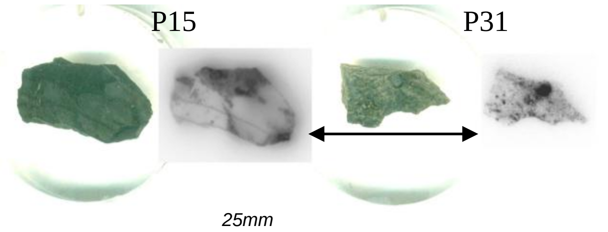

Figure 1. Photographs of the samples studied embedded in acrylic (designated P15 and P31) and their corresponding radiographic images.

Autoradiographic images and photographs of the samples are shown in Figure 1. Uranium-rich areas of the sample or hot spots are visible as dark spots in the autoradiographic images. Quantification of the hot spots show they contain ~2 mg 238-U/g material (sample marked P31) and ~25 mg 238-U/g material (sample P15).

1.1 Experimental

µ-XRF and µ-XANES measurements are recorded at Beamline L at the Hamburger Synchrotron Labor (HASYLAB). A confocal irradiation-detection geometry is used, providing added depth information and allowing probing sample volumes below the surface, thereby avoiding any surface oxidation artifacts caused by cutting and polishing the clay sample. A schematic drawing of the confocal set-up along with photographs is depicted in Figure 2. The sample is fixed onto a slide frame with polycarbonate tape and mounted on a x,y,z positioning stage so that the sample surface is 45° to the incident beam. The incident radiation is focused with the primary polycapillary (PC1) half-lens mounted on a hexapod positioning unit. The secondary polycapillary (PC2) half-lens is attached to the "nose"-end of the fluorescence detector. In these experiments a Si drift detector (Vortex, SII NanoTechnology USA Inc., Northridge, CA) is used. The volume probed in the sample is defined by the PC1 focus (full-width at half maximum, FWHM) and the PC2 focus. The focal spot diameter is approximately 16 µm

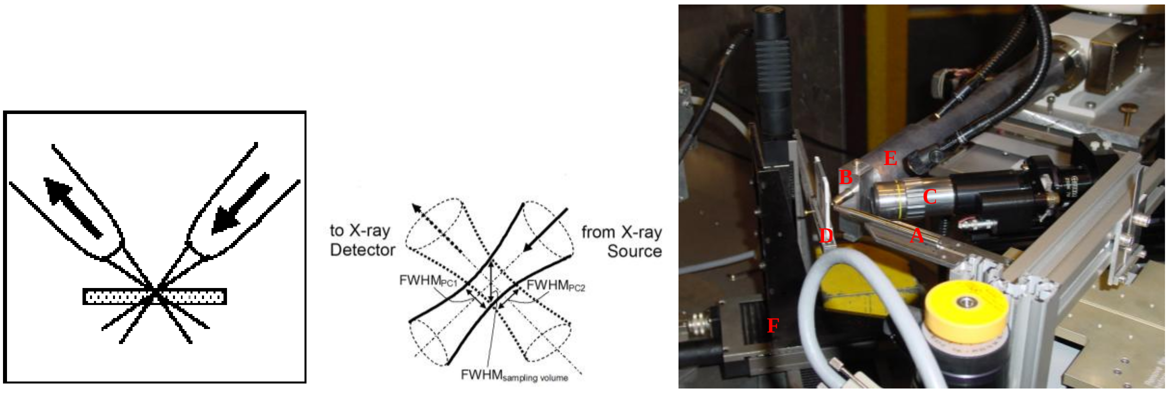

Figure 2. Schematic representation of the confocal set-up (top, left), the sampling volume defined by the primary polycapillary (PC1) half-lens focus (full-width at half maximum, FWHM) and the secondary polycapillary (PC2) half-lens (top, right), and a photograph of the experimental set-up used (bottom). A: PC1 half-lens, B: PC2 half-lens C: microscope, D: sample mounted on a slide frame, E: detector head with lead shielding, F: sample positioners.

and the depth resolution estimated to be 20 to 30 µm (Figure 2). By scanning arbitrary sample areas (x,y scans) at different depths (z) using the confocal setup, stacks of tomographic cross sections can be easily recorded (Denecke et al. 2005, Janssens et al. 2004). We used a band pass of wavelengths with an average weighted energy of 17.6 keV delivered by a Mo/Si multilayer pair (AXO Dresden GmbH, Germany) as excitation source to extract elemental distribution maps is selected sample volumes by plotting recorded relative fluorescence intensities for individual elements in each pixel and scaling them with a linear color code, with dark pixels corresponding to high count rates. U L3 µ-XANES are recorded using monochromatic X-rays at selected sample volumes of high U concentration identified in the µ-XRF maps.

Both XANES and EXAFS are measured at positions of high U concentration at the INE-Beamline at the Ångströmquelle Karlsruhe, ANKA (Dardenne et al. 2009), which are identified by recording line scans of windowed U Lα counts registered with a high purity Ge detector (Canberra). The measured beamspot used at the INE-Beamline is 300µm. Si(111) and Ge(422) crystals are used in the double crystal monochromator at HASYLAB and ANKA, respectively, and the energy is calibrated relative to the first inflection point in the K XANES of a Y foil (defined as 17.038 keV).To record scanning µ-XRD images, a Mo/Si multilayer pair with a small band pass of wavelengths centered at 17.4 keV, focused to 15 µm by means of an elliptical single-bounce monocapillary, and a high resolution CCD camera (MAR CCD, MARUSA Co.) positioned 278 mm behind the sample are used. The exposure time was 10 s. The incident beam

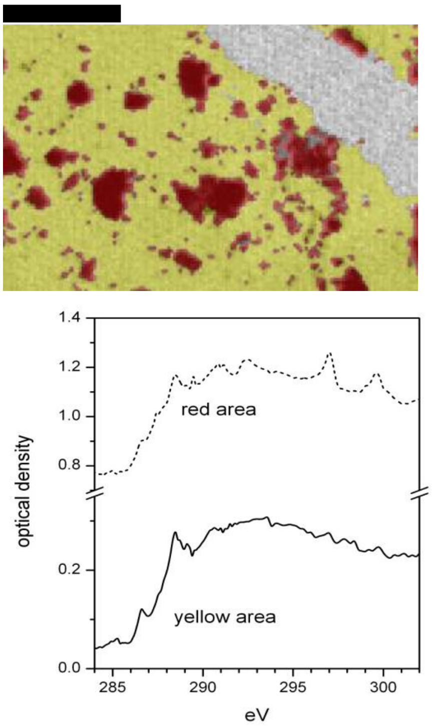

Figure 3. (top) STXM PCA and cluster analysis results showing two distinguishable clusters in the distribution of organic functionality. No C absorption is in the grey area. The black scale bar is 10 µm. (bottom). Average C(1s) XANES of the yellow and red areas.

energy, experimental geometry and detector parameters are calibrated against the pattern measured for LaB_6 (lattice parameter= 0.415690 nm, ICSD data sheet 340427). Experimental details and analysis are found in (Denecke et al. 2009b).

Scanning transmission X-ray microscopy (STXM) investigations are conducted on the X1A1 undulator beamline at the National Light Source Synchrotron (NSLS), operated by the State University of New York at Stony Brook. The principle of this technique is described in detail elsewhere Jacobsen et al. (1998). For STXM and µ-FTIR measurements, transmission mode ~100 nm thick sulfur embedded ultra-microtomes mounted on copper TEM grids are prepared (MVA, Inc., Norcross, GA, USA). Carbon K and potassium L-edge spectra are recorded at an undulator gap of 36.8 mm. The Fresnel zone plate used at X1A1 has a diameter of 160 µm and an outermost zone width of 45 nm. The spherical grating monochromator energy is calibrated using the CO_2 gas absorption band at 290.74 eV (Hitchcock & Mancini 1994).

µ-FTIR measurements are performed at beamline U10B (NSLS) using a Nicolet Magna 860 Step-Scan FTIR instrument coupled to a Spectra-Tech Continuum IR microscope, which is equipped with a 32x Schwarzschild objective and a dual remote masking aperture (Dumas & Miller 2003). Data acquisition is controlled with the Atlµs software (Thermo Nicolet Instruments), using a 8 µm x 8 µm aperture and 1024 scans per point in the mid-IR range (600 to 4000 cm^{-1}), under transmission mode with 4 cm^{-1} spectral resolution. The background signal is measured in sample-free regions of the TEM grid.

1.2 STXM and IR results

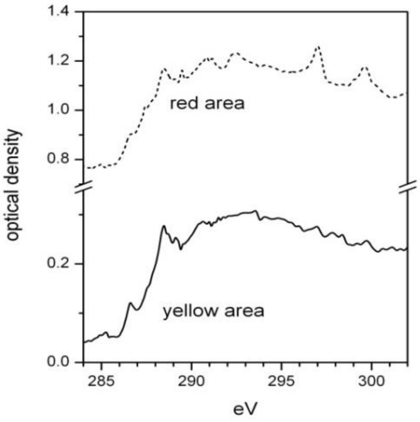

The results of principle component analysis (PCA) and cluster analysis of STXM data ( ) reveal two areas marked yellow and red differing in their optical density (OD) and K content. The red areas exhibit a significantly higher OD below the carbon K-edge and absorption bands at K $L_{2,3}$-edge energies. This indicates that this organic material is associated with clay minerals possibly of illite-type. These areas also show a relatively large edge indicating that the clay is associated with rather large amount of organic material. The yellow areas are additional organic material not directly associated to these mineral phases. They have low OD below the carbon edge, which might indicate that they are of almost pure organic nature. The average cluster C(1s)-edge spectra extracted from both regions are generally similar, with yellow areas appearing to have a higher aromatic content (absorption at 285 eV) and the illite-clay associated organics in the red areas a higher

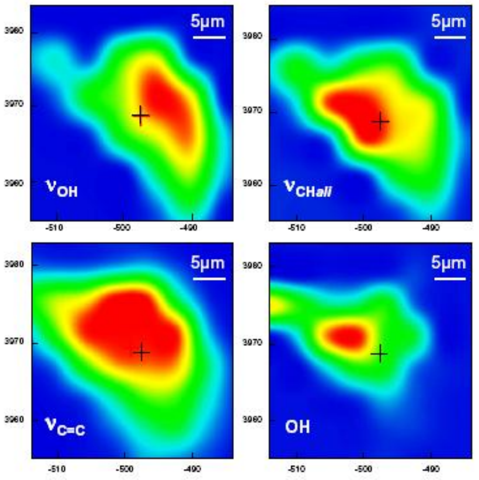

Figure 4. Maps of organic functional group distributions extracted from µ-FTIR data: alcohols (ν_{OH}; 3600-3100 cm^{-1}), aliphatics (ν_{CHali}; 3000-2800 cm^{-1}) and aromatics ($\nu_{C=C}$; 1750-1500 cm^{-1}), as well as OH vibrations of clay minerals (‘OH’ 3720-3680 cm^{-1}).

aliphatic character or metal complexation (absorption in the 287 eV region (Plaschke et al., 2005).

In IR spectral maps are extracted from scanning μ-FTIR data (Figure 4) to image the spatial distribution of functional groups in the sample including aliphatics ($\nu_{CH\mathit{ali}}$; 3000-2800 cm^{-1}), aromatics ($\nu_{C=C}$; 1750-1500 cm^{-1}), alcohols (ν_{OH}; 3600-3100 cm^{-1}) or OH vibrations of clay minerals (‘OH’; 3720-3680 cm^{-1}). We observe a correlation between the clay mineral vibration bands (‘OH’) and the organic matter functionalities ($\nu_{CH\mathit{ali}}$, $\nu_{C=C}$, ν_{OH}) in these distribution maps. This is accordance with the K (i.e., illite-type clay mineral) – organic matter correlation observed in the STXM results.

1.2 μ-XRF, μ-XANES, μ-EXAFS and μ-XRD results

The measured distributions for K, Ca, Ti, Fe, Zr, and U in the area with the highest radioactivity at the top of sample designated P15 are shown in Figure 5. These distributions demonstrate three general observations from this sample: 1) distinct patterns of element distributions are observed, despite the sample’s general heterogeneous optical appearance 2) the U distribution is often correlated with the distributions of lighter weight elements K, Ca, and Ti (especially notable in the round features in the upper right corner of the maps) and 3) the U distribution is generally inversely correlated to areas of high Fe content.

A comparison of elemental distributions for an area of sample P31 is depicted in Figure 6. A red-green-blue (RGB) overlay image of regions exhibiting the highest Ti, Fe, and U fluorescence intensities, respectively, is also shown. We observe a direct correlation between Ti and U, visible as purple areas in the RGB image, but none between Fe and U; the Fe-rich areas remain green in the RGB overlay. As opposed to the positive correlation between Ca and U qualitatively observed in the distributions shown in Figure 5 for sample P15, no correlation between Ca and U is observed here.

In order to determine the valence state of the U in the pelites, U L3 μ-XANES (Figure 7) and μ-EXAFS are recorded at volumes and areas with high U L_α intensity. The energy position of the most prominent absorption peak in the XANES (the white line, WL) measured for three different sample regions at two different beamlines all lie within less than 1 eV of that for the U(IV) reference. The XANES features themselves also provide further evidence that the U hot spots contain U(IV). No multiple scattering feature at around 10 eV above the WL, indicative of U(VI) (Denecke et al., 2006), is

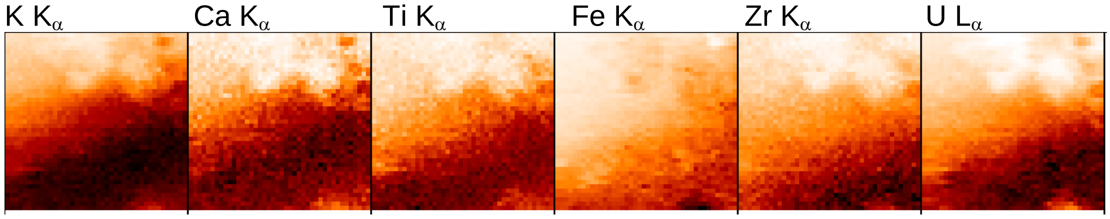

Figure 5. Distribution maps for the elements indicated in a 800 x 760 μm^2 section (20 × 20 μm^2 step size), recorded near the surface of sample P15.

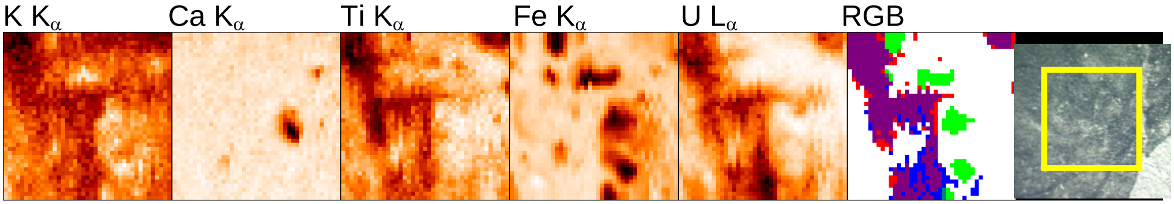

Figure 6. Distribution maps for K, Ca, Ti, Fe, and U in a 400 x 400 μm^2 section (10 × 10 μm^2 step size, 1s counting time), recorded under the surface of the P31 sample area marked in the microscope image at far right. A red-green-blue (RGB) overlay image for regions of highest Ti, Fe, and U concentrations is also shown.

observed. We conclude from XANES results in Figure 7 that U is likely present in the sample in the tetravalent state.

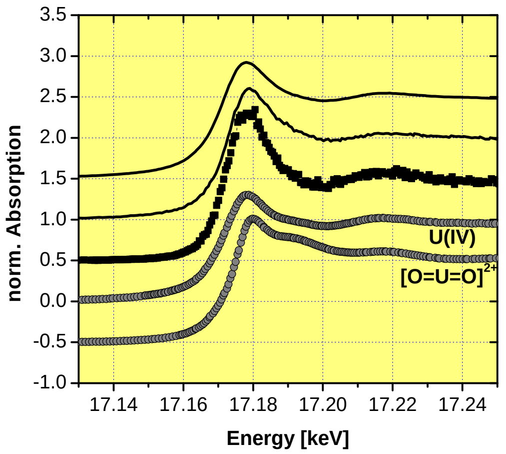

Figure 7. U L3 µ-XANES recorded at U hot spots with a microfocus at Beamline L (symbols) and with a 300 µm beam spot at the INE-Beamline at ANKA (lines) compared to two U(IV) and U(VI) reference spectra (bottom).

This interpretation is corroborated by the U L3 EXAFS spectrum. The data is well fit beginning with a structural model similar to uraninite, UO_2 (Rundel et al., 1948). Best results are obtained with 4-5 O atoms at 2.29 Å with σ^2 = 0.013 Å^2 and 2-3 U atoms at 3.78 Å with σ^2= 0.008 Å^2. The distances are 2-3% smaller than expected for UO_2 and the intensities lead to a much smaller coordination number than expected (N(O)=8; N(U)=12). This may indicate the UO_2-like phase is present as a nano-particulate material with large surface area having relaxed (shortened) distances at the surface. Note that no short U-O distance expected for the U(VI) uranyl moiety is found in the EXAFS spectrum (Denecke 2006).

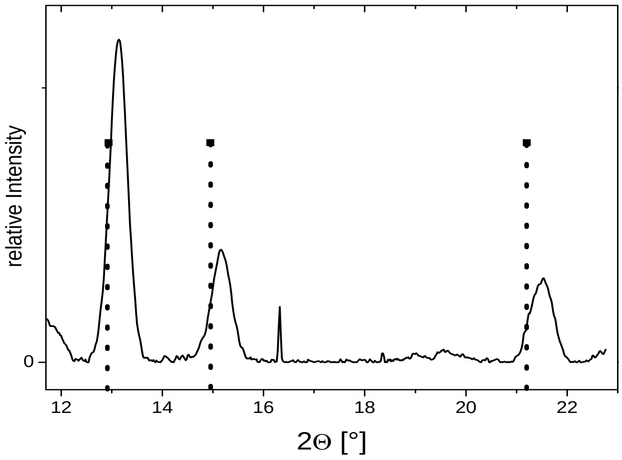

Figure 8. One dimensional µ-XRD obtained from summed diffraction images of U-rich pixels. The dotted vertical lines show the expected values for uraninite (Rundel et al. 1948).

We conclude from both the XANES and EXAFS results that the U in this clay formation is tetravalent. In the area investigated with EXAFS it found to be present as a UO_2-like phase, most likely nanocrystalline. In order to confirm this, we registered µ-XRD images over a 1000 x 1000 µm area and summed up numerous images in areas of high U fluorescent intensity. The 1D diffractogram extracted from a powder ring pattern from such a U-rich area is shown in Figure 8. The decrease in interatomic distances observed in the EXAFS is also reflected in the µ-XRD pattern. The expected 2Θ positions for uraninite drawn in Figure 6 show an obvious shift of the (111), (002) and (022) peaks for the UO_2 in the clay sample to higher 2Θ values, indicating approximately a 2% shortening of the lattice parameter and associated shortening of interatomic distances to values similar to those determined in the EXAFS analysis.

1.3 Conclusions

The U distribution in our sample is observed to be positively correlated to the distribution of lighter weight elements using different techniques. Furthermore, there is a correlation between clay minerals of illite-type and organic matter in the sample. This observation is based on both the STXM result that K (as indicator element) is found associated with organic carbon and the observed spatial coincidence between µ-FTIR clay 'OH' vibrations and vibrations of organic functional groups. From the µ-XAFS and µ-XRD analyses, we find that the U is present in its tetravalent form, likely as a nanoparticulate oxide.

Combining these observations allows us to offer a tentative hypothesis for the mechanism of uranium immobilization. Because no correlation between U and Fe was observed, we exclude ferrous minerals as the dominant reducing agent during immobilization of groundwater dissolved U(VI) to less soluble U(IV). Combining the knowledge that U is found associated with K and that clay minerals of illite-type are associated with organic matter we conclude that organic material associated with clay minerals might have been the reducing agent. This hypothesis remains to be tested and a number of open questions remain. For example, what role did the clay play? Did it act as a catalyst (Giaquint et al., 1997) or did it serve simply as an anchor for the organic material?

Reference

Denecke M.A., Brendebach B., De Nolf W., Falkenberg G., K. Janssens, Simon R. (2009) Spectrochim. Acta B 64, 791-795.

Denecke et al., in Section 4“Environmental Behavior of An Colloids and Nanoparticles „ Actinide Nanoparticle Research, Kalmykov&Denecke (Eds), Springer (2011)

Marignac C., Cuney, M. (1999) Mineralium Deposita 34, 472-504.

Mathis V., Robert, J.-P., Saint Martin, (1990) J Chron. Rech. Min. 499, 31-40.

Denecke M.A., Janssens, K., Proost, K., Rothe, J., Noseck, U. (2005) Environ. Sci. Technol. 39(7), 2049-2058.

Janssens K., Proost K., Falkenberg G. (2004) Spectrochim. Acta B59, 1637-1645.

Dardenne K, Brendebach B, Denecke M.A, Liu X, Rothe J, Vitova T (2009) New developments at the INE-Beamline for Actinide Research at ANKA, Journal of Physics: Conference Series 190, 012037.

Denecke M.A., Michel P., Schäfer T., Huber F., Rickers K., Rothe J., Dardenne K., Brendebach B., Vitova T., Elie M. (2009b) Spatially resolved XRF, XAFS, XRD, STXM and IR investigation of a natural U-rich clay, J. Physics: Conference Series 190, 012187.

Jacobsen C et al. (1991) Optics Commun. 1991 86 351-364.

Hitchcock A P and Mancini D C 1994 J. Electron Spectro. Related Phenom. 67 1-132.

Dumas P and Miller A (2003) Vibrational Spectrosc. 32 3-21.

Plaschke M, Rothe J, Altmaier M, Denecke M A, Fanghänel T 2005 J. Electron Spectro. Related Phenom. 2005. 148151-157.

Denecke, M.A. (2006) Coord. Chem. Rev. 250, 730–754.

Rundel R.H., Baenzinger N.C., Wilson A.S., McDonald R.A. (1948) J. Amer. Chem. Soc. 70(1), 99-105.

Application of NanoSIMS on Organo-Mineral Structures

Carmen Höschen*, Carsten W. Mueller, Katja Heister, Johann Lugmeier
and Ingrid Kögel-Knabner

Lehrstuhl für Bodenkunde, TU München, 85350 Freising-Weihenstephan, Germany (DE)

* Corresponding author: hoeschen@wzw.tum.de

Abstract

The elemental interaction in soil material happens on extremely small scales due to soils submicron particle size. As all chemical elements and their isotopes can be present in soil samples, and isotope enrichment can be used for tracing, the secondary ion mass spectrometry is the technique of choice to visualize elemental and isotopic distribution. SIMS sputters surface atoms and registers them in accordance to their atomic mass.

With the Cameca NanoSIMS an instrument with very high lateral resolution of down to 50 nm and additionally very high mass resolving power is available. This allows for visualising the elemental and isotopic distribution inside a sample although absolute quantification can hardly be achieved. For quantitative analysis measurements have to be compared to known standard samples. Therefore perfect crystallographic preparation is required to avoid sputter enhancement on topographic features.

Measurement data is available in binary format and can be processed by any image processing software providing adequate input filters.

Applications on montmorillonite soil fragments and organo-mineral structures are presented revealing the lateral resolution of the NanoSIMS technique and confirming their application to soil samples.

The technique also seems to be promising for the investigation of material transport on small lateral scale in clay material.

Introduction

The Lehrstuhl für Bodenkunde at WZW Freising, TU München, is running a NanoSIMS 50L instrument since March 2010. The investigations are focused on samples revealing answers to questions from soil sciences.

The NanoSIMS technology developed over the last years based on the SIMS technique delivers results about the elemental and isotopic composition at a high lateral resolution down to 50 nm.

1. SIMS Technique

1.1 SIMS principle

SIMS is short for secondary ion mass spectrometry. A primary ion beam hits a samples surface and releases particles from the sample. A fraction of these particles, atoms and molecule fragments, leaves the sample ionized and forms the secondary beam which can be analysed in a mass spectrometer.

Sputtering

Ions extracted from an ion source are accelerated to several keV towards the sample. The fast ions penetrate the sample up to a depth of several 10 nm. They lose their energy in collision cascades. The cascades can reach back to the samples surface and a surface atom or molecule fragment can be ejected. This process is called sputtering.

Thus, this technique is destructive although only very small sample volumes are consumed. Reaching a higher depth is mainly a question of primary ion current and time.

Secondary ion formation

A small fraction of about one percent of the sputtered particles leaves the surface ionized. To achieve a high secondary ion yield Cesium or Oxygen are often used as primary ions. These reactive elements get enriched in the investigated region during measurement enhancing the ionization.

Secondary beam analysis

The secondary ions are accelerated towards a mass spectrometer setup and can be analyzed by their mass to charge ratio. This allows estimating elemental and isotopic composition of the sample.

1.2 NanoSIMS 50L

The NanoSIMS 50L instrument from Cameca (Figure 1) uses a common coaxial setup for the primary and the secondary beam. This enables for highly efficient secondary ion collection, thus allows reducing the primary current to a minimum for best focusing of down to 50 nm spot size using Cs as primary ion.

Figure 1. NanoSIMS instrument (NanoSIMS 50L #23, Cameca) at Lehrstuhl für Bodenkunde, WZW Freising, TU München, Germany.

Under standard measurement conditions using about 1 pA Cs^+ ion beam the lateral resolution ranges between 100-200 nm, calculated according to the knife edge method (Figure 2).

Working with the O^- primary beam (about 6pA) the lateral resolution is poorer.

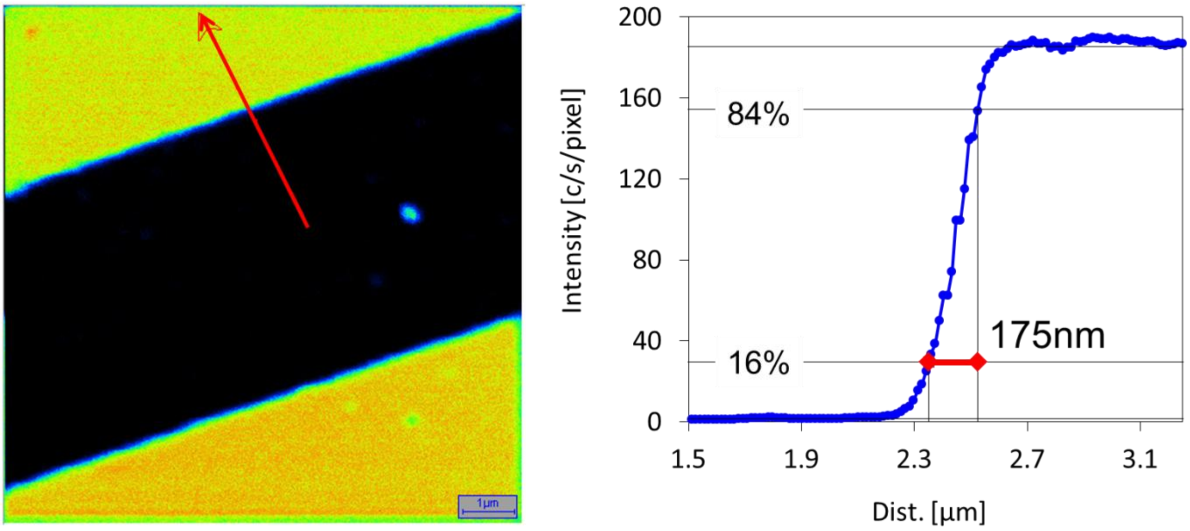

Figure 2. Lateral resolution estimation for standard working conditions, Cesium$^+$, 1 pA, field of view: 10 x 10 µm, 512 x 512 pixel, acq. time: 4.5 min.

A second feature of this instrument is the large magnetic mass spectrometer with seven independent detectors. The simultaneous measurement of multiple species permits for accurate analysis of elements originating from the identic sample volume.

One benefit of the NanoSIMS device is working at high mass resolution while still having high transmission. With all apertures open (100% transmission) the mass resolving power (MRP) is about 2500 ($m/\Delta m$), while narrowing some slits to have an MRP of about 6000 the transmission only decreases to 55%. As example, mass interferences at mass number 43 solved by the NanoSIMS technique will be shown. In soil samples element associations like $^{12}C^{31}P$, $^{27}Al^{16}O$, $^{12}C^{16}O^{15}N$ and $^{30}Si^{12}C^{1}H$ are common. Their differentiation needs an MRP of about 16000. By choosing the right beam deflection in front of the detector it is possible to measure these masses independently.

1.3 SIMS constraints

1.3.1. SIMS

The SIMS technique delivers results which are qualitative or semi quantitative. The ionization efficiency of the elements highly depends on the surrounding elemental composition (matrix effect). The absolute quantitative determination of the elemental composition at high precision is hard to obtain and implicates careful measurements of standard materials having a known composition very similar to the investigated sample (Düsterhöft et al. (1999)).

Isotopic ratio estimations can be influenced by the topography of the sample (Kita et al. (2009)). For quantitative measurements flat polished samples are required.

Artifacts could appear by analyzing nonconductive samples due to charging effects. Surface charging of the sample strongly influences the secondary ion formation. By coating the sample with a gold layer and/or using an electron flood gun charging can be compensated.

1.3.2 NanoSIMS

Due to the coaxial setup the primary and secondary beams have to have opposite charge. It means that by using the Cs source, (Cs^+ primary beam) only the negative secondary ions can be extracted and counted, e.g. $^{12}C^-$, $^{16}O^-$, $^{28}Si^-$, and vice versa in the case of working with the Oxygen source, e.g. $^{24}Mg^+$, $^{28}Si^+$, $^{40}K^+$.

Species with masses between 1 and 400 amu can be analyzed by NanoSIMS. Due to its magnet size and the physical size of the detection system (trolleys) there are some constraints regarding the masses measured simultaneously. The minimum mass interval between two neighboring detections depends on the maximally measured mass. Up to mass 58 each mass differing by 1 amu can be registered. At higher masses the interval increases. The highest detectable mass is related to the smallest required mass in accordance to the relation: $M_{max} = M_{min} * 21$.

2. Sample requirements

The samples to be investigated by NanoSIMS technique have to meet special requirements. Because the analysis occurs in ultra-high vacuum (10^{-10} to 10^{-11} mbar) the sample must be vacuum resistant and non-degasing. To get accurate measurements it is required to have a flat polished sample surface. The sample should be electrically conductive. If this is not the case charging effects could be compensated by coating the sample with a gold layer (about 30nm) and complementary using the electron flood gun (only in Cs^+ mode).
In the analysis chamber the sample has an upright position. This imposes that the sample must be well fixed to the sample holder to not fall down. Only specific sizes for the sample or sample carrier can be loaded (10 mm, ½ inch, 1 inch diameter).

Due to the small scale investigation a good documentation of the investigated area by other microscopic techniques like optical microscopy or scanning or transmission electron microscopy is strongly recommended.

3. Data processing

The NanoSIMS 50L offers several modes of analysis. The mostly used mode is the imaging mode. In this mode up to seven elemental images and one secondary electron image of the sample surface are generated by scanning the beam. The number of counts per pixel is registered together with the corresponding measurement time. The data files can be opened either by special Cameca analysis software or, with adequate import filters, by any other image processing software. Image processing allows for any calculations like element or isotope ratios, threshold settings or drift corrections as beam drifts can occur in long term measurements.
Achieving better counting statistics within shorter time only single lines or points on the sample can be measured (Line scan/spot mode).
Recording multiple images over time allows for the reconstruction of depth profiles.

4. Application examples

Examples of the application of the NanoSIMS technique with the NanoSIMS 50L instrument at the Lehrstuhl für Bodenkunde at WZW Freising, TU München, are presented.
Besides the simple elemental mapping of known minerals, e.g. montmorillonite (Figure 3.), the technique gives information on interfaces developed after the incubation of artificial soils. Organic matter was found to occur in patchy structures attached to clay minerals (Heister et al. (2012)).
By the application of organic matter enriched in ^{15}N (algal amino acid solution) to natural soil (Haplic Chernozem) aggregates, we were able to track the incorporation (possible diffusion) of fresh organic matter (OM) (indicated by ^{15}N) into soil aggregates and therefore the new formation of interfaces at particulate OM within aggregated soil spheres. By the calculation of the $^{15}N/^{14}N$ ratio a locally high enrichment of ^{15}N was demonstrated for the inner sphere of the soil aggregate (Mueller et al. (2012)).

Table 1. Chemical composition of montmorillonite in % (Heister et al. (2012))

SiO_2	Al_2O_3	TiO_2	Fe_2O_3	MgO	CaO	Na_2O	K_2O
69.8	15.3	0.1	1.0	3.4	1.9	0.9	0.9

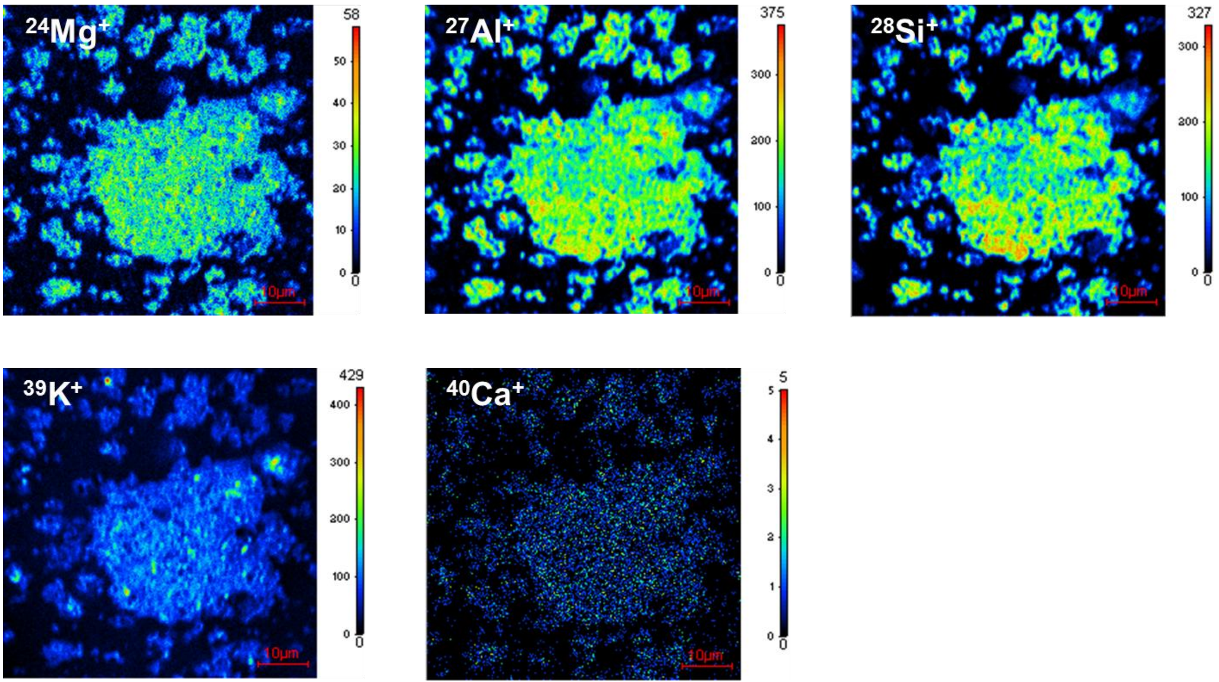

Figure 3. NanoSIMS images (60x60µm, 512x512 pixel) of the $^{24}Mg^+$, $^{27}Al^+$, $^{28}Si^+$, $^{39}K^+$, $^{40}Ca^+$ elements acquired for montmorillonite clay mineral with an O^- primary ion beam of a current of ~6pA with a dwell time of 1ms/pixel. The hue scale indicates the counts per pixel of the secondary ions.

Using techniques from reflected light microscopy, scanning electron microscopy with EDX to NanoSIMS the architecture and elemental composition of intact soil aggregates is evaluated

Summary and Conclusions

With the NanoSIMS technology material surfaces can be investigated by sputtering the uppermost atomic layers and analysing their elemental and isotopic composition by mass spectrometry at high lateral resolution. The samples have to be vacuum compatible and their surfaces should be well-polished. For quantitative analyses known standards of similar composition are required for calibration. The technique was successfully applied to study the architecture of organo-mineral structures and can reveal insight into soil dynamics. Examples from soil investigations were presented.
The technique seems to be promising for the investigation of material transport on small lateral scale in clay material.

Acknowledgement

Deutsche Forschungsgemeinschaft is acknowledged for the funding of the NanoSIMS instrument at the Lehrstuhl für Bodenkunde at TU München (KO 1035/38-1). We are grateful to Dr. Marianne Hanzlik (Institute of Electron Microscopy, TU München, Garching) for assistance in SEM-EDX measurements, to Dr. Ulrich. Ehrke (Cameca GmbH Germany) and Dr. Michael Wiedenbeck (GFZ, Potsdam, Germany) for fruitful discussions and advices.

References

Düsterhöft H., Riedel M., Düsterhöft B-K. (1999). Einführung in die Sekundärionenmassenspektrometrie “SIMS”. Teubner, Stuttgart.

Heister K., Hoeschen C., Pronk G. J., Mueller C. W., Kögel-Knabner I. (2012). NanoSIMS as a tool for characterizing soil model compounds and organomineral associations in artificial soils. In press in J Soils Sediments, 12(1) 35-47.

Kita N. T., Ushikubo T, Fu B. and Valley J. W.(2009). High precision SIMS oxygen isotope analysis and the effect of sample topography. Chem. Geol., 264, 43-57.

Mueller C. W., Kölbl A., Hoeschen C., Hillion F., Heister K., Herrmann A., Kögel-Knabner I. (2012). Submicron scale imaging of soil organic matter dynamics using NanoSIMS - from single particles to intact aggregates. Org. Geochem.42(12) 1476-1488.

POSTER PRESENTATIONS

A SEM-EDX Study of the Processes at the Concrete/Compacted Bentonite Interface

Raúl Fernández*,[1], Ana Isabel Ruiz[1], Raquel Vigil de la Villa[1], Jaime Cuevas[1] and María Jesús Turrero[2]

[1]Department of Geology and Geochemistry, Faculty of Science, Autonomous University of Madrid,
Campus de Cantoblanco, 28049. Madrid (SPA)
[2]CIEMAT, Department of Environment, Avda. Complutense 22, 28040, Madrid (SPA)

* Corresponding author: raul.fernandez@uam.es

Abstract

A 4.7 years column experiment was performed to study the interaction between concrete and compacted FEBEX bentonite (1.6 g/cm^3; dry density). The experiment was dismantled under the development of the PEBS project. A SEM-EDX study was performed along a polished section of the concrete-bentonite column. The calcium front exceeded the first two mm of interface confirming the alkaline diffusion. Calcite, mainly in the bentonite, and calcium silicates (aluminates) hydrates (C–S–A–H) type materials were identified in secondary electrons mode. The SEM-EDX technique provides valuable data on spatial development of reaction fronts produced in bentonite, but XRD and FTIR are also fundamental tools to confirm spatial reaction front results, and unavoidable to update the nature of mineral phases formed.

Introduction

Several long-term composite column experiments studying Ordinary Portland Cement (OPC) concrete-bentonite interaction are running since May 2006. The experiments consisted in medium scale cells in which a reference Spanish clay formation pore water (Na-Mg-SO_4-Cl-dominant solution, approximately 0.2 M; pH 7.6) was injected through a 30 mm thickness, 70 mm diameter cylindrical OPC concrete probe. The concrete is held in direct contact with a 71.5 mm compacted FEBEX bentonite cylinder (1.6 g/cm^3, dry density) of the same diameter (Figure 1; Escribano *et al*., 2007; Turrero *et al*., 2008). The column remained confined and sealed in a rigid Teflon sleeve and temperature was fixed to 25 ºC in the water injection port and to 100 ºC at the opposite side by means of controlled heat source.
Similar experiments were run during 0.5, 1 and 2.5 years. They were already dismantled and analysed to provide experimental evidences on the physical, chemical and mineralogical changes due to the concrete compacted bentonite interaction. A thin layer of white-precipitate was found at the concrete/bentonite interface in all cases. The precipitate consists of a superposition of different secondary minerals identified by means of Scanning Electron Microscope in combination with Energy-Dispersive X-ray spectroscopy (SEM-EDX): portlandite [$Ca(OH)_2$], C–S–H gels (Ca/Si = 0.6), brucite [$Mg(OH)_2$] and ettringite $Ca_6Al_2[(SO_4)_3(OH)_{12}]\cdot 26H_2O$). On the bentonite side, the mineralogical composition at the interface changes slightly and a brucite-saponite-like smectite mixture has been observed. Fernandez *et al*. (2009) made 1 year isothermal diffusion experiments with a K-Na-OH, 0.5

M pH=13.5 OPC pore water solution in contact with a Mg-saturated compacted FEBEX bentonite. They also found discrete brucite at 60 ºC and a brucite-montmorillonite intercalation complex mixed with a tri-octahedral Mg-sheet silicate phase at 90 ºC.

Recently, the 4 years concrete-bentonite medium scale experiment has been dismantled under the development of the PEBS project (Long-term Performance of Engineered Barrier Systems). The expected outcome of these relative long-term interaction tests is 1) the confirmation of the low impact of the alkaline plume predicted by previous investigations in terms of mineralogical alteration thickness, and 2) the precise establishment and evolution over time of the new formed by-products and how they produce a porosity reduction process affecting diffusive transport.

This communication is part of the preliminary results of characterization of these long-term concrete-bentonite interface studies and is focused to the SEM-EDX work actually performed.

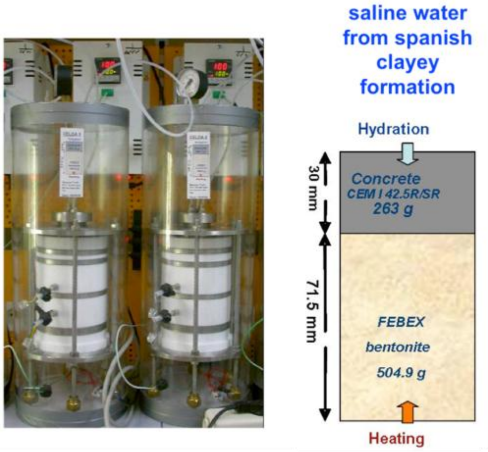

Figure 1. Experimental Setup and diagram of the medium cells for concrete-bentonite interaction long-term study.

Methods and Results

In the dismantling of the experiment, a slice of the column (30 mm concrete and 15 mm bentonite thickness) was wrapped by a textile adhesive tissue and then covered with a non permeable elastic adhesive band. Two 10 mm separated parallel vertical cuts 20 mm deep were rapidly done with a water refrigerated diamond disc from the concrete side without entering in the first 10 mm near the bentonite. The other 25 mm cut was performed with a diamond included stainless steel wire saw (Well2000™) without any cutting fluid entering near the concrete-bentonite interface. Each cut takes 7-10 days to be completed. The obtained slice was immersed in liquid nitrogen for 1h and then was vacuum dried (10^{-1} – 10^{-2} Pa) at 20 ºC for 3 days. After this treatment the slice was embedded under vacuum in a low viscosity LR-white™ resin. The hardening process is a modification of the method described by Kim *et al.* (1995). The embedded bentonite sample was polished for SEM-EDX analyses. The polished longitudinal section was used for optical inspection and to analyze three parallel profiles of the chemical composition along the column axis as measured by SEM-EDX with an INSPECT FEI COMPANY microscope. A series of (2.89 × 2.6 mm) spots (20 s, 25 kV) were measured for EDX analyses along the vertical axis in order to obtain longitudinal chemical profiles. Then a contour map with quantitative elemental chemistry results was represented with the data analysis and graphing software ORIGIN, version 8 (Figure 2). This has been performed as a first step in the localization of diffusion fronts and to measure the extent of chemical alteration considering a cm scale portion of the concrete-bentonite interface. In addition, some chips at the concrete side and at the bentonite interface were observed and analyze also by means of electron microscopy. From the maps it can be outline an irregular Mg increase and Al depletion in the first millimetres of interface. The calcium front has exceeded the first two mm of interface confirming the alkaline diffusion. The distribution of Si and Na is very heterogeneous and not any diffusion trend can be derived from the results. S and Al show a gradient of concentration in the interface related with the different composition in both materials.

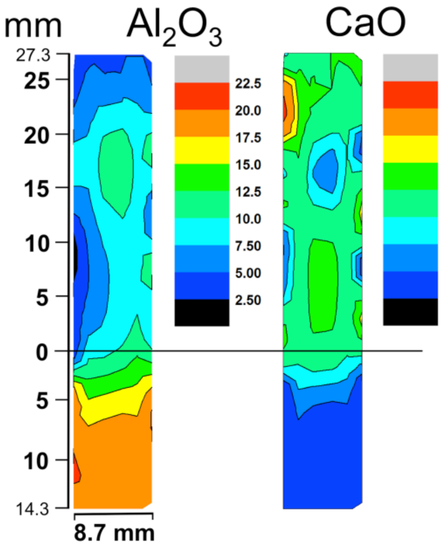

Figure 2. Contour chemical maps for Al and Ca showing the OPC cement-concrete interface. The interface is at 0 in the scale, the upper part corresponds to concrete and the lower part to bentonite.

A detailed observation of the interface in the backscattering electron mode reveals the existence of desiccation cracks at microscale and a sub-millimetric gap presumable developed by an instant drying interface separation during the dismantling. In any case, a 1mm portion of the bentonite interface is crossed by subparallel whitish veinlets, characteristic of calcium enrichments (Figure 3). A fresh fractured chip of these bentonite interface rims was observed in secondary electrons mode and analyzed. Calcite, mainly in the bentonite, and calcium silicates (aluminates) hydrates (C–A–S–H) type materials were identified (Figure 4).

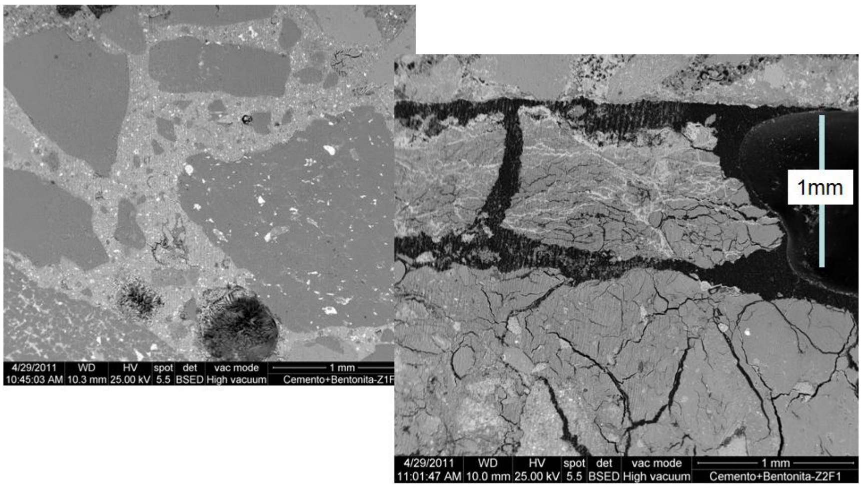

Figure 3. SEM Back-scattering image of the OPC concrete-bentonite interface.

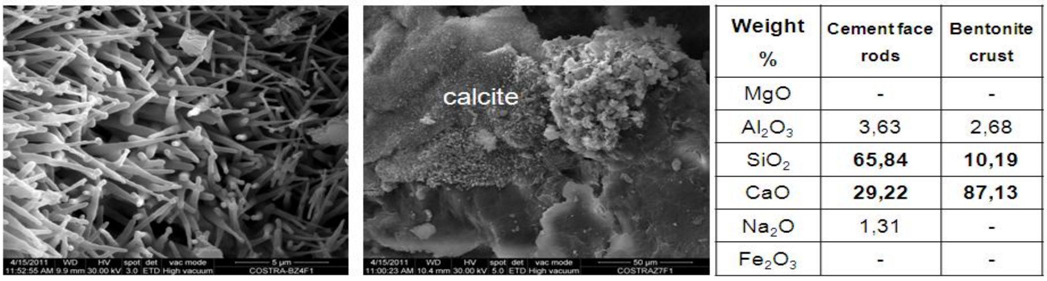

Weight %	Cement face rods	Bentonite crust
MgO	-	-
Al_2O_3	3,63	2,68
SiO_2	**65,84**	**10,19**
CaO	**29,22**	**87,13**
Na_2O	1,31	-
Fe_2O_3	-	-

Figure 4. SEM micrographs and chemical data from the OPC-bentonite interface.

X-Ray Diffraction (XRD) and Fourier Transform Infrared spectroscopy (FTIR) are fundamental tools to confirm spatial reaction front results and unavoidable to update the nature of mineral phases formed. Brucite, calcite and aragonite have been identified to be precipitated at the saline water-concrete interface. FTIR data indicated that small quantities of brucite and portlandite are components remaining in the concrete matrix after 4 years, but XRD of cement matrix powder (< 0.1 g) scraped along the concrete section reveal that calcite and ettringite were the predominant cement minerals. Neither brucite, nor portandite remained in significant proportions. Calcite and ettringite are depleted near the hydration source in response to the leaching of the concrete probe. In the bentonite interface, calcite and aragonite were identified in the first mm of the bentonite face, but C–S–H or C–A–S–H has not been conclusively characterized. XRD profiles match with the presence of a low Ca-anorthite C–A–S–H phase, but the presence of 11Å-tobermorite cannot be actually neglected because of the superposition of Na-smectite peaks. In order to fix these points, clay fraction separation is needed to characterize the clay minerals. On the other hand, additional spectroscopic techniques and further SEM or TEM observations are needed to fully characterize the nature of the alkaline alteration of bentonite. Moreover, in the field of quantifying the alteration front, improvements on the preservation of the interface and better resolution of the chemistry in this area will be of great interest.

Acknowledgement

The research leading to these results has received funding from the European Atomic Energy Community`s 7th framework Program (FP7/2007-2011) under grant agreement nº 249681.

References

Escribano, A., Melón, A.M., Turrero, M.J., Fernández, A.M., Torres, E., Martín, P.L. (2007). Concrete-Febex bentonite interaction: results on column and infiltration experiments. NFPRO Fourth Workshop, Brussels, Belgium, 15-17 October.

Fernández, R., Mäder, U., Rodríguez, M., Vigil de la Villa, R., Cuevas, J. (2009). Alteration of compacted bentonite by diffusion of highly alkaline solutions. Eur. J. Mineral. 21, 725-735.

Kim, J., Peacor, D., Tessier, D., Elsass, F. (1995). A technique for maintaining texture and permanent expansion of smectite inter-layer for TEM observations. Clays Clay Miner. 43, 51.

Turrero, M.J., Torres, E., Martín, P.L., Barcala, J.M. (2008). Final activity report for CIEMAT (WP 2.3). ENRESA. NF-Pro Chemical (thermo-hydro-mechanical) evolution of the EBS: evolution of porewater chemistry; effects of canister corrosion, concrete degradation and radionuclide retention. Intern report 03/2008, p. 77-196.

A Method for on-Line Measurements of pH in Compacted Bentonite

Arto Muurinen*, Torbjörn Carlsson

VTT Technical Research Centre of Finland

* Corresponding author: arto.muurinen@vtt.fi

Abstract

This paper describes a method for on-line pH measurement in compacted water-saturated bentonite with a solid IrOx electrode. The results obtained in different experimental arrangements and different pH conditions are presented to illustrate the applicability of the method. The results show that it is possible to measure the pH in compacted bentonite and follow the change of the conditions as a function of time in long-term experiments.

Introduction

The combination of the low content of free water and high swelling pressure makes direct measurement of the pH difficult in the porewater of compacted bentonite – a material planned to be used as a buffer in spent nuclear fuel disposal. Therefore, the pH is mostly determined in batch experiments at low clay content or by separating water from the compacted bentonite by squeezing. Geochemical modelling has also been used for determination of the pH (Wersin 2003). The uncertainty related to the methods above can be avoided by measuring the pH directly inside the bentonite. This paper presents the results of on-line measurements of the pH with an IrOx electrode in water-saturated, compacted bentonite under well-controlled conditions. The measurements were carried out in closed cells and in cells where the bentonite was in contact with an outside solution, such that the conditions in the bentonite changed during the experiment.

Arrangement of the pH measurements

Measurement method

The pH measurements were carried out with solid IrOx electrodes prepared by forming an oxide layer on an iridium wire of 0.15 mm in diameter at 870 ^{o}C in a lithium carbonate melt (Yao et al. 2001, Muurinen and Carlsson 2007). Because the electrode may change during the measurement, it is preferable to calibrate the electrode in pH buffer solutions both before and after the measurement. A commercially available, small Ag/AgCl electrode from Innovative Instruments, Inc., USA was used as the reference electrode, which was placed in a solution in contact with the bentonite. The pH is calculated from the measured potential difference between the IrOx and reference electrodes using the calibration curve.

pH measurement in a squeezing cell

Figure 1 presents the arrangement of the pH measurement in the squeezing cell. The bentonite sample was compacted in the cell before placing the IrOx electrodes in the bentonite. The reference electrode was in contact with bentonite via the tube filled with solution. Compacted bentonite samples taken from a separate experiment can also be trimmed and placed in the cell for pH measurement (Muurinen 2009).

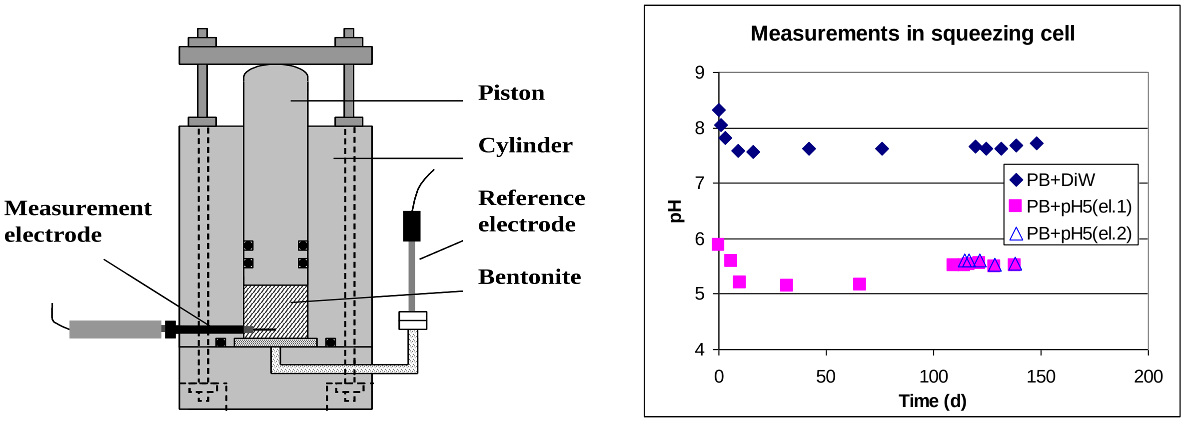

Figure 1. Arrangement of pH measurement in a squeezing cell (left). Examples of obtained pHs in squeezing cell measurements on the right. PB+DiW: sample prepared from purified bentonite and deionized water. PB+pH5(el.1) and PB+pH5(el.2): sample prepared from purified bentonite and a buffer solution of pH 5.

Figure 1 presents the pH as a function of time in two measurements. The sample PB+DiW was compacted from purified MX-80 and deionized water to a dry density of 1.5 g/cm^3. In the other sample (PB+pH5(el.1), PB+pH5(el.2)) the purified bentonite was first treated with a buffer solution containing 0.3 M NaCl and 0.1 M acetic acid at pH 5. The extra solution was then separated by centrifuging and squeezing until the desired dry density of 1.5 g/cm^3 was obtained. The pH in the squeezed solution was 5.2. The pH values are as expected: in the first case between 7 and 8, and in the latter somewhat over 5. The pH in the latter sample started to increase after 70 days, indicating that the chemical reaction between the porewater and bentonite continues. The increased pH was obtained also with a new electrode (el. 2) placed later into the sample.

pH measurements in diffusion cells

In the diffusion cell measurement (Figure 2), the effect of a high-pH solution on the conditions in bentonite was studied. The compacted bentonite sample was prepared using anaerobic MX-80 bentonite and anaerobic deionized water. The dry density of the bentonite sample was about 1.5 g/cm^3. Three pH electrodes were placed in the bentonite at different distances from the bentonite-solution interface and anaerobic deionized water was added to the external vessel. After 271 days the external solution was replaced with a high-pH, saline solution (0.19 M NaCl, 0.1 M $CaCl_2$, pH 11.8) in order to simulate the effect of cement on bentonite in saline groundwater. After 1 900 days, when the pH of the external solution had been kept between 11 and 11.8 by periodically changing the external solution, the pH in the bentonite 5 mm from the interface increased to about 11.8 and the pH 10 mm from the interface to 10.2. The electrode at the depth of 20 mm stopped working after 631 days, which shows that the pH electrode may be sensitive to the mechanical damage caused, for example, by bentonite movement and coarse grains.

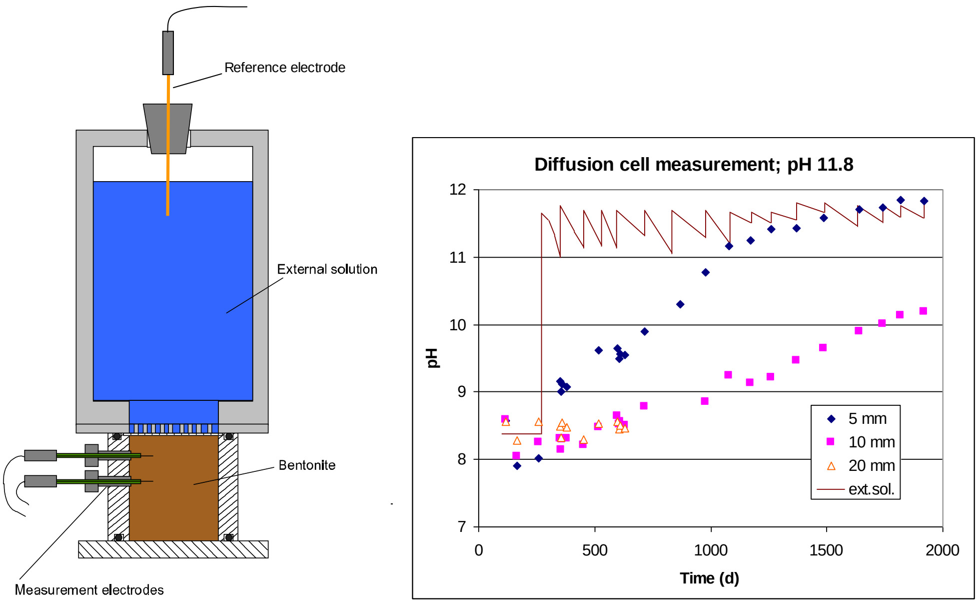

Figure 2. pH measurement in a diffusion cell where the bentonite is in contact with the solution at one end. On the right are presented the measured pH values at different depths in the bentonite and in the external solution. The solution chemistry was changed at 271 days from low-pH to high-pH.

Figure 3 presents an experiment where the progress of the pH change caused by an acetate buffer was studied in a sample compacted from purified MX-80 and deionized water to a dry density of 1.5 g/cm^3. The ends of the 18 mm long cylinder were exposed to an external solution of 0.3 M NaCl and 0.1 M acetic acid at pH 5. The effects were monitored by measuring the pH in the bentonite at 5 mm and 9 mm from the solution-bentonite interface as a function of time. The pH closer to the interface approaches more quickly the pH of the external solution, as seen in Figure 3.

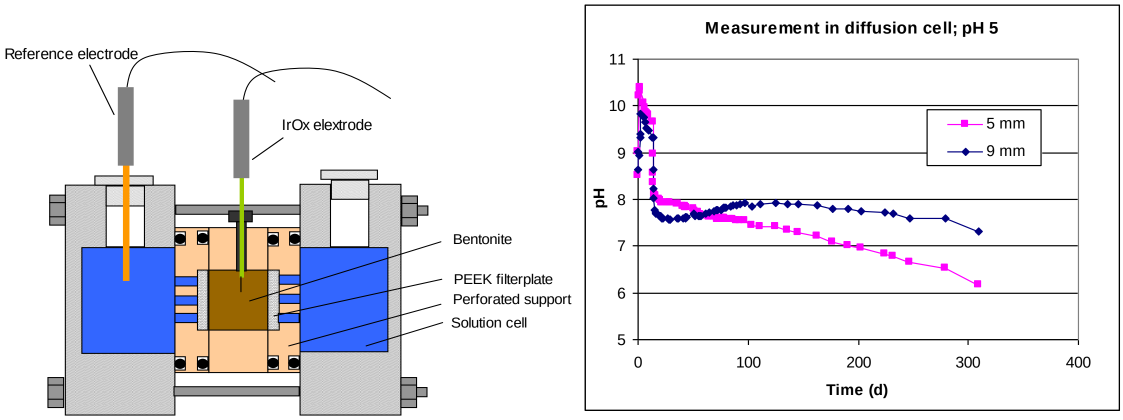

Figure 3. pH measurement in a diffusion cell where the bentonite is in contact with the solution at two ends. The external cells were filled with an acetate buffer at pH 5. The measured pH values at different depths in the bentonite are presented on the right.

Conclusions

The results show that it is possible to measure pH in compacted bentonite and follow the change of the conditions as a function of time in long-term experiments.

Acknowledgments

The studies have been funded by Posiva Oy, the European Commission (Integrated Project NF-PRO) and VTT.

References

Muurinen, A., Carlsson, T. 2007. Development of methods for on-line measurements of chemical conditions in compacted bentonite. Physics and chemistry of the earth 32 (2007) 241 – 246.

Yao, S., Wang, M., Madou, M., 2001. A pH electrode based on melt-oxidized iridium oxide. Journal of The Electrochemical Society, 148, (4) H29 – H36.

Muurinen, A. 2009. Studies on the Chemical Conditions and Microstructure in the Reference Bentonites of Alternative Buffer Materials Project (ABM) in Äspö. Posiva Working Report 2009 – 42.

Wersin, P. 2003. Geochemical modelling of bentonite porewater in high-level waste repositories. Journal of Contaminant Hydrology 61, 405 – 422.

Characterization of Colloids Extracted from Two Synthetic Clay Materials by Flow Field Flow Fractionation (FFFF) Coupled to ICP-MS Detector

Muriel Bouby[1*], Nicolas Finck [1], Laurent Truche[2], Jocelyne Brendlé [3], Thorsten Schäfer[1,4], Horst Geckeis[1]

[1] KIT-CN, Institut für Nukleare Entsorgung (Germany)
[2]G2R/UMR/CNRS, Univ. Henri Poincaré (France)
[3]Institut de Sciences des Matériaux de Mulhouse (IS2M), Equipe Matériaux à Porosité Contrôlée, CNRS-LRC 7228, UHA (France)
[4]Institute of Geological Sciences, Hydrogeology Group, Freie Universität Berlin (Germany)

* Corresponding author: Muriel.Bouby@kit.edu

Abstract

Clay minerals may incorporate actinide upon formation in aqueous systems. The Flow Field-Flow Fractionation technique coupled to an ICP-MS detector (FFFF/ICP-MS) is used to characterize colloids extracted from two synthetic clay solids in which a foreign element (Zn or Lu) has been incorporated in the structure via a Mg substitution process. The size distribution of the clay colloidal fraction which can be mobilized is determined. The homogeneous Zn and Lu distributions over the entire colloidal fraction, as measured by the FFFF/ICP-MS, support the previously proposed structural incorporation process and prove that the foreign element incorporated remains in the colloidal fraction extracted.

Introduction

The presence of aquatic colloids/nanoparticles (NPs) is a key question in performance assessment of an underground nuclear waste disposal site. Their high surface area to volume ratio and their potential stability allow them to interact with radionuclides and to transport them over long distances. From the near-field to the far-field of a repository, colloids / NPs may originate from the corrosion of the engineered barriers via the formation of secondary phases in which some actinides can be incorporated, from the intrinsic actinides colloids formed by exceeding the solubility limit, from the chemistry of the host rock/backfill material (compacted bentonite being potentially one of it) via some erosion process due to water intrusion or from aquatic media where they occur naturally (e.g., humic substances, Al/Si/Fe-oxides/hydroxides, clays..).

To predict the impact of the clay colloids on the radionuclides migration, it is important to know the size distribution of the fraction which can be mobilized and if this one still contains the actinides which have been incorporated.

Flow Field-Flow Fractionation (FFFF) coupled with an ICP-MS detector has been used to characterize the clay colloids and their interaction with actinides or with their non radioactive chemical surrogates the lanthanides (Bouby et al, 2011).

In this work, the capabilities of the pre-cited hyphenated technique to characterize colloids extracted from two synthetic clay solids in which foreign elements have been structurally incorporated (or are supposed to) are outlined.

Material and method

Zn-labeled montmorillonite (Zn-Mt)

A Zn-Mt powder containing Zn in its octahedral sheet is used. The full Zn-Mt synthesis protocol and solid characterization is described by Reinholdt et al. (2001). 250 mg of Zn-Mt powder are equilibrated in 50 mL of a high pH and low ionic strength groundwater (GGW) sampled from the Grimsel underground laboratory (Grimsel Test Site, Switzerland, www.grimsel.com) during 10 days in order to achieve a high degree of delamination. The GGW composition can be found in Duro et al. (2000). The colloid suspension was obtained by repeating four time cycles of suspending, centrifugating for 30 min at 4000 rpm and resuspending the separated solid in GGW, starting from the equilibrated suspension. The final supernatant, containing Zn-Mt colloids, is taken as the colloid stock suspension and stored in a fridge until use. According to the structural formula of Zn-Mt, the colloid concentration is 120 mg/L based on direct Al concentration determined by ICP-MS. The colloidal fraction of this material is characterized by FFFF/ICP-MS after two successive injections of the colloidal stock suspension previously diluted by 10 in the FFFF eluent to avoid any concentration effects (see Bouby et al. (2008) for more details) but without any other pre-treatment.

Hectorite co-precipitated in presence of Lu (Hec-Lu)

A co-precipitated hectorite sample containing Lu in its octahedral sheet is used. The full Hec-Lu synthesis protocol and solid characterization is described by Finck et al. (2009). The solid sample still in contact with demineralised ultra-pure water is centrifuged 30 min at 4000 rpm. The supernatant is then collected and constitutes the colloidal stock suspension. According to the structural formula of the hectorite, the colloid concentration is ~ 688 mg/L based on direct Mg concentration determined by ICP-MS The colloidal fraction of this material is characterized by FFFF/ICP-MS after two successive injections of the colloidal stock suspension previously diluted by 10 to avoid any concentration effects (see Bouby et al. (2008) for more details) but without any other pre-treatment.

Flow Field-Flow Fractionation (FFFF) coupled to an ICP-MS detector

The general principle of the FFFF method is described in detail in Schimpf et al. (2000).The experimental equipment applied in this study has been detailed in Bouby et al. (2008) and Bouby et al. (2011) with numerous schemes and with the description of the calibration and quantification processes. Only the main principle is recalled here: Size fractionation of colloids is carried out in a thin ribbon-like channel according to their diffusion coefficient. Up to ~ 800 nm as reported by Luo et al. (2006), smaller colloids are eluted prior to larger particles with smaller diffusion coefficients.

The AsFlFFF system (HRFFF 10.000 AF4) is provided by Postnova Analytics (Landsberg, Germany) and runs with an ultra filtration membrane made of regenerated cellulose (cutoff 5 kDa), a trapezoidal spacer of 0.5 mm thick. In this study, the carrier solution consists of ultra pure water adjusted to pH 9.3 by addition of ultra pure NaOH 1 M (Merck). pH stability was checked by daily measurements (max. ~8 hours). The carrier solution was prepared and degassed prior to use by the vacuum degasser. 100 µL are injected for each measurement. A linearly decreasing cross-flow is applied over 2700 s.

Results and discussion

Zn-labeled montmorillonite(Zn-Mt)

Al ICP-MS signal is used as the colloid fingerprint. The Al and Zn-fractograms obtained are presented in the Figure 1.

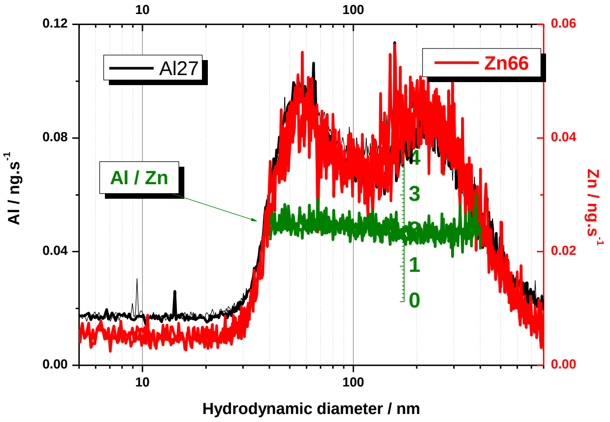

Figure 1. Al and Zn ICP-MS fractograms obtained after injection of the stock suspension diluted by 10. 100 µL injected. pH 8.3. Two successive measurements reported.

Colloids are obviously present and detected. Two colloidal fractions, with sizes at ~ 50-70 and 200 nm are observed with a rather broad size distribution (in agreement with additional AFM results, not shown here). The Al recovery is 98 % which represents the percentage of colloidal Al. 73.5 % of the Zn is found under colloidal form. The Al and Zn signals are strongly correlated over the entire size range which is greatly in favour of a Zn incorporation into the Al colloids or a homogeneous Zn sorption onto Al colloids. The Al to Zn mass ratio is constant over the entire peak range at a value of 1.9 – 2.0. It corresponds to a Al / Zn mol ratio of 4.86 witch is in good agreement with the theoretical value (4.21) deduced from the Zn-Mt structural formula. In conclusion, the FFFF/ICP-MS data support result of the previous work (Reinholdt et al. 2001) and show that the Zn remains associated with the montmorillonite in the colloidal fraction which can be mobilized.

Hectorite co-precipitated in presence of Lu (Hec-Lu)

Mg and Si ICP-MS signals are used as the colloid fingerprint. The Mg, Si and Lu-fractograms obtained are presented in the Figure 2.

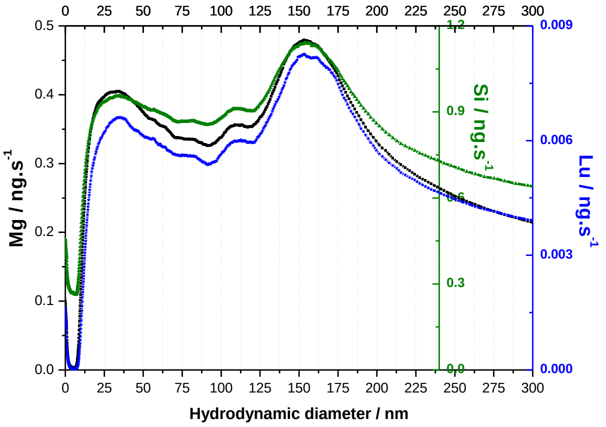

Figure 2. Mg, Si and Lu ICP-MS fractograms obtained after injection of the stock suspension diluted by 10. 100 µL injected. Mean of two successive measurements.

Here as well, colloids are obviously present and detected. A plurimodal size distribution is visible, < 300 nm. The Si recovery is 51 %, the Mg and Lu recoveries are 61 %. The Mg, Si and Lu signals are strongly correlated over the entire size range which is greatly in favour of a Lu incorporation in the hectorite or to a homogeneous sorption. The Mg/Si mass ratio determined by FFFF/ICP-MS: 0.54±0.02 is in agreement with the theoretical value determined from the structural formula: 0.57. The Mg/Lu mass ratio presents very similar variation over the entire size range. This support the incorporation hypothesis previously proposed in Finck et al. (2009). It demonstrates that the Lu remains associated with the colloidal fraction extracted.

Summary and Conclusions

FFFF/ICP-MS delivers useful informations on the clay colloidal size fraction which can be mobilized showing that incorporated element are still present. If the colloids are considered representative of the bulk solid, these data can be used to support previously proposed structural incorporation processes. This technique presents many advantages: it is quantitative, very reproducible, does not require any sample pre-treatment, allows to collect individual fraction, may be coupled on/off-line with many detection systems for further analysis, present good limit of detection (those of the associated detectors) and a good size resolution (few nm). Drawbacks have to be mentioned like the possibility to underestimate the colloid size if the amount injected is too high and it remains an invasive technique: the separation and elution conditions have to be properly defined to allow a good sample recovery.

Acknowledgement

The authors gratefully thank the Bundesministerium für Wirtschaft und Technologie (BMWi) / Projektträger Karlsruhe – Wassertechnologie und Entsorgung (PTKA-WTE) for considerable financial support within the “KOLLORADO-2” project.

References

Bouby, M., Geckeis, H. Geyer, F. (2008). Application of asymmetric flow field-flow fractionation (AsFlFFF) coupled to inductively coupled plasma mass spectrometry (ICPMS) to the quantitative characterization of natural colloids and synthetic nanoparticles. *Anal. Bioanal. Chem.* **392**, 1447-1457.

Bouby, M., Geckeis, H., Lützenkirchen, J., Mihai, S., Schäfer, T. (2011). Interaction of bentonite colloids with Cs, Eu, Th and U in presence of humic acid: a Flow Field-Flow Fractionation study. Geochim. Cosmochim. Acta, 75, 3866-3880.

Duro, L. et al. (2000) Prediction of the solubility and speciation of RN in FEBEX and Grimsel Waters. Colloid and Radionuclide Retardation project. *NAGRA Technical Report 99-218*, Nagra, Wettingen, Switzerland.

Finck, N., Schlegel, M., Bosbach, D. (2009) Sites of Lu(III) sorbed to and coprecipitated with hectorite. Environ. Sci. Technol., 43, 8807-8812.

Luo, J., Leeman, M., Ballagi, A., Elfwing, A., Sua, Z., Janson, J.-C., Wahlund, K.-G. (2006) Size characterization of green fluorescent protein inclusion bodies in *E. coli* using asymmetrical flow field-flow fractionation–multi-angle light scattering. *J. Chrom. A* **1120**, 158–164.

Reinholdt, M., Miehè-Brendlé, J., Delmotte, L., Tuilier, M.H., Le Dred, R., Cortès, R., Flank,A.M. (2001). Fluorine route synthesis of montmorillonites containing Mg or Zn and characterization by XRD, Thermal Analysis, MAS NMR, and EXAFS spectroscopy. *Eur.J. Inorg. Chem.*, **2001**, 2831-2841.

Schimpf, M., Caldwell, K., Gidding, J.C. (2000). Field-Flow Fractionation Handbook. Wiley-Inerscience, A John Wiley & Sons Inc. New York, 3-30 and 257-278.

Mineralogical and Microfabric investigation of the Sandy Facies of Opalinus Clay (Mont Terri)

Annette Kaufhold[1*], Reiner Dohrmann[2], Siegfried Siegesmund[1], Werner Gräsle[2], Ingo Plischke [2]

[1] Department of Structural Geology and Geodynamic, Georg-August University-Göttingen, Goldschmidtstr. 3, 37077 Göttingen (DE)
[2] Federal Institute for Geosciences and Natural Recources, Stilleweg 2, 30655 Hannover (DE)

* Corresponding author: annette.kaufhold@gmail.com

Introduction

In the field of geological disposal of radioactive waste in many countries argillaceous formations are considered as potential host rock. For the understanding of the long-term behaviour of clay host rock, it is important to understand the interaction between mechanical behaviour, microfabric, and mineral composition (Bock et al. (2010)).

Previous publications (e.g. Klinkenberg et al. (2009)) showed that particularly the carbonate content and the arrangement of the carbonate grains (as cement in the matrix or as shells) determines the mechanical strength of Opalinus Clay and Callovo Oxfordian Clay specimens, respectively. Klinkenberg et al. (2009) studied the shaly facies of Opalinus Clay, however, the actual deposit is planned to be built in the sandy facies of Opalinus Clay. The aim of the present study is to investigate the relation between microfabric, mineral composition, and mechanical properties of different samples derived from the sandy facies (BLT-A2).

Materials and Methods

The investigated core samples of the sandy facies (Opalinus Clay) are derived from the Rock Laboratory Mont Terri (St. Ursanne, Switzerland). The samples of the sandy facies are more heterogeneous than those of the shaly facies. The homogeneous scale of the sandy facies is in the dm to m scale (Nagra (2002)). Test specimens were derived from 2 cm long drill core pieces. Specimens were sampled and analyzed using:

- XRD (X-ray-diffraction), XRF (X-ray-fluorescence), and LECO (carbon, sulphur, oxygen, and nitrogen analysis) standard methodology of BGR (Hannover, Germany) for characterisation of mineralogical and chemical composition as well as organic carbon content.
- the CEC (cation exchange capacity) method based on Cu-Triethylenetetramine (Meier & Kahr (1999)).
- a core scanner (DMT CoreScan®) for the macroscopic image investigation. Here the unrolled core mantle has a resolution of 20-40 pixels per mm.

- a FEI Quanta 600 F operated in low-vacuum mode (0.6 mbar) for E-SEM (environmental scanning electron microscope) investigation. The microscope is equipped with the EDX-system Genesis 4000 of EDAX.

Results

For the quantitative phase analysis the Rietveld methods was used (Ufer et al. (2008)). The data of the geochemical and mineralogical analysis were compared with each other resulting in a plausibility-checked mineralogical composition (Table 1).

Table 1. Semi-quantitative mineral content, CEC, Corg-, and carbonate content of the sandy-facies. Ill= illite, Smt=smectite, Musc.=muscovite.

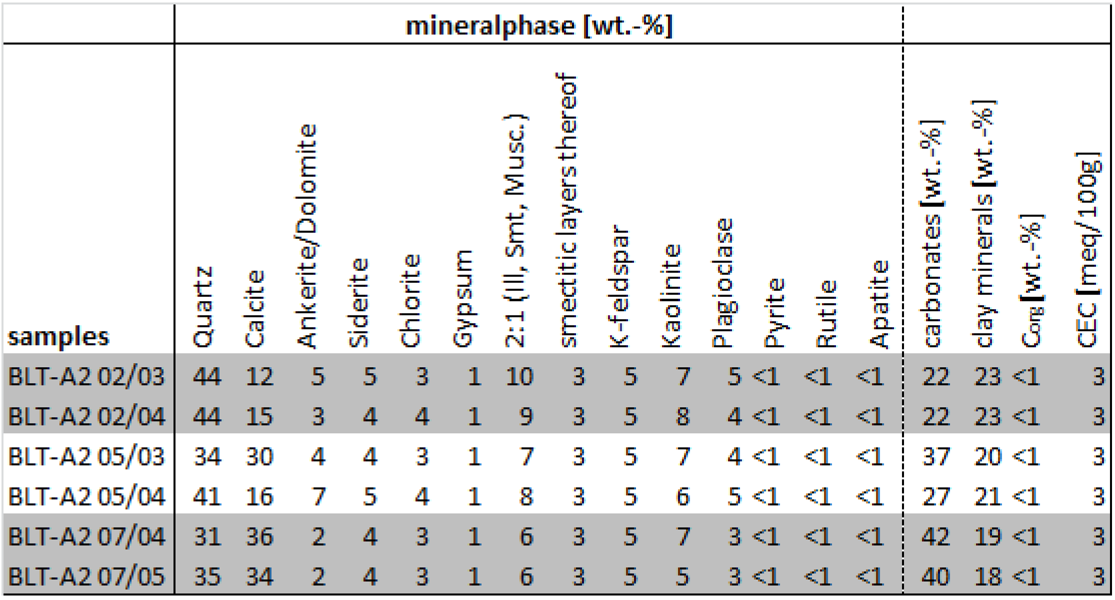

	mineralphase [wt.-%]																	
samples	Quartz	Calcite	Ankerite/Dolomite	Siderite	Chlorite	Gypsum	2:1 (Ill, Smt, Musc.)	smectitic layers thereof	K-feldspar	Kaolinite	Plagioclase	Pyrite	Rutile	Apatite	carbonates [wt.-%]	clay minerals [wt.-%]	C_{org} [wt.-%]	CEC [meq/100g]
BLT-A2 02/03	44	12	5	5	3	1	10	3	5	7	5	<1	<1	<1	22	23	<1	3
BLT-A2 02/04	44	15	3	4	4	1	9	3	5	8	4	<1	<1	<1	22	23	<1	3
BLT-A2 05/03	34	30	4	4	3	1	7	3	5	7	4	<1	<1	<1	37	20	<1	3
BLT-A2 05/04	41	16	7	5	4	1	8	3	5	6	5	<1	<1	<1	27	21	<1	3
BLT-A2 07/04	31	36	2	4	3	1	6	3	5	7	3	<1	<1	<1	42	19	<1	3
BLT-A2 07/05	35	34	2	4	3	1	6	3	5	5	3	<1	<1	<1	40	18	<1	3

Carbonates and quartz predominate in all samples. The samples from the drilling BLT-A2 show increasing carbonate contents (22 to 42 wt.-%) with depth (cored section 02→05→07) while the quartz content decreases (44 to 31 wt.-%). The clay mineral content is slightly decreasing (23 to 18 wt.-%) with depth.

For the image analysis multi scales were considered. On the macroscopic (mm-m) scale a core scanner was used to get unrolled core images (Figure 1).

Figure 1. Left side: picture of a core sample (BLT-A3) and on the right side: unrolled core sample (BLT-A3).

The ESEM was used to get information in the mm to µm scale. Relevant microstructural components are clay minerals and carbonates, and their distribution in the sample.

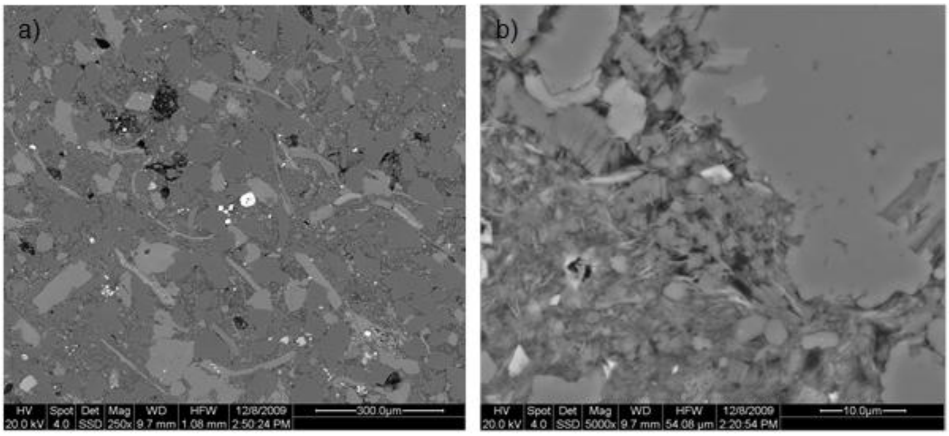

Figure 2: BSE images a) overview of the sandy facies, scale bar 300.0 µm b) clay mineral aggregates in the inter-particle pore space, scale bar 10.0 µm (BLT-A2 03/02).

E-SEM results prove that the carbonates (Figure 2, light grey particles) are mainly forming the matrix as cement, but were also observed as particles in the fine sand fraction (63-200 µm). Biogenic carbonates may appear as a secondary component. Quartz (Figure 2, dark grey particles) is observable in the silt and fine sand fraction (20- 200 µm). Clay mineral aggregates fill the interparticle space between the carbonates and quartz (Figure 2b).

Mechanical testing vs. carbonate content

Mechanical testing on the sandy facies of the drilling BLT was carried out by BGR (Gräsle and Plischke (2011)). In Figure 3 the results of the strength tests of the drilling BLT-A2 were compared with the carbonate content derived from the mineral phase analysis (Table 1).

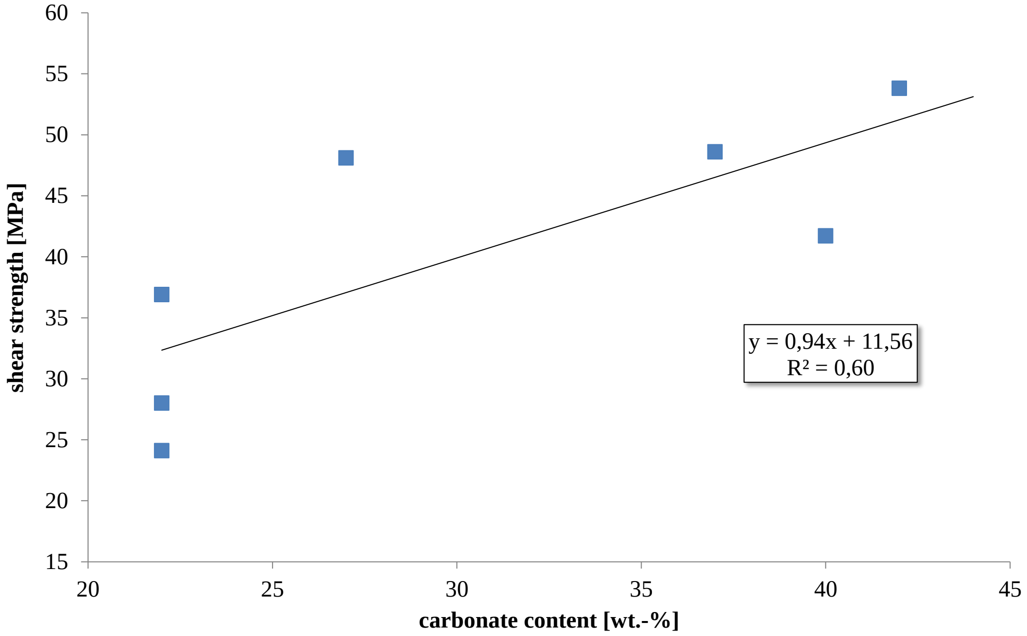

Figure 3: Shear strength ((Gräsle and Plischke (2011)) vs. carbonate content of the drilling BLT-A2 (maximum principle stress parallel to the bedding).

The samples of the drilling BLT-A2 (sandy facies) show a clear tendency (Figure 3): the shear strength increases with increasing carbonate content.

Summary and Conclusions

Image analysis showed that the carbonates in the sandy facies mainly occur as 1) matrix which in turn acts as cement. Carbonates also occur 2) in the fine sand fraction and 3) biogenic carbonates as traces. The carbonates of the sandy facies, therefore, appear to be similar to the carbonates of the Callovo Oxfordian Clay with respect to their possible influence on failure strength (Klinkenberg et al. (2009)). The mechanical testing showed that the shear strength increases with increasing carbonate content. This phenomenon was also observed for the samples of the Callovo Oxfordian Clay (Klinkenberg et al. (2009)), while the opposite relation was found for the shaly facies of the Opalinus Clay. Preliminary results presented here, indicate that the sandy facies (drilling BLT-A2) and Callovo Oxfordian Clay show similar mechanical properties – in detail: 1) Microfabric: carbonates predominate in the matrix, 2) Mineralogy: high carbonate content and 3) Mechanical testing: shear strength increases with increasing carbonate content, where the type of carbonates which controls the increase of strength has to be identified more extensively.

References

Bock, H., Dehandschutter, B., Martin, C.D., Mazurek, M., de Haller, A., Skoczylas, F., Davy, C. (2010.) Self-sealing of fractures in argillaceous formations in context with the geological disposal of radioactive waste. OECD/NEA report 6184, OECD Nuclear Energy Agency, Paris, France, 312 pp, ISBN 978-92-64-99095-1.

Gräsle, W. and Plischke, I. (2011). LT-A Experiment: Mechanical Behavior of Opalinus Clay Data report -from Phase 15. Technical Note 2010-86, Mont Terri Projekt, Switzerland. In press.

Klinkenberg, M., Kaufhold, S., Dohrmann, R., Siegesmund, S. (2009). Influence of carbonate microfabrics on the failure strength of claystones. Engineering Geology, 107, 42–54.

Meier, L.P., Kahr, G. (1999). Determination of the cation exchange capacity (CEC) of clay minerals using the complexes of Copper (II) ion with Triethylenetetramine and Tretraethylenepentamine. Clays and Clay Minerals, 47, 386 – 388.

Nagra. (2002). Projekt Opalinuston, Synthese der geowissenschaftlichen Untersuchungsergebnisse, Entsorgungsnachweis für abgebrannte Brennelemente, verglaste hochaktive sowie langlebige mittelaktive Abfälle. Nagra tech. Ber. NTB 02-03.

Ufer, K., Stanjek, H., Roth, G., Dohrmann, R., Kleeberg, R., Kaufhold, S. (2008). Quantita-tive phase analysis of bentonites by the Rietveld method. Clays and Clay Minerals, 56, 272-282.

X-ray Microspectroscopic Investigations of Ni(II) Uptake by Argillaceous Rocks of the Boda Siltstone Formation IN Hungary

Dániel Breitner[1*], János Osán[1], Szabina Török[1], István Sajó[2], Rainer Dähn[3], Zoltán Máthé[4], Csaba Szabó[5]

[1]KFKI Atomic Energy Research Institute (HU)
[2]Chemical Research Centre of the Hungarian Academy of Sciences (HU)
[3]Laboratory for Waste Management, Paul Scherrer Institute (CH)
[4]MECSEKÉRC Plc. (HU)
[5]Lithosphere Fluid Research Lab, Eötvös Loránd University (HU)

* Corresponding author: breitner@aeki.kfki.hu

Abstract

Synchrotron-based µ-focused X-ray fluorescence, X-ray diffraction and X-ray absorption spectroscopy were applied to identify the potential minerals responsible for the uptake of Ni in microscopically heterogeneous clay-rich rock samples, originating from the Boda Siltstone Formation (BSF, Hungary). The X-ray fluorescence measurements indicate a correlation of Ni with Fe- and K-rich regions suggesting that Ni is predominantly taken up by these phases. X-ray diffraction identified the Fe- and K-rich regions as illite and iron oxides, respectively. X-ray absorption spectroscopy demonstrated that under the experimental conditions employed inner-sphere complexation of Ni(II) to clay minerals prevail, indicating that illite and iron oxides are an effective sink for Ni(II) in BSF.

Introduction

One of the main aspects for evaluating the safety case of a potential radioactive waste repository in a deep geological formation is to understand and quantify the geochemical and physical processes that influence the mobility of the radionuclides in the geochemical environment imposed by the host rock. This information is needed to make reliable predictions of the long-term retardation behaviour of radionuclides. The present study focuses on the interaction of a key radionuclide with the host-rock of the planned high level radioactive waste (HLW) repository in Hungary (BSF). The aim is to investigate the uptake mechanisms of selected metals representing fission products on clays and other minerals present in the host rock.

Materials and methods

Small pieces of selected Boda core samples from a depth of 540 m were ground down to ca. 30 µm and mounted onto high purity Si holder and polished by 0.25 µm diamond paste. Based on the XRD study of the bulk sample, its mineral composition is 34 wt.% clay minerals, 7 wt.% albite, 16 wt.%

analcime, 28 wt.% quartz, 10 wt.% calcite and 5 wt.% hematite. The samples were equilibrated for 72-hour with a 1 mM $NiCl_2$ solution at pH = 7.05 in a 0.1 M NaCl background electrolyte.

The structure and mineral heterogeneity of the rock matrix of the BSF samples and the Ni distribution on the sample surface after the sorption experiment was studied by low-vacuum FEI Quanta 3D scanning electron microscope using 15 kV acceleration voltage. The analyses were performed at Eötvös Loránd University, Budapest. Combined µ-XRF/XRD measurements were performed at HASYLAB Beamline L (Hamburg, Germany) and at the ANKA FLUO Beamline (Karlsruhe, Germany) using a multilayer monochromator at a fixed energy of 17.5 keV. The single-bounce capillary at HASYLAB resulted in a beam diameter of 20 µm, whereas the compound refractive lens employed at ANKA resulted in a beam footprint of 3 µm (V) × 8 µm (H) on the sample. µ-XRF maps were recorded from pre-selected areas of the samples, using a step size comparable to the beam size (20 µm at HASYLAB and 5 µm at ANKA) and 1 s counting time per pixel. The µ-XRF maps were analysed using the AXIL software. The elemental maps served as a basis for selection of small areas of interest where µ-XRD images were collected by a CCD detector. The µ-EXAFS measurements were measured in fluorescence mode at HASYLAB Beamline L, using a Si(111) monochromator and a polycapillary half-lens, resulting in a beam diameter of 20 µm for certain points of interest (POI).

Results and discussion

The scanning electron microscopic (SEM) investigations showed that the average size of the mineral grains in the rock matrix is ca. 5 microns surrounded by finer clay rich materials. The identified minerals in the matrix are illite, hematite, rutile, quartz, K-feldspar and calcite/dolomite (Figure 1). The X-ray mapping demonstrated that Ni is present mainly in iron oxide grains and the clay rich regions surrounding larger grains such as K-feldspar and quartz (Figure 1), and practically no Ni was identified on quartz and K-feldspar.

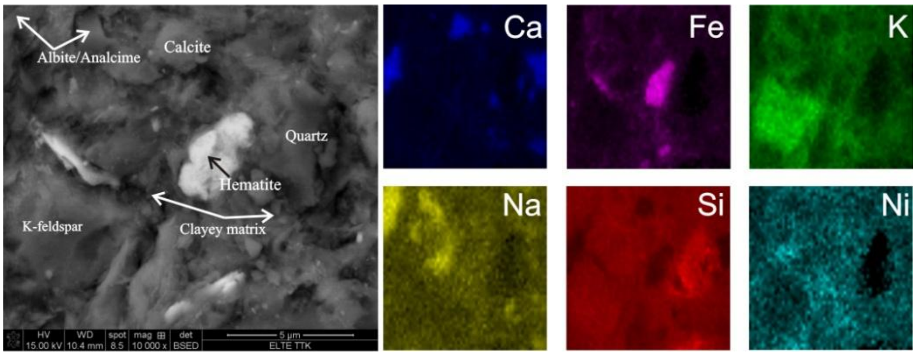

Figure 1. Back scattered electron image of Boda sample and the identified minerals and the X-ray maps of the selected elements at the selected sample area.

Based on the SEM measurements two areas for µ-XRF analysis were selected (Ib4cr1 and Ib4cr4, Figure 2 and 3, respectively). The correlations of elemental intensities in the area Ib4cr1 indicate that Ni is well correlated with K and Fe, with correlation coefficients of ~0.8, and anti-correlated with Ca (Figure 2).

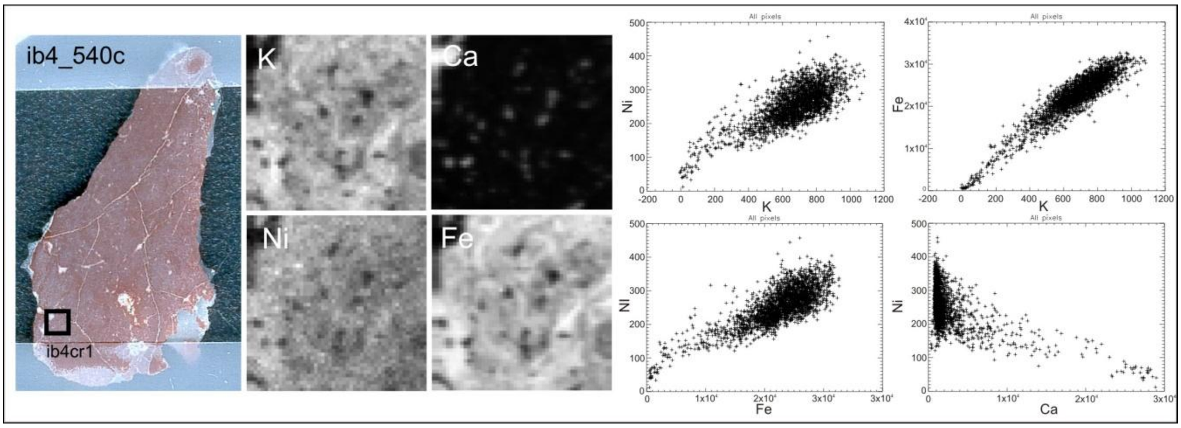

Figure 2. Optical image of the thin section ib4-540c; elemental maps of the selected area ib4cr1 (1x1 mm, indicated as black square on the optical image) and scatter plots of characteristic X-ray intensities of elements measured at beamline L/HASYLAB.

The mineralogical characterisations were complemented by μ-XRF/XRD measurements at the FLUO (ANKA) beamline with a much smaller spatial resolution (Figure 3). The correlation coefficients between K and Ni, as well as Fe and Ni are below 0.5, which are significantly lower than for the larger (20 μm) beam. The μ-XRF map exhibits only a few Ni hotspots. The distribution maps indicate that Ni is mainly associated to K- and Fe-rich phases (Figure 3). With the smaller beam the K-Fe correlation coefficient is also lower (0.73) compared to the area ib4cr1 (0.92, as plotted in Figure 2), due to the lower counting statistics. μ-XRD analyses with a 5 μm beam diameter indicate that the composition of the argillaceous rock matrix on the micro-scale agree well with the mineral composition of the clay rich areas obtained by bulk-XRD measurements. The good correlation of Fe with K is caused by the high K content in illite (a K-rich 2:1 clay mineral) and the coexistence of small (ca. 10 nm) hematite particles.

The μ-EXAFS spectra for various POI's can be attributed to two different species (Figure 4). One of the species exhibited a strong second peak in the radial structure function (RSF) at a R + ΔR position of 2.75 Å, which is characteristic for Ni-Ni backscattering pairs, and is indicative for a Ni-precipitate. For other POI this Ni-Ni backscattering pair is absent. Instead, these spectra can be fitted well, with Ni-O, Ni-Al, and Ni-Si backscattering pairs. The resulting coordination numbers and distances are consistent with the formation of inner sphere complexes at clay edge sites (Dähn et al., 2003).

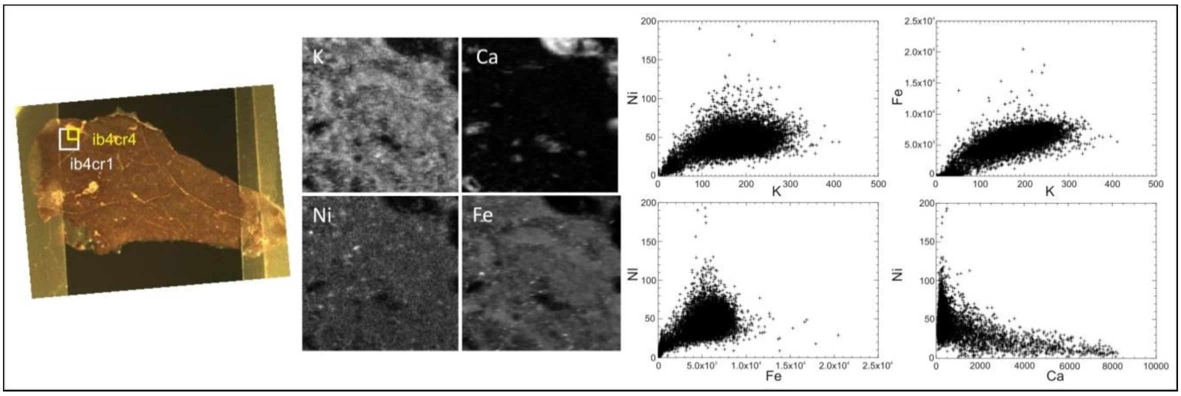

Figure 3. Optical image of the thin section ib4-540c; elemental maps of the selected area ib4cr4 (0.5x0.5 mm, indicated as yellow square on the optical image) and scatter plots of characteristic X-ray intensities of elements measured at beamline FLUO/ANKA.

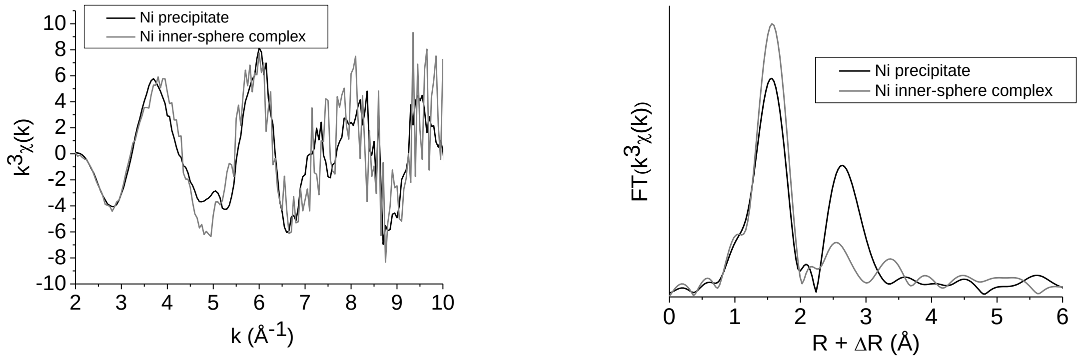

Figure 4. k^3-weighted Ni K-edge micro-EXAFS spectra representative for the formation of Ni-precipitates and inner-sphere complexes, and the corresponding RSF's, obtained by Fourier transforming the micro-EXAFS spectra in the range from 2 to 10 Å^{-1}.

Summary and Conclusions

The formation of Ni precipitated phases such as Ni-phyllosilicates has important geochemical implications because layered silicates are stable minerals in mildly acidic to basic pH conditions and can irreversibly bind metals in waste and soil matrices. The uptake of contaminants on mineral surfaces forming inner-sphere complexes strongly reduces the mobility of metals in the geosphere. The results of the analyses demonstrated that for Ni(II) the clay mineral illite and iron oxide are the most effective sinks in the BSF sample.

Acknowledgement

The research greatfully acknowledges funding from the Swiss-Hungarian Cooperation Programme through Project n° SH/7/2/11 and from the European Community's Seventh Framework Programme (FP7/2007-2013) under grant agreement n° 226716. The authors would like to thank Karen Appel and Manuela Borchert (HASYLAB), and Rolf Simon (ANKA) for the support during the measurements.

References

Dähn, R., Scheidegger, A.M., Manceau, A., Schlegel, M.L., Baeyens, B., Bradbury, M.H., and Chateigner, D. (2003). Geochim. Cosmochim. Acta 67, 1.

Y(III) Binding to the Smectite Hectorite

Nicolas Finck*, Kathy Dardenne

Institute for Nuclear Waste Disposal (INE), Karlsruhe Institute of Technology (KIT), Campus North,
P.O. Box 3640, D-76021 Karlsruhe, Germany (GER).

* Corresponding author: Nicolas.finck@kit.edu

Abstract

The smectite hectorite was synthesized in the presence of trivalent yttrium. The solid phases associated with the multi-step synthesis procedure were characterized by X-ray diffraction. The crystal-chemical environment surrounding Y(III) during distinct stages was probed by EXAFS spectroscopy. The trivalent cation is found 6-fold coordinated by oxygen atoms and located successively in a brucite-like and in a clay-like environment. The compelling formation of inner-sphere surface complexes or of an Y(III)-containing amorphous silica phase upon clay crystallization is ruled out.

Introduction

Several countries are currently investigating the safety and reliability of disposing high level nuclear waste (HLW) in deep geological repositories. In such repositories, the migration of radionuclide (RN) released from the waste matrix would be retarded by interacting with the alteration products, the engineered barriers and the host rock. In this multi-barrier system, clay minerals are foreseen to play a key role. Clay rocks may host HLW repositories in several countries and bentonite, made mostly of smectites, may be used as backfill material. Additionally, the magnesian smectite hectorite has been identified in the alteration layer in long-term glass corrosion experiment (Thien et al., 2010). Radionuclide may be retained by formation of surface complexes, but also by incorporation in the bulk structure of clay minerals, resulting in long-term immobilization.

In a previous study, the Lu(III) uptake sites by coprecipitation with and by sorption on hectorite was deciphered (Finck et al., 2009). In the present work, we focused on the retention of Y(III). This trivalent cation is larger ($r(^{VI}Y(III)) = 0.90$ Å (Shannon, 1976)) as the heavier Lu(III) ($r(^{VI}Lu(III)) = 0.86$ Å) and is closer in size to that of the long-lived and radiotoxic actinides (e.g., $r(^{VI}Cm(III)) = 0.97$ Å, $r(^{VI}Am(III)) = 0.98$ Å). The Y(III) binding mechanisms by coprecipitation with and by sorption on hectorite was deciphered by EXAFS spectroscopy.

Experimental Section

Sample preparation and characterization

Hectorite was crystallized (Finck et al., 2009) in the presence of Y(III) (Mg:Y = 1000:1; sample Yco-pHect)). Briefly, an Y(III)-containing $Mg(OH)_2$ sol was refluxed in the presence of LiF and a silica sol. Separately, Y(III) ions were sorbed on undoped hectorite ($[Y(III)]_{tot} = 50$ µM, m/V = 2 g/L, pH =

7.8(1), 0.5 M $NaClO_4$ (sample YsorbHec)) and an Y(III)-containing $Mg(OH)_2$ precursor (Ybru) was prepared. Prior to EXAFS investigations, XRD data (Cu Kα radiation) were collected for YcopHec and Ybru.

EXAFS measurements

Yttrium K-edge EXAFS data were collected at the INE-Beamline (Dardenne et al., 2009) at the synchrotron light source ANKA (Karlsruhe, Germany). All spectra were collected in fluorescence-yield detection mode using a 5 element LEGe detector (Canberra). Analysis of the EXAFS data was performed following standard procedures by using Athena and Artemis interfaces to the Ifeffit software (Ravel and Newville, 2005). Data fit was performed in R-space using phase and amplitude functions calculated with feff8 (Ankudinov et al., 1998).

Results and Interpretation

X-ray Diffraction

The XRD patterns indicated that the solid phases consist in smectite (YcopHec) and brucite (Ybru). No compelling separate Y-containing phase could be detected, confirming the dispersion of Y in trace amounts within the matrices. Furthermore, the presence of Y did not significantly influence the synthesis of hectorite or degree of crystallinity. This corroborates previous results on the small impact of large metal cations at trace concentrations on the hectorite crystallization (Finck et al., 2009).

EXAFS Spectroscopy

Information on the crystal-chemical environment was obtained by modeling the EXAFS data. Figure 1 shows the experimental and modeled Fourier transforms (FT) of all samples and the fit results are presented in Table 1. The FT of $Y(III)_{aq}$ has a single FT contribution at R + ΔR of 1.8 Å (uncorrected for phase shift) which was modeled considering a single oxygen shell located at 2.35(2) Å and containing 8 atoms. This result is well in agreement with reported values (Diaz-Moreno, 2000). For all solid phases, the first FT contribution was modeled considering two oxygen subshells located at d(Y-O1) = 2.23-2.25 Å and d(Y-O2) = 2.39-2.41 Å, and containing ~3 (YcopHec, YsorbHec) or ~5 (Ybru) atoms, and between ~1 and ~3 backscatterers, respectively.

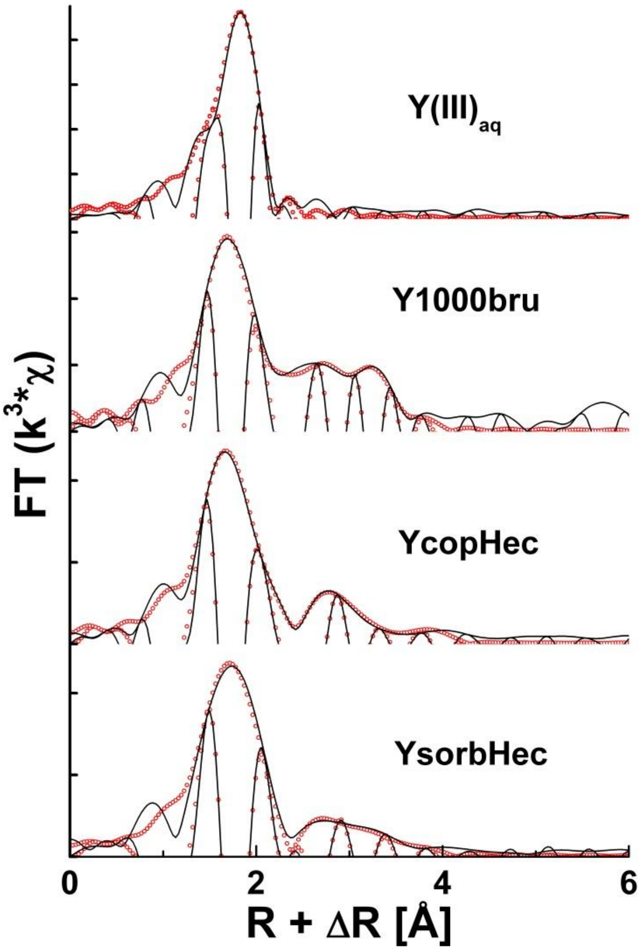

Figure 1. Experimental (solid lines) and simulated (dotted lines) amplitudes and imaginary parts of the Fourier transforms of the EXAFS data collected for $Y(III)_{aq}$, Ybru, YcopHec and YsorbHec.

Higher distances cationic shells were detected in all solid samples. For Ybru, Mg shells were detected at 3.29(1) (N_{Mg1} ~4 atoms) and 3.50(2) Å (N_{Mg2} ~2 atoms). For YcopHec and YsorbHec, Mg and Si backscatterers were used to model the FT contribution at ~3 Å. These shells are located at higher distances for surface sorbed Y (d(Y-Mg1) = 3.50(2) Å and d(Y-Si1) = 3.62(1) Å) than for coprecipitated Y (3.35(2) Å and 3.47 Å, respectively). The fits were also improved by addition of a C shell (<1 atom at d(Y-C) = 2.71(2) Å) for all solid phases. No neighboring Y was detected in any compound, ruling out the precipitation of $Y(OH)_{3(s)}$.

Table 1. Quantitative EXAFS analysis of the investigated samples. Number in parentheses indicates the uncertainties. R: distance, N: coordination number, σ^2: mean square displacement (Debye-Waller factor), R_f: goodness of fit. A C shell was considered to fit the data for all solid samples (0.5(1) atom at 2.71(2) Å).

Sample	Shell	R [Å]	N	σ^2 [$Å^2$]	R_f
$Y(III)_{aq}$	Y−O1	2.35(2)	8.0	0.007	0.0050
Ybru	Y−O1	2.25(2)	4.9(1.0)	0.007	0.0075
	Y−O2	2.41(2)	1.4(3)	0.007	
	Y−Mg1	3.29(1)	3.9(8)	0.006	
	Y−Mg2	3.50(2)	1.5(3)	0.006	
	Y−O3	3.79(2)	4.8(9)	0.005	
	Y−O4	4.11(2)	1.5(1.0)	0.005	
YcopHec	Y−O1	2.23(1)	3.3(2)	0.005	0.0058
	Y−O2	2.39(2)	2.1(4)	0.005	
	Y−Mg1	3.35(2)	1.0(2)	0.004	
	Y−Si1	3.47(1)	3.1(6)	0.008	
	Y−Si2	4.35(4)	1.1(6)	0.008	
YsorbHec	Y−O1	2.25(1)	3.3(2)	0.005	0.0042
	Y−O2	2.41(2)	2.5(2)	0.005	
	Y−Mg1	3.50(2)	3.1(6)	0.007	
	Y−Si1	3.62(1)	2.2(3)	0.008	
	Y−O3	4.11(2)	1.7(7)	0.008	

Discussion

The EXAFS data show that Y(III) is located in distinct environment in each step of the synthesis protocol. Brucite is made up of $Mg-O_6$ octahedra (d(Mg-O) = 2.10 Å) sharing edges (Catti et al., 1995). The simplest hypothesis is to assume that Y substitutes for Mg in Ybru. Considering the increase in size (0.18 Å) from Mg to Y, six O atoms could be expected at 2.28 Å. The fit results indicate the presence of N_{O1} = 4.9(1.0) O atoms at d(Y-O1) = 2.25(2) Å, very close to the expected values. Furthermore, considering edge sharing between Mg and Y polyhedra, d(Y-Mg) = 3.34 Å would be expected, reasonably close to the fit result (d(Y-Mg1) = 3.29 Å). Finally, d(Y-O3) = 3.79(2) Å and d(Y-O4) = 4.11(2) Å are in agreement with reported values (Catti et al., 1995).

Upon YcopHec crystallization from Ybru, the first coordination shell was almost unchanged, except the lower coordination number. The larger size of Y(III) results in yttrium being located at a strained site. Consequently, no change in first and second coordination shells may be expected, in agreement with observations, but contrary to the crystallization of undoped hectorite (Breu et al., 2003) from $Mg(OH)_2$ (Catti et al., 1995). The first coordination shell in YsorbHec also consists in two O subshells: this is usually explained by binding of trivalent cations (Stumpf et al., 2001) to the surface of the clay (O1 subshell) and ligation to hydration molecules (O2 subshell). Still, the fit results suggest distinct environment surrounding Y upon coprecipitation and surface sorption. In YcopHec, d(Y-Mg1) = 3.35(2) Å may possibly be explained by edge sharing between Mg and Y polyhedra. However, the calculated value (3.24 Å) is slightly shorter than the experimental value, but the difference could be accounted for by structural strain. In contrast, d(Y-Mg1) = 3.50(2) Å in YsorbHec may only be explained by the formation of Y(III) surface complexes. The actual interpretation is that Y binds to hectorite at the layer edges. However, because of the large interatomic distance, Mg and Y polyhedra may not bind by sharing edges. Yttrium may rather bind to oxygen atoms belonging to the corner of the Mg octahedra and tilted out of the hectorite plane. This configuration may then also account for d(Y-Si1) = 3.62(1) Å.

Summary and Conclusions

Hectorite was crystallized in the presence of Y(III). Data show that Y is 6-fold coordinated by oxygen and is successively located in a brucite-like and in a clay-like environment. The data suggest that trivalent cations may be incorporated in the octahedral sheet of clay minerals by coprecipitation in aqueous systems, but result in large strain. It can be anticipated that such a binding mechanism would be even more difficult for larger trivalent actinides. This study implements the molecular-level understanding of trivalent cation binding to clay minerals.

Acknowledgement

ANKA is acknowledged for provision of synchrotron radiation beamtime.

References

Ankudinov, L.A.; Ravel, B.; Rehr, J.J., Conradson S.D. (1998). Real-space multiple-scattering calculation and interpretation of XANES. Phys. Rev. B58, 7565-7576.

Breu, J.; Seidl, W. and Stoll A. (2003). Disorder in smectites in dependence of the interlayer cation. Z. Anorg. Allg. Chem. 629, 503-515.

Catti, M.; Ferraris, G.; Hull, S., Pavese, A. (1995). Static compression and H disorder in brucite to 11 GPa: a powder neutron diffraction study. Phys. Chem. Minerals 22, 200-206.

Dardenne, K.; Brendebach, B.; Denecke, M.A.; Rothe, J., Vitova, T. (2009). New developments at the INE-Beamline for actinide research at ANKA. J. Phys. Conf. Series 190, 012037.

Diaz-Moreno, S.; Munoz-Paez, A. and Chaboy, J. (2000). X-ray absorption spectroscopy (XAS) study of the hydration structure of yttrium(III) cations in liquid and glassy states: eight or nine-fold coordination? J. Phys. Chem. 104, 1278-1286.

Finck, N.; Schlegel, M.L. and Bosbach, D. (2009). Sites of Lu(III) sorbed to and coprecipitated with hectorite. Environ. Sci. Technol. 43 (23), 8807-8812.

Ravel, B and Newville, M. (2005). ATHENA, ARTEMIS, HEPHAESTUS: data analysis for X-ray absorption spectroscopy using IFEFFIT. J. Synchrotron Rad. 12, 537-541.

Shannon, R.D. (1976). Revised effective ionic radii and systematic studies of interatomic distances in halides and chalcogenides. Acta Crystallogr. A32, 751-767.

Stumpf, T.; Bauer, A.; Coppin, F., Kim, J.I. (2001). Time-resolved laser fluorescence spectroscopy study of the sorption of Cm(III) onto smectite and kaolinite. ES&T 35, 3691-3694.

Thien, B.; Godon, N.; Hubert, F.; Angeli, F.; Gin, S. and Ayral, A. (2010). Structural identification of a trioctahedral smectite formed by the aqueous alteration of a nuclear glass. Applied Clay Sci. 49, 135-141.

SESSION –II “PORE STRUCTURE AND CONNECTIVITY”

BIB-SEM of Representative Area Clay Structures: Insights and Challenges

Guillaume Desbois[1*], Janos L. Urai [1], Maartje Houben[1], Susanne Hemes[1], Jop Klaver[1]

[1] Structural Geology, Tectonics and Geomechanics, RWTH Aachen University, Lochnerstrasse 4-20, 52056 Aachen (DE)

* Corresponding author: g.desbois@ged.rwth-aachen.de

Abstract

BIB polishing in combination with SEM imaging is used to study the pore microstructures and -fabrics in clay-rich host-rocks on 2D mm^2 flat and undamaged CS with resolutions down to a few nanometers in REA. BIB-SEM approach allows both qualitative and quantitative investigations of porosity and targeting for nano-FIB tomography. These results in the characterization of porosity-homogeneous and -predictable islands, which form the elementary components of an alternative concept of porosity/permeability model based on pore microstructures.

Introduction

A major contribution to understanding the sealing capacity, coupled flow, capillary processes and associated deformation in clay-rich geomaterials is based on detailed investigation of the rock microstructures. However, the direct characterization of pores in REA and below µm-scale resolution remains challenging. To investigate directly the mm- to nm-scale porosity, SEM is certainly the most direct approach, but it is limited by the poor quality of the investigated surfaces. The recent development of ion milling tools (BIB and FIB; Desbois et al, 2009, 2011-a; Heath et al., 2011; Keller et al., 2011) and cryo-SEM allows respectively producing exceptional high quality polished cross-sections suitable for high resolution porosity SEM-imaging at nm-scale and investigating samples under wet conditions by cryogenic stabilization. This contribution focuses mainly on the SEM description of pore microstructures in 2D BIB-polished CSs of Boom (Mol site, Belgium) and Opalinus (Mont Terri, Switzerland) clays down to the SEM resolution. Pores detected in images are statistically analyzed to perform porosity quantification in REA. On the one hand, BIB-SEM results allow retrieving MIP measurements obtained from larger sample volumes. On the other hand, the BIB-SEM approach allows characterizing porosity-homogeneous and -predictable islands, which form the elementary components of an alternative concept of porosity/permeability model based on pore microstructures.

Samples

Authors are interested in pore-related microstructures in all types of low porous and low permeable host-rocks: rocksalts (Desbois et al., 2008, 2011-b), clays from reference sites for research (BC-clay, OP-Clay-ShF, OP-Clay-SaF and To-Clay, Desbois et al., 2009; Houben et al., submit.), tight gas reservoir sandstones (Desbois et al., 2011-a), organics-rich shale, coal, mortar and cements. Samples OP-Clay-ShF (Gallery 98-BCS-2), BC-Clay-HADES (EZE55, Core 77c122, Bed 90), BC-Clay-CG (EZE52, Core 48c, Bed 114) and EZE54 and BC-Clay-FG (Core 65c, Bed 100) are extensively presented in this contribution but pictures from To-Clay (CN4-STD-05-600) and organic-rich shale are also shown.

Methods

Sample preparation

Core samples, originally stored in Al barrier foil, are slowly dried in air at room temperature. Subsamples (ca. < 0.5 cm^3) are cut dry with very low-speed diamond saw and glued on BIB sample holders. The quality of BIB-CS is optimized by pre-polishing using carbide paper (down to grit size 1200) which reduces the surface roughness to ca. 20 µm. The BIB (JEOL-SM 09010, 6 kV, 8hrs) removes a slice of 100 µm, which eliminates the damage from the pre-polishing, and produces high quality surface. The CS is coated with carbon or gold.

Ion beam techniques for surface preparation and SEM

BIB-FIB-SEM are powerful combination to prepare 2D flat undamaged CS (curtaining less than 5 nm deep, Figure 1). Two main types of ion sources are available. (1) A BIB (few mA, Ar-source) is suitable to produce large polished CS area of few mm^2 (Figure 1.a). BIB cross sectioners are available as standalone machines able to produce single polished CS. (2) FIB are based on Ga-ion sources (1pA ->50nA) to produce typical CS of a few µm^2. FIB sources are commercially embedded into SEM to allow serial sectioning for 3D tomography. BIB has two main advantages: (1) it is potentially less damaging since it is based on noble gas source and (2) it produces CS which fits better to the typical length scale range of microstructures and REA.

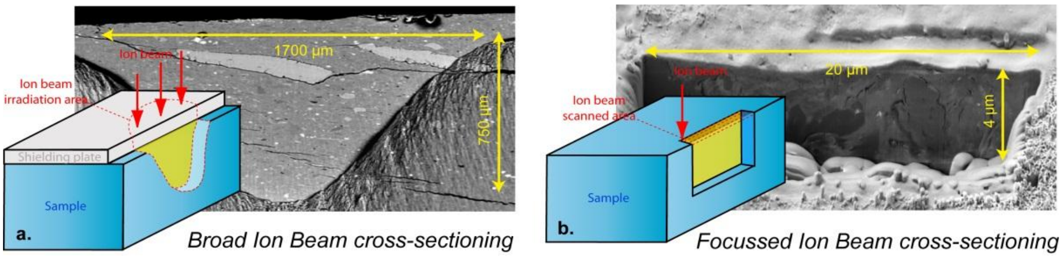

Figure 1. The principle of BIB and FIB sectioning and overviews of produced CS. (a) the ion beam irradiates the edge of a sample un-masked by the shielding plate to create high quality polished CS suitable for SEM imaging. (b) The FIB scans the region of interest to be milled.

Cryo methods can be coupled to SEM in order to track in situ fluids in pore space. This approach is based on the fast freezing of the samples to very low temperatures, which effectively quenches the fluid-filled pores, followed by high resolution electron microscopy at cryostatic temperatures. Cryo-SEM is now commercially combined with a FIB milling (Holzer et al., 2010; Desbois et al., 2008, 2009). A BIB-cryo-SEM is actually in development at RWTH-Aachen University (Desbois et al., 2011-b) to combine all advantages.

Microstructures and fabrics imaging, and image processing

The SEM used is a Zeiss Supra 55 equipped with SE2, SE-inlens, BSE and EDX detectors. Typically, SE imaging is performed at <10KV while BSE and EDX imaging at 20-25 kV, both at WD < 10 mm. The point counting method based on the mineralogy with different square box sizes determines the REA for the pores present in a BIB-CS. In order to image the REA with sufficient pore resolution, SE micrographs are combined into one high-resolution image (>100 million pixels) using Autopano giga

2.0 software. Porosity is statistically evaluated using the PolyLX Matlab toolbox from microstructures manually digitized in ARCMAP 9.3 from the SE-mosaic.

Qualitative investigations of pore space from mm^2 scale area down to pore scale

Overviews of BIB-SEM performed on BC-Clay-HADES, OP-Clay-ShF, To-Clay and organic-rich shale (Figure 2) show characteristic fabrics. BC-Clay-HADES is mainly made of highly porous CM with few embedded non-clay, poorly porous minerals. OP-Clay-ShF is built with numerous non-clay minerals with significant intra-grain porosity (fossils and pyrite framboid) embedded in CM less porous than BC-Clay-HADES. Porous fossils and pyrite framboid are also common in To-Clay but much more dispersed in very tight CM. Shale fabric is similar to OP-Clay-ShF but with very tight CM.

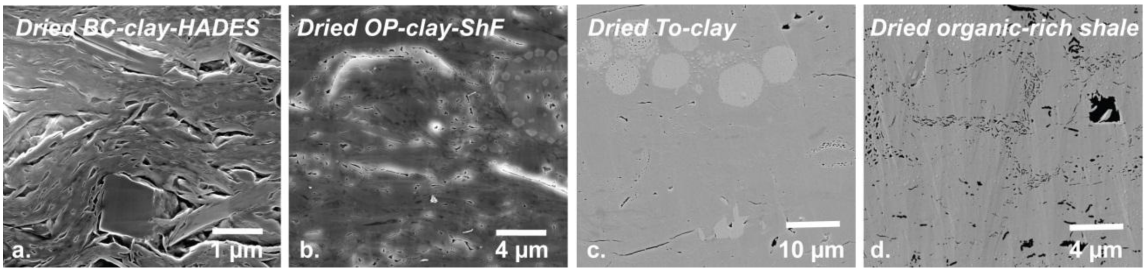

Figure 2. Overviews of pore fabrics in four different types of clay-rich host-rocks.

Resolution of SE-mosaics (Figure 2), allows zooming in to detect single pores close to the SEM resolution (ca. 5 nm) in the CM of BC-Clay-HADES (Figure 3) and OP-Clay-ShF (Figure 4), and typical single pores found in fossil (Figure 4a), in siderite (Figure 4b) in pyrite framboid (Figure 4d) phases as well as in fractures (Figure 4c) from OP-Clay-ShF.

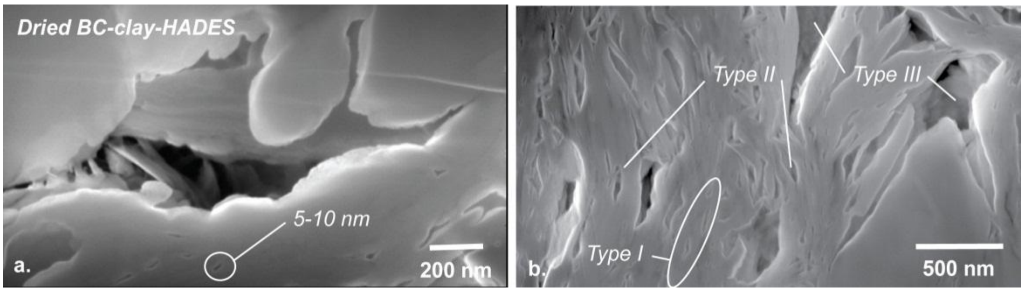

Figure 3. Single pores from CM in BC-Clay-HADES, at high resolution.

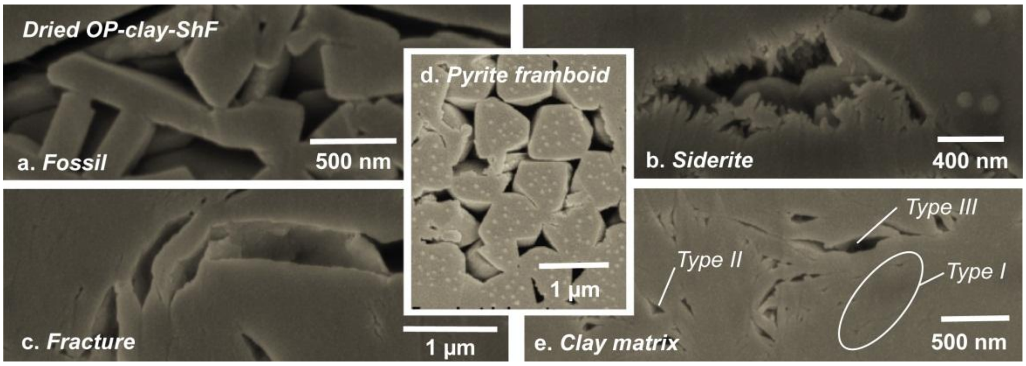

Figure 4. Diversity of single pore morphologies in different mineral phases of OP-Clay-ShF

In OP-Clay-ShF (Figure 4), five different porous phases were found: (1) *Siderite grains* are parallelogram-shaped with elongated to circular pores with jagged edges non-connected to each other and to the CM; (2) *Fossils* are usually half-moon shaped with angular pores of 500 nm in diameter connected to each other's and with the CM; (3) *Quartz* are rounded grains with a diameter up to 30 µm and can contain rare round pores, with smooth edges; (4) *Pyrite framboid* –are up about 5 µm in diameter and made of sub-µm single pyrite grains with between pores of about 500 nm in size; (5) *CM* consists of grains of size < 2 µm with three kinds of pore: Type I - the elongated pores between similarly oriented clay sheets, Type II - crescent shaped pores in saddle reefs of folded sheets of clay and Type III - large jagged pores surrounding clastic grains. In BC-Clay-HADES (Figure 3), only the CM is significantly porous and pore types are the same than those found in OP-Clay-ShF. In addition for both samples, within the CM, cracks are also present and oriented along the bedding.

In OP-Clay-ShF, REA is measured to be about 100 x 100 µm^2; about 70 x 70 µm^2 in BC-Clay-HADES and BC-Clay-FG; and 140 x 140 µm^2 in BC-Clay-CG. The REA is interpreted as the minimum area to be investigated to describe representative pore microstructures and fabrics. Coupling the information from quantitative (EDX) and qualitative (BSE) chemical composition measurements with single pores detection in REA, maps of porosity are drawn to describe the 2D distribution of pore space as a function of the nature and the distribution of mineralogy (Figure 5).

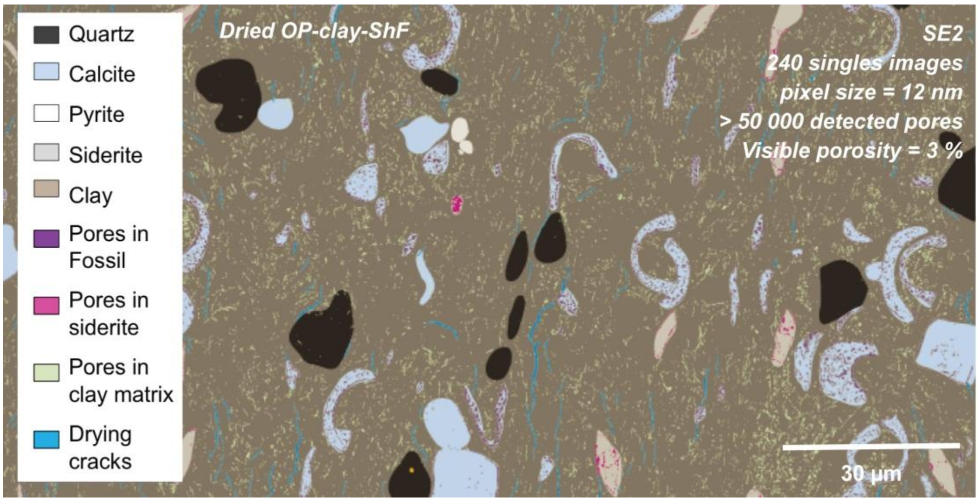

Figure 5. 2D map of porosity in OP-Clay-ShF vs. mineralogy.

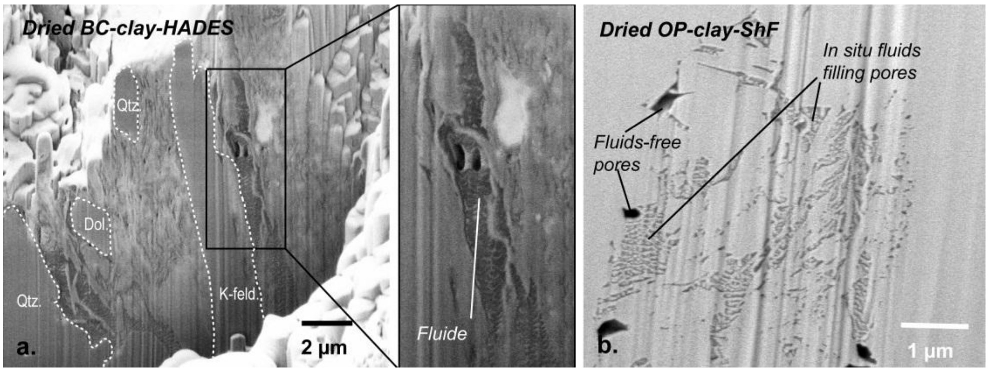

Figure 6. Fluid-filled pores in BC-Clay-HADES (a.) and OP-Clay-ShF (b.) by FIB-cryo-SEM.

Figure 6 shows in situ fluids in the clay matrix pores of type III in sample prepared by FIB-cryo-SEM. Imaging frozen fluids in pore type I and II is more difficult since at higher magnification the energy of the e^--beam sublimes the fluids before an image can be recorded. Tracking in-situ fluid-filled pores should offer new insights for the study of fluid-rock interaction. Cryo-stabilization should also be considered as an alternative method to stabilize the pore microstructures without damage.

Quantitative investigations of pore space

Pores visible in SE-micrographs are statistically analyzed in REA. Due to the complexity of pore morphologies (Figure 3a), usual algorithms for object detection do not provide efficient segmentation. Therefore, pores are manually segmented. This is time consuming but allows accurate description of the spatial and size distributions, morphologies and orientation of the pores. More over these data are also used to develop alternative automatic pore detection as benchmark data. For example, a REA of studied OP-Clay-ShF (Figure 5) contains more than of 50 000 detected pores corresponding to 3% of visible porosity at the resolution of SEM.

Porosity from BIB-SEM in OP-Clay-ShF vs. MIP

From BIB-SEM data, pores in clay-matrix are power law distributed with D = 2.3 (Figure 7a). Assuming that pores, which are not visible at the SEM resolution, are also distributed following the same power law, the extrapolation of this down to 3-4 nm pore diameter gives an estimated total porosity of 17-23 % born by the CM (Figure 7b). BIB-SEM shows fossils and pyrite framboids as well as cracks are directly connected to the CM adding about 1.5-4 % of porosity. Therefore, based on BIB-SEM and assuming that pores in CM are connected, the total connected porosity is estimated in the range of 18.5-27%. This matches quite well the porosity measured on similar samples by MIP (Figure 7d). Based on MIP measurement, connected pore follow also a power law distribution with D = 2.2 (Figure 7c), which fits quite well the value inferred from BIB-SEM. Thus, this suggests that the CM mainly controls the connectivity of the OP-Clay-ShF. These analogies show also that BIB-SEM investigations can be up-scaled to bulk porosity based on larger sample volume (MIP).

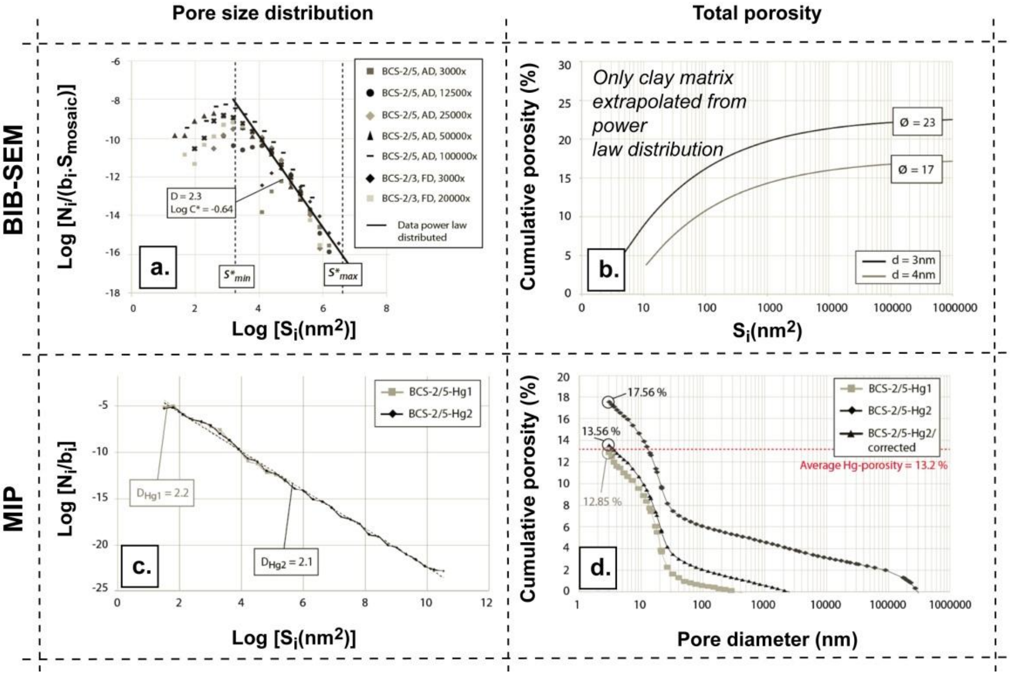

Figure 7. Pore size distribution and total porosity data from BIB-SEM (respectively a. and b.) and MIP (respectively c. and d.) in OP-Clay-ShF.

Porosity vs. grain size in clay-rich islands from BC-Clay

At first look, the overall fabrics of BC-Clay-HADES, BC-Clay-FG and BC-Clay-CG (Figure 8.a, b, c respectively) look different for similar areas of investigation. However, at scale of CM regions, statistics for pores < 300 nm in size have same pore size distribution (Figure 8d), same D = 1.7 (Figure 8e), same pore orientation (// to the bedding), same pore types and same pore morphologies, independently of the grain size. Pore of > 300 nm in size are preferentially located surrounding the clastic grains (Figure 8a). This is confirmed by plotting, for each grain, the pore area as a function of distance from the grain (Figure 8f). This suggests that the biggest pores are constrained by the clastic grains. Further work is still needed to check if the mineralogy and the size of single clastic grains play a role.

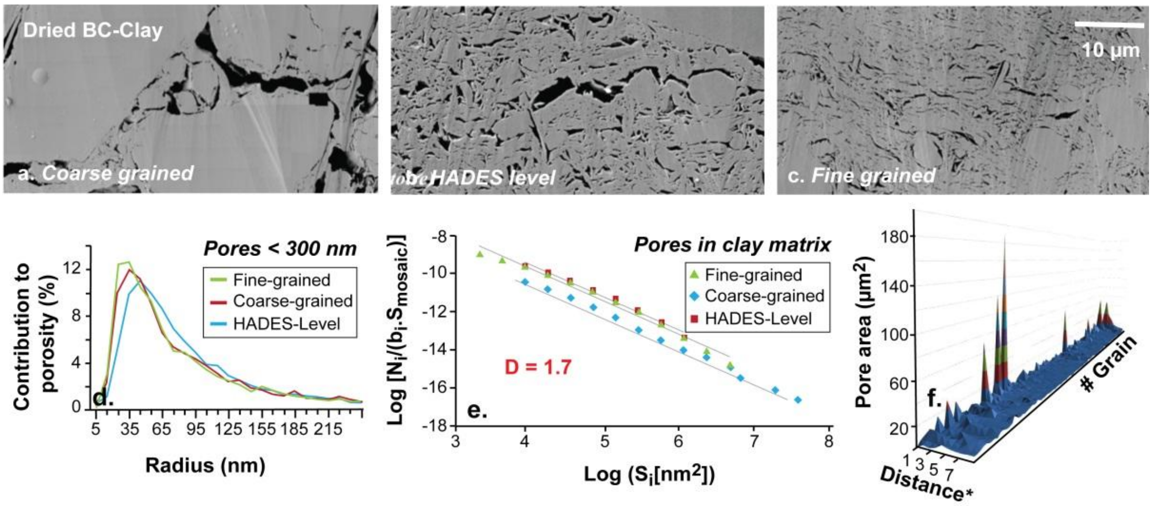

Figure 8. (a., b. and c.) Pore fabric overview in BC-Clay-CG, BC-Clay-Hades and BC-Clay-FG, respectively. (d) Contribution to porosity as a function of pore radius. (e.) Pore size distribution. (f) Pore area vs. distance from single grain.

The concept: pore fabric based on porosity-homogeneous and -predictable islands

Surprising is that BIB-SEM observations give clear evidences that the non-clay minerals and CM form distinct islands with homogeneous and predictable pore space characteristics in the same BIB-CS. All kinds of islands are considered as “elementary components”, which form the overall fabric of the claystones when combined all together (Figure 9).

For example, the overall fabric of OP-Clay-ShF, defined by a REA of 100 x 100 µm^2, results then in grains of non-clay minerals (pyrite, mica, quartz, calcite, fossils, pyrite) embedded in CM and randomly distributed along the bedding planes. In terms of connectivity and at the scale of SEM, different kind of islands can be classified into 3 classes: (1) the CM, (2) the porous regions connected to the CM (fossils, pyrite, cracks), and (3) others non-porous islands (quartz, organics, mica, calcite) and porous regions but not connected to the CM (siderite). Thus, from a microstructural point of view, the heterogeneous OP-Clay-ShF can be seen as the combination and juxtaposition of homogeneous and predictable porous islands: regions of high and highly connected porosity (fossils, pyrite, cracks) and non porous (or non connected) regions are isolated and embedded within the low permeable and low porosity CM. Islands with high and highly connected porosity are connected to each other via the low permeable and low porous CM. Following this, the flow properties of OP-Clay-ShF should be mainly controlled by the porosity and permeability of the CM.

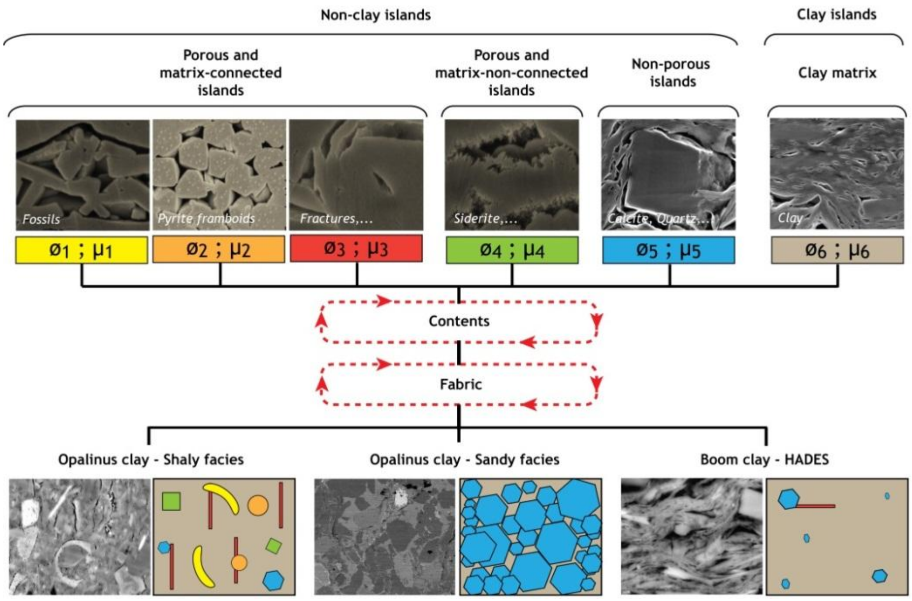

Figure 9. An alternative concept of porosity/permeability model based on pore microstructures

Conclusions and outlooks

BIB-SEM approach enables: (1) imaging the porosity in 2D flat and undamaged REA down to the SEM resolution; (2) investigating pore morphologies; (3) classifying pore types as a function of mineralogy and fabrics when BSE and EDX tools are used; (4) quantifying the porosity from digitized pores which results in prediction of pore characteristics for each porous phases; (5) linking pore microstructures to conventional MIP based on larger sample volumes. From these, emerges an alternative concept of porosity/permeability model based on pore microstructures, where the BIB-SEM approach allows characterizing porosity-homogeneous and -predictable islands. BIB-SEM combination appears then as necessary to bridge the µ-CT to nano FIB tomography methods.

To continue the deeper understanding of pore microstructures in natural clay-rich host-rocks, further work is still needed: (1) BIB-SEM approach should be used complementary to µ-CT to describe 3D-mineral fabrics at larger scale and to FIB-SEM to build natural 3D pore network as basic for permeability calculation of local islands. (2) How does the pore distribution in clay-rich islands evolve as a function of depth or local tectonics? (3) Then, may the power law exponent of pore distribution in clay-rich islands define the origin of clay? (4) Can other conventional porosimetry measurements be retrieved from BIB-SEM studies? (5) Image analysis algorithms need to be especially designed for automatic pore segmentation from BIB-CS to speed up the interpretation of images. (6) Because, pore throats are typically below 10 nm (Keller et al., 2011): do we need to include TEM methods in microstructural studies or/and perform Wood's metal intrusion combined with BIB-SEM to evaluate directly the intrusion process? (7) Tracking the in-situ fluid-filled pores and drying effect by using cryo-SEM approaches.

Acknowledgement

We thank DFG, NAGRA, SCK-CEN, Wintershall Holding AG and Swiss Topo for funding and supporting our projects. We are also grateful to Uwe Wollenberg for technical support with SEM and HIWIs from the GED institute of RWTH-Aachen who helped with the image and data processing.

References

Desbois G. Urai J., Burkhardt C., Drury M., Hayles M. and Humbel B. (2008). Cryogenic vitrification and 3D serial sectioning using high resolution cryo-FIB SEM technology for brine-filled grain boundaries in Halite: first results. Geofluids, 8: 60-72.

Desbois G., Urai J.L. and Kukla P.A. (2009) Morphology of the pore space in claystones - evidence from BIB/FIB ion beam sectioning and cryo-SEM observations. E-Earth, 4, 15-22.

Desbois G., Urai J.L., Kukla P.A., Konstanty J. and Baerle C. (2011-a, in press). High-resolution 3D fabric and porosity model in a tight gas sandstone reservoir: a new approach to investigate microstructures from mm- to nm-scale combining argon beam cross-sectioning and SEM imaging . Journal of Petroleum Science and Engineering, in press.

Desbois G., Urai J.L., Kukla P.A., Wollenberg U., Pérez-Willard F., Radí Z. and Sandor R. (2011-b, in press). Distribution of brine in grain boundaries during static recrystallization in wet, synthetic halite: insight from Broad Ion Beam sectioning and SEM observation at cryogenic temperature. Contribution to Mineralogy and Petrology, in press.

Heath J.E., Dewers T.A., McPherson B.J.O.L., Petrusak R., Chidsey, Jr. T.C., Rinehart A.J., and Mozley P.S. (2011) Pore networks in continental and marine mudstones: Characteristics and controls on sealing behavior. Geosphere; 7, 429–454.

Holzer, L., Münch, B., Rizzi, M., Wepf, R., Marschall, P., Graule, T., 2010. 3D-microstructure analysis of hydrated bentonite with cryo-stabilized pore water. Applied Clay Science 47, 330-342.

Houben M.E., Desbois G. and Urai J.L. (submit.). Pore morphology and distribution in the shaly facies of Opalinus clayn (Mont Terri, Switzerland): insigths from representative 2D BIB-SEM investigations on mm- to nm- scales. Applied Clay Sciences.

Keller L.M., Holzer L., Wepf R., Gasser P. (2011). 3D geometry and topology of pore pathways in Opalinus clay: Implications for mass transport, Applied Clay Sciences, 52, 85-95.

X-ray Tomography and Impregnation Methods to Analyze Pore Space Hetreogeneities at the Hydrated State

D. Prêt[1*], E. Ferrage[1], E. Tertre[1], M. Pelletier[2], J.C. Robinet[1], M. Faurel[1], I. Bihannic[2], F. Hubert[1]

[1] HydrASA, University of Poitiers, France

[2] EST-LEM, Nancy, France

* Corresponding author: dimitri.pret@univ-poitiers.fr

Background

For clay based materials, the investigation of both mineral skeleton and pore space organization as well as water distribution remains a key and challenging task. Such information is however required in order to fully understand and model their macroscopic hydro-mechanical or transport properties.

In particular, as far as swelling clay minerals are involved, even pure clay materials are well known to represent spatially heterogeneous, anisotropic and deformable media from the nanometre (i.e., the crystal/interlayer scale) to the centimetre scale (i.e., the sample size involved in macroscopic experiments) (Figure 1). Probing their organization over such extremely large scale range requires the combination of different techniques providing quantitative results that can be used to feed global balances of water and pore distributions. Bulk physical measurements (e.g., gaz adsorption, mercury intrusion, scattering or diffraction approaches) have been used for decades for analyzing clay systems at the dry state or for hydrated states under free macroscopic swelling conditions of samples (i.e., the sample could swell and shrink; Figure 2). These approaches need to be associated to reveal the complexity of the pore space network. Indeed, all probes exhibit contrasted accessibilities (as well as for different solute species) and provide data on the basis of simple geometrical models either about pore or neck/throat size for a given size range. The main interest of imaging techniques is their ability to reveal the spatial heterogeneities of organization as well as the real morphology of pores. Still, they are poorly documented in literature as preparation procedures and extraction of quantitative data are not straightforward for clay materials.

Clay organization is highly reactive and is, for example, a function of the resin/water removal technique used during embedding process, the content/composition of pore water or the pressure applied. Imaging techniques based on electron beam generally requires vacuum conditions around the sample and imply its impregnation by a resin. It is then generally difficult to assess the hydration state corresponding to the organization observed. Coupling different techniques is thus only possible when similar environmental conditions and preparations are used. In case of methods able to deal with wet atmospheres and nanometre resolution, sub-sampling millimetre or micrometre size hydrated samples without inducing shearing or fractures is also not still proven. Optimization of impregnation procedure for water saturated clay samples still plays a pivotal role for applying the most advanced imaging techniques at the nanometre scale.

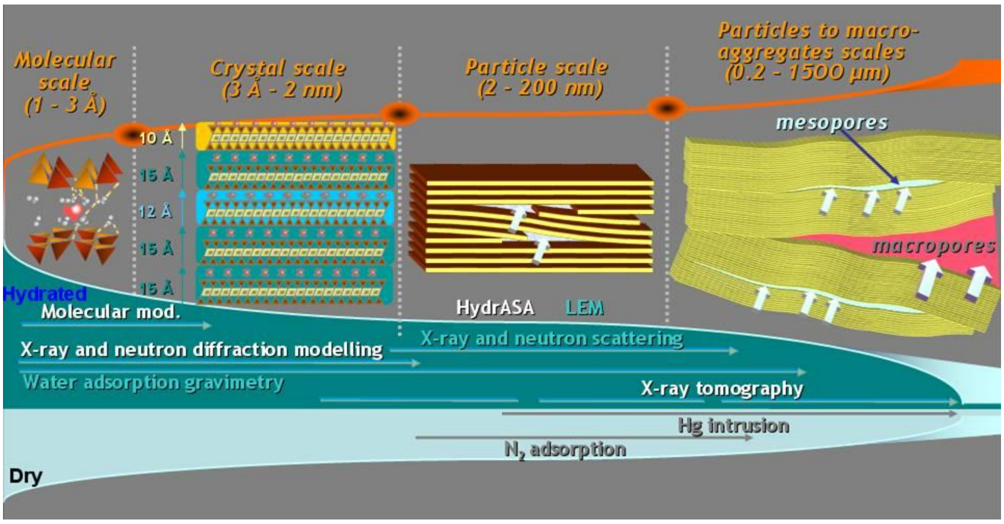

Figure 1. Multiscale heterogeneous organization of pure swelling clay media and a possible coupling of techniques used in the Hydrasa laboratory to analyze it.

In addition, natural clay rocks in sedimentary basins or engineered barriers in deep repositories could not swell or shrink by changing their macroscopic volume. Such case corresponds to constrained swelling conditions that implies a distribution of pore and water highly contrasting with dry state and hydrated state in free swelling conditions (Figure 2). Moreover, swelling rate could potentially be limited down to the crystal scale. As probing in-situ the organization of hydrated and compacted clay materials into an oedometer set-up is challenging, it is really poorly documented in literature. Note that opening an oedometer setup and analyzing a sample is not a constrained swelling condition: immediate swelling and change of pore space occurs (e.g., it is a phenomenon classically studied in geotechnics through the swelling index).

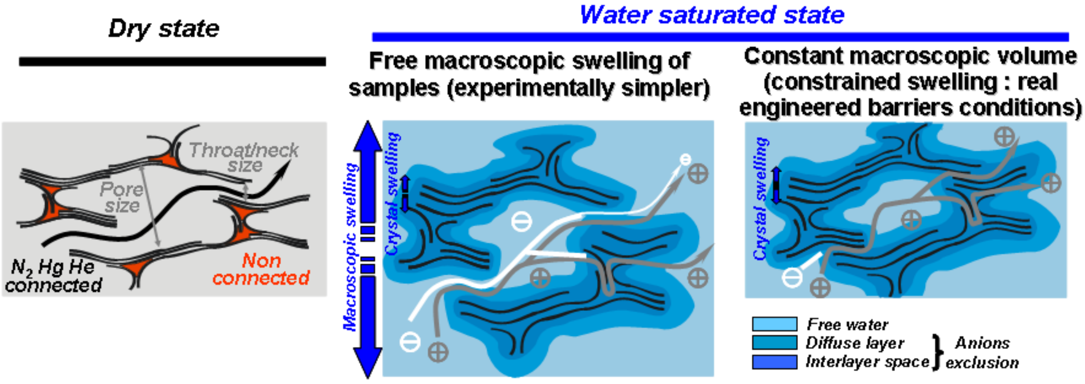

Figure 2. Evolution of mineral skeleton, pore and water distributions, accessibility to different probes as a function of hydration and constraints imposed on macroscopic swelling.

Natural clayey rocks in sedimentary basins display additional spatial variations of mineral and porosity distributions with contrasted spatial frequencies or gradual evolutions due to sedimentation cycles, temporal evolutions of climate, variations of sources, diagenesis, etc. At the scale of a laboratory sample (i.e., the decimetre scale), geological history still imposes a heterogeneous spatial distribution of mineral and pore space downscaling to the crystal scale (e.g., sedimentary laminae, bioturbations, diagenetic mineral growing and dissolution). Localizing samples with a millimetre size or less against the heterogeneities encountered at larger scale is thus important before analyzing it with a nanometre resolution. The best is to follow a continuous downscaling approach all along the characterization of the organization, keeping the sample in a similar state between each technique.

Here we propose a method to fully impregnate up to decimetre sample in constrained volume conditions and with a resin fixing the clay as in its hydrated state (not like fully saturated in some cases). Such preparation allows a downscaling characterization of the pore space heterogeneities when using laboratory and synchrotron X-Ray µtomography (µCT) by facilitating sub-sampling. In order to reveal the interest/limitations of this 3D non destructive imaging technique, a few comparisons will be done with other 2D techniques for the same samples. Finally, as X-Ray beams are well adapted to wet samples, we report a characterization of the pore space/ water distribution upon hydration for pure swelling clay media at different scales.

An impregnation technique fixing clay hydrated and the resulting downscaling approach for characterizing pore space heterogeneities

Impregnation protocols for clayey rocks have been largely studied in the 60's and 70's, mainly paying attention to the choice of adequate organic solvents or freeze-drying approaches for removing water without artefact. Here a freeze drying approach has been compared to oven drying. But some points as crucial are less documented.

A consolidated clayey rock sample generally swells and sometimes is totally disaggregated when putting it into a water vial. If the resin chosen for an impregnation protocol is able to mimics the same phenomenon, it has the potential to fix the organization of hydrated clay. It is rarely the case and it is then important to understand what is the equivalent hydration state obtained. But such basics behaviour imposes that any impregnation process for a latter study of organization in constrained swelling conditions needs to be applied through the use of confining cells. Strong swelling pressures generated by such resins or water are not balanced by a simple resin surrounding of samples or organics capsules. Thus we developed specific impregnation cells to avoid biased results. Systematically, a post-control of impregnation/confining efficiency is done as well as demonstrating that no macroscopic change of sample volume occurs.

As sub-sampling wet clay samples without artefact is difficult, the best is to impregnate a centimetre scale sample before sawing it. The choice of the resin is thus constrained by its ability to saturate the pore space through good dynamical properties and long impregnation times. Fixing the hydrated state is the other objective. These points are not fully demonstrated when using the commercial resin already tested in literature. Studying their interaction with clay is not simple as they content several organic components with contrasted properties. Here we select a pure monomer, the Methyl MethAcrylate (MMA), able to imply both crystalline swelling and strong macroscopic swelling pressures. We then characterize the resin/clay interaction and the efficiency/limits of both the resin and confining systems by coupling different imaging techniques with XRD, FTIR and TGA. The organization obtained mimics hydrated clays just below water saturation (i.e., a relative humidity of 98%) as osmotic swelling at crystal scale is not reproduced. This is the case for Na saturated smectites but a better reproduction of the water saturated state is expected with other interlayer cations. The full impregnation of confined decimetre samples is also successfully proven (Figure 4). But we demonstrate that lot of attention should be paid to the choice of confining systems (Figure 3), the initial sample sawing/storing (Figure 4) and the impregnation time that reaches several months.

Starting from decimetre scale and fully impregnated samples, sawing or coring well localized subsamples without creating artefacts is facilitated even at millimetre scale or less. A downscaling approach could be then applied by selecting the techniques in function of the resolution and field of view needed.

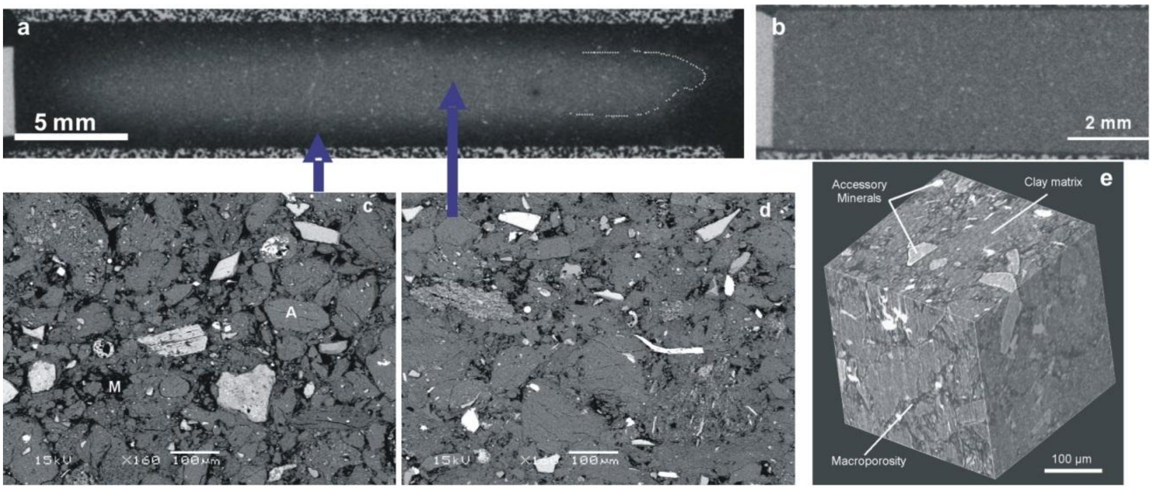

Figure 3. Centimetre scale compacted MX80 bentonite samples impregnated by MMA in constrained volume conditions (dry bulk density of 1.6g/cm^3). a) Autoradiograph showing a local porosity increase (darker) in the border of the sample due to decompaction by swelling through the confining sinters. b) Autoradiograph of a homogeneous and well constrained sample when using low pore size sinters. c-d) SEM BSE image of the organization at low scale in the decompacted border and well preserved core previously recognized on the autoradiograph (M: macropores ; A: mesoporous aggregates). e) Synchrotron X-ray µCT volume of the same sample subsampled using coring (ESRF, BM05 beamline, resolution 1.4µm).

For clay rocks, the poor contrast achieved by µCT on decimetre or centimetre scale samples only allows the detection of heavy minerals and the largest fracture networks leading from dehydration/mechanical stress. The comparison of laboratory µCT and 2D autoradiograph porosity mapping clearly demonstrates that this latter technique is more adapted to reveal spatial heterogeneities of pore space from the decimetre scale down to a few tens of microns. 2D autoradiograph porosity mapping is based on a full impregnation with a ^{14}C or ^{3}H labelled resin coupled with image processing. Sensibility, spatial resolution and contrast are better and a quantitative mapping is achieved by including all pores whatever their sizes, even interlayer spaces (Figure 4; Gaboreau et al. (2011), Prêt et al. (2004), Sardini et al. (2009)). The use of laboratory µCT is thus better adapted to (i) the control of clay samples before experiments such as transport experiences or (ii) to the 3D localization of sub-sampling into water saturated samples for latter techniques forbidding the use of a resin (Schlegel et al. (2010)).

At millimetre scale down to the micron or sub-micron scale, the comparison we did between 3D synchrotron µCT and 2D Back-Scattered Electron/SEM imaging also reveals a worse contrast even if it is improved for small samples (Figure 3). It is especially challenging to distinguish quartz grains from the surrounding clay matrix. Image analysis is then facilitated by using 2D BSE images in order to provide quantitative data with a similar resolution. Mineral/porosity mapping by processing SEM/EPMA chemical maps provides the best discrimination between all rock forming minerals (Prêt (2010a)). The local estimation of the nanometre pore amounts including interlayers and with a resolution of a few micrometres is also obtained (Prêt, 2010b). It is a unique way for measuring the porosity associated to each mineral for such finely divided materials and maps the heterogeneities of the spatial distribution. For artefact-free sub-sampling of natural clay samples of a few millimetres, resin impregnation is recommended. But the main interest of using synchrotron µCT then remains for revealing the 3D morphology of a macropore network or a clay matrix. Segmentation of these poorly contrasted features is really challenging and needs specially developed algorithms to preserve their connectivity and contents. Such time consuming approaches is justified when the data then support 3D numerical modelling of macroscopic solute diffusion experiments for example (Robinet et al., submitted).

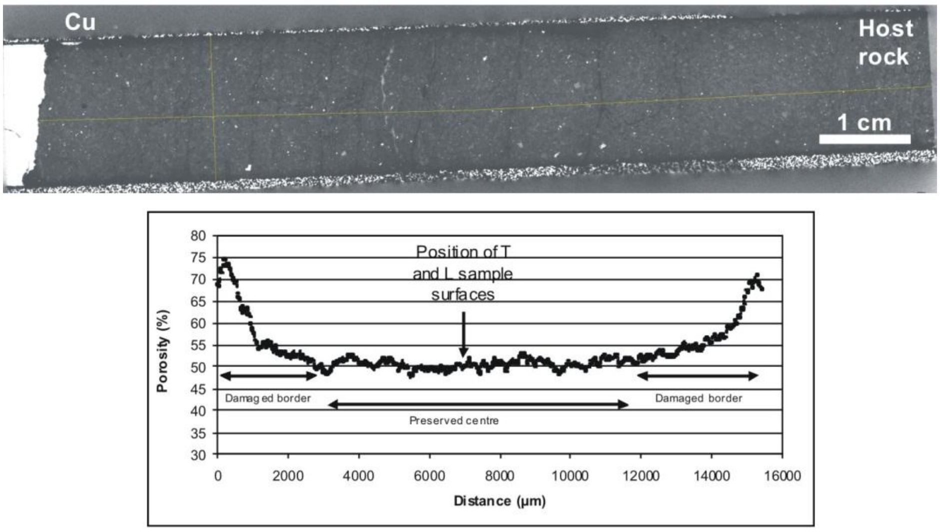

Figure 4. Decimetre scale compacted MX80 bentonite sample impregnated by ^{14}C-labelled MMA in constrained volume conditions (SKB-LOT experiment) Note that storing before impregnation induces irreversible shrinkage artefacts. Up: Autoradiograph on a polished thick parallel to the impregnation direction: yellow lines indicate the position of the porosity profiles. Down: Mean porosity profile along the vertical yellow line on the autoradiograph indicating a damaged zone on a thickness of 2.5mm due to sawing.

Influence of hydration on multi-scale pore space and water distribution of swelling clay

To our knowledge, constraints on data acquisition or treatment actually does not allow the quantitative study of water saturated and compacted samples in constrained volume conditions, i.e., in the main organization state of engineered barriers involved in nuclear waste repositories. For example, preparation needed for electron microscopy is never performed in constrained swelling conditions and fixing water saturated state is still not fully proven for water removal approaches and resins used. X-ray or neutron diffraction/small angle scattering models are also limited for non-oriented wet samples and design of suitable setup for in-situ analysis of sample representative of engineered barriers is a real experimental constraint for X-ray or electron beams. Only a few works exploiting confining setups for in-situ analysis and neutron beams provides qualitative approaches (Devineau et al.(2006)) or promising methods for data treatment of SAXS data which are under progress.

Hydration of model samples in free swelling conditions using laboratory µCT

A preliminary, technically possible but still challenging task is to couple different methods quantitatively for studying the impact of hydration on organization at different scales of partially saturated samples in free swelling conditions. In addition of the cross-validation of the methods used, constraints on organization and processes involved just below water-saturation conditions could be provided.

An alternative way for studying the impact of hydration at different organization scales is to use the same technique, here laboratory X-ray tomography, on different controlled macroscopic samples (up to 1 cm) which mimic either only one swelling crystal (here a mono-crystal of Santa Olalla vermiculite) or one oriented clay powder grain (here a mono-aggregate of purified MX-80 smectite). For the latter sample, the additional contribution of mesopores between the particles will both impact the swelling properties and water distribution. Both samples have been Na saturated. By developing specific measurement cells for controlling the relative humidity around the samples, the non-destructive visualization of their 3D morphology in hydrated conditions was achieved with a resolution of 10µm

(Figure 5; Prêt et al. (in prep)). Their sample thickness evolutions at different relative humidities have been quantified using image analysis to derive macroscopic swelling rate in adsorption/desorption conditions. Such swelling rates are then compared with the total amounts of adsorbed water provided by water adsorption/desorption gravimetry.

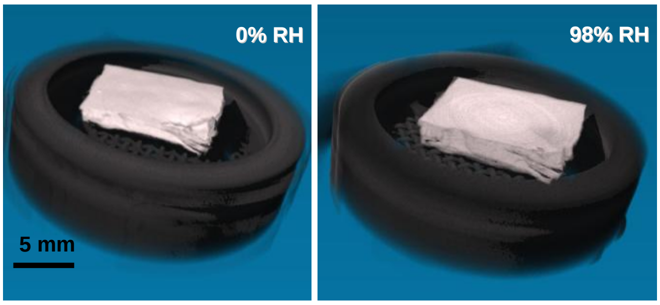

Figure 5. 3D visualization of the MX80 aggregate swelling by X-ray microtomography.

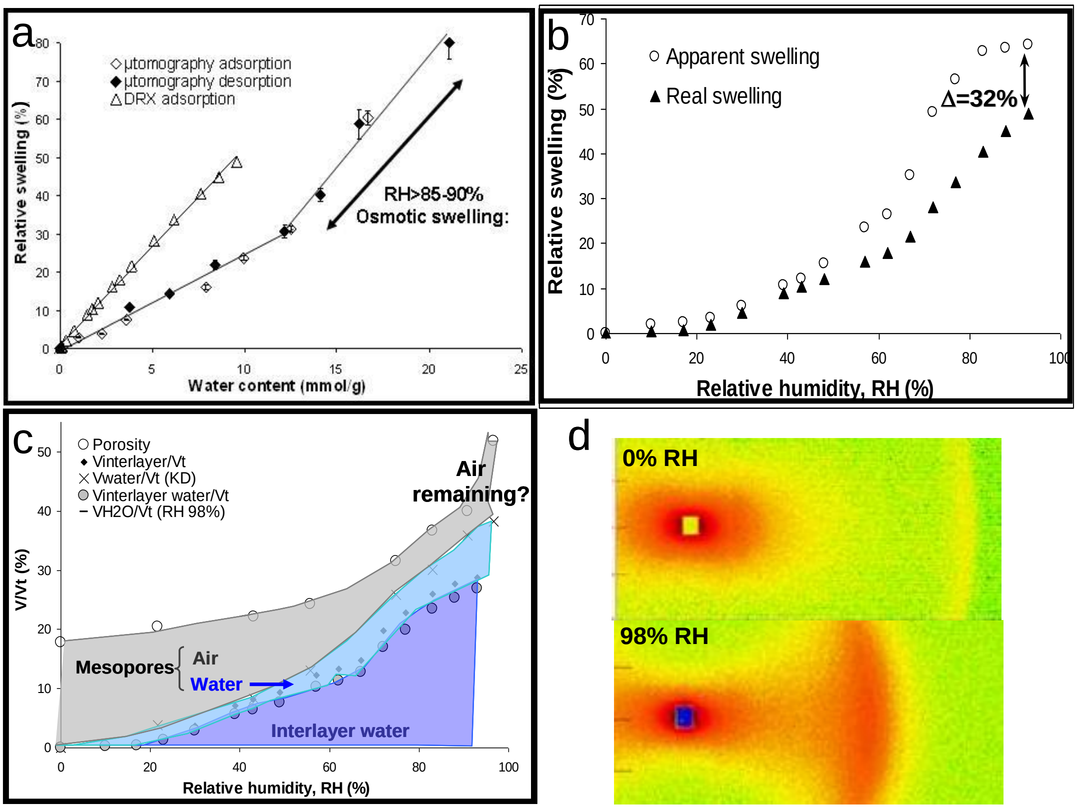

Figure 6. a) Comparison of the MX80 aggregate swelling rate at crystalline (XRD) and macroscopic (µtomography) scales with water content (water gravimetry). b) Comparison of crystal swelling rates measured using the apparent 00l reflection positions in the pattern and the real ones provided by a modelling approach. c) Quantitative balance of air and water distribution for the MX80 aggregate as a function of pore types with hydration. d) SANS 2D pattern highlighting the anisotropy of the mesopore network.

Furthermore, experimental XRD patterns recorded as a function of RH were compared to calculated profiles using a trial-and-error procedure for both samples. The obtained structural models allow describing the hydration behaviour of the swelling interlayers, and more especially their content and thickness as a function of RH. The interlayer water content determined from XRD profile modelling discriminates the relative contributions of H2O molecules from mono- and bi-hydrated interlayers (crystalline water; Ferrage et al. (2010, 2011). Crystal swelling rate/ interlayer water content relationships could then be derived from XRD data and compared to X-ray tomography results and water adsorption isotherms.

For the Santa Olalla monocrystal characterized only by crystal swelling and interlayer water adsorption, the quantitative cross validation of the three methods is demonstrated. Unexpected linear relationships between crystalline water content and swelling are also provided and are fully superimposed for adsorption and desorption mechanisms (not shown).

For the macro-aggregate of purified MX80, the same linear relationship is provided at the crystal scale by XRD but macroscopic swelling rate/total adsorbed water amount coupling strongly differs (Figure 6a). Two linear trends similar for adsorption and desorption are observed and correspond to additional swelling/adsorption processes linked to osmotic effect leading to a strong swelling/adsorption rate at relative humidity higher than 80%. In addition, a dramatic bias of measured crystal swelling rate has been detected when comparing results of accurate pattern modelling and rough estimation through XRD 001 peak position as commonly done for estimating interlayer water content in compacted clays (Figure 6b). These quantitative data were also used for feeding a balance of distribution of each type of pores (i.e., interlayer spaces, mesopores) and their respective water/air contents upon hydration. First, a mesopore collapsing is detected even if the total porosity increases with the macroscopic swelling (Figure 6c). It is explained by a swelling rate which is systematically larger at the crystal scale than at the macroscopic scale. Secondly, unsuspected remaining air is detected even through the osmotic regime.

Finally, complementary small angle neutron scattering (SANS) and neutron diffraction data have been recorded on D16 beamline of ILL Grenoble as a function of RH for both type of sample. SANS results confirm that mesopore content decreases upon hydration and mesopores are strongly anisotropic and oriented according to the sedimentation plane (Figure 6d).

Hydration of compacted bentonite in constrained swelling conditions using synchrotron µCT

The investigation of compacted powders of MX-80 bentonite mimicking real engineered barriers introduces larger inter-aggregate macropores in comparison to model samples described above. Such pores can be imaged through the use of high resolution (700nm) and better contrasted synchrotron X-ray µCT when using small samples (diameter of 1.4mm). Samples have to be compacted directly into specially developed environmental cells permitting their in-situ observation (i.e., enough transmission rate for low X-ray energies) but resisting to the strong swelling pressure generated. This has been successfully done for dry bulk density of 1.4 on the TOMCAT beamline of the Swiss Light Source.

In agreement with the previous results, a strong macro-aggregates swelling is detected when relative humidity reaches 91%, leading to a partial closure of the macropores networks without reaching a total collapsing even at 98% (Figure 7). But small swelling rates detected below the relative humidity of 80% are not observed here. Crystal swelling upon hydration thus strongly impacts the inter-particle mesopores before closing the macropores which are better preserved. Quantifying the macropore content evolution by image analysis is more challenging as contrast with the neighbouring clay aggregates is weak. Only specially developed algorithm based on mathematical morphology tools permits the segmentation and macropore content estimation. At the relative humidity of 98%, this amount is well in agreement with the content obtained on BSE image of compacted bentonite impregnated with MMA in constrained conditions. The organization fixed by this resin is thus close to that encountered for highly hydrated Na saturated clays just below water saturation.

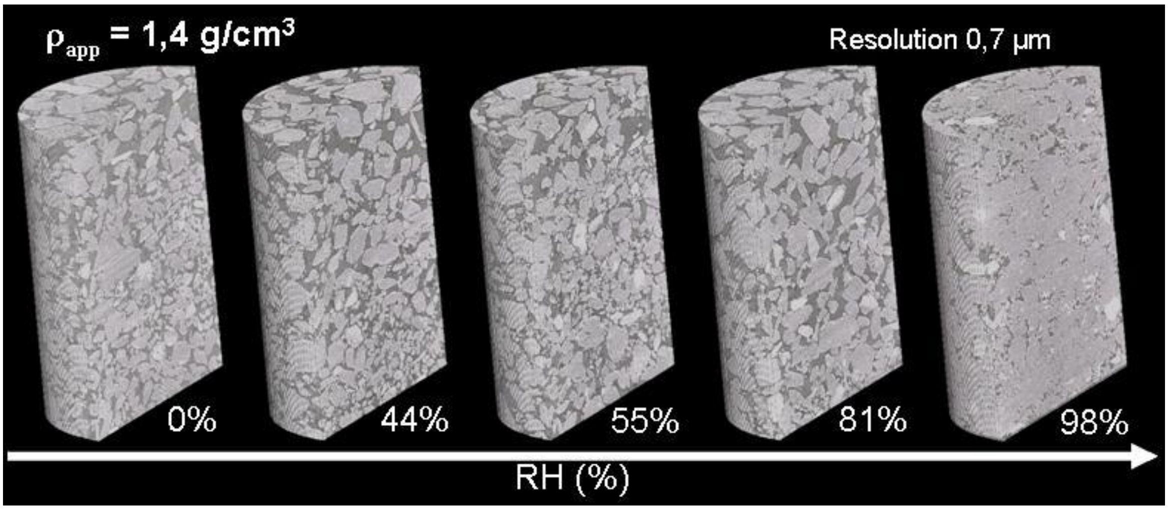

Figure 7. Macropore evolution upon hydration of compacted MX80 bentonite in constrained swelling conditions by synchrotron X-ray tomography.

References

Devineau K., Bihannic I., Michot L., Villiéras F., Masrouri F., Cuisinier O., Fragneto G., Michau N. (2006) In situ neutron diffraction analysis of the influence of geometric confinement on crystalline swelling of montmorillonite. Applied Clay Science,31 , 76-84.

Ferrage E., Sakharov B., Michot L.J., Delville A., Bauer A., Lanson B., Grangeon S., Frapper (2011) Hydration properties and interlayer organization of water and ions in synthetic Na-smectite with tetrahedral layer charge. Part 2. Towards a precise coupling between molecular simulations and diffraction data. Journal of Physical Chemistry C, 115, 1867-1881.

Ferrage E., Lanson B., Michot L.J. (2010) Hydration properties and interlayer organization of water and ions in synthetic Na-smectite with tetrahedral layer charge. Part 1. Results from X-ray diffraction profile modeling. Journal of Physical Chemistry C, 114, 4515-4526.

Gaboreau S., D. Prêt, E. Tinseau, F. Claret, D. Pellegrini, D. Stammose (2011)15 years of in situ cement – argillite interaction from Tournemire URL: characterisation of the multi-scale spatial heterogeneities of pore space evolution. Applied Geochemistry, In Press.

Prêt D., Sardini P., Beaufort D., Sammartino S. (2004) Porosity distribution in a clay gouge by image processing of 14C-PolyMethylMethAcrylate (14C-PMMA) autoradiographs. Case study of the fault of St Julien (Basin of Lodève, France). Applied Clay Science, 27, 107-118.

Prêt D., S. Sammartino, D. Beaufort, A. Meunier, L. Michot (2010a) A new method for quantitative petrography based on image processing of chemical element maps : I. Mineral mapping applied to compacted bentonites. American Mineralogist, 95, 1379-1388.

Prêt D., S. Sammartino, D. Beaufort, M. Fialin, A. Meunier (2010b) A new method for quantitative petrography based on image processing of chemical element maps: II. Semi-quantitative porosity mapping superimposed on mineral map. American Mineralogist, 95, 1389-1398.

Robinet J.-C., P. Sardini, D. Coelho, J.-C. Parneix, D. Prêt, S. Sammartino and S. Altmann Effects of mineral distribution at mesoscopic scale on solute diffusion in a clay-rich rock. Example of the Callovo-Oxfordian mudstone of Bure. Water Ressource Research. Submitted.

Sardini P., A. El Albani,. D. Pret,. S. Gaboreau, M. Siitari-Kauppi, D. Beaufort (2009) Mapping and quantifying the clay aggregate microporosity in medium- to coarse-grained sandstones using the 14C-PMMA method. Journal of Sedimentary Research, 79, 584–592.

Schlegel M., Bataillon C., Blanc C., Prêt D., Foy E. (2010) Anodic Activation of Iron Corrosion in Clay Media under Water-Saturated Conditions at 90 °C: Characterization of the Corrosion Interface. Environmental Science and Technology, 44, 1503–1508.

Spatial analysis of tomographic data and its implications on mass transport in Opalinus Clay

Lukas Keller[1*] **& Lorenz Holzer** [1]

[1] EMPA, Materials Science and Technology, CH-8400 Dübendorf, Switzerland

* Corresponding author: Lukas.Keller@empa.ch

Abstract

The potential use of focused ion beam nanotomography (FIB-nT) in characterizing the 3D geometry of pore space in clay rocks and bentonite was tested. In order to preserve the microstructure and to reduce sample preparation artefacts we used high pressure freezing and subsequent freeze drying to prepare the samples. Resolution limitations placed the lower limit in pore radii that can be analyzed by FIB-nT to about 10-15 nm. Image analysis and the calculation of pore size distribution revealed that pores with radii larger than 10 nm are related to a porosities of about 1-3 vol. %. To validate the method, we compared the pores size distribution obtained by FIB-nT with the one obtained by N_2 adsorption analysis. The latter yielded a porosity of 10-12 vol. %. This means that FIB-nT can describe around 20-30 % of the total pore space. For pore radii larger than 10 nm the pore size distribution obtained by FIB-nT and N_2 adsorption analysis were in good agreement. This suggests that FIB-nT can provide representative data on the spatial distribution of pores for pore sizes in the range of about 10-100 nm. A 3D graph representation permitted determination of the spatial distribution of pore space geometrical properties such as pore path orientation, pore path tortuosity and pore path length. Pore-paths in Opalinus clay show a preferred orientation within the bedding plane in combination with a comparatively low pore path tortuosity. Pore path tortuosity perpendicular to the bedding plane is higher by a factor of as much as five. Anisotropy in pore space is caused by spatial density variations of pore path orientation (i.e. preferred orientations of pore paths) in combination with an elongated pore shape (i.e. low tortuosity).

Introduction

Clay rock formations are proposed as potential host rocks for the disposal of radioactive waste (Andra, 2005; Nagra, 2002, 2004). An evaluation of the isolation potential of the rock requires an understanding of the mass transport mechanism and processes in the rock as well as in the bentonite buffer. The transport properties are primarily controlled by the structure of the accessible network for mass transport. Clay rocks contain a network of micro to macropores with pores sizes ranging between 1-100nm which most likely dominates the flow and transport properties in the rock (e.g. Marschall et al., 2005). Concerning the crucial issue of gas transport, the geometry of those pores that corresponds to comparable larger pores (i.e. > 10nm) may control potential gas flow. Thus, information on larger pore connectivity, geometry and distribution are important.

Due to preferred orientation of clay minerals attained during sedimentation and compaction, clay rocks behave anisotropic (e.g. Lash and Blood, 2004; Wenk et al., 2008). Thus, a pore space anisotropy can be expected because the pore space architecture is likely linked to the surrounding frame of clay minerals. In the case of Opalinus Clay, experiments indicated anisotropic diffusion of solute species with fast diffusion parallel and slow diffusion perpendicular to the bedding plane (e.g. Van Loon et al., 2004). Anisotropic diffusion is suggested to be related to an anisotropy in pore path tortuosity (Van Loon et al., 2004).

A proper understanding of fundamental phenomena such as anisotropic transport requires analysis of the pore space in 3D and the construction of realistic pore space models as a first and essential step. In a second step realistic pore models allow for a quantitative analysis and the prediction of transport properties.

With a few exceptions (e.g. Fredrich et al., 1995; Lindquist and Venkatarangan, 1999; Nakashima et al., 2004; Zabler et al., 2008) 3D characterizations of the pore space in geomaterials and in clay rocks in particular are largely absent. The resolution of the used methods was not sufficient to characterize the pore space of consolidated clay rich sediments of which pore sizes range in the nano scale.

In our present approach we used Focused Ion Beam nanotomography (FIB-nt) as fundamental tool to construct a realistic 3D structure of nano-scale pore space in Opalinus Clay and MX-80 bentonite (Holzer et al., 2004, 2010, 2011; Keller et al. 2011). Our analytical workflow starts with sample preparation. In order to preserve the delicate pore structure and to avoid sample preparation artefacts we applied cryo sample preparation techniques (i.e. high pressure freezing and freeze drying) to the prepare the clay rock samples. Then a well-polished and flat surface is prepared by broad ion beam (BIB) polishing. SEM imaging of this surface allows the characterization of the pore microstructure on a i) larger scale (i.e. mm scale) and a ii) distinction between laterally different microstructures which are related to "pressure shadows" and its more compacted lateral equivalent. Focused ion beam nanotomography (FIB-nT) was then used to characterize the pore structure in 3D at specific sites which correspond to different microstructures. Also at this specific sites we prepared

TEM foils which were investigated by transmission electron microscopy (TEM) in order to explore pores with radii < 10 nm which cannot be resolved by FIB-nt (see Keller et al. 2011 for further discussion). In order to explore larger pores in Opalinus Clay we applied also X-ray tomography with a resolution of 2.56 μm voxel size.

Porosity and pore size distribution in Opalinus Clay

Focused ion beam nano-tomography

The porosity obtained by FIB-nt is a physical porosity as we directly determined the void volume of the sample. Using the complete segmented SE image stack obtained by FIB-nt as input data we obtained a porosity, which ranges between 1-3 vol. % (Figure 1, Keller et al. 2011). Considering that the pores are predominately located within the clay mineral matrix, the porosity in the small-grained clay mineral matrix ranges between 2-3.5 vol.%.

Fundamental conceptual differences between the methods to determine the pore size or pore size distribution from SE images exist (Münch and Holzer, 2008). In order to account for the complex pore geometries we calculated the so-called continuous pore size distribution (Figure 1) (Münch and Holzer, 2008). As a consequence of the chosen voxel size (i.e. around 10^3 nm^3) the smallest pore radii detected by FIB-nt were around 5 nm and the most frequent pore radii ranged between 10 and 50 nm.

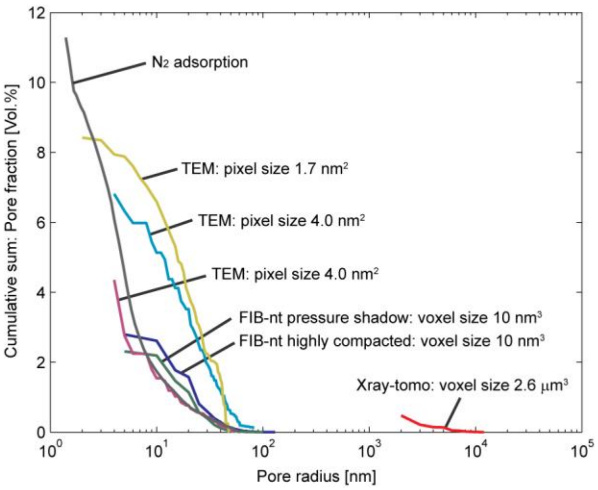

Figure 1. Compilation of pore size distributions determined by FIB-nt, N_2 adsorption analyzes, X-ray tomography and transmission electron microscopy. Note the spatial resolution of the respective methods. All methods were applied to the same Opalinus Clay sample.

N_2 adsorption analysis yielded a BET specific surface area of around 20-21 m^2/g which corresponds to a pore surface density of around 45-47 µm^{-1} by assuming a rock density of 2.28 g/cm^3 (Bossart and Thury, 2008). Since nitrogen molecules do not penetrate into the interlayer region of expandable clay minerals, the measured specific surface area is the external surface area of the minerals and can thus be compared to the pore surface area obtained on the base of FIB-nt. A pore size distribution can also be calculated from the N_2 adsorption isotherms. Using the "modelless" method implemented in the Beckman Coulter Sorption Analysis software for analyzing the desorption branch of the isotherms yielded a porosity of about 10-12 vol. %. Furthermore, it turned out that pores with radii > 10 nm have a physical porosity of about 1.7-2.2 % which is in surprisingly good agreement with FIB-nt (Figure 1). Thus, the majority of the pores have radii ranging between 1.5 and 10 nm related to a porosity of about 10 vol. % which could not be resolved with a FIB-nt voxel size of 10^3 nm. It is suggested that those smaller pores form connecting links between the larger pores that appear as distinct separate objects in the FIB-nt image volume (Figure 3).

X-ray tomography

Bearing in mind the voxel size of 2.56 µm the lower limit of analyzed pore radii was around 2 µm. The porosity of the resolved pore space was < 1 vol. % and pore space consists of isolated and non-connected pore objects. The calculated continuous pore size distribution is depicted in Figure 1.

Transmission electron microscopy

An electron transparent clay rock specimens was prepared in form of a site-specific TEM foil with the dimension of around 10x10x0.100 µm by using the focused ion beam (FIB) technique. TEM investigations were done on a Philips CM30 transmission electron microscope operated at 300 kV. TEM reveals numerous interparticle pores with small radii < 10 nm (Figure 2).

Within the interlayer region layer spacing is about 1.3 nm and also some interlayer pores with a spacing of about 1 nm can be observed (Figure 2). A rough estimate of the interparticle porosity based on pores which were segmented from TEM images suggests porosities up to 8 vol. % (Figure 1).

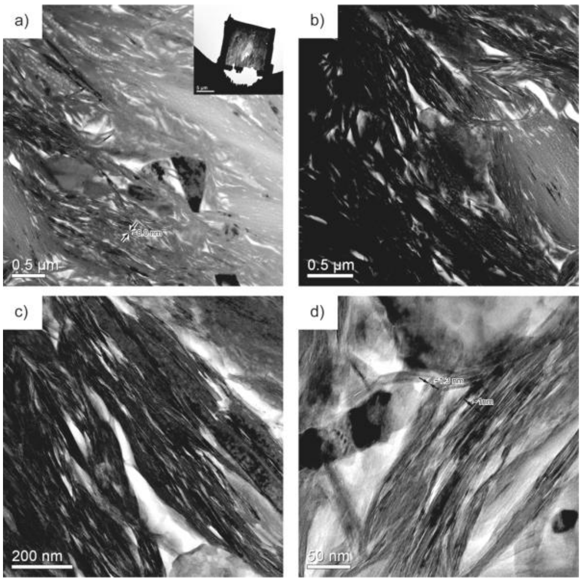

Figure 2. Transmission electron images showing the pore microstructure in Opalinus clay. a) and b) Overview of the microstructure. The bright areas correspond to pores or low density areas. The arrows mark the spacing of interparticle pores. c) and d) Close ups. The arrows mark the interlayer spacing and the spacing of suggested interlayer pores.

Spatial distribution of pore space geometrical properties

Material properties of clay-rich rocks important to the transport of fluids and gas include the porosity and the geometry (i.e. tortuosity, path length and path orientation) of pore paths within the pore space. FIB-nt provides voxel based 3D data of pore space and revealed that the clay rocks consist of a large number of individual pores or pore objects not connected to each other. Each of these objects has numerous pore paths. In order to analyze the 3D pore geometry we largely followed the approach described by Keller et. al (2011). The pore space was skeletonized and vectorized which results in graph representation of pore space. Such a 3D graph consists only of line segments. The graph presentation allows for an effective computation of orientation data (i.e. pore path orientation) and associated numeric values (i.e. pore path length and pore path tortuosity). These data were then visualized in stereographic projections and show the spatial distribution of pore path densities, pore path length and pore path tortuosities (see Keller et al. 2011 for further details). The pore space of the examined sample consists of numerous individual pore objects and orientation data were calculated for all possible paths of an individual pore object. Combining the data of all pore objects reveals potential bulk anisotropies in pore space. Pore paths orientations show a girdle distribution of which orientation is in good agreement with the orientation of the bedding plane (Figure 3). This indicates a near parallel orientation of the majority of pore paths with respect to the bedding plane. Numeric stereographic projections clearly reveal anisotropy of the mean path tortuosity with low values parallel and higher values perpendicular to the bedding plane (Figure 3). Furthermore, the mean pore path length is longer parallel to the bedding plane (see Keller et al. 2011 for further discussion).

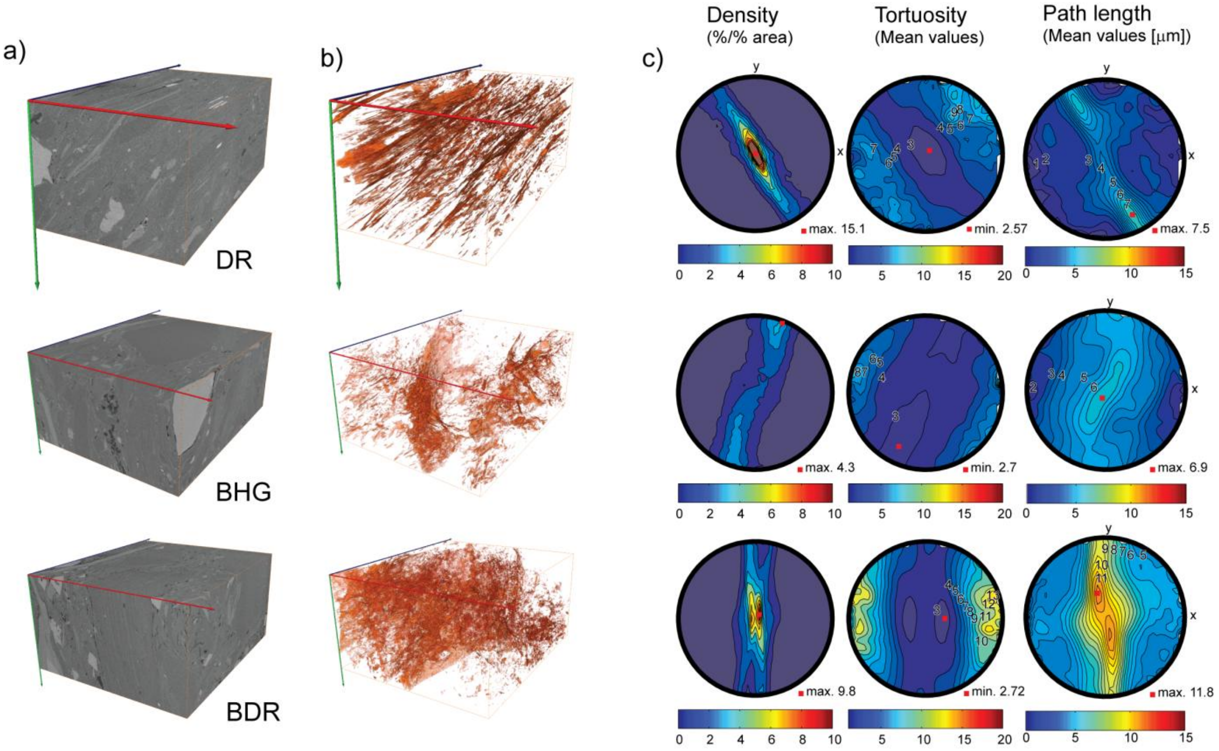

Figure 3. Stages of FIB-nt data processing and lower equal area projections showing the spatial distribution of pore path geometrical properties in the analyzed volume of the samples. a) 3D reconstruction of the analyzed volume based on BSE images. b) 3D visualization of the segmented pore space. c) left: Contoured plot showing the orientation density (=number of orientations in % per 1% area), middle: Mean path tortuosity distribution, right: Mean path length distribution. The colors in the plots are related to a specific numeric value which can be extracted from the color bar.

Summary and Conclusions

FIB-nT has a high potential to provide useful 3D data which allow for a characterization of the 3D pore and mineral organization in low-permeability clay rocks. In general, the resolution limit of SEM's and the accuracy of FIB milling restricts the application to a pore size exceeding 5-15 nm and only a small fraction of the total porosity can be analyzed by this method. The chosen voxel size of 10-15 nm resolves around 20-30 % of the total pore space. Concerning the usage of the obtained 3D data in the context of gas flow processes, this limitation is not a serious drawback since the imbibition of a gas phase into the existing pore space is restricted to the larger pores (Marschall et al. 2005). Regarding the extraction of structural information from digital images obtained by SEM, FIB-SEM instruments have the advantage of obtaining images from high quality surfaces because ion milling produces very smooth and damage free surfaces.

There is a surprisingly good agreement between the continuous pore size distribution determined on the base of FIB-nT and the one modelled on the base of the N_2 adsorption isotherms. This result in combination with the fact that volume analyzed by the N_2 adsorption techniques is much larger when compared to those analyzed by FIB-nT suggests that the 3D data obtained by FIB-nT provides representative information on the bulk properties and does not only reflect local structural features.

The major advantage of 3D porosity data compared to those obtained by indirect methods is that they provide a link to information on heterogeneities and anisotropies in the pore space. Attempts to extract information on orientation anisotropies in the pore space reveal a preferred orientation of pores within the bedding plane. The pores are not only parallel to the bedding plane, which can intuitively be expected, but show also a preferred orientation within the bedding plane. Readers interested in an extensive discussion, including the connectivity issue, regarding the spatial analysis of the pore space in Opalinus clay and the relevance of the derived material properties for transport of fluids and gas are referred to Keller et al. (2011).

First results obtained by transmission electron microscopy imaging of site specific TEM foils suggest that this technique resolves a large fraction (>~ 50 vol. %) of the total pore space which corresponds to the pore space characterized by pore radii >~ 2nm. This result is very promising as it opens up new perspectives for future attempts in constructing realistic 3D pore models for clay rocks.

The porosity determined on the base of X-ray tomography with resolution on the micron scale (voxel size 2.6 μm) is < 1 vol. % and its usage for retrieving transport relevant parameters related to the pore space in Opalinus Clay is not evident.

Acknowledgement

This work was funded by the Swiss National Cooperative for the Disposal of Radioactive Waste (NAGRA) as part of the SHARC consortium, a research collaboration between the Commonwealth Scientific and Industrial Research Organization (CSIRO), Curtin University of Technology and NAGRA. The authors thank to Philippe Gasser, Falk Lucas and Miriam Lucas, who provided help with data acquisition.

References

Andra, 2005. Dossier 2005 Argile – evaluation de la faisabilité du stockage géologique en formation argileuse profonde – Rapport de synthèse. Juin 2005, Andra, France. Available at: <<http.//www. Andra.fr>>

Bossart, P., Thury, M., 2008. Mont Terri Rock Laboratory: Project, Programme 1996-2007 and Results. Reports of the Swiss Geological Survey, No. 3.

Fredrich, J.T., Menendéz, B., Wong, T.F., 1995. Imaging the pore structure of geomaterials. Science 268, 276-279.

Holzer, L., Indutnyi, F., Gasser, Ph., Münch, B., Wegmann, M. 2004. Three-dimensional analysis of porous BaTiO3 ceramics using FIB nanotomography. Journal of Microscopy 216, 84-95.

Holzer, L., Münch, B., Rizzi, M., Wepf, R., Marschall, P., Graule, T. 2010. 3D-microstructure analysis of hydrated bentonite with cryo-stabilized pore water. Applied clay science 47, 330-342.

Holzer, L., Cantoni, M., 2011. Review of FIB-tomography. In: Russell, P., Utke, I., Moshkalev, S. (Eds.). Nanofabrication using focused ion and electron beams. Oxford University Press, NY, USA, ISBN 9780199734214. in press.

Keller, L.M., Holzer, L., Wepf, R. & Gasser, P. 2011 3D Geometry and topology of pore pathways in Opalinus clay: Implications for mass transport. Applied clay sciences, 52, 85-95.

Lash, G.G., Blood, D.R. 2004. Origin of shale fabric by mechanical compaction of flocculated clay: evidence from upper Devonian Rhinestreet Shale, Western New York, U.S.A. Journal of sedimentary research 74, 110-116.

Lindquist, W.B., Venkatarangan, A. 1999. Investigating 3D geometry of porous media from high resolution images. Physics and chemistry of the Earth (A) 25, 593-599.

Marschall, P., Horseman, S., Gimmi, T. 2005. Characterisation of Gas transport properties of the Opalinus Clay, potential host rock formation for radioactive waste disposal. Oil & Gas Science and Technology 60, 121-139.

Münch, B., Holzer, L. 2008. Contraticting geometrical concepts in pore size analyzes attained with electron microscopy and mercury intrusion. Journal of American Ceramic Society 91, 4059-4067.

Nagra, 2002. Projekt Opalinuston – Synthese der geowissenschafftlichen Untersuchungsergebnisse. Entsorgungsnachweis für abgebrannte Brennelemente, verglaste hochaktive sowie langlebige mittelaktive Abfälle. Nagra technical report NTB 02-03, Nagra Weinfelden, Switzerland.

Nagra, 2004. Effects of post-disposal gas generation in a repository for spent fuel, high-level waste and long-lives intermediate waste sited in the Opalinus Clay. Nagra Technical report NTB 04-06, Nagra, Wettingen, Switzerland.

Nakashima, Y., Nakano, T., Nakamura, K., Uesugi, K., Tsuchiyama, A., Ikeda, S. 2004. Three-dimensional diffusion of non-sorbing species in porous sandstone: computer simulation based on X-ray microtomography using synchrotron radiation. Journal of contamination hydrology 74, 253-264.

Van Loon, L.R., Soler, J.M., Müller, W., Bradbury, M.H., 2004. Anisotropic diffusion in layered argillaceous rocks: A case study with Opalinus Clay. Environmental Science and Technology 38, 5721-5728.

Wenk, H.-R., Voltolini, M., Mazurek, M., Van Loon, L.R., Vinsot, A., 2008. Preferred orientation and anisotropy in shales: Callovo-Oxfordian shale (France) and Opalinus Clay (Switzerland). Clay and Clay Minerals 56, 285-306.

Zabler, S., Rack, A., Manke, I., Thermann, K., Tiedermann, J., Harthill, N., Riesemeier, H. 2008. High resolution tomography of cracks, voids and microstructures in greywacke and limestone. Journal of structural Geology 30, 876-887.

X-ray Micro toMography as a Tool for Studying Localized Damage / Deformation in Clay Rock

Gioacchino Viggiani*, Pierre Bésuelle and Jacques Desrues

UJF-Grenoble 1 / Grenoble-INP / CNRS UMR 5521, Laboratoire 3SR, Grenoble, France

* Corresponding author: cino.viggiani@3sr-grenoble.fr

Introduction

Deformation in geomaterials (soils, rocks, concrete, *etc*.) is often localized, *e.g*., in the form of shear bands or fractures. In experimental analysis of the mechanical behavior of such materials, standard laboratory methods are insufficient as the majority of measurements are made at the sample scale and rarely at a local scale. X-ray tomography monitoring during loading allows high-resolution full-field observation of the development of deformation. However, such images only indicate clearly the deformation when there are significant changes in material density (*i.e*., volume changes) that produce a change in x-ray absorption. As such 3D Digital Image Correlation (DIC) approaches have been developed that allow quantification of the full strain tensor field throughout the imaged volume. This paper presents results from triaxial compression tests on a clay rock (Callovo-Oxfordian argillite) with *in situ* synchrotron x-ray micro tomography imaging providing complete 3D images of the specimen at several stages throughout the test. These images have been analyzed using 3D DIC to provide full-field displacement and strain measurements, which allowed the detection of the onset of strain localization and its timing relative to the load peak plus insight into the 3D structure of the localized zone. The paper concludes with a few general remarks concerning the lessons learned from this study and perspectives for current and future work.

Example of results: localized deformation in a clay rock

The results of this study, already presented in Bésuelle *et al*. (2006) and Lenoir *et al.* (2007), come from a large experimental program on a clay rock called Callovo-Oxfordian argillite, issued from the ANDRA Underground Research Laboratory in France. The testing program was carried out at the European Synchrotron Radiation Facility (ESRF) in Grenoble, making use of x-ray micro tomography at beamline ID15A. The tests were conducted using a specifically built setup that could be placed in the x-ray beam, so that the specimens were scanned under load (*in situ*). Synchrotron x-ray radiation was selected because it is the only one that can provide, thanks to its high photon flux, a combination of both fast scanning and high spatial resolution. The former is desired to minimize axial load relaxation, while keeping the specimen at constant axial strain during scanning (the acquisition of an entire specimen required four to six sections and in the most recent tests took 12 to 15 minutes). High spatial resolution allows fine detail on the deformation process to be obtained (a voxel size of 14 μm was achieved for specimens 10 mm in diameter).

Figure 1 shows the experimental setup, which included a triaxial apparatus and a loading system. The former is practically the same as a conventional triaxial testing system, except for its much smaller size and the shape of the confining cell. The cells were made from Plexiglas or polycarbonate to be as transparent to the x-rays as possible. Contrary to a conventional system, the tensile reaction force is carried by the cell walls and not by tie bars, which provides a clear path to the specimen for the x-ray beam, free of any obstacle (apart from the cell walls). The axial load and hence the deviator stress are applied using a motor-driven screw actuator. The loading system is placed in the x-ray beamline without interfering with the tomographic scans. See Lenoir (2006) for further details.

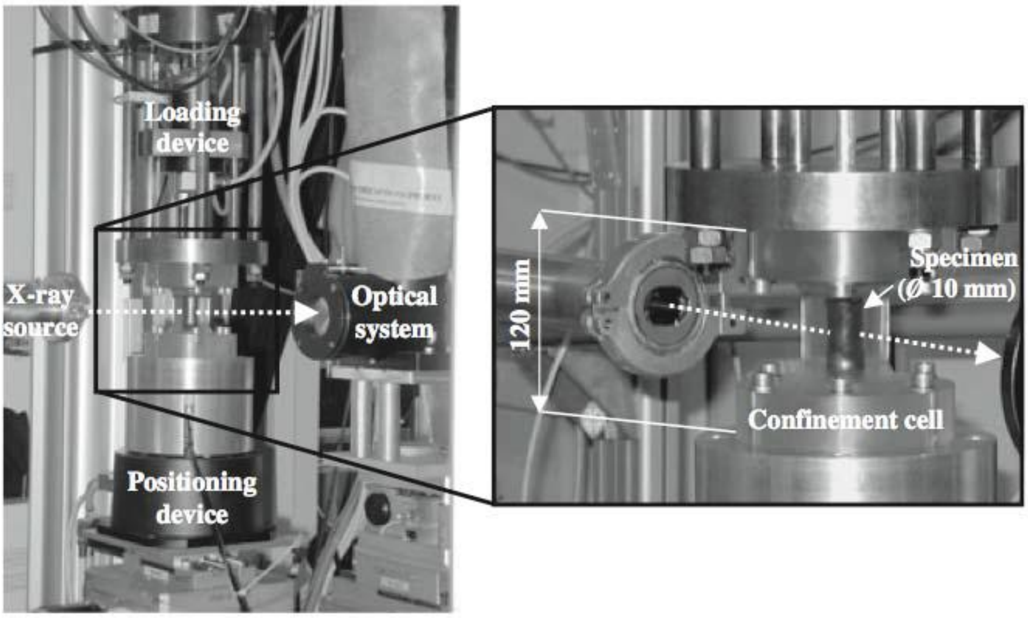

Figure 1. Experimental setup for in situ triaxial x-ray tomography experiments: the complete set-up on the beamline (left) and zoom on the specimen inside the triaxial cell (right) (after Lenoir et al. 2007)

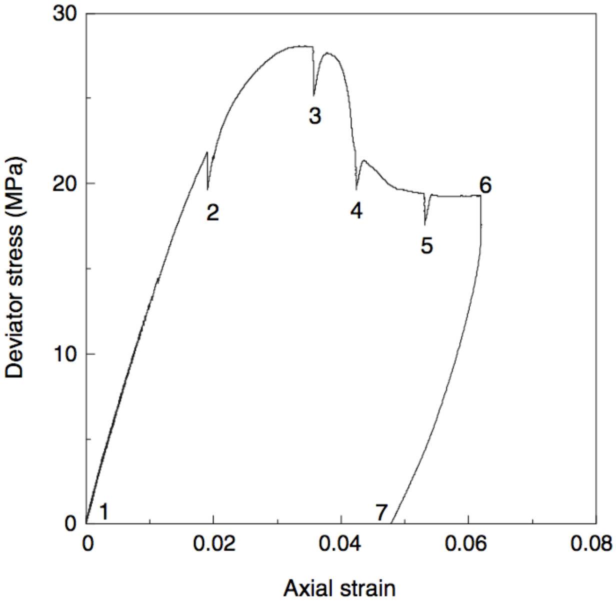

Figure 2. Load curve (deviator stress versus axial strain response) for the discussed triaxial compression test on the Callovo-Oxfordian argillite at 10 MPa confining pressure. The numbers indicate the times at which CT images were acquired (after Lenoir et al. 2007)

Callovo-Oxfordian argillite is a sedimentary rock composed of particles of calcite and quartz in a clay matrix, with a clay fraction of 40–45%. At the investigated depth (approximately 550 m below the ground surface), the material has an extremely low permeability (10^{-20}–10^{-22} m^2), a porosity of 15%, and a water content of 6%. The uniaxial compressive strength is about 20 MPa. Figure 2 shows the stress-strain response obtained from an undrained triaxial compression test on a 10 mm diameter specimen at 10 MPa confining pressure. The specimen was scanned at different steps: before and right after applying the confining pressure (steps 0 and 1, respectively), at different levels of axial strain during deviatoric loading (steps 2-7), and finally after removal of the confining pressure (step 8).
Figure 3 shows four horizontal CT slices at different steps. The slices at steps 1, 3, 7 and 8 have been selected following a set of material points which were visible at step 1 and could be found on all subsequent images. At step 8, two open cracks can be seen at the specimen edges. Comparison of the images at steps 7 and 8 clearly indicates that crack opening in this test was essentially due to the removal of the confinement pressure. At the earlier step 3, which corresponds to the peak stress, no localized deformation is evident – even knowing where the cracks are eventually opening up later in the test. Furthermore, no visible difference can be seen between steps 1 and 3. In fact, localization becomes just visible in the CT images at step 4 (not shown in the figure – see Bésuelle *et al* 2006).

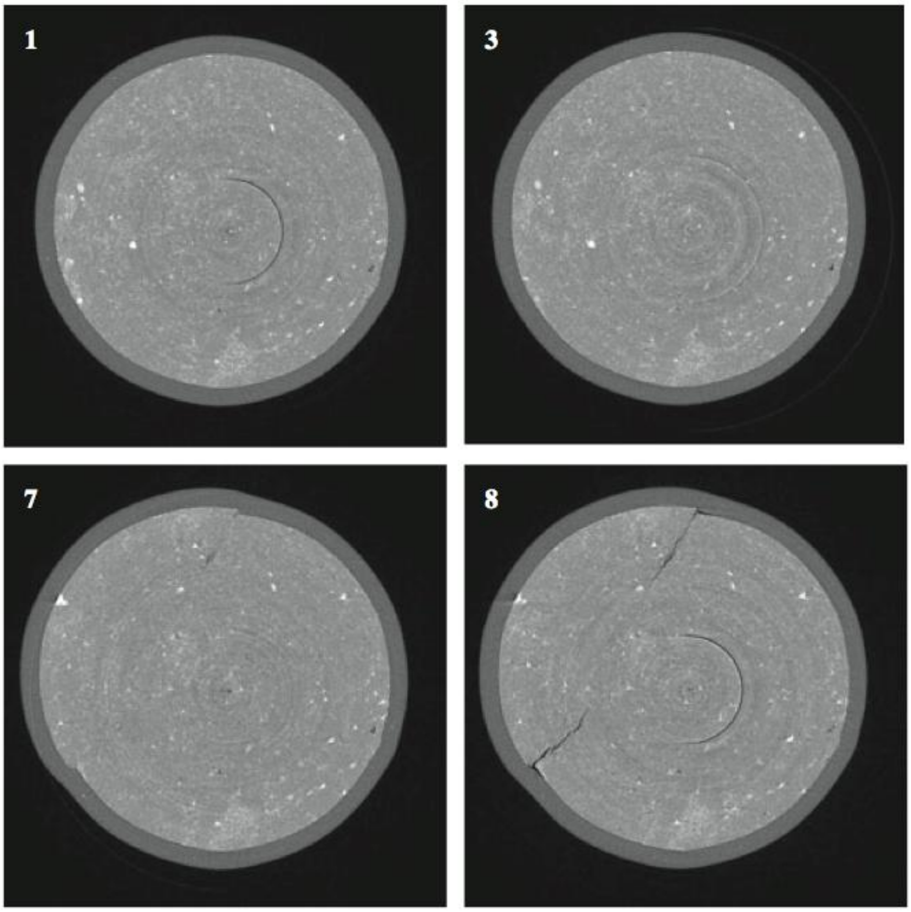

Figure 3. Horizontal slices through the CT image volume of the Callovo-Oxfordian argilite specimen (ø = 10 mm) at four different time steps (see Figure 2) (after Lenoir et al. 2007)

Interestingly, the existence of distinct calcite inclusions in the argillite was particularly helpful to highlight relative displacement in the specimen otherwise invisible in the CT images. Figure 4a shows an example of one such inclusion, having an elongated vein shape and a length of a few millimeters. Figure 4b shows the same inclusion (in yellow) and the open fracture (in red) at step 8, *i.e.*, at the end of the test. Figure 4c-h illustrate how, upon loading, this inclusion was severely strained by the localization. Shearing of the inclusion is apparent starting from step 5, which becomes more and more pronounced for increasing deformation (steps 6 through 8). However, this intense shearing is not accompanied by a variation of density measurable within the resolution of the x-ray CT. This indicates that the region of localized deformation in the central part of the specimen is undergoing shear without substantial volume changes, whereas crack opening can be observed towards the edge of the specimen.

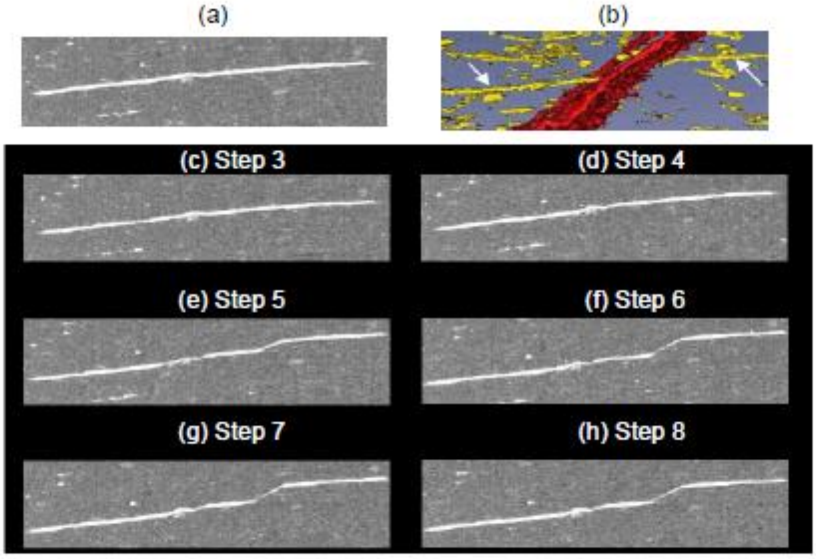

Figure 4. (a) An inclusion in the Callovo-Oxfordian argilite at the start of the test (the image is a small vertical section extracted from the x-ray tomogram and the inclusion is a few millimeters long). (b) 3D view of the same inclusion (yellow) and cross-cutting open fracture (red) at step 8 (the end of the test) highlighted through thresholding and false-coloring of the gray-scale image. (c)-(h) the inclusion at different stages through the test showing increasing shearing (after Bésuelle et al. 2006)

The above discussion illustrates a fundamental difficulty with experimental detection of strain localization through the use of x-ray CT, which is associated to the very nature of localized strain. The issue is that while localization can sometimes induce large volumetric deformation – either dilatancy (or crack opening) or compaction (compaction bands), depending on the material and loading conditions, in general volumetric strain in a shear band is small compared to the shear strain. Unfortunately, CT images only represent local mass density fields. If the material inside the region of localized deformation dilates (or contracts), then local mass density variations can be an effective means to track the regions of localized deformation. For these experiments on the argillite, this was only the case with open cracks, where voids are created between the crack edges that are clearly visible on the tomographic images (*e.g.*, step 8 in Figure 3). If the localized deformation is isochoric (no volume change), *e.g.*, it consists of closed, shearing cracks, then it is invisible in CT images (except for the “lucky” cases where the shear cuts markers such as the inclusion in Figure 4).

We will show hereafter how such a limitation can be in fact overcome by complementing x-ray CT with 3D Digital Image Correlation. 2D DIC was applied to x-ray radiographs already in the late 1980s; applications of DIC in three dimensions are more recent, *e.g.*, Bay *et al.* 1999, Bornert *et al.*2004, and many others (see the references quoted in Viggiani and Hall 2008). Our application of 3D DIC to the x-ray CT images of Callovo-Oxfordian argillite demonstrates that correlation of 3D digital images from x-ray tomography provides a means to effectively detect (within a given accuracy) localized deformation, independent of its nature (shear or volumetric strain). The details of the 3D DIC method used are thoroughly discussed elsewhere in Lenoir *et al*. (2007). Herein it will be sufficient to bear in mind that each 3D image is decomposed into several cubical subsets, each of them containing 203 voxels. Due to the small deformation experienced by the argillite specimens, for this study the transformation between two images was assumed to be a rigid translation without any rotation or distortion.

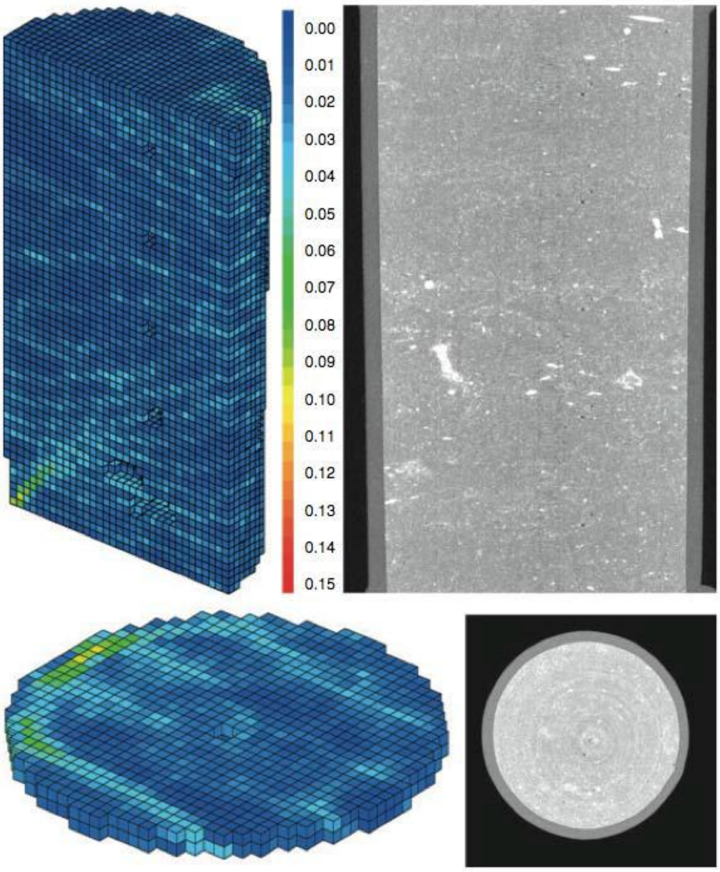

Figure 5. DIC-derived deformation maps for load increment 2-3 (before peak load - see Figure 2) of the triaxial test on the Callovo-Oxfordian argillite (ø = 10 mm). Top and bottom right: vertical (along the specimen axis) and horizontal (close to the bottom of the specimen) sections through the CT volume image at step 3. Top and bottom left: incremental maximum shear strain maps for the equivalent sections (color scale is [0, 0.15]) (after Lenoir et al. 2007)

Figure 5 and Figure 6 show vertical and horizontal cuts through the DIC-derived (incremental) shear strain field volumes. In the pre-peak increment (2–3, see Figure 2), the onset of strain localization is visible at the bottom left corner of the vertical cut through the shear strain map (Figure 5). The horizontal cut in Figure 5 suggests that during this increment the localization developed with a conical shape. Note that the x-ray sections of the specimen at the end of the increment do not reveal any trace of localized deformation. In the post-peak increment (3–4, see Figure 2), a fully developed shear band through the specimen can be observed (Figure 6). As compared to the pre-peak increment, the zone of localized deformation is more planar both in the vertical and in the horizontal cuts. In fact, the post-peak localization band partly coincides with the pre-peak cone of localized deformation in the lower region, suggesting that the later shear zone evolved from the initial one. As for the previous increment, no clear sign of strain localization is visible in the x-ray sections of the specimen at the end of the increment. It is worth noting that the thickness of the shear bands in these strain volumes is exaggerated with respect to real size. This is due to the lower limit to resolvable thickness dictated by the dimensions of DIC subsets (280 μm side length), whereas CT images indicate that the thickness of the localization zones (be these dilating shear bands or open cracks) in the tested specimens was typically less than 70 μm.

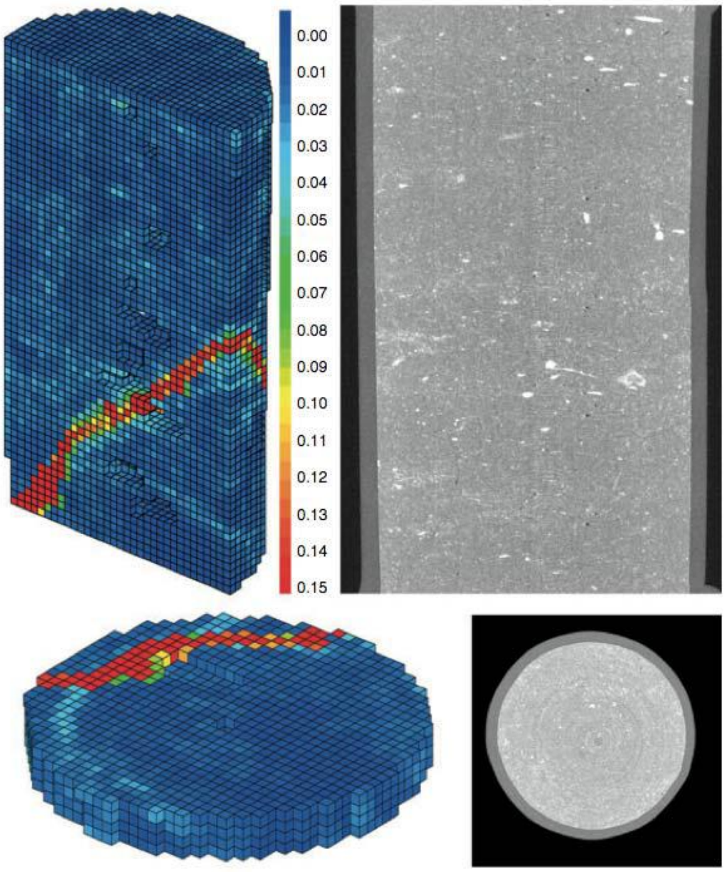

Figure 6. As Figure 5 but load increment 3-4, i.e., after peak load (after Lenoir et al. 2007)

One of the key conclusions from this study is that, through 3D DIC, it was shown that localized shear had initiated in the specimen already prior to the stress deviator peak. The important general message here is that the DIC analysis of 3D images from x-ray tomography can reveal patterns of deformation that could not be observed using only the gray scale images, in which they may remain hidden (if they do not involve significant volume changes); this is even with high resolution synchrotron micro tomography.

What's next: experimental rock mechanics at even smaller scale

Clay rocks, just as any other geomaterials, are equipped with a microstructure. While in classical models we are happily ignoring such a microstructure, this will at times come back to haunt us. This happens when deformation is localized in regions so small that the detail of the rock's particular structure cannot safely be ignored. Failure is the perfect example of this.

Researchers in geomechanics (and more generally in solid mechanics) have long since known that all classical continuum models typically break down when trying to model failure. All sorts of numerical troubles ensue – all of them pointing to a fundamental deficiency of the model: the lack of microstructure (it should be noted that the term microstructure does not prescribe a dimension (*e.g.*, microns), but rather a scale – the scale of the mechanisms responsible for failure).

A possible remedy to this deficiency is represented by the so-called “double scale” models, in which the small scale (the microstructure) is explicitly taken into account. Typically, two numerical problems are defined and solved – one at the large (continuum) scale, and the other at the small scale. This sort of approach requires a link between the two scales, to complete the picture. Imagine we are solving at the small scale a simulation of a rock volume of a few millimeters in side, using the Discrete Element Method or the Finite Element Method, whose results are in turn fed back to the large scale Finite Element simulation. See, *e.g*., Nitka *et al.* (2011) and Andrade *et al*. (2011) for further details about how multi-scale computations actually work.

The key feature of a double scale model is that one can inject the relevant physics at the appropriate scale. The success of such a model crucially depends on the quality of the physics one injects: ideally, this comes directly from experiments. In Grenoble, we have been doing this for sand, for which x-ray tomography allows the evolution of the 3D microstructure of a small sample to be followed while it deforms. Individual grains can be distinguished in such time-lapse 3D images and the full 3D kinematics of all the grains can be measured. See Andò *et al.* (2012a, 2012b) for the description of the techniques (combining DIC and Particle Tracking) and a few examples of results.

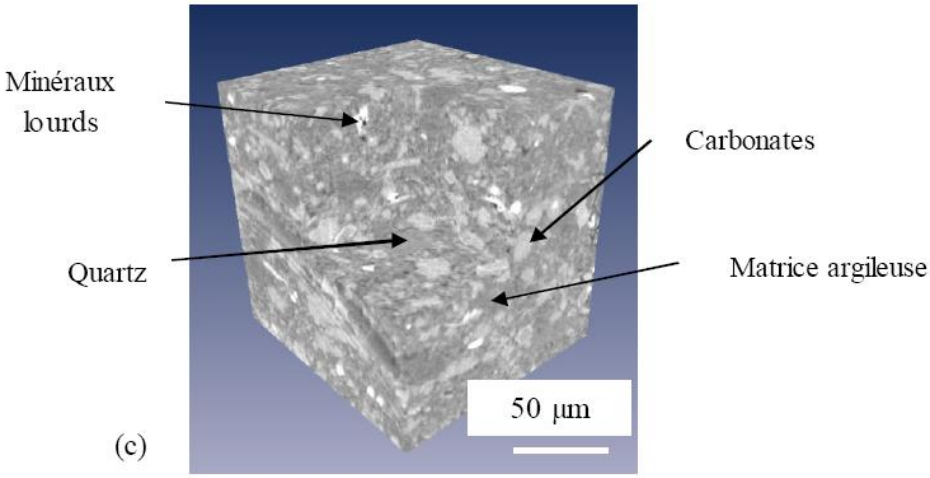

Figure 7. Example of the x-ray CT images of Callovo-Oxfordian argillite obtained at ESRF (beamline 19) on rock cylinders 1.4 mm in diameter, with a voxel size of 0.7 µm (after Robinet 2008)

As far as strain localization in clay rocks is concerned, the ‘relevant’ size of the microstructure, *i.e.*, the size at which the ‘interesting’ physics is occurring at the small scale, is possibly larger than the clay particles’ size. Recent tomographic images of Callovo-Oxfordian argillite obtained at the ESRF by Robinet (2008) suggest that a spatial resolution of 0.7 µm is able to provide us with sufficient details of the microstructure of the rock – see for example Figure 7. Motivated by the work of Robinet (2008), in Grenoble we plan to implement the combination of x-ray micro tomography and 3D DIC (just as we have described above) on experiments on extremely small specimens of Callovo-Oxfordian argillite – we plan to run triaxial compression tests on 1mm diameter cylinders of clay rock, with a spatial resolution of about 0.7 mm (the experiments will be carried out at the ESRF in Grenoble). The experimental challenge will be in the specimen preparation, which will possibly require using non-conventional techniques such as ion beam thinning and focused ion beam. In this way, we will be able to image, in three dimensions and at small scales, the deformation processes accompanying (localized) failure in clay rocks. This will allow us to understand these processes and subsequently to define models at a pertinently small scale.

Acknowledgements

We would like to thank Nicolas Lenoir (now at Laboratoire Navier, IFSTTAR) who is (at least) as much responsible as us of the results presented in this paper. We also thank Marco Di Michiel from the ESRF for his invaluable contribution to the x-ray CT experimental program, and to Michel Bornert at Laboratoire Navier, for his fundamental help with the DIC analysis. The experiments reported in this paper were conducted within the context of the Ph.D. thesis by N. Lenoir, funded by the French agency ANDRA.

References

Andò, E., Hall, S.A., Viggiani, G., Desrues, J. and Bésuelle, P. (2012) – Grain-scale experimental investigation of localised deformation in sand: a discrete particle tracking approach. Acta Geotechnica, 7, No. 1, 1-13.

Andò, E., Hall, S.A., Viggiani, G., Desrues, J., and Bésuelle, P. (2012) – Experimental micromechanics: grain-scale observation of sand deformation. Géotechnique Letters, http://www.icevirtuallibrary.com/content/serial/geolett

Andrade, J.E., Avila, C.F., Hall, S.A., Lenoir, N., Viggiani, G. (2011) – Multiscale modeling and characterization of granular matter: From grain kinematics to continuum mechanics. Journal of the Mechanics and Physics of Solids, 59, 237–250

Bay, B.K., Smith, T.S., Fyhrie, D.P. and Saad, M. (1999) – Digital volume correlation: three-dimensional strain mapping using X-ray tomography. Experimental Mechanics, 39, No. 3, 217–226.

Bésuelle, P., Viggiani, G., Lenoir, N., Desrues, J. and Bornert, M. (2006) – X-ray Micro CT for Studying Strain Localization in Clay Rocks under Triaxial Compression. In: Advances in X-Ray Tomography for Geo-materials, J. Desrues et al. Eds, ISTE, London, 35–52.

Bornert, M., Doumalin, P., Maire, E. and Moulinec, H. (2004) – Full 3D investigation of the local strain field in particulate metal matrix composites. Proc. 12th Int. Conf. on Experimental Mechanics ICEM12, Bari, Italy, 1-8.

Lenoir, N. (2006) – Comportement mécanique et rupture dans les roches argileuses étudiés par micro tomographie à rayons X. Ph.D. thesis, Université de Grenoble (http://tel.ccsd.cnrs.fr/tel-00011996).

Lenoir, N., Bornert, M., Desrues, J., Bésuelle P. and Viggiani, G. (2007) – Volumetric digital image correlation applied to X-ray micro tomography images from triaxial compression tests on argillaceous rocks. Strain, International Journal for Experimental Mechanics, Vol. 43, No. 3, 193–205.

Nitka, M., Combe, G., Dascalu, C., Desrues, J. (2011) – Two-scale modeling of granular materials: a DEM-FEM approach. Granular Matter, 13, 3, 277-281.

Robinet J.C. (2008) – Minéralogie, porosité et diffusion des solutes dans l'argilite du Callovo-Oxfordien de Bure (Meuse/Haute-Marne, France) de l'échelle centimétrique à micrométrique. Ph.D. thesis, Université de Poitiers.

Viggiani, G. and Hall, S.A. (2008) – Full-field measurements, a new tool for laboratory experimental geomechanics. Keynote paper, in: Deformation Characteristics of Geomaterials, S.E. Burns, P.W. Mayne and J.C. Santamarina Eds, IOS Press, Vol. 1, 3-26.

POSTER PRESENTATIONS

On-Going Bentonite Pore Water Studies by NMR and SAXS

Torbjörn Carlsson [1*], Arto Muurinen [1], Andrew Root [2]

[1] VTT Technical Research Centre of Finland (FIN)
[2] MagSol (FIN)

* Corresponding author: torbjorn.carlsson@vtt.fi

Abstract

Compacted water-saturated MX-80 bentonite is presently being studied by SAXS and NMR in order to quantify the major pore water phases in the bentonite. The SAXS and NMR measurements gave very similar results indicating that the porewater is mainly distributed between two major phases (interlayer and non-interlayer water) and also indicate how these phases depend on the bentonite dry density.

Introduction

The repository

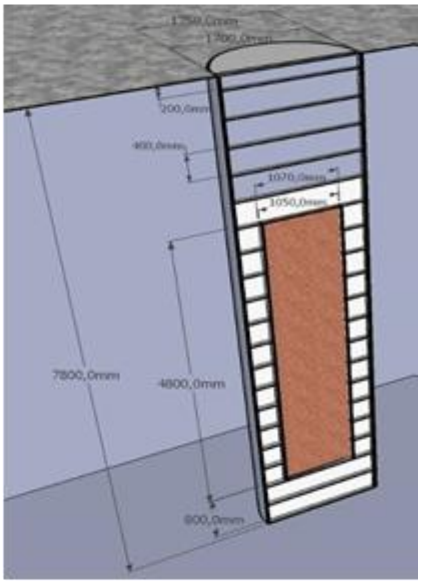

Figure 1. Conceptual image of a filled deposition hole (Posiva 2010).

The planned Finnish repository for spent nuclear fuel is based on the well-known KBS-3 concept. This means that the nuclear waste is contained in iron/copper canisters placed at a depth of 400-500 m in solid bedrock. Each canister is located in a deposition hole, which contains compacted bentonite as a buffer between the rock and the canister (Figure 1).

The pore water

One of the safety functions of bentonite is to hinder radionuclide transport in case of canister failure. In the long-term, the bentonite is expected to be completely water-saturated and possible radionuclide transport through the bentonite is thought to occur in the pore water. Understanding and modelling of the behaviour of bentonite require, inter alia, data on how the pore water is distributed between different phases under various conditions. The pore water is mainly found to be distributed between two phases, which in the following are denoted 'interlayer water' and 'non-interlayer water'. These terms refer to the water located in the pore space between montmorillonite unit layers and to the water filling the remaining part of the total pore space, respectively.

Rationale for the study

The state of water in various clay/water systems has been studied for several decades. Examples of early studies are the development of a structural model of water in contact with a montmorillonite surface (Forslind 1948), the work on the nature and properties of water in montmorillonite (Low 1979), and the development of a general microstructural model for water-saturated bentonite (Pusch et al. 1990). These, as well as numerous other early studies, improved the understanding of how water is organised in saturated bentonite. Subsequent recent research benefits from the development of new techniques, access to more advanced computers and analytical software, etc., and can therefore improve our knowledge further. Recent studies have shown, for example, the number of water phases in compacted saturated Kunigel-V1 bentonite (59.3 wt% montmorillonite) by ^{1}H NMR (Ohkubo et al. 2008) and provided quantitative 3D-characterisations of the bentonite pore structure by FIB-nanotomography combined with high pressure freezing (Holzer et al. 2010).

The use of more than one analytical method is advantageous, since the combined results from different methods might, at least ideally, add more to the understanding of the bentonite microstructure, than results based on one method alone. This is why a series of parallel bentonite studies, one of which is the present one, is being carried out at VTT. This paper presents the results of SAXS and ^{1}H NMR experiments/measurements performed in order to quantify the relative proportions of different water phases in saturated MX-80 bentonite. Briefly, the objective of the ongoing work is to determine the number of water phases and also to quantify their relative amounts in saturated MX-80 under the experimental conditions considered.

Experimental

The material consisted of water-saturated compacted MX-80 bentonite (from American Colloid Company). The dry density ranged from 0.7 to 1.6 g/cm^3. The temperature of the samples was 25 ˚C. The ^{1}H NMR measurements were carried out using a Chemagnetics CMX Infinity 270 MHz spectrometer. A CPMG pulse sequence was used with a very short (22μs) refocusing delay, τ, and acted as a spin locking pulse. This effectively measured the relaxation in the rotating frame, referred to as $T_{1\rho}$, with a spin locking field of $1/2\tau$. The relative amounts of the water phases were determined by peak-o-mat, a data analysis and curve fitting program suitable for fitting of discrete exponential decays (Kristukat 2008).

The SAXS measurements were made by a Bruker MICROSTAR microfocus rotating anode X-ray source with Montel Optics. Details on the SAXS measurements are found in Muurinen (2009).

Results

The results from the SAXS measurements are shown in Figure 2, where scattering data are plotted vs. basal space for four water-saturated MX-80 samples. The graphs differ with regard to both the positions of the diffraction peak, and the slopes seen at higher basal space values. The curves were analysed in accordance with procedures described elsewhere (Muurinen 2009 and references therein). The results indicate the presence of two different clay/water fractions in the samples; a ‘soft fraction’ and a ‘dense fraction’. By combining the information from SAXS measurements with chloride exclusion data, it was possible to evaluate the pore sizes in each fraction.

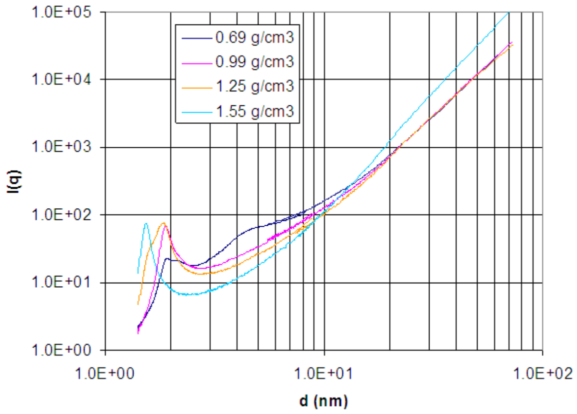

Figure 2. SAXS scattering data as a function of the basal space for the MX-80 samples (Muurinen 2009).

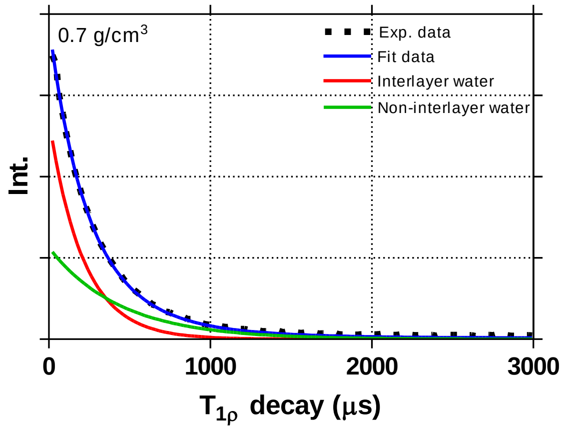

Figure 3. NMR $T_{1\rho}$ decay curves indicating the presence of two water phases, interpreted as 'interlayer water' (red graph) and 'non-interlayer water' (green graph)[3].

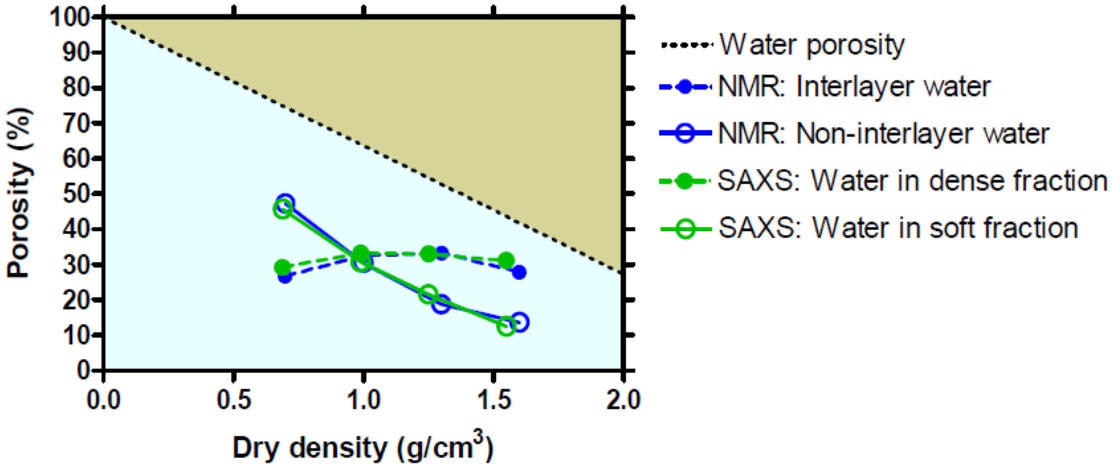

Figure 4. SAXS- and NMR-data suggest for a given dry density the same relative amounts of interlayer and non-interlayer water in compacted water-saturated MX-80.

The results from the $T_{1\rho}$ relaxation measurements indicate the presence of two major pore water phases in the MX-80 samples, which were interpreted as being 'interlayer water' and 'non-interlayer water'. A typical example of a $T_{1\rho}$-decay and its two associated discrete exponentials is seen in Figure 3.

The combined results from the SAXS and the NMR measurements are presented in Figure 4, which shows the relative amounts of the different water phases as a function of the dry density. The two methods are seen to give very similar results; the way water is found by SAXS to be distributed between a soft and a dense fraction is almost identical to the way water is found by NMR to be distributed between a non-interlayer and an interlayer phase. This way of combining the results by different methods, seems to provide more reliable data, than using a single method alone.

Conclusions

The results from the SAXS and NMR studies at VTT indicate the same thing:

- The pore water in water-saturated compacted (ρ_{dry} = 0.7-1.6 g/cm^3) bentonite is divided into two main phases: interlayer water and non-interlayer water.
- The amounts of these pore water phases can be determined quantitatively with the above methods.

Acknowledgement

This work has been sponsored by Posiva Oy.

References

Carlsson, T., Root, A. (2011). NMR study of water in MX-80 bentonite and in Na- and Ca-montmorillonite. (Unpublished study for Posiva Oy). Denna ref har nr 3 i texten.

Forslind, E. (1948). The clay-water system I – crystal structure and water adsorption on clay minerals. Bulletin No. 11, Swedish Cement and Concrete Research Institute, Royal Institute of Technology, Stockholm.

Holzer, L., Münch, B., Rizzi, M., Wepf, R., Marschall, P., Graule, T. (2010). 3D-microstructure analysis of hydrated bentonite with cryo-stabilized pore water. Applied Clay Science 47, 330-342.

Kristukat, C. (2008). Peak-o-mat. https://sourceforge.net/project/showfiles.php?group_id=67624.

Low, P.F. (1979). Nature and properties of water in montmorillonite-water systems. Soil Science Society of America Journal, 43, 651-658.

Muurinen, A. (2009). Studies on the Chemical Conditions and Microstructure in the Reference Bentonites of Alternative Buffer Materials Project (ABM) in Äspö. Posiva WR 2009-42, Posiva Oy. Denna ref har nr 2 i texten.

Ohkubo, T., Kikuchi, H., Yamaguchi, M. (2008). An approach of NMR relaxometri for understanding water in saturated compacted bentonite. Physics and Chemistry of the Earth, 33, S169-S176.

Posiva (2010). TKS-2009 Nuclear Waste Management at Olkiluoto and Loviisa Power Plants Review of Current Status and Future Plans for 2010-2012, Posiva Oy. Denna ref har nr 1 i texten.

Pusch, R., Karnland, O., Hökmark, H. (1990). GMM – A general microstructural model for qualitative and quantitative studies of smectite clays. SKB TR-90-43. SKB, Stockholm.

Homogeneity vs. Heterogeneity of Porosity in Boom Clay

Susanne Hemes[1*], Guillaume Desbois[1], Janos L. Urai[1], Mieke De Craen[2], Miroslav Honty [2]

[1] Structural geology, Tectonics and Geomechanics, RWTH Aachen University (Germany)
[2] SCK-CEN, Belgian Nuclear Research Centre (Belgium)

* s.hemes@ged.rwth-aachen.de

Abstract

Microstructural investigations on Boom Clay at nano- to micrometer scale, using BIB-SEM methods, result in porosity characterization for different mineral phases from direct observations on high resolution SE2-images of representative elementary areas (REAs).
High quality, polished surfaces of cross-sections of ~ 1 mm^2 size were produced on three different samples from the Mol-Dessel research site (Belgium). More than 33,000 pores were detected, manually segmented and analyzed with regard to their size, shape and orientation. Two main pore classes were defined: Small pores (< 500 nm (ED)) within the clay matrices of samples and 'big' pores (> 500 nm (ED)) at the interfaces between clay and non-clay mineral (NCM) grains. Samples investigated show similar porosities regarding the first pore-class, but differences occur at the interfaces between clay matrix and NCM grains. These differences were interpreted to be due to differences in quantitative mineralogy (amount of non-clay mineral grains) and grain-size distributions between samples investigated. Visible porosities were measured as 15 to 17 % for samples investigated. Pore-size distributions of pores in clay are similar for all samples, showing log-normal distributions with peaks around 60 nm (ED) and more than 95 % of the pores being smaller than 500 nm (ED). Fitting pore-size distributions using power-laws with exponents between 1.56 and 1.7, assuming self-similarity of the pore space, thus pores smaller than the pore detection resolution following the same power-laws and using these power-laws for extrapolation of pore-size distributions below the limit of pore detection resolution, results in total estimated porosities between 20 and 30 %. These results are in good agreement with data known from Mercury Porosimetry investigations (35-40 % porosity) and water content porosity measurements (~ 36 %) performed on Boom Clay (Boisson, 2005).

Introduction

The aim of this study is to characterize and quantify the vertical variability of Boom Clay porosity on a nano- to micrometer scale, using Broad Ion Beam (BIB) – Scanning Electron Microscopy (SEM) method. All samples investigated in this study are from the Mol1-borehole and part of the EZE sample series. Samples were chosen due to end-member mineralogical compositions and grain-size distributions within the Mol1-borehole/EZE sample series. Sample 1 (EZE55) is from the level of the HADES-research laboratory (~ 225 meters depth) and of an intermediate mineralogical composition (~ 50 wt % clay) as well as grain-size distribution. Sample 2 (EZE52) is a very coarse-grained example of Boom Clay and very poor in clay minerals (only ~ 34 wt %). It originates from a lower depth of the

Mol1-borehole (~ 197 meters). Sample 3 (EZE54) is the most fine-grained and clay-rich (~ 60 wt % clay) sample investigated in this study and from ~ 214 meters depth.

Method

Samples were received pre-dried, in cores of ~ 10 cm diameter. After cutting into smaller pieces of ~ 1 x 0.5 x 0.3 cm size using a razorblade, samples were dried in an oven at 60°C for 72 hours. Afterwards samples were pre-polished using carbide-sandpapers of several grain-sizes to improve the quality of the BIB-milling. BIB polishing was performed for 7.45 hours at 6 kV using a stand alone 'JEOL SM-09010' BIB-polisher. High quality polished cross-sections of ~ 1 mm^2 size were produced for high resolution SEM-imaging. Before SEM-imaging samples were coated with a thin layer of gold to prevent them from charging. SEM-imaging was performed on a 'ZEISS, supra 55'. To be able to investigate porosities in REAs and at pore-scale, hundreds of high resolution single SE2-images were taken as mosaics and stitched together afterwards automatically using 'Autopano'. Pore detection and segmentation was done according to grey-values of SE2-images, either manually in ArcGIS or automatically using a combined 'thresholding-sobel edge detection' approach in Matlab. Pore-sizes, shapes and orientations were calculated and analyzed in ArcGIS, Matlab (toolbox PolyLX, Lexa et al., 2005) and Microsoft Excel.

Results

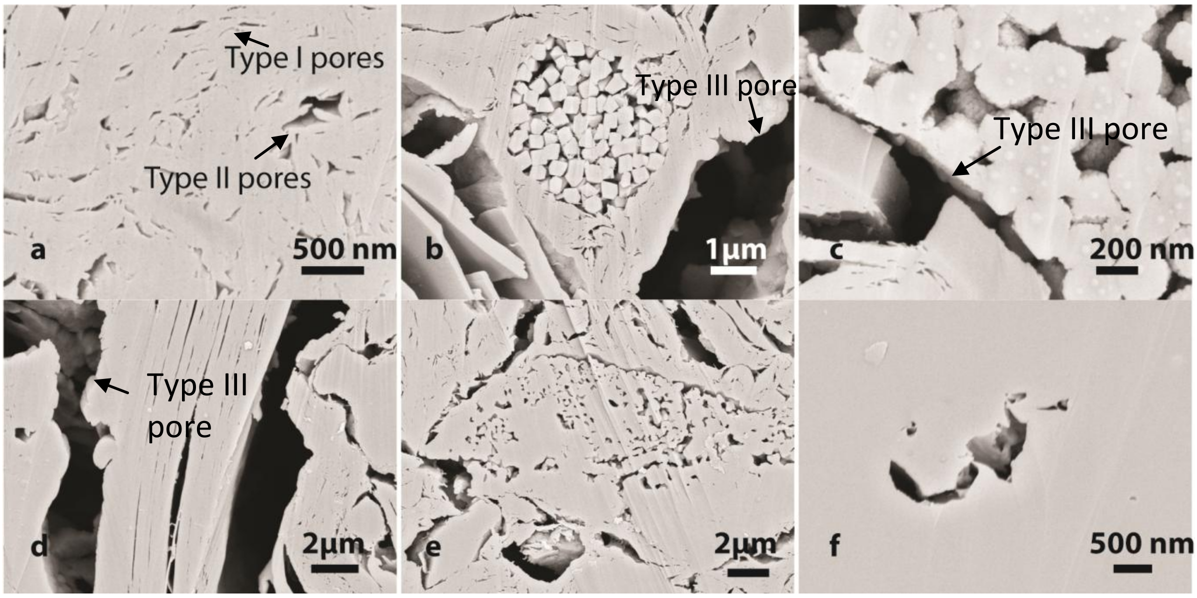

Figure 1. Pore morphologies in different mineral phases (a: Clay, Type I and Type II pores as described in Desbois et al., 2009, b+c: Pyrite, d: Mica, e: Fossil, f: Quartz).

More than 33,000 pores were detected and outlined manually. Characteristic pore morphologies were found for each mineral phase, present in the investigated samples. Similarities were found for pores within the clay matrices of samples investigated, regardless of the samples' origin, mineralogical composition and grain-size distribution. Pores within clay are as described in Desbois et al., 2009 (Figure 1a, type I and type II pores). Most (> 95 %) of them are smaller than 500 nm (ED) with prevailing orientations parallel to the bedding of samples. Much bigger – up to 2 µm (ED) in the two finer grained samples and up to 20 µm (ED) in the coarse-grained sample, mostly elongated – pores with long-axis orientations sub-parallel to the grain boundaries or of triangular shape with no preferred orientations, were found at the clay-NCM interfaces (type III pores, Desbois, 2009).

Pores in pyrite framboids are usually < 500 nm (ED) and of shapes controlled by the pyrite single grains' arrangement (Figure 1b and c). Pores in mica are elongated with very high aspect ratios and short axis typically < 200 nm (Figure 1d). Pores inside fossils show rounded edges and are typically smaller than 500 nm (ED) (Figure 1e). Pores inside quartz and feldspar grains occur only in very few amounts and are usually < 500 nm (ED) (Figure 1f).

Pore-size distributions were calculated for pores within the clay matrices of samples (Figure 2). More than 95 % of the pores within the clay matrices are smaller than 500 nm (ED), but whereas in the two finer grained samples no pores > 2 µm (ED) have been detected, in the coarse-grained sample pores up to an equivalent diameter of ~ 20 µm were found. Pore-sizes in the clay matrices are log-normally distributed with peaks around 60 nm (ED) in all samples investigated.

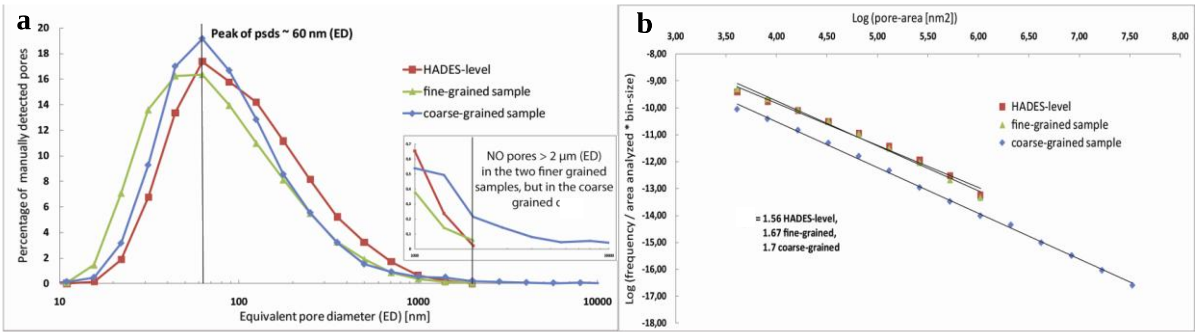

Figure 2. Pore-size distributions of visible pores measured within the clay matrices of samples; b: Power-law fitting of psds with power-law exponents between 1.56 and 1.7.

Total visible porosities were measured as 16.4 % for the HADES-level sample, 16.5 % for the coarse-grained sample and 15.2 % for the fine-grained sample. In the two finer grained samples pores > 500 nm (ED), which mostly occur at the clay-NCM interfaces account for ~ 50 % of the total visible porosity, whereas in the coarse-grained sample these big pores close to NCM grains account for ~ 80 % of the total visible porosity.

Power-laws were used to fit pore-size distributions, with power-law exponents between 1.56 and 1.7. Pore-size distributions were extrapolated below the pore detection resolution (pdr) (~ 50-60 nm (ED)) down to equivalent pore diameters of 1 nm, using these power-laws. Extrapolation of pore-size distributions results in total estimated porosities of 20 % for the coarse-grained sample, 24 % for the fine-grained sample and 30 % for the HADES-level sample.

Discussion and Conclusions

Pore morphologies within the clay matrices of samples investigated are similar, irrespective of the samples' origin, mineralogical composition or grain-size distribution. Differences occur at the interface between clay and NCM-grains: Pore-sizes depend on the grain-size of the sample. Differences in total observed porosities between samples investigated are interpreted to be due to differences in mineralogical composition (NCM-content) and grain-size distribution of samples.

Visible porosities of 15-17 % from BIB-SEM investigations in a pore-size range between ~ 50 nm (pdr) and 2,000/20,000 nm (ED) (largest pores found in REAs investigated) are lower than expected for Boom Clay (e.g. from Mercury Porosimetry injection: 35-40 % or water content porosity measurements: ~ 36 %, Boisson, 2005).

However, estimated porosities from extrapolation of pore-size distributions below the limit of pdr, assuming self-similarity of the pore space, are in the range of values expected and measured for connected porosities in BC. This leads to the conclusion that connecting pore throats in Boom Clay are smaller than 10-50 nm (pore throat diameter), since no interconnected pores were observed at the scale of resolution.

The presented method delivers a mean to visualize, characterize and quantify porosity of argillaceous materials in REAs down to the nm-resolution. It has been shown that up-scaling from microstructural investigations at pore-scale to bulk sample properties is possible, making some general assumptions.

Acknowledgement

Thanks to ONDRAF/NIRAS and SCK/CEN for funding and support.

References

Boisson, J.Y. (2005) Clay Club Catalogue of Characteristics of Argillaceous Rocks, OECD/NEA/RWMC/IGSC (Working Group on Measurement and Physical Understanding of Groundwater Flow through Argillaceous Media). *Report NEA No.* ***4436.*** *OECD/NEA Paris, France (p. 72).*

Desbois, G., Urai, J.L. and Kukla, P.A. (2009) Morphology of the pore space in claystones – evidence from BIB/FIB ion beam sectioning and cryo-SEM observations. *e-Earth* ***4****,* 1-8/15-22.

Lexa, O., Štípská, P., Schulmann, K., Baratoux, L. and Kröner, A. (2005) Contrasting textural

record of two distinct metamorphic events of similar P-T conditions and different durations. *Journal of Metamorphic Geology* ***23 (8)***, 649–666.

Qualitative and Quantitative Characterization of Porosity in a Low Porous and Low Permeable Organic Rich Shale by Combining Broad Ion Beam and Scanning Electron Microscopy (BIB-SEM)

Jop Klaver[1*], Guillaume Desbois [1], Janos L. Urai[1]

[1] Structural Geology, Tectonics and Geomechanics, RWTH Aachen University (DE)

* Corresponding author: j.klaver@ged.rwth-aachen.de

Abstract

This contribution focuses on the characterization of porosity in low porous shale using a broad ion beam (BIB) polishing technique combined with a conventional scanning electron microscopy (SEM). Porosity was traced in certain representative elementary areas (REA) and pores detected are segmented from mosaics of secondary electron (SE) images. Traced pores could be classified into two major pore-size classes. Relative large pores (> 0.5 μm^2) were found in the organic matter and matrix. They contribute strongly to the overall porosity content of the shale. Nevertheless the far majority of the pores traced have equivalent radius less than 400 nm. Including the latter pore class, the imaged porosity from both samples gives similar results in the order of < 1 %.

Introduction

This combined BIB-SEM technique of imaging and mapping of pores in shales enables to work on large areas and to actually see the pores and study the pore morphology. With the use of a BIB cross-section polisher the area of the polished surface increased by a factor of several thousand compared to focused ion beam (FIB) techniques, enclosing an area of roughly 1-2 mm^2 and allows working on REA. Conventional SEM imaging allows analysis of pores down to the nanometer scale. Two adjacent organic rich core samples from a shale interval (3.5 km depth) were investigated. From each sample one BIB polished cross-section was made and pores were segmented from several mosaics consisting of hundreds of images.

Method and technique

Studied material was stored in foil at room temperature and atmospheric pressure and stored in a tight plastic barrel. From the air-dried sample material, small pieces (~0.5 x 0.5 x 0.5 cm^3) were cut off with a low speed diamond saw machine (Figure 1). After cutting, the sample was pre-polished using sandpaper reducing surface roughness down to 10μm. Pre-polishing maximizes the quality of the cutting of the BIB cross-section. Eventual damage on the surface of the shale sample created by the pre-polishing will be removed by the BIB. Subsamples were preserved in an excicator under low vacuum.

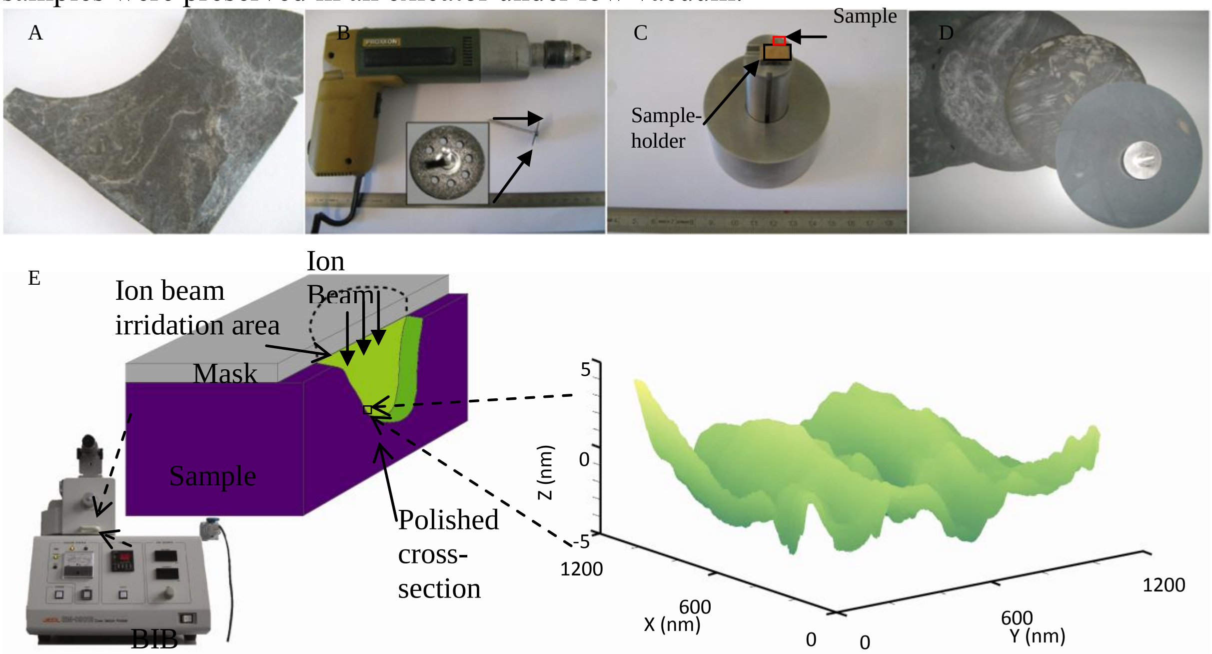

Figure 1. Picture of shale investigated (A). Electric low speed drill (B) used for sawing of the shale with diamond saw (pop-up). A polish tool (C) was used to create perpendicular edges with sandpaper (D). JEOL cross-section BIB polisher SM-09010 and sample setup and Atomic Force Microscopy (AFM) plot of a scanned BIB-polished surface (E).

The dry subsample was put in the BIB cross-section polisher for the argon polishing. On top of the sample a mask is placed and argon ions mill into the sample that is not covered by the mask. In 8 hours of milling under vacuum (1 x 10^{-3}-10^{-4} Pa), a 1 mm^2 polished cross-section was created with an amplitude less than 5 nanometers (Figure 1E). Here after the polished cross-section was coated to prevent charging by the SEM. Imaging in the SEM was done under high magnification with the back scatter electron (BSE) detector and the secondary electron detector (Inlens or SE2) with a pixel size of a few nanometers for the SE detectors. Minor micro-scale cracks was interpreted as ex-situ damage and subtracted during analysis. REA mosaics were created by stitching hundreds of images together with a bicubic interpolation algorithm in Autopano 2 (http://www.kolor.com/image-stitching-software-autopano-giga.html). Pores were traced manually in ArcGIS 10 from mosaics of SE images. After pore segmentation, shapes were analysed in MATLAB with PolyLX (Lexa (2010)). Classification and mapping of mineral phases were done using grey values from BSE images verified and calibrated by a combination of energy-dispersive x-ray spectroscopy (EDX) and bulk X-ray diffraction (XRD) analyses. REA was determined with the box counting method applied on the classified BSE mosaic and turned out to be 80 x 80 μm^2.

BIB-SEM technique has been applied recently on salt and clays too (Desbois et al. (2009), Desbois et al. (2011), Hemes et al. (2010) and Houben et al.(2011)). Challenges that needs to be overcome are serial cross-sectioning to get a better understanding of the 3D pore structure.

An appropriate automated pore detection algorithm has to be designed to deal with the huge amount of pores in images covering REA.

Results

Quantitative analyses

Traced pores in both samples resulted in a very low visible porosity in all the different mosaics down to the different SEM resolutions. 99% of the pores are in the range of 20-400nm equivalent radius (r_{eq}, Figure 2A), and porosities are the same in this range for both samples. However most of the pore space, 82% in cross-section 1 and 42% in cross-section 2 are in the 1% largest (≥400nm r_{eq}) pore size range. These largest pores are predominantly found in the clay rich matrix, and organic matter. Most pores (>6600) were found in the clay rich matrix, and results in an average relative porosity of 0.12% at the magnifications used. Pores together have a power law distribution in all the phases over three orders of magnitude of pore sizes (Figure 2B) and this infers a fractal dimension (Mandelbrot (1982)).

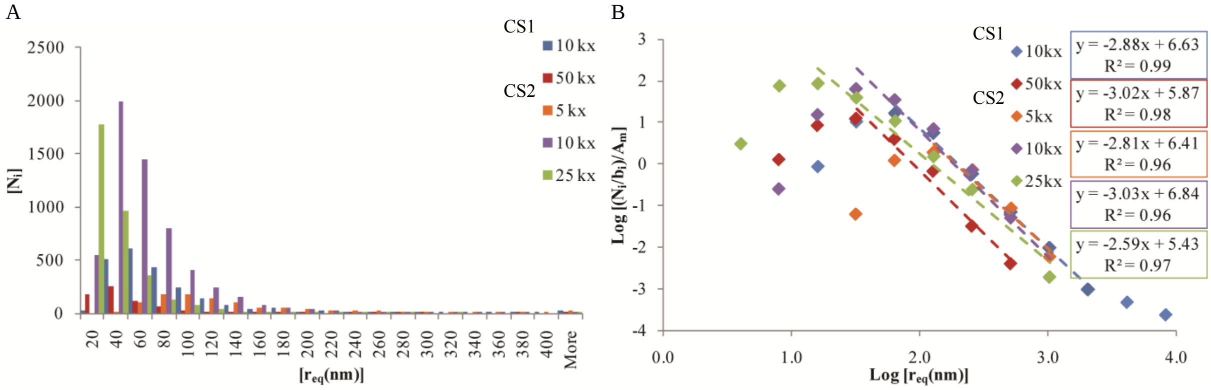

Figure 2. A. Equivalent pore radius distributions of both cross-sections (CS 1 and 2) at different magnifications. B. Power law exponent (gradient of the fitted line, given in the boxes) of segmented pores in the clay rich matrix traced at different magnifications.

Qualitative investigation

Pores traced in the clay rich matrix are isolated and therefore not connected at the resolutions used (Figure 3A). However intragranular pores in pyrite and rutile are clustered and are connected (Figure 3B and C). Pore orientation of the organic matter is sub-parallel with the bedding and most occurs at the interface of the organic matter and the surrounding phase (Figure 3D). A pore throat is seen in the clay-rich matrix (Figure 3E).

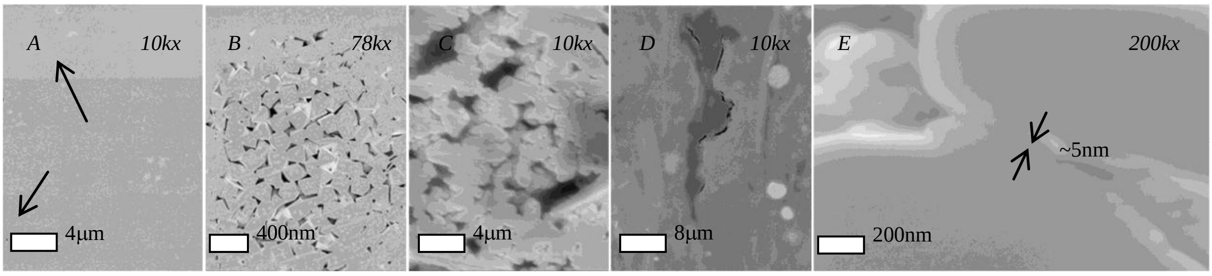

Figure 3. A. Isolated relative small pores (arrows) in the clay-rich matrix. B. Intragranular pores in rutile and pores in pyrite framboids (C). D. Elongated pores along organic matter (BSE image). E. Pore throat between pores in clay rich matrix.

Summary and Conclusions

Porosity in both samples is very low (<1%) at resolutions used and are similar in the smaller pore range ($r_{eq} < 400$nm). The pore size distributions show similar power law exponents for each phase and at different magnifications. Each phase has its own typical pore characteristics, regardless of the sample. BIB-SEM is a very suitable technique for the study of porosity in shale.

Acknowledgement

We would like to acknowledge U. Wollenberg for his help with the XRD analyses, BIB milling and SEM imaging and Dr. rer. nat. Anke Aretz for the AFM analyses.

References

Desbois, G., Urai, J. L., and Kukla, P. A. (2009). Morphology of the pore space in claystones – evidence from BIB/FIB ion beam sectioning and cryo-SEM observations. eEarth, 4, 15-22.

Hemes, S., Desbois, G., Urai, J. L., De Craen, M. and Honty, M. (2011). Comparative study on porosity in fine- and coarse-grained Boom Clay samples (Mol-Dessel reference site, Belgium).- Mol, Belgium: SCK•CEN, 2011.- 46 p.- (External Report of the Belgian Nuclear Research Centre; ER-157.

Houben, M.E., Desbois, G., Urai, J.L. (submit.). Pore morphology and distribution in the shaly facies of Opalinus Clay (Mont Terri, Switzerland): insights from representative 2D BIB-SEM investigations on the mm to nm scale. Applied Clay Science.

Lexa, O. (2010). PolyLX - the MATLAB™ toolbox for quantitative analysis of microstructures. Ondrej Lexa Website.

Mandelbrot, B. (1982). The Fractal Geometry of Nature, W. H. Freeman.

SAXS and TEM Investigation of Bentonite Structure

Michał Matusewicz [1,2*], Ville Liljeström [3], Arto Muurinen [1], Ritva Serimaa [3]

[1] VTT Technical Research Centre of Finland (FI)
[2] Jyväskylä University (FI)
[3] Helsinki University (FI)

* Corresponding author: michal.matusewicz@vtt.fi

Abstract

A preliminary investigation of bentonite structure using Small-Angle X-ray Scattering (SAXS) and Transmission Electron Microscopy (TEM) is presented. Three types of clay were used: unchanged MX-80 bentonite and purified clays with sodium or calcium ions. Quantitative information in nano-scale – basal spacing, mean crystallite size - was obtained from SAXS, which was complemented by TEM to give qualitative information from micron to nanometre scale.

Introduction

This abstract presents the initial results of on-going studies of bentonite structure using Small-Angle X-ray Scattering (SAXS) and Transmission Electron Microscopy (TEM). Three types of water saturated clay compressed to a dry density of 1.3 $g \cdot cm^{-3}$ were investigated: unchanged MX-80 bentonite and purified clays saturated with sodium or calcium ions. The purification was based on the method by Tributh and Lagaly (1986).

SAXS

SAXS measurements were performed at the University of Helsinki. The measurements were done with two different set-ups, i.e. with large sample-to-detector distance (smaller q-range) and smaller sample-to-detector distance (larger q-range). The clay sample was a disk of water-saturated MX-80 bentonite, 5 mm in diameter and 0.5 mm thick, cut out of a larger pellet. During the measurement it was kept in a sample holder tightly sealed with Mylar foil.

The results presented in Figure 1 show the character of the montmorillonite nano structure, which is known to form from montmorillonite platelets stacked together. From the scattering profiles it can be seen that there are some small differences between the samples. The differences are most visible in the peaks: the profiles showing sharp and clear peaks are related to better lamellar order. Those profiles showing weak and broad peaks are related to smaller crystallites and worse lamellar order. Broadening can also be related to small peaks from different basal spacing that overlap the main peak. In one of the samples, the effect of drying can be seen, as with time the diffraction relating to the lamellar distances splits into two peaks.

As can be seen in Figure 1, the different peak shape of the samples may be interpreted such that the MX-80 sample has a higher order in the nano-scale than purified clays. The Na- and Ca-clays seem to have smaller stacks of platelets but also their basal spacing can have larger variations than the spacing in the MX-80 sample (the basal spacing has wider distribution than when the peak splitting occurs). The strong correlation peaks for all the samples correspond to a distance of 19.4±0.3 Å.

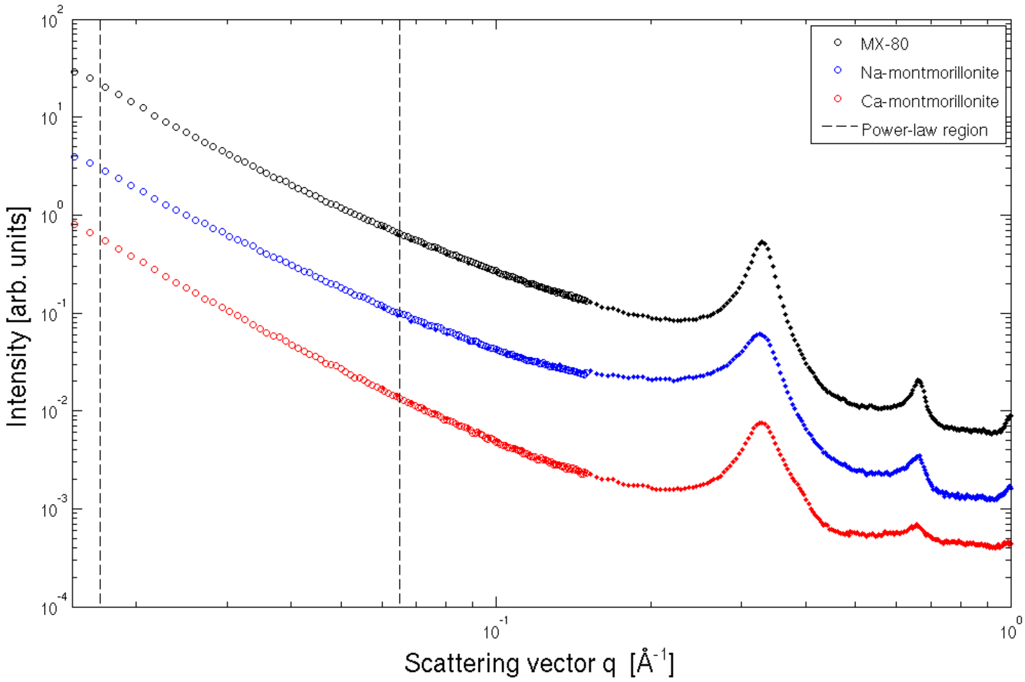

Figure 1. Scattering profiles of all the samples; the curves are shifted in intensity for clarity of the image. At small scattering vectors the power law can be fitted. All the samples obeyed the power-law between -2.5 and -2.8. At larger q-values the diffraction from the lamellar structures is seen. The MX-80 sample shows the most distinct peaks which are strongly present also as higher order peaks.

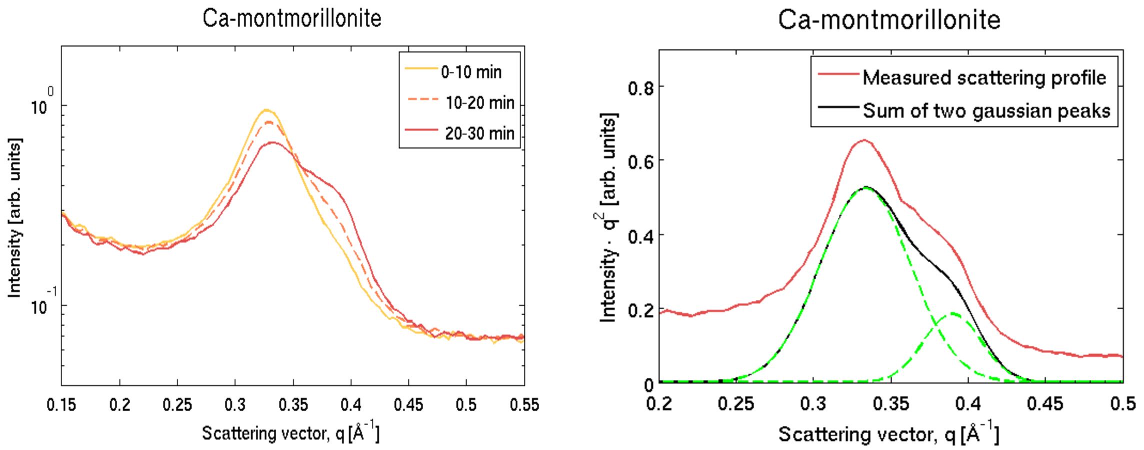

Figure 2. Peak splitting when the sample is drying – Left figure: Unexpectedly the correlation peak of the Ca-montmorillonite sample split into two peaks during the measurement. At the same time, it can be seen that the main peak is shifted from 0.33 Å^{-1} (corresponding to 19.0 Å basal spacing) to 0.34 Å^{-1} (18.5 Å). Right figure: The positions of the fitted peaks are 0.339 Å^{-1} and 0.392 Å^{-1} which corresponds to distances of 18.5 Å and 16.0 Å, respectively.

As can be seen in Figure 2, splitting of the peak during the measurement was observed. This is interpreted as drying of the sample due to a fault in closing the sample holder.

TEM

Transmission Electron Microscopy was performed on 90 nm thick sections of epoxy embedded bentonite clay. Prior to embedding, the clay had been high pressure frozen (Studer et al. (2001)) with a Leica EM Pact machine and vitreous ice was freeze-substituted first with acetone and finally low-viscosity Epon resin. The samples were cut using microtome and imaged with an FEI Tecnai 12 microscope at a working voltage of 120 kV.

Correct interpretation of the TEM micrographs is not easy as they are shadowgrams that may additionally contain various artefacts originating from freezing, substitution or sectioning. Looking at Figure 3, the influence of the purification procedure on the clay structure seems to be evident. The structure of the MX-80 sample is more aggregated, containing larger pores, whereas purified clays appear to be more homogenous.

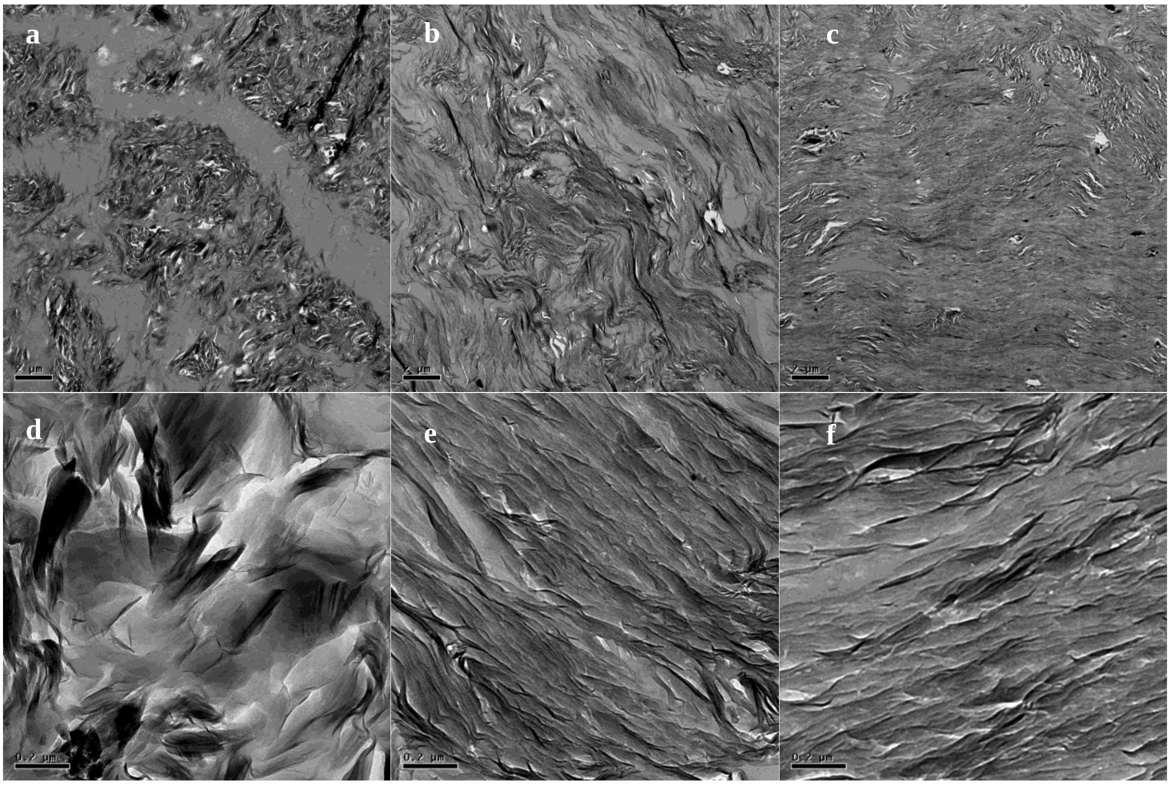

Figure 3. Comparison of micrographs of original MX-80 clay and two purified clays. In the imaged areas, calcium montmorillonite seems to be more homogenous, whereas the MX-80 sample has clearly visible pores and denser clay areas. From the left: MX-80, Na – exchanged montmorillonite and Ca – exchanged montmorillonite. Upper row: magnification of 890x, lower row 13000x.

Figure 4 shows segmentation of the grey-scale image into four components using ImageJ (Abramoff et al. (2004)) software. This facilitates perception of phases of different densities in the system and clearly shows the thresholds used.

It should also be noted that, due to the small area of observation, one should avoid drawing far-fetched conclusions based on this method alone. Nevertheless, information acquired here can be an interesting support for hypothesis based on other methods.

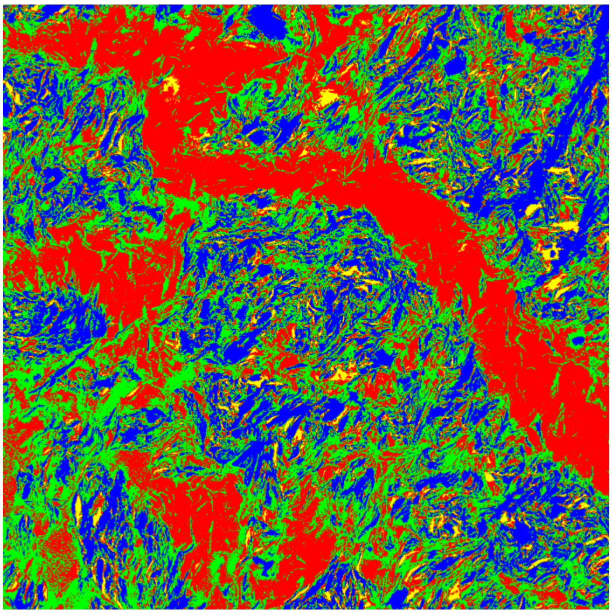

Figure 4. Micrograph of MX-80 bentonite (from Figure 3a) segmented into four components. Blue colour corresponds to accessory minerals and denser clay regions, green to less dense clay, red to epoxy and yellow to empty spaces and thinner parts of the section.

Summary and Conclusions

SAXS seems to be a more reliable source of quantitative data than TEM. SAXS gives the averaged information about basal spacing. TEM in this study gives more qualitative information, but in a greater resolution range. The presented work is a starting point to combine more methods to obtain a better idea of bentonite structure.

Acknowledgement

These studies form part of the Finnish KYT2014 programme. Financial support from the VTT Graduate School is acknowledged (MM). TEM imaging was carried out in the EM Unit of the Institute of Biotechnology at Helsinki University. Fruitful discussions with Torbjörn Carlsson and Markus Olin (VTT) are kindly acknowledged.

References

Abramoff, M.D., Magalhaes, P.J., Ram, S.J., 2004, Image Processing with ImageJ, Biophotonics International, 11, 36-42.

Studer, D.; Graber, W.; Al-Amoudi, A.; Eggli, P., 2001, A new approach for cryofixation by high-pressure freezing, Journal of Microscopy, 203, 285-294

Tributh, H., Lagaly, G., 1986, Aufbereitung und Identifizierung von Boden- und Lagerstättentonen. I. Aufbereitung der Proben im Labor. GIT-Fachzeitschrift für das Laboratorium 30, 524-529.

Discriminating between Interlayer Pores and Macropores in Na Montmorillonite

Martina Bestel [1,4]*, Fanni Jurányi [1], Cecile Marcelot-Garcia [1], Gerald .J. Schneider [2], Luc Van Loon [3], Thomas Gimmi [3,4], Larryn W. Diamond [4]

[1] Laboratory for Neutron Scattering, Paul Scherrer Institut, 5232 Villigen PSI, CH
[2] Forschungszentrum Jülich, Centre for Neutron Science at FRM II, 85747 Garching, DE
[3] Laboratory for Waste Management, Paul Scherrer Institut, 5232 Villigen PSI, CH
[4] Institute of Geological Sciences, University of Bern, 3012 Bern, CH

* Corresponding author: martina.bestel@psi.ch

Abstract

Swelling clays are used as barrier material for the nuclear waste management. Since the interlayer water can be significantly undercooled the fixed window scans technique on neutron backscattering spectrometer with high energy resolution is a good method to discriminate and quantify the amount of water in the interlayers with respect to the one in the macropores as a function of the bulk dry density (hydration process).

Introduction

Swelling clays, like Na montmorillonite, play an important role as barrier material for radioactive waste repositories. The main transport mechanism for released radionuclides is molecular diffusion through the pore water. In this context the diffusion of water and ions in smectite-rich porous media is an important topic. The diffusion properties strongly depend on the geometry of the pores (the structure of the pore space), and notably on the distribution of pore water between different pore compartments (Bourg *et al.* (2010)). Depending on the bulk dry density, water is located in the nanoporous interlayers and in surrounding macropores. In highly compacted Na montmorillonite only interlayer pores exist (Pusch *et al.* (2001)) and diffusion has to occur through these interlayers. At lower bulk dry density macropores between clay particles exist in addition to interlayer pores, which enhance the diffusive transport.

Aim

Our aim was to discriminate and quantify the two water populations (interlayers, macropores) in Na montmorillonite samples at different densities. For that purpose, we made use of the fact that water in the interlayers is partly bound to internal surfaces and interlayer cations and thus can be significantly undercooled, whereas water in the macropores shows a bulk-like behavior, i.e. it freezes at ca. 273 K. Accordingly, water in interlayers remains partly mobile at temperatures below 273 K, whereas water in macropores loses its molecular mobility.

Methods and Results

Hydrogen has the largest total neutron scattering cross section of all natural elements (source: Center for Neutron Research (NIST)). Hence, the total scattering observed in a neutron scattering experiment is heavily dominated by the hydrogen belonging to the clay sheets or to the water molecules in the macropores in Na montmorillonite. Neutron scattering provides informations about position and motion of the hydrogen in Na montmorillonite.

The clay studied is a montmorillonite from Milos (Decher, 1997) which was conditioned to the homoionic Na form. For the neutron scattering experiments clay powder with desired amount of water was compacted to pellets of (5 * 1.5 * 0.06) cm^3. The sample is encapsulated in an aluminium sample holder.

We are using neutron-diffraction on MORPHEUS with λ = 5.0 Å at Paul Scherrer Institut (SINQ, PSI, Villigen, Switzerland) to study the stepwise intracrystalline swelling as a function of the bulk dry density.

Quantification of water population were done by Fixed Window Scans (FWS) on the backscattering spectrometer SPHERES (FRM II, Garching, Germany) with λ = 6.27 Å, ΔE (FWHM) = 0.65 µeV, Q = 0.6 - 1.8 A^{-1}. Vanadium was used for detector efficiency calibration and to determine the energy resolution of the instrument. The empty sample holder was measured for the background. In this technique, neutrons with equal initial and final wavelengths are counted. This makes it possible to study the elastic intensity of the scattered neutrons within a fixed energy window (within the instrument resolution), usually as a function of temperature. Dynamic processes which are slower than the instrument are resolved and seen as static properties, which are proportional to the elastic intensity. The FWS technique was previously proved to be successful to study the freezing behaviour of supercooled water in highly compacted clays (Gonzalez *et al.* (2008)). We applied this technique to Na montmorillonite from high (1.75 g/cm^3, 2 water layer (wl) in the interlayers (il)) to low (0.80 g/cm^3, 3 wl in the il) densities (Figure 1).

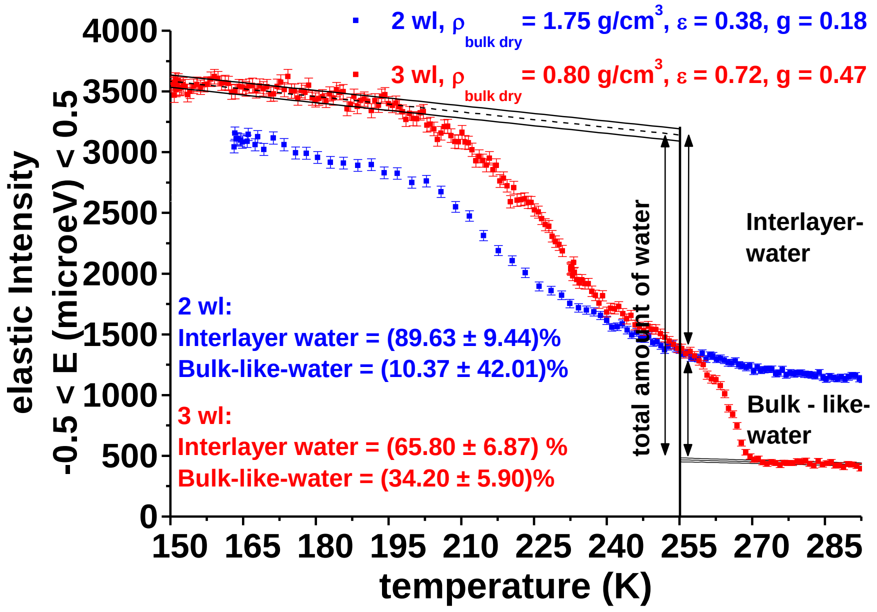

Figure 1. Fixed Window Scans (FWS). The jump in intensity below 270 K is proportional to the amount of bulk-like water in the macro-pores. The difference in intensity between the 'plateau' at the highest and lowest temperatures is proportional to the total amount of water.

From the quantification of the interlayer and macropore water with FWS, the hydration of the two different pore compartments in Na montmorillonite as a function of bulk dry density can be obtained (Figure 2). At high bulk dry densities and low water content all water is located with 1-2 water layer (wl) in nanoporous interlayers (il). At lower bulk dry densities also the macropores between clay particles starts to contain water, while the water in the il increases. Bulk-like water in the macropores becomes a noticeable fraction for 3 or more wl in the il.

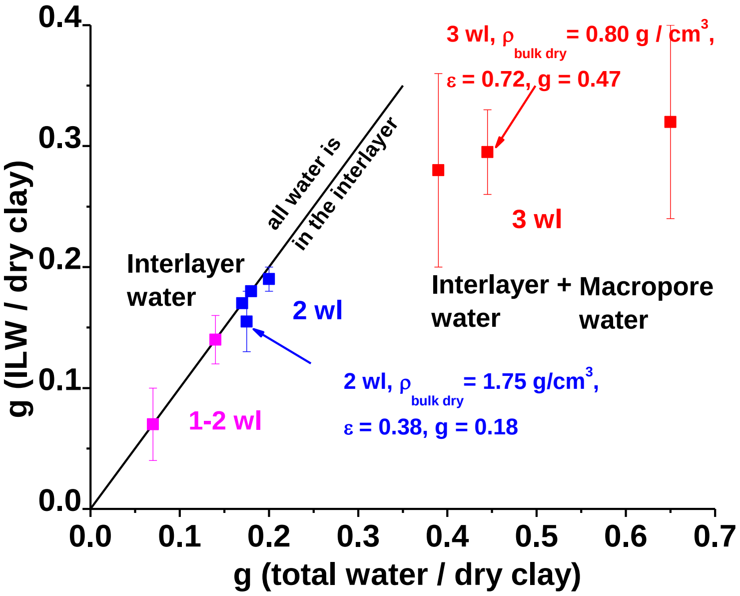

Figure 2. FWS. Amount of water in the interlayers as a function of the total amount of water.

Combining the data from SPHERES and MORPHEUS (Figure 3) a linear increase of the average d-spacing with the amount of water in the interlayers is observable. The diameter of the cation (Na^+) in the interlayer determines the start of this dependence.

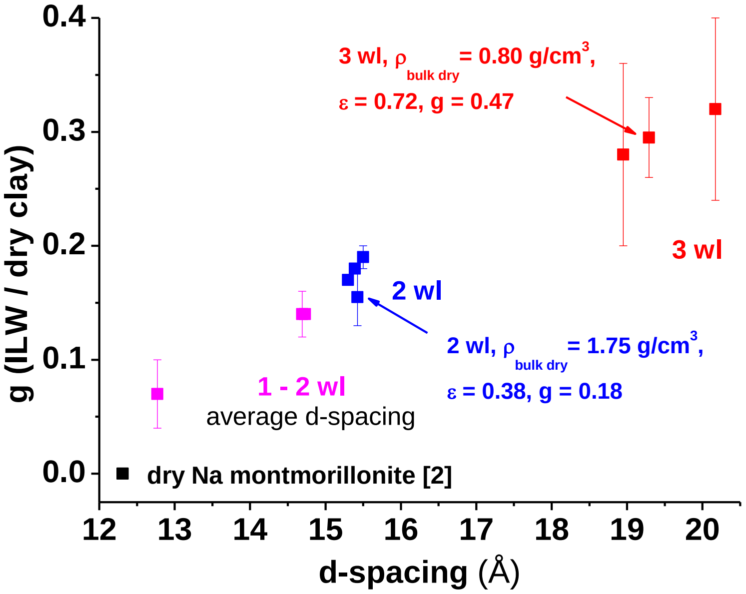

Figure 3. Combining data from fixed window scans and Neutron-diffraction a linear increase of the average d-spacing with amount of water in the interlayers is observable.

Summary and Conclusions

Fixed window scans on a neutron backscattering spectrometer with high energy resolution is a good technique to quantify the water population in the nanoporous interlayers and macropores of swelling clays. Linear swelling in the interlayer exists already from 1 to 2 water layer in Na montmorillonite. Macropores get continuously, but not linearly, saturated. These data will be used later to interpret results of microscopic and macroscopic diffusion experiments through identical clay samples.

References

Bourg, I.C., Sposito, G. (2010). Connecting the molecular scale to the continuum scale for diffusion processes in smectite-rich porous media. Environmental Science and Technology 44, 2085-2091.

Center for Neutron Research (NIST): www.ncr.nist.gov

Decher, A., (1997). Bentonite der Insel Milos, Griechenland. In: T.H. Aachen (Germany). ISBN: 3-86073-602-7.

González-Sánchez, F., Jurányi, F., Gimmi, T., Van Loon, L., Unruh, T. (2008). Dynamics of supercooled water in highly compacted clays studied by neutron scattering. J. Chem. Phys. 129, 174706.

Pusch, R. (2001). The microestructure of MX-80 clay with respect to its bulk physical properties under different enviromental conditions. In: ISSN 1404-0344. Swedish Nuclear Fuel and Waste Management Co. (SKB).

Comparing Microstructure and Pore Size Distribution of the Shaly and Sandy Facies in Opalinus Clay (Mont Terri, Switzerland)

Maartje Houben [1,*], Guillaume Desbois [1], Janos L. Urai [1]

[1] Structural geology, Tectonics and Geomechanics, RWTH Aachen University, Lochnerstraße 4-20,
52056 Aachen, Germany

* Maartje Houben: m.houben@ged.rwth-aachen.de

Abstract

Broad-Ion-Beam polishing is used in combination with Scanning Electron Microscopy to study the microstructure and porosity in the Shaly and Sandy facies of Opalinus Clay (Mont Terri, northern Switzerland). With resolutions of a few nm, areas of around one mm^2 were studied, sufficiently large to be statistically representative for the microstructure of this clay. Qualitative description of the minerals present is combined with quantitative description of porosity present in the different minerals. Pores are mainly elongated, oriented along the bedding and follow a power law distribution with an exponent of 2.3.

Introduction

Clay rich formations are investigated thoroughly as candidate host rocks for the deep geological storage of radioactive waste. In the Mont Terri Rock Laboratory (Switzerland) Opalinus Clay is investigated with the aim to analyze its hydrological, geochemical and rock mechanical properties (Bossart & Thury, 2007). Detailed investigation of the pore morphology and pore space contributes to understanding of sealing capacity, coupled flow and associated deformation in clay (Marschall et al., 2005). The Opalinus Clay formation is a fine-grained sedimentary rock deposited 180 Ma ago in a shallow sea (NAGRA, 2002), compacted to a low porosity (9% to 25% depending on the measuring method used, Boisson et al., 2005) and low permeability (depending on the orientation the hydraulic conductivities are in the range of 1.10^{-14} m/s to 1.10^{-12} m/s, Boisson et al. 2005). On the regional scale the lateral variability of facies and lithology is low (NAGRA, 2002), with three lithological sub-facies (Pearson et al., 2003): Shaly, Sandy and Sandy-Carbonate rich.

Methods

To minimize damage of the clay microstructure the samples investigated here were slowly dried in air at room temperature. Here after they were polished with Ar-ions using a BIB-polisher to produce a high quality cross-section without microstructural damage (Desbois et al., 2009, 2011). The produced cross-sections were than imaged using a SEM. This method allowed direct imaging of the clay fabric and porosity down to the nm scale on ~1 mm^2 areas. The REA for pores present in a polished cross-section of Opalinus Clay was defined by the point counting method based on the mineralogy, where a fine grid consisting of different square box sizes was placed over a BSE image. The smaller the box size the larger the fluctuation in measured porosity, mineralogy and pore size distribution (Kameda et al., 2006). In order to image the REA with sufficient resolution to detect pores, SE micrographs were combined into one high resolution image (> 100 million pixels) using Kolor Autopano giga 2.0 software (Kolor,2008). Visible porosity in the SE-micrographs was traced manually using ARCMAP 9.3 (ESRI, 2008).

Results

Shaly facies

The Shaly facies of Opalinus Clay constitutes of dark grey siltly calcerous shale with diagenetic minerals like carbonates (calcite, siderite), quartz and pyrite. Minerals, fossils and organic matter are embedded in the clay matrix and homogeneously distributed (Figure 1A). Based on EDX point measurements the chemical composition of a mineral is verified, where after these minerals can be segmented using its characteristic shape and grey value in BSE-images. Size of the minerals is up to 30 µm in diameter. Identified porous phases found in studied samples are classified (Desbois et al., 2009; Heath et al., 2011), overall six different types of pores are identified. Pores are present in siderite minerals, pyrite framboids, fossil shells and three different pore types are present in the clay matrix (Figure 1B, C, D, E). When attempting to link porosity to permeability it is important to understand pore connectivity, the percolating pore network. Characterisation of porosity at pore scale shows that pore networks in fossils, pyrite framboids and cracks are connected to the clay matrix, whereas pores in siderite are mainly within one mineral and not interconnected. Overall, pores are mainly oriented along the bedding and are elongated in the non-clay phases to very elongated in the clay matrix. Furthermore, pores are mainly in the µm – nm scale, but pores in the clay matrix are overall one to two orders of magnitudes smaller than pores present in the pore bearing minerals. Pore sizes in the clay matrix are distributed following a power law distribution with a power law exponent of 2.3 for pores with an area in the range of 30 – 10^{10} nm^2. Visible porosity inferred from the SEM micrographs is in the range of 1-4%.

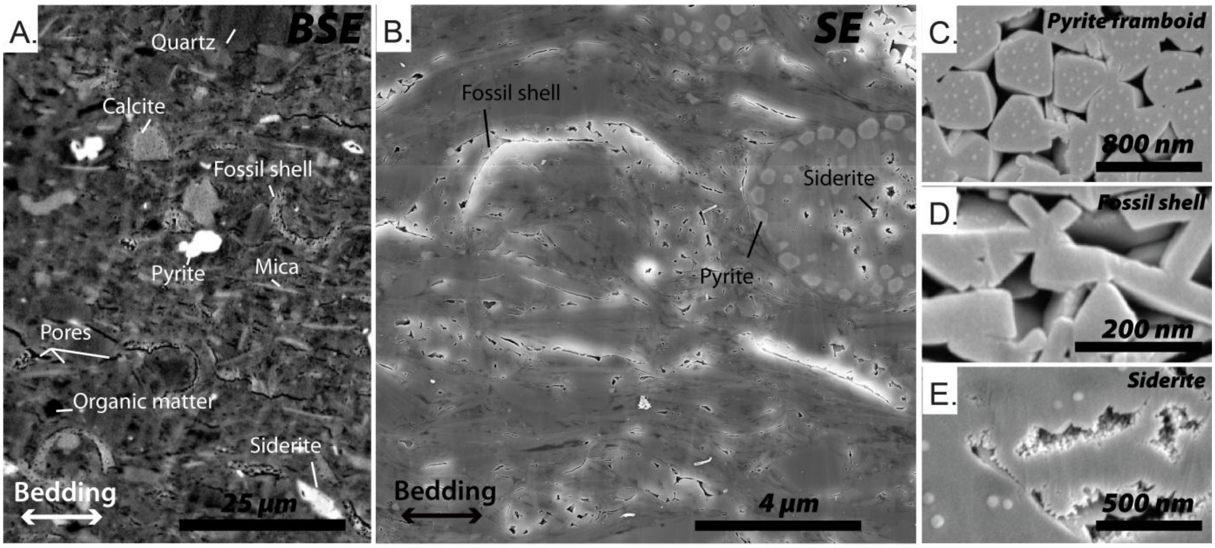

Figure 1. A) Typical microstructure BSE micrograph of the Shaly facies of Opalinus Clay. The most abundant minerals are indicated in the micrograph. B) SE micrograph of the Shaly facies featuring the pores present in the clay matrix, fossil shell and siderite. C), D), E) Typical pore morphologies of pores in respectively framboidal pyrite, fossil shell and siderite.

Sandy facies

Drill cores from the Sandy facies are on the cm-mm scale more heterogeneous than the samples from the Shaly facies, with alternating clay-rich and sand-rich layers and carbonate-rich lenses (Figure 2). Sand layers exist of quarts, K-feldspar and calcite grains up to 50 µm in diameter with in between the grains the clay matrix, siderite and pyrite minerals, whereas the clay layers exists mainly of a clay matrix with some quartz, calcite, mica, pirite and siderite minerals embedded in the matrix. The carbonate-rich lens mainly exists of calcite (up to 100 µm diameter grains) with siderite, quartz, pyrite and clay matrix in between calcite minerals. The difference in microstructures is mainly due to a difference in grain size of the minerals and the amount and type of minerals present. Pore morphologies in the minerals and clay matrix in the different layers in the Sandy facies are similar to those present in the Shaly facies. Pores in the clay matrix are mainly oriented along the bedding and very elongated. Furthermore, pores in the clay matrix are following a power law with a distribution coefficient of 2.3 and visible porosity is in the order of 0.5-4%.

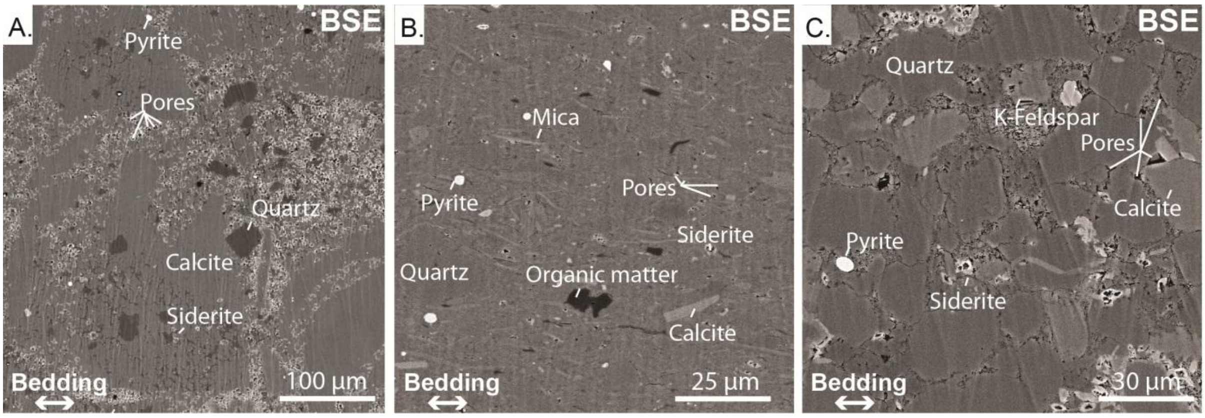

Figure 2. Overview of BSE micrographs illustrating the different layers present in the Sandy facies of Opalinus clay. A) Microstructure present in Carbonate-rich lenses. B) Shale-rich layer. C) Sand-rich layer.

Summary and Conclusions

A combination of BIB-milling and SEM imaging allows large representative area investigation of porosity, morphology and pore size distribution of undamaged clay microstructures. This approach is able to provide a qualitative study of porosity as well as quantification of the pores directly from images at the µm – nm scale. It allows prediction of pore characteristics. Although microstructure differs per layer and per facies, the pores are in all facies mainly oriented along the bedding and are elongated (in minerals) to very elongated in the clay matrix. The pores in the clay matrix are furthermore distributed following a power law with an exponent of 2.3 and this value is similar in all studied cross-sections.

Acknowledgement

We would like to thank NAGRA for funding and supporting this project and in particular Dr. Daniel Traber. Uwe Wollenberg (GIA RWTH-Aachen) is thanked for help with sample preparation and SEM imaging. Jochen Hürtgen, Jan Schneider and Jörg Schoel and the late Christian Diebel should be thanked for their assistance with manual pore detection.

References

Boisson, J. Y. (2005): Clay Club Catalogue of Characteristics of Argillaceous Rocks, OECD/NEA/RWMC/IGSC (Working Group on measurement and Physical understanding of Ground-water flow through argillaceous media) august 2005 Report NEA no. 4436 (Brochure and CD-Rom including data base). OECD/NEA Paris, France, 72.

Bossart, P. & Thury, M. (2007) Research in the Mont Terri Rock laboratory: Quo vadis?, Physics and Chemistry of the Earth, 32, 19-31.

Desbois G., Urai J.L. and Kukla P.A. (2009) Morphology of the pore space in claystones - evidence from BIB/FIB ion beam sectioning and cryo-SEM observations. E-Earth, 4 :15-22.

Desbois G., Urai J.L., Kukla P.A., Konstanty J. and Baerle C. (2011) High-resolution 3D fabric and porosity model in a tight gas sandstone reservoir: a new approach to investigate microstructures from mm- to nm-scale combining argon beam cross-sectioning and SEM imaging . Journal of Petroleum Science and Engineering. In press.

ESRI (2008) ArcMap 9.3, In: Arcinfo Desktop 9.3. ESRI, Redlands, California, U.S.

Heath J.E., Dewers T.A., McPherson B.J.O.L., Petrusak R., Chidsey, Jr. T.C., Rinehart A.J., and Mozley P.S. (2011) Pore networks in continental and marine mudstones: Characteristics and controls on sealing behavior. Geosphere; 7(2): 429–454; doi: 10.1130/GES00619.1

Kameda, A., Dvorkin, J., Keehm, Y., Nur, A., Bosl, W. (2006) Permeability-porosity transforms from small sandstone fragments, Geophysics, 71, 1, N11-N19.

Kolor (2008) Autopano Giga 2.0, Challes-les Eaux, France.

Marschall, P., Horseman, S., Gimmi, T. (2005) Characterisation of gas transport properties of the Opalinus Clay, a potential host rock formation for radioactive waste disposal, Oil & Gas technology, 60, 1, 121-139.

NAGRA (2002) Technischer Bericht 02-03, Projekt Opalinuston: Synthese der geowissenschaftlichen Untersuchungsergebnisse, Dezember.

Pearson, F.J., Arcos, D., Bath, A., Boisson, J.-Y., Fernandez, A.M., Gäbler, H.-E., Gaucher, E., Griffault, L., Hernan, P., Waber, H.N. (2003) Mont Terri Project – Geochemistry of water in the Opalinus Clay formation at the Mont Terri Rock Laboratory, Reports of the FOWG, no. 5, Bern.

SESSION –III & IV “WATER AND ION MOBILITY, UPSCALING AND IMPLEMENTATION IN MODEL APPROACHES”

Effects of Organics on the Adsorption and Mobility of Metal Cations in Clay Systems: Computational Molecular Modeling Approach

Andrey G. Kalinichev[1,2*], **Brice F. Ngouana Wakou**[1], **Narasimhan Loganathan**[1]

[1] Laboratoire SUBATECH, Ecole des Mines de Nantes (FRANCE)
[2] Department of Chemistry, Michigan State University (USA)

* Corresponding author: kalinich@subatech.in2p3.fr

Abstract

Understanding and prediction of many natural and anthropogenic environmental processes ultimately depend on a fundamental understanding of the chemistry occurring at the mineral-fluid interfaces. Clay-related minerals and natural organic matter (NOM) are ubiquitous in the environment, and metal-NOM complexation induces strong correlations between the NOM concentration in water and the capacity of clay particles to bind metals, thus affecting their speciation, solubility and toxicity in the environment. Despite significant geochemical, environmental and technological interest, the molecular-level mechanisms and dynamics of the physical and chemical processes involving NOM are not yet well understood.

In this presentation we compare three different molecular dynamics (MD) computer simulations of metal-NOM complexation in aqueous solutions. The simulation results indicate that despite some obvious quantitative variations in the computed values depending on the size of the simulated system and on the parameters of the force field models used, all three simulations are quite robust and consistent. In particular, approximately 35-50% of Ca^{2+} ions in all simulations are associated with the carboxylic groups of NOM at near-neutral pH. The stability of bidentate-coordinated contact ion pair complexes is also always strongly preferred.

Easy association of metal cations with negatively charged NOM functional groups and negatively charged clay surfaces allows us to predict that cationic bridging could be the most probable mechanism of NOM association with clays in natural environments. New MD simulations are currently in progress to quantitatively assess these predictions on a molecular scale for nuclear waste disposal applications. New larger-scale clay models incorporate a more realistic representation of the structural and compositional disorder of natural illites and smectites and employ CLAYFF – a fully flexible general force field suitable for the molecular simulations of hydrated mineral systems in the presence of organics.

Background and Motivation

Callovo-Oxfordian (COx) clay formations contain significant amounts (up to 1.5 mass %) of total organic carbon, and the soluble fraction of these natural organic substances is a potential vector in the transport of radionuclides (Andra, 2010). Recent measurements in batch and diffusion experiments with actual COx samples have demonstrated that organic acids are noticeably mobile, despite the observed significant degree of irrerversible adsorption, even leading to a complete saturation of clay adsorption sites (Durce, 2010). These processes can also be strongly affected by the presence of Ca^{2+} ions (Durce, 2010). The molecular mechanisms of the adsorption and transport phenomena in such complex systems are not well understood yet, but this knowledge is essential for a reliable predictive modeling of radionuclide behavior in natural and engineered barriers of nuclear waste repositories over the time periods spanning many orders of magnitude from picoseconds to a million of years.

Computational molecular modeling is one of the most powerful tools to develop quantitative atomistic understanding of such complex systems and phenomena and to unravel fundamental molecular-scale correlations between the structural, thermodynamic, spectroscopic, and transport properties of materials (e.g., Cygan et al., 2009). However, there are several sources of uncertainty which can potentially limit the applicability of these powerful computational molecular modeling techniques to the systems involving natural organic matter (NOM) and clays. First of all, NOM itself is structurally and compositionally heterogeneous, with reported apparent molecular weights ranging orders of magnitude from several hundred to several hundred thousand Daltons. Whether NOM represents a true macromolecular chemical entity or is only a supramolecular aggregate of much smaller molecules held together by relatively weak non-covalent interactions is still under discussion, although the most recent experimental evidence tends to support the latter view (Sutton and Sposito, 2005). These compositional and structural uncertainties have limited generally applicable quantitative characterization of metal-NOM complexation in molecular-scale detail.

Compositional and structural heterogeneity of clays represent another source of uncertainties for molecular modeling (Cygan et al., 2004). Most common clay-related minerals are poorly crystalline and fine grained. In the absence of large single crystals suitable for X-ray refinement studies, detailed structural characterizations of these materials are usually lacking. Clay minerals typically possess low crystal symmetry and are characterized by a variety of multicomponent substitutions in the tetrahedral and octahedral sheets. These substitutions lead to a net negative charge on the clay structural layers that allows for the intercalation of solvated metal cations, and other charged complexes, within the interlayer region. However, the chemical diversity and structural disorder introduced by such site substitutions in clays makes their molecular modeling an especially challenging task.

Nevertheless, a significant progress has been achieved in recent years in the molecular modeling of cation-NOM interactions in aqueous solutions (Sutton et al., 2005; Xu et al., 2006; Kalinichev and Kirkpatrick, 2007; Iskrenova-Tchoukova et al., 2010; Kalinichev et al., 2011), as well as the molecular modeling of the structure and dynamics of ions and water molecules at clay surfaces and in its interlayers (Cygan et al., 2004; Marry et al., 2008; Rotenberg et al., 2010). However, the interaction of organic molecules with clay and other mineral surfaces has been studied only rarely (Shevchenko and Bailey, 1998; Perry et al., 2006; Sutton and Sposito, 2006; Kalinichev et al., 2010), and the focus is usually on the structure and properties of synthetic polymer-clay nanocomposites (e.g., Chen et al., 2008; Cygan et al., 2009; Fu and Heinz, 2010), rather than on natural clay-organic systems.

Therefore, we have recently launched a new research program of detailed quantitative studies of the energetic, structural, and dynamic aspects of different interaction mechanisms between metal cations (including radionuclides), organic molecules (including NOM), and clay particles (illite and smectite) using classical MD simulation methods. The free energies of adsorption and other thermodynamic and structural parameters obtained through these simulations will then be utilized to improve the predictive capabilities of the thermodynamic and geochemical models currently used for the performance assessment of nuclear waste repositories.

Force Field Models and Preliminary Results

To describe all the interatomic interactions of the clay layers, we are using the CLAYFF force field (Cygan et al., 2004) which has already proven to provide very reliable molecular description of various layered mineral structures (e.g., Cygan et al., 2009; Kalinichev et al., 2010). It is specifically designed to treat a great variety of isomorphic substitutions in the tetrahedral as well as in the octahedral layers. However, the actual ordering in the location of these substitutions is often exaggerated in MD simulations due to the application of periodic boundary conditions to the simulated structure and due to the relatively small size of the simulated systems. Therefore, as a first step in the construction of our larger-scale clay models, we are taking special care to represent the structural and compositional disorder of illites and smectites as realistically as possible. For this purpose, we have developed a set of new clay models with different degrees of ordering in the tetrahedral and/or octahedral layers up to a fully random distribution of the substitutions in both clay layers (Figure 1). These models are currently being used in the preliminary MD simulations and will allow us also to evaluate the dependence of the simulation results on the degree of tetrahedral and/or octahedral ordering for the same clay composition.

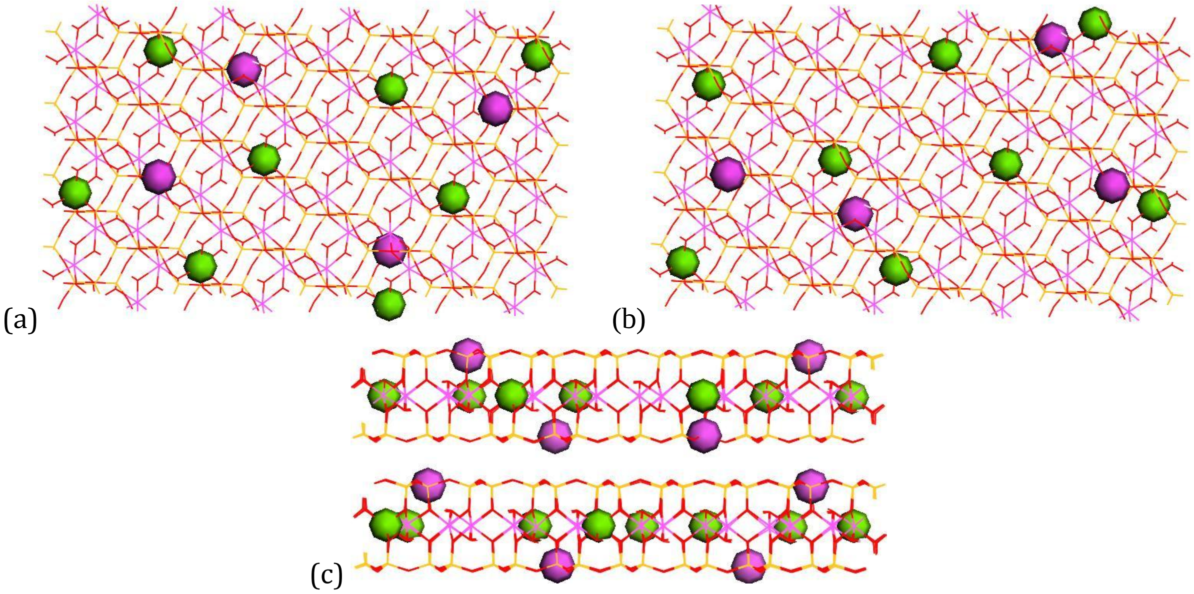

Figure 1. Random distribution of isomorphic substitutions in a new montmorillonite model. (a) and (b) are top and bottom layers viewed from the top along the z direction; (c) is the side view along the x axis. Al/Si substitutions in the tetrahedral layers are shown as pink balls, Mg/Al substitutions in the octahedral sheets are shown as green balls.

The choice of the force field parameters to describe the interactions with the organic part of the system is not so obvious, because many different force field parameterizations for (bio-)organic molecules are available in the literature. In order to test the severity of potential force field dependence of our MD modeling results, we ran a series of simulations with three different force fields for the same molecular model of NOM interacting with Na$^+$, Mg^{2+}, Ca^{2+}, and Cs$^+$ in aqueous solutions (Kalinichev et al., 2011). The TNB model of an NOM molecular fragment (Sein et al., 1999) was used in all simulations. It has a molecular weight of 753 Da and contains three carboxylic groups, three carbonyl groups, two phenolic groups, two amine groups, and four other R-OH alcohol groups. In terms of the molecular weight, atomic composition, degree of aromaticity and total charge density the TNB model fragment is in good agreement with available experimental characterizations and theoretical considerations (e.g., Sutton and Sposito, 2005). The composition of the TNB model is also quite close to the composition of Suwannee River NOM (SRNOM), which is often used in experiments as a typical representative of natural organic matter (e.g., Xu et al., 2006; Ahn et al., 2008).

To quantitatively assess the structural and dynamic effects of metal-NOM complexation, we calculated the radial distribution functions (RDFs) and running coordination numbers using standard procedures (e.g., Allen and Tildesley, 1987). The running coordination numbers of species *j* around species *i* in the solution, $n_{ij}(r)$, are calculated from the RDFs as

$$n_{ij}(r) = 4\pi\rho_j \int_0^r g_{ij}(r)\, r^2 dr \qquad (1)$$

where ρ_j is the number density of species *j* in the system, $g_{ij}(r)$ are the atom-atom RDFs.
Potentials of mean force (PMFs) for the interaction between the Ca^{2+} cations and the carboxylic groups of the NOM fragments were also calculated. The PMF characterizes the change in the free energy of the system due to the changes in its configuration (e.g., Kollman, 1993). If the free energy of a system in thermodynamic equilibrium in the *NVT* statistical ensemble is

$$F = -k_B T \ln Z \qquad (2)$$

where *Z* is the canonical partition function and k_B is the Boltzmann constant, then the potential of mean force, $W(r)$, for two interacting species is defined as the potential that would generate the mean force between the two species, averaged over all orientations, for each separation distance *r*. Thus, the PMF represents the free energy profile of the system as a function of *r*, and it can be shown that

$$W(r) = -k_B T \ln g(r) \qquad (3)$$

where $g(r)$ is the corresponding radial distribution function for this pair of species with the standard normalization for large separations, $g(r) \rightarrow 1$ at $r \rightarrow \infty$. Thus, $W(r)$ asymptotically approaches zero with large separation distance. A detailed analysis of the PMF calculations for the metal cation complexation with the carboxylic groups of NOM molecules and the resulting estimates for the metal-NOM association constants have been recently published elsewhere (Iskrenova-Tchoukova et al., 2010).
For the neutral pH conditions modeled in our simulations, the three carboxylic groups of the NOM fragments can be assumed to be completely deprotonated (pK_a values between 4 and 5), whereas the hydroxyl groups are protonated (pK_a values of ~ 9). The deprotonated carboxylic groups of NOM are known to be the principal source of the NOM negative charge development at the near-neutral pH range. These negatively charged carboxylic groups are the most important binding sites for metals, and Ca^{2+} appears to be among the most strongly NOM-associating ions (e.g., Leenheer et al., 1998; Wall and Choppin, 2003).
Metal cations can associate with these carboxylic groups via several typical and relatively stable coordination geometries (Iskrenova-Tchoukova et al., 2010; Kalinichev et al., 2011). In a *bidentate* contact ion pair (CIP) configuration, the cation is coordinated simultaneously with the two oxygen atoms of the carboxylic group and stays approximately equidistant from both of them predominately near the bisector plane orthogonal to the plane of the carboxylic group. In a *monodentate* CIP configuration, the cation is coordinated with only one of the carboxylate oxygen atoms. Thus, in both bidentate and monodentate cases, the H_2O molecules in the first coordination shell of cations are partially replaced by the carboxylate oxygens. In contrast, in an outer-sphere coordination, the cation is separated from the NOM carboxylate oxygens by a mono-molecular layer of H_2O, and one can consider this coordination as a fully hydrated metal ion weakly associated with the carboxylic group forming a solvent separated ion pair (SSIP).
A comparison of potentials of mean force for Ca^{2+} interaction with the carboxylic groups of NOM obtained in MD simulations with two different force fields (AMBER and CHARMM) is presented in

Figure 2(a). Both simulations consistently result in a potential well of about –3.0 kcal/mol characterizing the bidentate cation-carboxyl coordination at interatomic separations of about 3.0 Å and in a shallower and broader potential well of –0.7 kcal/mol at about 5.5 Å corresponding to a solvent-separated ion pair coordination. However, the potential barrier between the CIP and SSIP coordinations is higher by almost 1 kcal/mol for the CHARMM force field, indicating a stronger preference for inner-sphere vs. outer-sphere coordination for the latter model. This model dependence is also visible in the energy of monodentate-coordinated CIPs between the two force fields. For the CHARMM force field, the corresponding potential well (red line in Figure 2(a) at about 3.5 Å) is located in the region of positive energies, indicating that such metal-NOM coordinations, although relatively stable, are generally unfavorable.

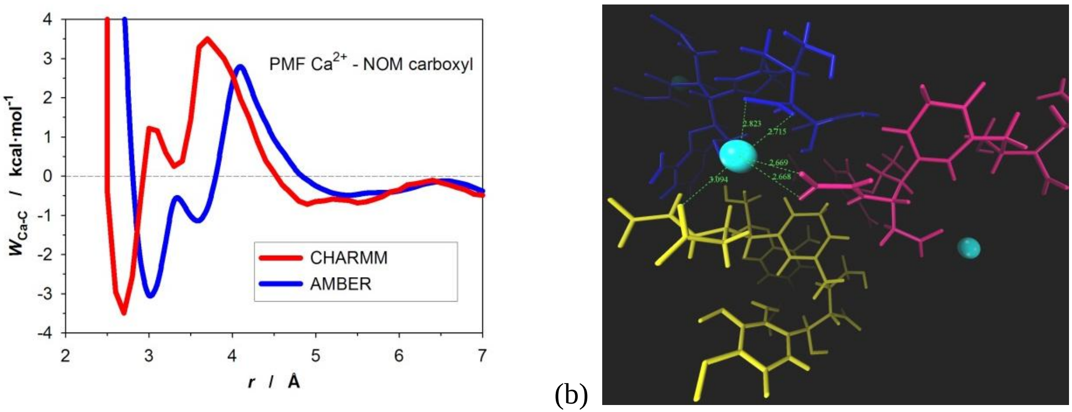

(a) (b)

Figure 2. (a) Potentials of mean force for interactions of Ca^{2+} ions with carboxylic group of NOM from the results of two different MD simulations. (b) A snapshot from MD simulations illustrating the NOM complexation and aggregation in the presence of Ca^{2+} ions. H_2O molecules and other ions are removed for clarity.

The analysis of larger-scale MD simulations reveals that when Ca^{2+} ions are present in the system, not only a stronger degree of metal-NOM complexation is observed, but also a significant degree of supramolecular NOM aggregation (Iskrenova-Tchoukova et al., 2010; Kalinichev et al., 2011). A snapshot from such simulation is presented in Figure 2(b), where three aggregating NOM fragments are shown in different colors, Ca^{2+} ions are shown as the light blue balls, and all H_2O molecules are removed for clarity. One Ca^{2+} ion is seen here in a strong bidentate CIP coordination with the carboxylic groups of two different NOM molecules (red and dark blue in Figure 2(b) and, simultaneously, in a weaker monodentate CIP coordination to a third NOM molecule (yellow in Figure 2(b)). Such simultaneous coordination of Ca^{2+} ions by two carboxylic groups of the same NOM molecule was also observed in our simulations. This picture is in good agreement with an earlier hypothesis that Ca^{2+} ions are capable of accepting up to four NOM carboxylic groups in their inner-sphere coordination shell (Leenheer et al., 1998). This observation also suggests that the complexation with Ca^{2+} ions may affect the supramolecular NOM aggregation in two different ways. Ca^{2+} ions can directly affect aggregation by bridging carboxylic groups of different NOM molecules, effectively bringing and holding them together. In addition, simultaneous Ca^{2+} coordination with two carboxylic groups of the same NOM molecule can produce a metal-NOM complex with reduced net negative charge, thus allowing such complexes to approach each other more readily and to coordinate with each other via weaker hydrogen bonding interactions.

Conclusions

Clays and NOM are two good examples of complex natural materials which, for natural reasons, cannot be completely characterized in full atomistic compositional and structural detail. This makes it particularly hard to approach a quantitative investigation of their behavior with traditional computational molecular modeling techniques. We have analyzed and quantitatively assessed the degree of possible model-dependence in the results of such molecular computer simulations taking the complexation of Ca^{2+} with a realistic and well defined TNB model of NOM as an important example (Kalinichev et al., 2011). Some degree of dependence of the simulated results on the size of the simulated system and on the parameters of the force field models is, indeed, observed. However, we find it quite encouraging, that the main results are very robust and quite consistent with available experimental data and other results of molecular modeling. Independent on the force field used, all MD simulations indicate that about 35-50% of the NOM carboxylic groups are associated with Ca^{2+} cations and provide other valuable molecular scale information concerning the structure, energetics, and dynamics of the metal-NOM association. This includes bidentate vs. monodentate configuration of the complexes, inner-sphere (CIP) vs. outer-sphere (SSIP) coordination of the ion pairs and their relative stability (Iskrenova-Tchoukova et al., 2010). The degree of supramolecular aggregation of NOM in aqueous solutions can also be addressed in such simulations, at least semi-quantitatively. However, much larger scale simulations (both in terms of the sizes of the modeled systems and the duration of the simulations) would have to be performed for Ca^{2+}–containing systems with different and more structurally diverse NOM models to further explore and quantify the phenomenon of aggregation, the relative importance of different aggregation mechanisms and the thermodynamic stability and transport properties of such aggregates.

The same conclusions should generally hold for the association of metals with clay surfaces. In view of the well-known strong association of metal cations with negatively charged clay surfaces and negatively charged NOM functional groups, it is natural to expect that cationic bridging could be the most probable mechanism of NOM association with clays in natural environments. New MD simulations are currently in progress to quantitatively assess these predictions on a molecular scale for the clay compositions, organic molecules, and metal cations most relevant for nuclear waste disposal applications.

Acknowledgement

This work is supported by the industrial chair “Storage and Management of Nuclear Waste” at the Ecole des Mines de Nantes (funded by ANDRA, Areva, and EDF), and by the US Department of Energy, Office of Basic Energy Sciences, Division of Chemical Sciences, Geosciences, and Biosciences (grant number DE-FG02-08ER-15929).

References

Ahn W.Y., Kalinichev A.G., Clark M.M. (2008) Effects of background cations on the fouling of polyethersulfone membranes by natural organic matter: Experimental and molecular modeling study. J. Membr. Sci., 309, 128-140.

Allen M.P., Tildesley D.J. (1987) Computer Simulation of Liquids. Oxford University Press, New York, 385 pp.

ANDRA (2010) 2006 – 2009: 4 ans de recherches scientifiques à l’ANDRA pour les projets de stockage. Agence nationale pour la gestion des déchets radioactifs. Report 383, Juin 2010.

Chen B., Evans J.R.G., Greenwell H.C., Boulet P., Coveney P.V., Bowden A.A., Whiting A. (2008) A critical appraisal of polymer-clay nanocomposites. Chem.Soc.Reviews, 37, 568-594.

Cygan R.T., Liang J.J., Kalinichev A.G. (2004) Molecular models of hydroxide, oxyhydroxide, and clay phases and the development of a general force field. J. Phys. Chem. B, 108, 1255-1266.

Cygan R.T., Greathouse J.A., Heinz H., Kalinichev A.G. (2009) Molecular models and simulations of layered materials. J. Mater. Chem., 19, 2470-2481.

Durce D. (2010) Interactions et transfert de macromolécules organiques et de colloïdes dans l'argilite nanoporeuse du Callovo-Oxfordien, PhD Thesis, SUBATECH, Nantes.

Fu Y.-T., Heinz H. (2010) Structure and cleavage energy of surfactant-modified clay minerals: Influence of CEC, head group and chain length. Philos. Magazine, 90, 2415 - 2424.

Iskrenova-Tchoukova E., Kalinichev A.G., Kirkpatrick R.J. (2010) Metal cation complexation with natural organic matter in aqueous solutions: Molecular dynamics simulations and potentials of mean force. Langmuir, 26, 15909-15919.

Kalinichev A.G., Kirkpatrick R.J. (2007) Molecular dynamics simulation of cationic complexation with natural organic matter. European Journal of Soil Science, 58, 909-917.

Kalinichev A.G., Kumar P.P., Kirkpatrick R.J. (2010) Effects of hydrogen bonding on the properties of layered double hydroxides intercalated with organic acids: Molecular dynamics computer simulations. Philos. Magazine, 90, 2475-2488.

Kalinichev A.G., Iskrenova-Tchoukova E., Ahn W.-Y., Clark M.M., Kirkpatrick R.J. (2011) Effects of Ca^{2+} on supramolecular aggregation of natural organic matter in aqueous solutions: A comparison of molecular modeling approaches. Geoderma, in press, (published on-line October 25, 2010, http://dx.doi.org/10.1016/j.geoderma.2010.09.002).

Kollman P. (1993) Free energy calculations: Applications to chemical and biochemical phenomena. Chem. Rev. 93, 2395-2417.

Leenheer J.A., Brown G.K., MacCarthy P., Cabaniss S.E. (1998) Models of metal binding structures in fulvic acid from the Suwannee River, Georgia. Environ. Sci. Technol. 32, 2410-2416.

Marry V., Rotenberg B., Turq P. (2008) Structure and dynamics of water at a clay surface from molecular dynamics simulation. Phys. Chem. Chem. Phys.10, 4802-4813.

Perry T.D., Cygan R.T., Mitchell R. (2006) Molecular models of alginic acid: Interactions with calcium ions and calcite surfaces. Geochim. Cosmochim. Acta, 70, 3508-3532.

Rotenberg B., Marry V., Malikova N., Turq P. (2010) Molecular simulation of aqueous solutions at clay surfaces. J. Phys. –Cond. Matter, 22, 284114.

Sein L.T., Varnum J.M., Jansen S.A. (1999) Conformational modeling of a new building block of humic acid: Approaches to the lowest energy conformer. Environ. Sci. Technol., 33, 546-552.

Shevchenko S.M., Bailey G.W. (1998) Non-bonded organo-mineral interactions and sorption of organic compounds on soil surfaces - a model approach. Theochem. J. Mol. Structure, 422, 259-270.

Sutton R., Sposito G. (2005) Molecular structure in soil humic substances: The new view. Environ. Sci. Technol., 39, 9009-9015.

Sutton R., Sposito G., Diallo M. S., Schulten H.R. (2005) Molecular simulation of dissolved organic matter. Env. Toxicol. Chemi., 24, 1902-1911.

Sutton R., Sposito G. (2006) Molecular simulation of humic substance-Ca-montmorillonite complexes. Geochim. Cosmochim. Acta, 70, 3566-3581.

Wall N.A., Choppin G.R. (2003) Humic acids coagulation: influence of divalent cations. Appl. Geochem. 18, 1573-1582.

Xu X., Kalinichev A.G., Kirkpatrick R.J. (2006) ^{133}Cs and ^{35}Cl NMR spectroscopy and molecular dynamics modeling of Cs^+ and Cl^- complexation with natural organic matter. Geochim. Cosmochim. Acta, 70, 4319-4331.

Linking the Diffusion of Water in Compacted Clays at Two Different Time Scales: Tracer Through-Diffusion and QENS

Fanni Juranyi[1*], Fátima González Sánchez [2,3], Martina Bestel[1,3], Thomas Gimmi[2,3], Luc Van Loon[2] and Larryn W. Diamond[3]

[1] Laboratory for Neutron Scattering, Paul Scherrer Institut (CH)
[2] Laboratory for Waste Management, Paul Scherrer Institut (CH)
[3] Institute of Geological Sciences, University of Bern (CH)

* Corresponding author: fanni.juranyi@psi.ch

Abstract

Observable water diffusion processes in clays and their parameters depend on the spatial- and time-scale of the measurement. Comparing the diffusion coefficients of quasielastic neutron scattering and tracer through-diffusion, “chemical” and “geometrical” effects can be distinguished and quantified. Results for montmorillonite and illite in the Na- and Ca- form illustrate this very well. Swelling clays such as montmorillonite are especially interesting because of the interlayer water. This water is confined in form of few layers such that the diffusion occurs essentially in 2D. Furthermore the ratio of interlayer- and external- (macropore) water changes as a function of bulk dry density and degree of water saturation. Therefore it is of interest to describe the diffusion process using these parameters. Finally, the activation energy of the diffusion should be equal for both methods assuming that the geometrical factor does not depend on temperature. For the montmorillonites this was not the case, which might also indicate that the main processes on the two scales are different.

Introduction

Clays play an important role in radioactive waste management. In this context water diffusion in clays has to be understood and be predictable for various conditions (bulk dry density, hydration state, temperature and pressure).

It is well known that water diffusion in porous systems is different from that in the bulk. Diffusion can be measured by various techniques, but one should keep in mind that in such complex systems they may lead to different results because of the different spatial- and time-scales. Quasielastic neutron scattering measures diffusion on the atomic/molecular scale, whereas tracer through-diffusion measures it on the macroscopic scale of centimeters. Both have been applied already on clays (Cebula et al. (1981), Malikova et al. (2006), Skipper et al. (2006); Nakazawa et al. (1999), Suzuki et al. (2004)), however not systematically on the same samples.

Pure clays have been chosen as a compromise between complexity and closeness to reality. First, water diffusion in highly compacted clays with systematic structural differences (montmorillonite, illite and kaolinite) has been compared in order to recognize the main effects. Presently diffusion in Na-montmorillonite having different bulk dry densities is investigated. Bourg et al. (2006) used a simple equation to describe the diffusion in montmorillonite with different ratios of interlayer- and macropore water. We will try to apply this model and, if necessary, to further develop it.

Methods

Quasielastic Neutron Scattering (M. Bée, 1988)

The unusually large incoherent scattering cross section of hydrogen makes quasielastic neutron scattering (QENS) a powerful technique to study the water dynamics in bulk or in restricted geometries such as nanoporous materials. In a neutron scattering experiment the dynamics of the sample can be studied through the interaction (energy and momentum transfer) of the neutron with the atoms. The sample is described by the so called dynamical structure factor S(Q,E), which can be related to the pair-correlation function G(r,t) by double Fourier transformation (Q is the momentum transfer, E is the energy transfer). Different motions can be parameterised and transformed into a model S(Q,E) which is fitted to the measured data. Motions on different time scales can be separated, and S(Q,E) can be written as a multiplication of the sub-functions. A diffusion process usually results in Lorentzian shaped function(s) centered at zero energy transfer. The number of Lorentzians, and the Q dependency of their intensities and line widths give information about the diffusion process. The key parameter for an experiment is the energy resolution of the spectrometer, furthermore the range of momentum transfer should be suitable as well (the resolution in momentum transfer is usually sufficient). Different instrument types cover different ranges of available energy resolutions (meV-neV) and observation times (ps-ns): time-of-flight- , backscattering- and spin-echo spectrometers.

To study water diffusion in clays on the atomic scale we performed measurements mostly on time-of-flight spectrometers. Here a mono-energetic neutron beam in short pulses hits the sample, and the scattered neutrons are detected as a function of scattering angle and time-of-flight. For the scattering the energy- and momentum-conservation is valid. From the time-of-flight the energy(transfer) can be calculated, which in combination with the scattering angle gives the momentum(transfer). All spectra at different momentum transfers (Q) have been fitted by a model function, which describes an isotropic rotation of the water molecule around its center of mass and translational jump diffusion (the molecule stays for the so called residence time in place followed by a jump. From the Q dependent width of the narrowest Lorentzian the diffusion coefficient and the residence time can be obtained.

The measurement is running typically for some hours per temperature and sample. Beside, the empty cell (background) and vanadium (calibration and resolution function) have to be measured as well. Ideally, samples have a transmission of ~90% (0.2 mm effective thickness for pure water, and 0.3-0.5 mm for clay), and an area of 1-2 cm x 5 cm. They are vacuum-tightly enclosed in a pure aluminium sample holder.

Tracer through-diffusion

In porous media, such as compacted clays, diffusion of solutes in pore water depends on the geometrical constraints, i.e. the length and shape of the diffusion paths. This can be measured by tracer through-diffusion. In this method a piece of material (~1-2 cm^3) is located between two reservoirs (Figure 1). After the sample is water saturated, one of the reservoirs is labeled with a given amount of radioactive tracer (HTO for example). Transport then takes place from the labeled to the non-labeled compartment. The diffusion can be followed by monitoring the amount of solute transported from one reservoir to the other as a function of time. Figure 1 shows the flux and total accumulated activity vs. time in a typical through-diffusion experiment. There are two different regions: the increasing flux region (transient state) and the constant flux region (steady-state). The latter is used in the through-diffusion experiment to determine the diffusion coefficient using Fick's first law. A correction for the filter effects is performed.

Diffusion at different temperatures has been measured using the continuous method (Van Loon et al., 2005). In the continuous method, only the steady state phase is used. A diffusion experiment is started at a given temperature. As soon as the steady state phase is reached, the temperature is changed. A short transient state with respect to temperature (few hours) is followed by a steady state at the new temperature. The accumulated activity is linear for each temperature and the effective diffusion coefficient (D_{tracer}) can be extracted from the corresponding slope. However the intercept with the y-axis, α (rock capacity factor) can only be derived from the first transient phase of solute diffusion, i.e. at the starting temperature of the experiment. The measurement is running for several weeks for a 1cm long sample, which is enclosed in a special diffusion cell.

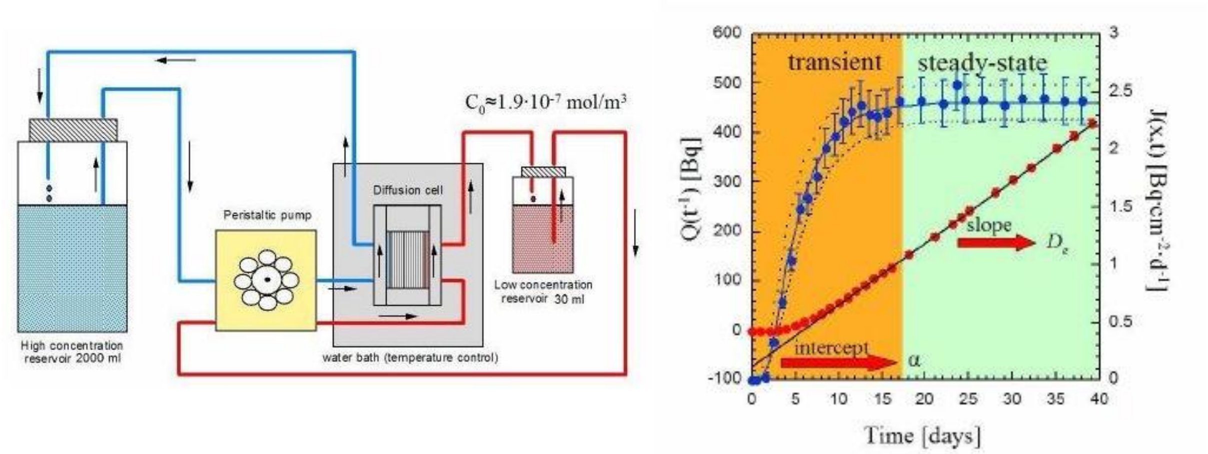

Figure 1. Left: Setup of the tracer through-diffusion experiments. Right: The measured flux and accumulated activation as a function of time [Van Loon et al. (2005)].

Linking the diffusion at the two scales

According to our knowledge this is the first time where diffusion in a porous medium has been compared on these very different time scales. Since QENS has an observation time of the order of picoseconds, the obtained translational diffusion coefficient (D_{QENS}) is determined by local effects (chemical bonding to other water molecules, interaction with dissolved ions and with the surfaces). It can be expressed as $D_{QENS} = q \cdot D_{bulk}$, where q is the electrostatic constraint and D_{bulk} represents the bulk water diffusion coefficient. The motion is detected on the atomic/molecular scale, and so the measured spectrum is a sum over all atoms in the sample. Tracer through-diffusion experiments (across the whole sample) are influenced additionally by the mesoscopic - macroscopic pore structure of the clays. The measured effective diffusion coefficient can be expressed as $D_{tracer} = \varepsilon \cdot q/G \cdot D_{bulk}$, where ε is the porosity and G is the geometrical factor including constrictivity and tortuosity. The large difference in the scale of the diffusion in case of the two selected techniques makes a direct comparison of water diffusivities impossible. Two ways of comparison could be established (González Sánchez et al., 2009): An indirect comparison by connecting the diffusion coefficients at the two different scales through the electrostatic constraint ($q = D_{QENS}/D_{bulk}$) and the geometrical factor ($G = \varepsilon \cdot D_{QENS}/D_{tracer}$); and a direct comparison through the activation energy (E_a), where E_a was estimated from the temperature dependence of the diffusion coefficients. The diffusion coefficients followed the Arrhenius law ($D = D_0\, e^{-E_A/k_B T}$) within the studied temperature range. Since the pore geometry is supposed to be essentially the same for all temperatures (i.e. ε and G independent of T), it is expected that the activation energies are equal at both observation scales.

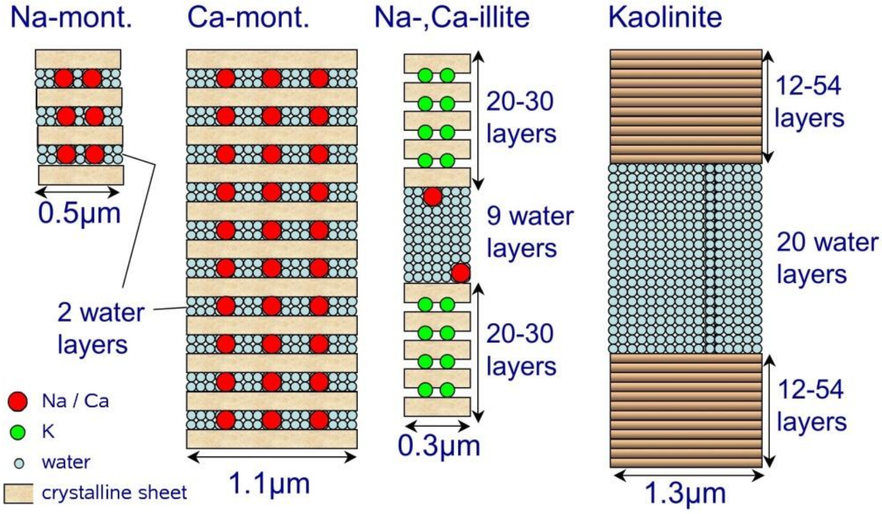

Figure 2. Microscopic structure of the investigated clays. Depending on the type of the clay, water can be located in the interlayer or in larger pores.

Samples

Investigated clays

Three different types of pure clays, two of them charged, namely montmorillonite (in the Na and Ca form) and illite (in the Na and Ca form), and one uncharged, namely kaolinite have been investigated (Figure 2). Their structural differences result in a signicantly different behaviour in contact with water. In case of montmorillonite water can be located in the interlayer space or in macropores. Montmorillonite is a swelling clay, the water uptake into the interlayer occurs stepwise (Kozaki et al., 1998), which can be measured by diffraction. The ratio of water in the interlayer and in macropores can be measured on a neutron backscattering spectrometer (Bestel et al., 2011). In illite, water is found only in between particles, because the interlayer surfaces are tightly linked by potassium cations. The layers of kaolinite are uncharged and therefore have no interlayers; thus water is located only in between particles. Parameters such as particle size, layer spacing, chemical composition, external and total surfaces and porosity were determined (González Sánchez et al., 1998).

Sample preparation

Sample requirements are different for the two methods, but samples could be prepared as identical as necessary. For both type of samples the starting clay powder was the same. Charged clay powders have been brought into a homo-ionic form (Na or Ca). For tracer experiments the calculated amount of dried clay powder has been pressed into the diffusion cell. Prior to the experiment the samples have been saturated with water. For the QENS experiments the dry powders have been kept under a humid atmosphere until the weight reached the calculated value, and then they were pressed in a form to the desired thickness and density. Unfortunately the accurate bulk dry density and water content can be determined only after the diffusion measurements by drying the pressed samples. This method was applicable for the study of highly compacted clays. The samples for tracer diffusion were completely hydrated. For QENS a high, but not full hydration could be reached. Since QENS measures the local diffusion, this is not a problem as far most of the water molecules are in the interlayer. However montmorillonite samples for the QENS measurements at lower bulk dry densities had to be saturated as well. Neutron and X-ray imaging together with neutron diffraction showed that for the pressed samples the thickness and the water/clay ratio are inhomogeneous. After saturation the samples became homogeneous.

Application of uniaxial pressure causes a preferred orientation of the clay particles, however the angular distribution is so broad, that it could not be quantified by diffraction.

Results

Diffusion at the microscopic scale studied by quasielastic neutron scattering

Quasielastic neutron scattering experiments were performed on different instruments using different setups to vary the energy resolution, which is a key parameter for the data analysis. The obtained parameters for the diffusion were consistent, which supports their validity. The most critical point in the data treatment is the choice of a proper model, which might introduce systematic errors. We applied several models from the literature ending up with similar values for translational diffusion. The systematic differences in the clay structures were reflected in their diffusion properties (González Sánchez et al., 1998). Charged clays presented lower diffusion coefficients than kaolinite, which had similar diffusion coefficients than that of bulk water. Within the charged clays the swelling clays like Na- and Ca-montmorillonite were found to clearly reduce the water diffusion, which is attributed to the strong confinement in the interlayer. The diffusion parameters of these two types of montmorillonite were similar. Because most water molecules are located in the interlayer, diffusive motion is probably more dominated by the geometrical confinement than by the difference in the saturating cation (Na or Ca). However when the cations are located on the external surfaces, as it is the case with the two types of illite, the water motion is differently affected depending on the type of cation. Ca reduces the water mobility stronger than Na, as it occurs also in aqueous solutions.

Similarly to aqueous solutions, the activation energy of the water diffusion in Ca-illite was larger than in the Na form due to the stronger tendency of Ca to order the water molecules (cosmotrope character) (Hribar et al., 2002). This was not observed for montmorillonite due to the strong confinement. The confinement itself reduces the activation energy.

Water in a highly compacted montmorillonite (ρ ~1.8g/cm^3) is located only in the interlayer, or close to the surfaces, therefore it is obvious that water diffusion on a certain length and time scale must be restricted perpendicular to the clay sheets, i.e. it must be described by a 2D model. Previous results indicated that by quasielastic neutron scattering with unusual small relative energy resolution and a large energy window it might be possible to observe the characteristics of 2D diffusion. The importance of the relative energy resolution (the intrinsic width of the quasielastic line compared to the energy resolution of the spectrometer) has been recognized by Lechner (1995), however according to our knowledge there is no other measurement, where the characteristic line shape would have been observed.

We succeeded to measure the 2D characteristics of water diffusion in Na-montmorillonite. In case of the 3D model the translational diffusion has a line shape of a Lorentzian, while the powder averaged 2D model has a spectrum with a cusp like singularity at zero energy transfer. The model function in both cases has to be convoluted by the nearly Gaussian shaped resolution function of the instrument. Only the data at most extreme conditions (highest temperature and highest Q value), where the relative energy resolution is the best, could not be fitted by the 3D model: the singularity of the 2D diffusion was obvious. However the complete data set from this measurement could be evaluated by the 2D model.

Diffusion at the macroscopic scale studied by tracer through-diffusion

As in the QENS studies, the systematic structural differences between the clays affected their macroscopic diffusion coefficients (González Sánchez et al., 2008). At the chosen high bulk density, the effective diffusion coefficients followed the order Na-montmorillonite < Ca-montmorillonite < Ca-illite < Na-illite <= kaolinite. The differences were interpreted in accordance with the independently estimated structural properties of the samples, which showed that Na montmorillonite had the smallest particle and pore sizes and thus was expected to have the largest tortuosities, followed by Ca montmorillonite, the illites, and kaolinite. The differences between the illites, which had similar structures, were interpreted to originate from differences in the solvation of Na and Ca ions.

Activation energies larger than those of bulk water were found for the montmorillonites, values similar or slightly lower than those of bulk water for the illites and the kaolinite. At present, the sequence of the activation energies is interpreted as being related to stronger or weaker interactions between water molecules and the specific clay surfaces. From our comparisons with QENS results (see below) some new and interesting aspects that deserve further attention became obvious. Notably, it seems possible that the larger activation energies for montmorillonites are a specific feature of these clays, related to the scale of observation.

Comparison (González Sánchez et al., 2009)

Diffusion coefficients

Na- and Ca-illite have a very similar structure, because of their similarities in the porosity, particle size and in their way of producing stacks of 20-30 particles. Difference in the diffusion should therefore be dominated by the electrostatic constraint. Contrary, in montmorillonite the geometrical factors should be different due to the different particle size and stacking. The obtained q and G factors nicely reflect the expected behavior, which gives confidence to the correctness of the method (Table 1).

Table 1. Electrostatic constraint, q, and geometrical factor, G, obtained from the quasielastic neutron scattering and tracer through-diffusion experiments.

Clay	$q = D_{QENS}/D_{bulk\ water}$	$G = \varepsilon \cdot D_{QENS}/D_{tracer}$
Na-illite	0.9 ± 0.1	3.9 ± 0.4
Ca-illite	0.6 ± 0.1	4.2 ± 0.4
Na-montmorillonite	0.5 ± 0.2	21.0 ± 2.0
Ca-montmorillonite	0.5 ± 0.1	8.0 ± 0.8
Kaolinite	1.2 ± 0.2	4.6 ± 0.5

Activation energy

It is known that the temperature dependence of the water diffusion can only be described approximately by the Arrhenius law, however it led to a good description of our data in the studied temperature range. For the clays with larger pores a very good agreement between E_a values obtained by the two methods (the two scales) was found (Figure 3). In montmorillonite however, where the majority of the water molecules were located in a form of a double-layer between the clay sheets, the activation energy obtained from macroscopic tracer through-diffusion measurements was much larger. There is not even a qualitative agreement in comparison with the other clays: they have the lowest value according to the QENS measurement, but the highest according to the tracer diffusion experiment. Further measurements on Na-montmorillonite, where a 2D model was necessary to describe the data, led to an activation energy of about 15 kJ/mol: larger than previously, but definitely smaller than the one observed by the tracer diffusion. QENS describe only local movements. The different activation energies for montmorillonite at the two scales may hint to a specific scale dependence of the diffusion in this clay. For instance the coupling between water and cation motion or geometrical changes on a time scale of weeks may play a role in this comparison.

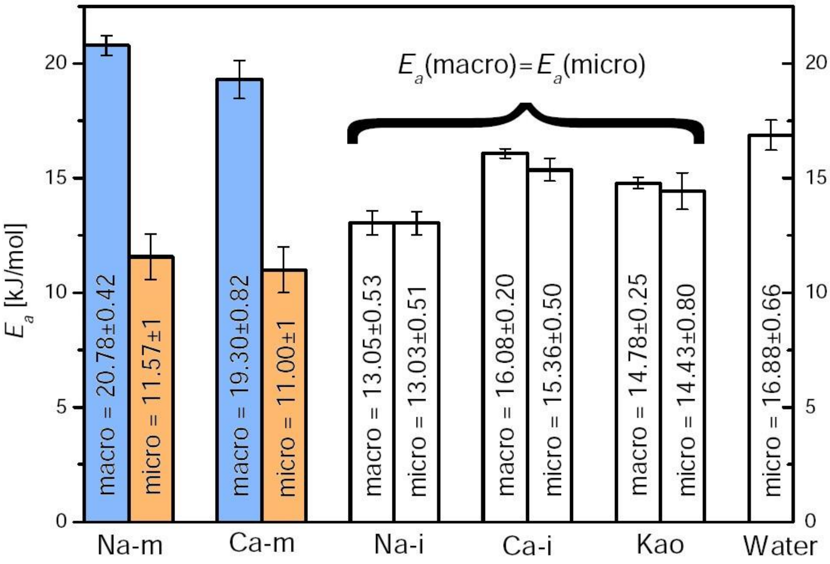

Figure 3. Activation energy of the water diffusion for different clays measured by tracer through-diffusion and quasielastic neutron scattering.

Summary and Conclusions

We conclude that the geometrical factor and the electrostatic constraint can be determined from a comparison of the diffusion coefficients measured by the two different techniques: quasielastic neutron scattering and tracer through diffusion. Furthermore, activation energies obtained at the two scales are similar for clays having no interlayer water. For montmorillonite the activation energy values are different. Further investigations are required to clarify the reason.

Acknowledgement

The authors acknowledge the financial support from FoKo PSI and SNF, furthermore the beam times at PSI (FOCUS and Morpheus), FRM II (TOF-TOF and Spheres) and at ILL (IN16 and IN10). The work of the local contacts (Jochen Stahn, Cecil Marcelot, Tobias Unruh, Gerald Schneider and Tilo Seydel) is appreciated.

References

Bée, M. (1988). Quasielastic Neutron Scattering (IOP Publishing LTD, ISBN 0-85274-371-8)

Bestel, M. et al. (2011). In this abstract book.

Bourg, I.C., Sposito, G., Bourg, A.C.M. (2006). Tracer diffusion in compacted, water-saturated bentonite. Clays Clay Miner. 54, 363-374.

Cebula, D.J., Thomas, R.K., White, J.W. (1981). Diffusion of water in Li-montmorillonite studied by quasielastic neutron scattering clay and clay minerals 29, 241-248.

González Sánchez, F.G., Gimmi, T., Juranyi, F., Van Loon, L., Diamond, L.W. (2009). Linking the Diffusion of Water in Compacted Clays at Two Different Time Scales: Tracer Through-Diffusion and Quasielastic Neutron Scattering. Environmental Science & Technology 43, 3487-3493.

González Sánchez, F., Van Loon, L.R., Gimmi, T., Jakob, A., Glaus, M.A., Diamond, L.W. (2008). Self-diffusion of water and its dependence on temperature and ionic strength in highly compacted montmorillonite, illite and kaolinite. Applied Geochemistry 23, 3840-3851.

González Sánchez, F.G., Juranyi, F., Gimmi, T., Van Loon, L., Unruh, T., Diamond, L.W. (2008). Translational diffusion of water and its dependence of temperature in charged and uncharged clays: A neutron scattering study. Journal of Chemical Physics 129.

Hribar, B., Southall, N.T., Vlachy, V. and Dill, K.A. (2002). How ions affect the structure of water. Journal of the American Chemical Society, 124, 12302-12311.

Kozaki, T., Fujishima, A., Sato, S., Ohashi, H. (1998). Self-diffusion of sodium ions in compacted sodium montmorillonite. Nuclear Technology 121, 63-69.

Lechner. R.E. (1995). Effects of low-dimensionality in solid-state protonic conductors. Solid State Ionics, 77, 280-286.

Malikova, N., Cadene, A., Marry, V., Dubois, E., Turq, P. (2006). Diffusion of water in clays on the microscopic scale: Modeling and experiment. Journal of Physical Chemistry B 110, 3206-3214.

Nakazawa, T., Takano, M., Nobuhara, A., Torikai, Y., Sato, S., Ohashi, H. (1999). Activation energies of diffusion of tritium and electrical conduction in water-saturated compacted sodium montmorillonite. In: ASME (Ed.), Radioactive Waste Management and Environmental Remediation. pp. 5.

Skipper, N.T., Lock, P.A., Titiloye, J.O., Swenson, J., Mirza, Z.A., Howells, W.S., Fernandez-Alonso, F. (2006). The structure and dynamics of 2-dimensional fluids in swelling clays. Chemical Geology 230, 182-196.

Suzuki, S., Sato, H., Ishidera, T., Fujii, N. (2004). Study on anisotropy of effective diffusion coefficient and activation energy for deuterated water in compacted sodium bentonite. Journal of Contaminant Hydrology 68, 23-37.

Van Loon, L.R., Müller, W., Iijima, K. (2005). Activation energies of the self-diffusion of HTO, $^{22}Na^{+}$ and $^{36}Cl^{-}$ in a highly compacted rock (Opalinus Clay). Appl. Geoch. 20, 961-972.

How is the Current Nano/Microscopic Knowledge Implemented in Model Approaches?

Benjamin Rotenberg[1*]

[1] CNRS and UPMC-Univ Paris 06, UMR7195, PECSA, Paris F-75005 (FRANCE)

* Corresponding author: benjamin.rotenberg@upmc.fr

Abstract

The recent developments of experimental techniques have opened new opportunities and challenges for the modelling and simulation of clay materials, on various scales. In this communication, several aspects of the interaction between experimental and modelling approaches will be presented and discussed. What levels of modelling are available depending on the target property and what experimental input is required? How can experimental information be used to validate models? What knowledge can modelling on different scale bring to the knowledge on the physical properties of clays? Finally, what can we do when experimental information is not available?

Introduction

The recent developments of experimental techniques have opened new opportunities and challenges for the modelling and simulation of clay materials, on various scales. In this non-exhaustive communication, several aspects of the interaction between experimental and modelling approaches will be discussed. I will first review the different levels of description available depending on the considered length and time scales, and exemplify the different types of required experimental input. Then I will illustrate how experimental information can be used to validate models, and what modelling on different scale brings to the knowledge on the physical properties of clays. Finally, I will discuss what can be done from a modelling point of view in the absence of experimental information.

What should we simulate?

Levels of description

Clays are multi-scale materials, in which processes occur over a very wide range of length and time scales. Chemical reactions (e.g. at the surface or and edge of a clay particle) involve electronic reorganization over a few Å and the elementary steps occur over a few ps. This can be captured only using Ab-Initio (AI) simulations, where electronic degrees of freedom are taken into account. The microscopic structure and dynamics of clay layers and interlayers requires descriptions over several nm and ns. This cannot be achieved with AI simulations and resort to simplified model of interactions between atoms is necessary. This is done in classical Molecular Dynamics (MD) simulations. Processes associated to clay particles and micropores occur require a description up to μm and μs. Further simplification is achieved in mesoscopic models, e.g. by considering only solute particles and treating the solvent as a continuum, either with explicit particles as in Brownian Dynamics (BD) or with implicit models dealing only with fields such as local concentrations as in classical Density Functional Theory (DFT) or Poisson-Boltzmann-like models. An intermediate level of modelling is found in kinetic theory, based on the probability of events (e.g. for particles to move in a particular direction, depending on the local flow and electric field) and usually implemented in lattice models of the Lattice Boltzmann (LB) type.

Experimental input
Prior to any simulation, one needs to define the system that is modelled. This generally involves several types of experimental input, both on the system itself:

- Composition: e.g. the unit cell, the charge density
- Structure: either crystallographic or on the mesoscale
- Conditions: dry density, water content

and on the associated features we use for the simulation, such as:

- Data: e.g. the microscopic diffusion coefficient for a Brownian Dynamics simulation
- Processes: e.g. assumption on transport pathways.

As an example of the latter, one could for example rely on the conclusion of Glaus et al. (2009) that interlayer diffusion dominates at high compaction of Na^+ and Sr^{2+} to setup a BD simulation of the diffusion of these ions on the μm and μs scale.

Do model predictions make sense?

A crucial issue for any model is that of its validation, by comparing its prediction to available experimental data. This allows assessing the relevance of the assumptions made and the parameters used, at least in a certain range of conditions. Examples on the microscopic scale include the comparison of MD results for water dynamics in the interlayer of montmorillonite with Quasi-Elastic Neutron Scattering (Malikova et al. (2006)) or for surface complexes of alkaline ions with basal surfaces of muscovite with X-ray reflectivity (Sakuma et al. (2011)).

The validation is even more convincing when the model simultaneously reproduces several experimental results obtained by different techniques in various conditions. Ferrage et al. (2011) showed that the CLAYFF force field is able to give a good description of the interlayer structure of saponite by comparing its predictions with neutron diffraction using both normal and deuterated water, as well as with X-ray diffraction, for two relative humidities. Furthermore, this comparison can be exploited to improve the models. In that same work, the authors suggested a refinement of CLAYFF to better reproduce the experimental data.

What can we learn from modelling?

Interpretation of experiments
The first use of modelling is to help in understanding experimental facts. In a recent EXAFS study, Dähn et al (2011) investigated the sorption of Zn^{2+} onto montmorillonite and could explain their results in the framework of a two-site model, with a strong and a weak site. Using AI simulation of Zn^{2+} in different environments and calculating the EXAFS signal for each of them, Churakov could identify the strong site with Zn incorporated in the layer, and the weak site as consisting of mono and bidentate complexes at edges. Moreover, the relative weight of each type in different samples could be determined from the combination of the individual contribution of each environment to the measured EXAFS signal.

Another illustration, on a larger scale, is the interpretation of the effect of the charge of tracers on their effective diffusion coefficient through clay samples. In addition to the Donnan effect, which induces an "effective concentration gradient" inside the sample, which differs from the one imposed by the reservoirs (Birgersson et al. (2009)), the role of the different pathways through the porosity depending on the tracer charge has to be discussed. The interplay between pore geometry, electrostatics and diffusion has for example been investigated using LB simulations in Rotenberg et al. (2010).

New microscopic knowledge
Microscopic simulations usually generate more information than what is accessible experimentally on a given system. They thus provide a complementary source of knowledge. For example, Marry et al. (2008) studied the structure and dynamics of the first water layer at the basal surface of montmorillonite, in particular the hydrogen bond network at the surface and the rates for the formation and breaking of H-bonds with the surface oxygen atoms.

(In)validate assumptions on small scale processes
Another utility of microscopic simulation is to test assumptions made to explain processes on larger scales. For example, using homogenization theory it is possible to understand the macroscopic (Darcy) scale flows from the pore scale (Stokes) ones. However, such theories assume the validity of continuous hydrodynamics on the microscopic scale, assuming in addition that the bulk viscosity of the fluid can be used, and that a no-slip boundary condition applies. These assumptions have recently been tested by Botan et al. (2011) who found that a continuous description, using the bulk viscosity, is relevant for pores larger than 4 nm, provided that a slip boundary condition, with a slip length derived from MD simulations is used. Even in that case, deviations from the continuous predictions are observed in the first water layers (within 1 nm from the surface).

Link between scales
Finally, microscopic simulations provide a link between the smaller and larger scales. Using random walks, Churakov et al. (2011) investigated the diffusion of tracers on the clay matrix scale by taking into account diffusion inside and outside the clay particles. On a larger scale, Robinet et al. (2008) used time domain diffusion on a Representative Elementary Volume from X-ray microtomography to analyze the effect of heterogeneities on the effective diffusion coefficient on the sample scale.

When experimental information is missing

Microscopic simulation is finally a complementary source of knowledge when experimental information is not available.

Protonation state of edge sites
The protonation state of the surfaces is a crucial issue for predicting the sorption of ions. While the overall acid/base behaviour of clay suspensions can be investigated by titration, the assignment of acidity constants to definite sites (e.g. silanol or aluminol edge groups) cannot be achieved without the help of a microscopic theory. Progress has been made in this direction using semi-empirical methods such as MUSIC (Tournassat et al. (2004)). More recently, Churakov used ab-initio simulations to estimate acidities of the different edge groups in pyrophyllite from bond dissociation energies in vaccum (Churakov (2006)) and demonstrated the hopping of protons between surface groups via surface water molecules (Churakov (2007)). We are currently adapting the thermodynamic integration method of Sulpizi et al. (2010) to compute the acidity constants of these sites in the presence of water.

Sorption/desorption rates

In order to include the sorption/desorption processes in a mesoscopic BD or LB simulation, one needs to know the associated rates on the different sites. These rates are generally not know experimentally. However, they can be estimated in MD simulations, producing long simulations analyzed in the framework of statistical thermodynamics. We are currently following a multi-scale approach in which ab-initio simulations are used to derive an accurate force field, for subsequent use in MD simulations to compute the sorption/desorption rates of multivalent ions at the edges of illite particles.

Transport on intermediate scales

Predicting the transport of charged species (electrolyte or tracers) through clays on the scale of several micrometers is particularly challenging, because one needs to account for the coupled electric / hydrodynamic / diffusion phenomena on a large system, but also because the complex structure of the porous material is not well know on the 10 nm - 1 μm scale. In the oil industry, transport over the μm-mm scale is usually simulated using Pore Network Modelling (PNM, see Bekri et al. (2002)). The PNM approach uses experimental data (capillary pressures, permeability and formation factor) to generate a "numerical sample" that reproduces the properties of the real material. In collaboration with Andra and IFP Energies Nouvelles, we are currently extending this approach to investigate transport of charged species through clays.

Summary and Conclusions

Models implement the current nano/microscopic knowledge using experimental input, taking advantage of multi-scale approaches, and providing data or insights complementary to experiments. Future work will greatly benefit from the recent experimental developments, in particular for 3D-imaging on intermediate scales, and should also address other properties, e.g. mechanical or thermal properties.

Acknowledgement

The author is grateful to his co-workers Pierre Turq, Virginie Marry, Alexandru Botan and Magali Duvail and acknowledges financial support of the Agence Nationale de la Recherche under grant ANR-009-SYSC-012 (SIMISOL project).

References

Bekri, S., Laroche, C., Vizika, O. (2002). Pore-network models to calculate transport properties in homogeneous and heterogeneous porous media. Develop. Water Sci. 47, 1115-1122.

Birgersson, M., Karnland, O. (2009). Ion equilibrium between interlayer space and an external solution - Consequences for diffusional transport. Geochim. Cosmochim. Acta 73 (6) 1908-1923.

Botan, A., Rotenberg, B., Marry, V., Turq., P., Noetinger, B. (2011). Hydrodynamics in clay nanopores. J. Phys. Chem. C 115 (32), 16109-16115.

Churakov, S.V. (2006). Ab-initio study of sorption on pyrophyllite: Structure and acidity of edge sites. J. Phys. Chem. B 110 (9) 4135-4146.

Churakov, S.V. (2007). Structure and dynamics of the water films confined between edges of pyrophyllite: A first principle study. Geochim. Cosmochim. Acta 71 (5), 1130-1144.

Churakov, S.V., Gimmi, T. (2011). Upscaling of molecular diffusion coefficients in clays: A two-step approach. J. Phys. Chem. C, 115 (14), 6703-6714.

Dähn, R., Baeyens, B., Bradbury, M.H. (2011). Investigation of the different binding edge sites for Zn on montmorillonite using P-EXAFS - The strong/weak site concept in the 2SPNE SC/CE sorption model. Geochim. Cosmochim. Acta, 75 (18), 5154-5168.

Ferrage, E., Sakharov, B.A., Michot, L.J., Delville, A., Bauer, A., Lanson, B., Grangeon, S., Frapper, G. Jimenez-Ruiz, M., Cuello, G.J. (2011). Hydration properties and interlayer organization of water and ions in synthetic Na-smectite with tetrahedral layer charge. Part 2. Toward a precise coupling between molecular simulations and diffraction data. J. Phys. Chem. C, 115 (5), 1867-1881.

Malikova, N., Cadène, A., Marry, V., Dubois, E., Turq, P., Zanotti, J.-M., Longeville, S. (2006). Diffusion of water in clays on the microscopic scale : Modeling and experiment. J. Phys. Chem. B, 110, 3206-3214.

Marry, V., Rotenberg, B., Turq, P. (2008). Structure and dynamics of water at a clay surface from molecular dynamics simulation. Phys. Chem. Chem. Phys. 10, 4802.

Robinet, J.-C., Sardini, P., Delay, F., Hellmuth, K.-H. (2008). The effect of rock matrix heterogeneities near fracture walls on the residence time distribution (RTD) of solutes. Transp. Porous. Media 72 (3), 393-408.

Rotenberg, B., Pagonabarraga, I., Frenkel, D. (2010). Coarse-grained simulations of charge, current and flow in heterogeneous media. Faraday Discuss. 144, 223.

Sakuma, H., Kondo, T., Nakao, H., Shirako, K., Kawamura, K. (2011). Structure of hydrated sodium ions and water molecules adsorbed on the mica/water interface. J. Phys. Chem. C 115(32), 15959-15964.

Sulpizi, M., Sprik, M. (2010). Acidity constants from DFT-based molecular dynamics simulations. J. Phys. Condens. Matt. 22 (28), 284116.

Tournassat, C., Ferrage, E., Poinsignon, C., Charlet, L. (2004). The titration of clay minerals II. Structure-based model and implications for clay reactivity. J. Coll. Interf. Sci. 273 (1), 234-246.

POSTER PRESENTATIONS

Interaction of Pu with Opalinus Clay Studied by µ-XRF, µ-XRD, and µ-XANES

U. Kaplan [1*], S. Amayri[1], D.R. Fröhlich[1], J. Drebert[1], D. Grolimund[2], T. Reich[1]

[1] Johannes Gutenberg-Universität Mainz, Institute of Nuclear Chemistry, D-55099 Mainz
[2] Paul Scherrer Institut, Swiss Light Source, CH-5232 Villigen PSI

* Corresponding author: kaplan@uni-mainz.de

Abstract

A combination of spatially-resolved synchrotron based techniques (µ-XRF, µ-XRD, µ-XANES) was used to study the distribution and speciation of Pu on Opalinus Clay (OPA) after sorption and diffusion processes. µ-XRF maps showed Ca, Fe, and Pu hot spots on the OPA surface of all investigated thin sections. Pu L_{III}-edge µ-XANES spectra on Pu hot spots confirmed that Pu(IV) is the dominating species on OPA, i.e., the highly soluble Pu(VI) was retained by OPA in the reduced and less mobile tetravalent oxidation state of Pu. Preliminary µ-XRD results indicate that Pu is localized on or in the close vicinity of the Fe(II) mineral siderite and the clay mineral kaolinite.

Introduction

Plutonium will be a major contributor to the radiotoxicity of high-level nuclear waste after a storage time of more than 1,000 years due to the long half-lives of ^{239}Pu, ^{240}Pu, and ^{242}Pu. Argillaceous rocks are under consideration as potential host rock formation for the construction of high-level nuclear waste repositories in several European countries, i.e., Belgium, France, Germany, and Switzerland [1]. The aim of our study was to improve our understanding of the interaction of Pu with natural opalinus clay at a molecular level. Such studies are important in the context of save disposal and long-term storage of hazardous radioactive wastes.

Experimental

The speciation of ^{242}Pu(VI) sorbed on OPA has been investigated by µ-XANES, µ-XRF, and µ-XRD measurements. For this study three samples were prepared: two thin sections of OPA on glass object slides and one sample from an intact OPA drill core, which was contacted with 20 µM ^{242}Pu(VI) in OPA pore water (pH= 7.6) for more than one month. In one sample, (20 µM, pH=7.6) ^{242}Pu(VI) solution was deposited directly by pipetting on the thin section. For the second sample, (20 µM, pH=7.6) ^{242}Pu(VI) was sorbed using a deposition cell. A summary of the employed sample preparation methods as well as the chemical conditions are listed in Table 1.

Table 1. Summary of the measured samples

Samples	Preparation	pH	Sample area (mm^2)	Activity of ^{242}Pu (Bq)	Pu (ng/mm^2)
^{242}Pu(VI)	Sorption	7.6	19.6	917	311
^{242}Pu(VI)	Deposition	7.6	50.7	750	96
^{242}Pu(VI)	Diffusion	7.6	510.4	400	7

Pu L_{III}-edge µ-XANES spectra were collected on several Pu hot spots. Background and energy correction of these spectra were performed using the software package Athena [2]. By using an iterative transformation factor analysis program (ITFA) [3], the amounts of different Pu oxidation states (IV, V, VI) on the measured hot spots were determined. XRD data was analysed using the Area Diffraction Machine software program [4]. All data were recorded using the dedicated radioactive X-ray microprobe setup of the microXAS beamline facility at the Swiss Light Source.

Summary and Conclusions

For all samples fluorescence maps with good signal intensity were collected for Pu, Ca, and Fe. Figure 1 shows, for example, the µ-XRF maps of Pu, Fe, and Ca on the sorption sample. In this sample several hot spots of Pu, Fe, and Ca can be found. In the regions where Pu localizes, the correlation between Pu and Fe was analyzed using the program XY-MAP DISPLAY [5]. The resulting correlation plots (not shown) do not immediately point towards an unequivocally correlation between the local concentrations of Pu and Fe. However, in all cases where elevated levels of Pu were detected, a moderately enhanced Fe concentration could be established as well. Areas of highest Fe concentrations, however, turned out to be free of Pu. Similar correlated detection of Pu and Fe was observed also in the diffusion sample.

Pu L_{III}-edge µ-XANES spectra of Pu hot spots show a complete reduction of Pu(VI) to Pu(IV) in all samples. Pu(IV) is the dominating oxidation state after sorption and diffusion processes. Figure 1 shows the Pu L_{III}-edge µ-XANES spectrum and µ-XRD images of the hot spot in the sorption sample. Preliminary results of µ-XRD measurements indicate that Pu potentially localizes on siderite and kaolinite mineral phases contained in OPA (see Figure 2).

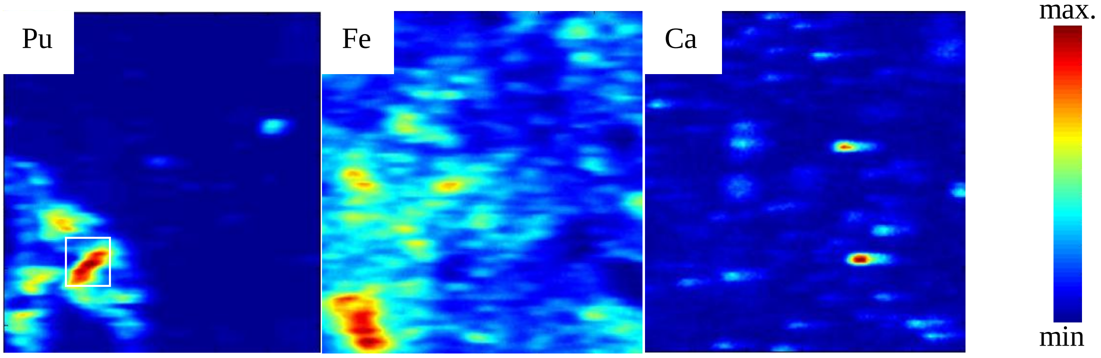

Figure 1. µ-XRF maps for Pu, Fe, and Ca of sorption sample (200µm X 200 µm). Square in the left figure indicates the selected location for recording µ-XANES.

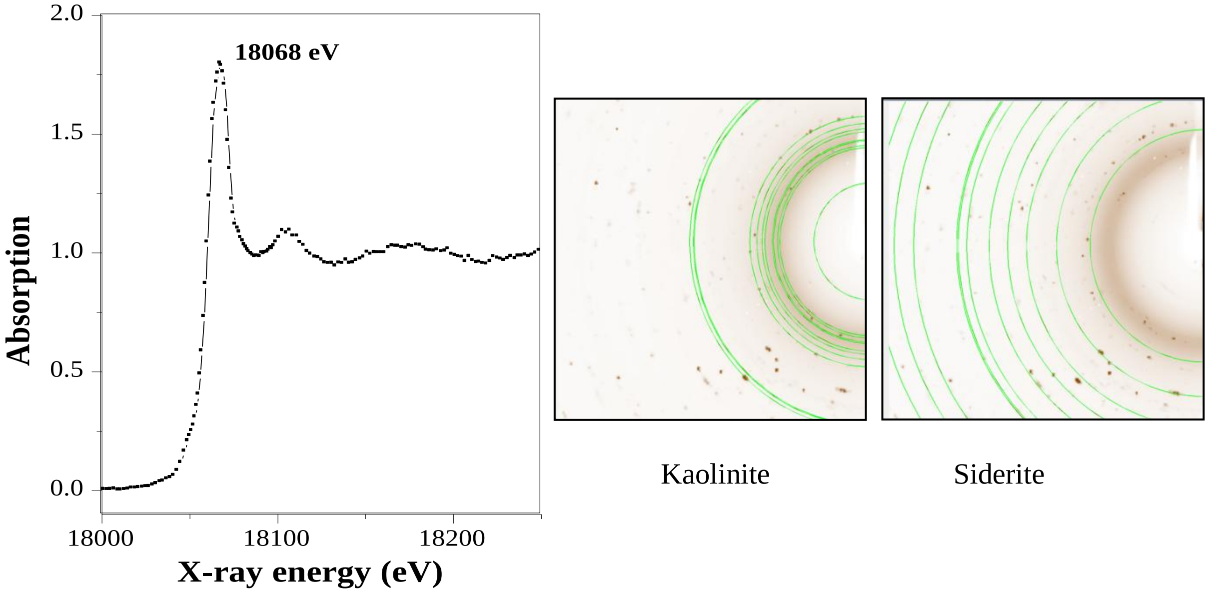

Kaolinite

Siderite

Figure 2. Normalized Pu L_{III}-edge µ-XANES spectrum and two dimensional µ-XRD image transmission mode of Pu hot spot in sorption sample. The Debye rings for kaolinite and siderite are shown in green.

Acknowledgement

This work was financed by the Federal Ministry of Economics and Technology (BMWi) under contract No. 02E10166 and the European Commission under the 7th Framework Programme: ACTINET-I3 (Grant no. 232631). Daniel Fröhlich has been supported by a fellowship of DFG-GRK 826. We are grateful to Dr. Camelia Borca at Swiss Light Source for her support during the measurements. Further we thank Dr. Christian Marquardt (Institute for Nuclear Waste Disposal, Karlsruher Institut für Technologie (KIT)) for providing the OPA samples. Maik Biegler (Max-Planck-Institute for Chemistry, Mainz) is acknowledged for preparation of the thin sections.

References

1. NAGRA: Projekt Opalinuston–Synthese der geowissenschaftlichen Untersuchungs-ergebnisse, Entsorgungsnachweis für abgebrannte Brennelemente, verglaste hochaktive sowie langlebige mittelaktive Abfälle. Technical Report NTB 02-03, NAGRA Nationale Genossenschaft für die Lagerung radioaktiver Abfälle, Wettingen/Switzerland (2002).

2. Ravel B. and Newville M., (2005). ATHENA, ARTEMIS, HEPHAESTUS: data analysis for X-ray absorption spectroscopy using IFEFFIT. Synchrotron Radiat. 12, 537-541.

3. Rossberg A., Reich T., and Bernhard G., (2003). Complexation of uranium(VI) with protocatechuic acid. Application of iterative transformation factor analysis to EXAFS spectroscopy; Anal. Bioanal. Chem. 376, 631-638.

4. Lande J. and Webb S., (2007). The Area Diffraction Machine software program http://code.google.com/p/areadiffractionmachine/.

5. Marcus M. (2007), The XY Map Display software program http://xraysweb.lbl.gov/uxas/Beamline/Software/Documentation/Documentation.htm.

Microstructural Analysis by X-ray Nano-CT and Its Implications on HDO Diffusion in Compacted Montmorillonite

Hiroaki Takahashi*

[1] Geological Isolation Research and Development Unit, Japan Atomic Energy Agency (JAPAN)

* Corresponding author: takahashi.hiroaki@jaea.go.jp

Introduction

Compacted bentonite is considered as a reference material to be used as an engineered barrier in deep geological repository of high level radioactive waste. The swelling capacity of the clay materials, that is important key function for retardation capability on the engineered barrier, would decrease during geochemical change. The diffusion of species in the compacted bentonite depends strongly on geometric parameters such as tortuosity and constrictivity. For aqueous-phase diffusion the relationship between the effective diffusion coefficient, D_e, the geometric parameters, and the diffusion coefficient in bulk water, D_0, is given by

$$D_e = \frac{1}{F} D_0 = \varepsilon_a \frac{\delta}{\tau^2} D_0 \qquad (1)$$

where F represents the formation factor, δ is the constrictivity, τ is the tortuosity, and ε_a is the diffusion accessible porosity. The aim of this work is to characterize the influence of the geochemical change upon the three-dimensional (3-D) microstructure of compacted bentonites and the diffusion properties of HDO in these samples. 3-D imaging using X-ray computed tomography (X-ray CT) is a promising in-situ observation technique for compacted bentonite (Tomioka et al. (2010)). However, it was limited by the machine resolution a few microns. Recently, CT scanning has been improved to be able to describe the sub-micron sized. In this study, comparative analyses of diffusivities and microstructures in compacted and saturated Na-montmorillonites and Cs-montmorillonite as clays with a different swelling capacity are carried out using X-ray nano CT.

Experimental

Used as samples are Na-montmorillonite, Kunipia-F, which is commercially available from Kunimine Industries, Japan and Cs-montmorillonite prepared by cation exchange on Kunipia-F. The effective diffusion coefficient, D_e of HDO is measured by through-diffusion tests with constant concentration in the inlet reservoir. The experiments are performed with 20-mm-diameter and 5-mm-thickness samples of compacted montmorillonites. HDO diffusion experiments are conducted on compacted Na-montmorillonites saturated with distilled water, 0.01, 0.1, 0.5, 1 M NaCl and compacted Cs-montmorillonite saturated with 0.1 M CsCl background solutions at a dry density of 0.8 Mg m^{-3}, respectively. HDO content in the outlet reservoir is determined by the ATR-FTIR spectroscopy. A linear regression analysis of data on the total accumulated HDO versus time is performed and D_e is derived.

Saturated compacted Na- and Cs-montmorillonite after through-diffusion tests and compacted dry Na-montmorillonite are non-destructively imaged with 270 or 360 nm spatial resolution by X-ray nano CT of SkyScan-2011 (Takahashi et al., 2010). The selection of a representative sample is performed by vertically putting a tube in compacted montmorillonite at the randomly selected position. The specimens are enclosed in PFA tube of 0.5 mm inside diameter and 0.7 mm outside diameter to maintain the hydrated and compacted condition during CT measurements. CT measurements are performed on with setting Z axis of diffusion direction. The CT images are reconstructed by the SkyScan NRecon software. The macroporosity are determined by using the software package VGStudio MAX 2.1. Some high-resolution, 3-D images are processed using the software package Exfact Analysis for Porous/Particles (Nihon Visual Science, Inc.) based on medial axis analysis (Lindquist et al. (1996)) to directly convert the pore structure to a network structure. Geometrical path tortuosity (Currie (1970), Bear (1972)) and radii of pore, r_p, and throat, r_t are determined by the processing. Constrictivity, δ, is determined from equation (2) (Currie (1960)) using the r_p and the r_t assuming that mean cross-section could be evaluated by linear approximation with average of maximum and minimum cross-section (Takahashi et al. (2009)).

$$\delta = \frac{(\text{maximum} \times \text{minimum cross-section})^{1/2}}{\text{mean cross-section}} = \frac{(\pi r_\mathrm{p}^2 \times \pi r_\mathrm{t}^2)^{1/2}}{\dfrac{\pi r_\mathrm{p}^2 + \pi r_\mathrm{t}^2}{2}} \qquad (2)$$

Results and discussion

The upper figures on Figure 1 show cross-sectional images by X-ray nano CT of compacted dry and saturated Na-montmorillonite by different ion-strength of solution and 0.1 M CsCl saturated Cs-montmorillonite. These observations indicate that Cs-montmorillonite has not swelled, whereas Na-montmorillonite has swelled and "lens-like" pores have separated by isolated clay minerals. The lower figures on Figure 1 show 3-D images of the lens-like pores (macropores) of these samples. The macroporosity, ε_m, of Figure 1 (a) to (g) are 0.54, 0.0025, 0.0077, 0.0083, 0.046, 0.20, and 0.67, respectively. The macroporosity and the size of the macropores are increased with ion strength of saturated solution on Na-montmorillonite. D_e of HDO on compacted Na-montmorillonite saturated with distilled water, 0.01, 0.1, 0.5, and 1 M NaCl and Cs-montmorillonite saturated 0.1 M CsCl are 0.8×10^{-10}, 0.94×10^{-10}, 1.03×10^{-10}, 1.03×10^{-10}, 1.00×10^{-10}, and 1.93×10^{-10} $\mathrm{m^2\ s^{-1}}$, respectively. These results show that D_e of HDO for Na-montmorillonite is a half value of the one for Cs-montmorillonite, therefore, it indicates that swelling has large contribution to retardation on HDO diffusion. In the case of Na-montmorillonite, observed small effect of ion-strength on D_e of HDO and the result which the macroporosity has increased with ion-strength imply little influence of the macroporosity on the diffusivity of HDO.

τ and δ of macropores in dry Na-montmorillonite and saturated Cs-montmorillonite have been provided using the 3-D image describing the sub-micron sized features, median of τ and δ are 2.05 and 0.623 for dry Na-montmorillonite and 2.05 and 0.718 for saturated Cs-montmorillonite. In the case of Cs-montmorillonite, $\varepsilon_\mathrm{m}\delta/\tau^2$ of 0.11 estimated by image analysis is good agreement with D_e/D_0 of 0.084 obtained by HDO diffusion. The D_0 value for HDO is taken to be 2.3×10^{-9} $\mathrm{m^2\ s^{-1}}$ at 298 K (Callaghan (1984)). In the case of Na-montmorillonite, observed smaller D_e/D_0 of 0.045 than $\varepsilon_\mathrm{m}\delta/\tau^2$ of 0.08 for dry condition indicate that formation factor is changed after saturation and swelling.

In the case of 0.1 M NaCl saturated Na-montmorillonite, particle and nodal pore and/or gel phase have been segmented based on the macroporosity at dry condition (Figure 2 (a) and (b)), although the basis on the threshold between particle and nodal pore and/or gel phases is still unclear at present. Shown in Figure 2 (c) and (d) are distributions of particle volume and nodal pore and/or gel volume on dry and 0.1 M NaCl saturated compacted Na-montmorillonite. These data indicate that decreasing these volumes by water-saturation. In the case of 0.1 M CsCl-saturated Cs-montmorillonite, these volumes are similar with dry Na-montmorillonite. These data indicate that the swelling changes formation factor. Detailed analysis on the formation factor for the saturated compacted Na-montmorillonite is under way.

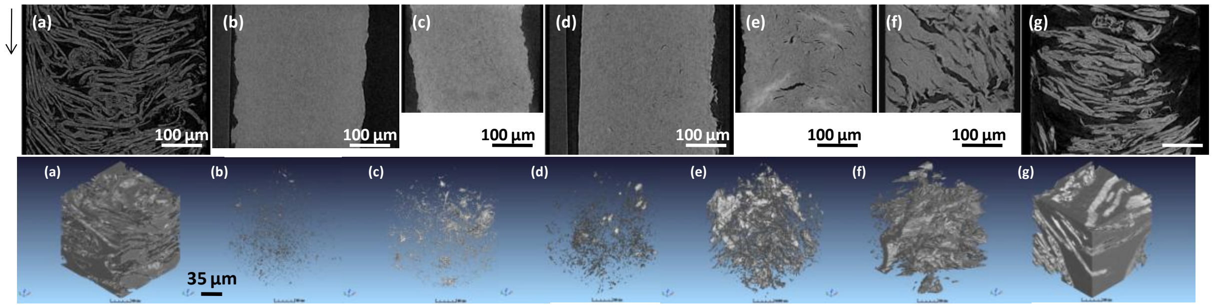

Figure 1. Cross-sectional images by X-ray nano (upper) CT and processed 3-D images (lower) of macro-pore (gray) of compacted (a) dry Na-montmorillonite and (b) distilled water, (c) 0.01 M, (d) 0.1 M, (e) 0.5 M, (f) 1 M NaCl saturated Na-montmorillonites and (g) 0.1 M CsCl saturated Cs-montmorillonites after diffusion test at a dry density of 0.8 Mg m^{-3}. The arrow shows the direction of compaction and diffusion.

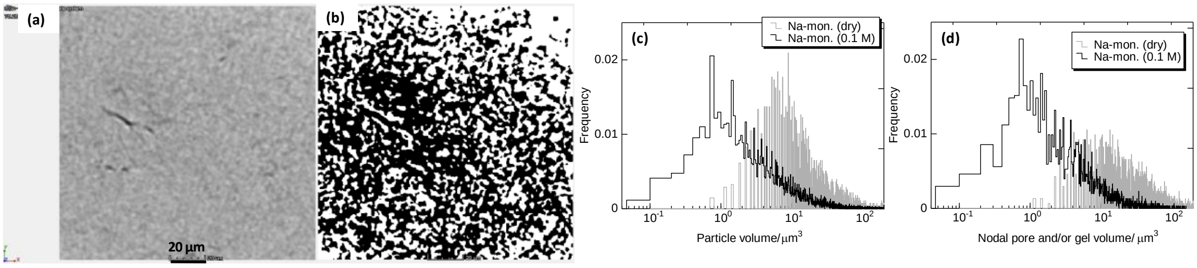

Figure 2. A cross-sectional of (a) gray scale image and (b) a binarized image into pore and/or gel (black) and particle (white) on 0.1 M NaCl saturated Na-montmorillonite. Distributions of (c) particle volume and (d) nodal pore and/or gel volume on dry and 0.1 M NaCl saturated Na-montmorillonite.

Summary and Conclusions

In the present work, a comparative analysis of HDO diffusivities and microstructures in compacted Na-montmorillonite saturated with aqueous solutions different in ion-strength and compacted Cs-montmorillonite saturated with 0.1 M CsCl by X-ray nano CT have been demonstrated:

- It is observed that Cs-montmorillonite has not swelled and Na-montmorillonite has swelled and “lens-like” pores have separated by isolated clay minerals.
- D_e of HDO for Na-montmorillonite is a half value of the one for Cs-montmorillonite.
- In the case of Na-montmorillonite, observed small effect of ion-strength on D_e of HDO and the result which the macroporosity has increased with ion-strength imply little influence of the macroporosity on the diffusivity of HDO.
- τ and δ of macropores in dry Na-montmorillonite and saturated Cs-montmorillonite have been provided using the 3-D image describing the sub-micron sized features.
- In the case of Cs-montmorillonite, $\varepsilon_m\delta/\tau^2$ estimated X-ray CT analysis is good agreement with D_e/D_0 obtained by HDO diffusion.

- In the case of Na-montmorillonite, observed smaller value of D_e/D_0 than $\varepsilon_m\delta/\tau^2$ on dry condition indicate that formation factor is changed after saturation and swelling.
- Distributions of particles and pores and/or gel volume show decreasing these volumes by 0.1 M NaCl saturation on Na-montmorillonite, in the case of 0.1 M CsCl-saturated Cs-montmorillonite, these volumes are similar with dry Na- montmorillonite.
- Soft X-ray microscopy and small-angle neutron scattering is under design for a quantitative estimation of micro-structure on the saturated and compacted Na-montmorillonite include the size on the clay particle, nodal pore and gel phase.

Acknowledgement

This work is supported by Ministry of Economy, Trade and Industry of Japan under “Project for Assessment Methodology Development of Chemical Effects on Geological Dispossal System”. The author acknowledges the technical contributions of K. Nemoto (Japan Atomic Energy Agency).

References

Bear J. (1972). Dynamics of fluids in porous media, American Elsevier, New York.

Callaghan, P. T. (1984). Pulsed field gradient nuclear magnetic-resonance as a probe of liquid state molecular organization, Aust. J. Phys. 37, 359-387.

Currie J. A. (1960). Gaseous diffusion in porous media. Part 2. - Dry granular materials, Br. J. Appl. Phys. 11, 318-324.

Currie, J. A. (1970). Movement of Gases in Soil Respiration, Sorption and Transport Processes in Soils, SCI Monograph, Vol. 37, Rothamsted Experimental Station, Harpenden, England

Lindquist, W.B., Lee, S.M., Coker, D.A., Jones, K.W. and Spanne, P. (1996). Medial axis analysis of void structure in three dimensional tomographic images of porous media, J. Geophys. Res., 101B, 8297-8310.

Takahashi H., Seida Y., Yui M. (2009). 3D X-ray CT and diffusion measurements to assess tortuosity and constrictivity in a sedimentary rock, Diffusion-fundamentals.org 11, 89, 1-11

Takahashi H., Seida Y., Yui M. (2010). Comparative study of diffusion of HDO in compacted Na- and Cs-montmorillonites characterized by three-dimensional X-ray tomographic imaging technique, Geochimica et Cosmochimica Acta 74, 12, Supplement 1, A1021.

Tomioka S., Kozaki T., Takamatsu H., Noda N., Nisiyama S., Kozai N., Suzuki S., Sato S. (2010). Analysis of microstructural images of dry and water-saturated compacted bentonite samples observed with X-ray micro CT, Appl. Clay. Sci, 47, 65-71.

Review of Studies of Clay Minerals as Significant Component of Potential Host Rocks or Engineering Barriers for Radioactive Waste Disposals Performed at Comenius University in Bratislava

Uhlík Peter[1*], Stríček Igor[2], Šucha Vladimír[1], Čaplovičová Mária[1]

[1] Department of Geology of Mineral Deposits, Faculty of Natural Sciences, Comenius University in Bratislava, (SK)
[2] Department of Geotechnics, Faculty of Civil Engineering, Slovak University of Technology in Bratislava, (SK)

* Corresponding author: uhlik@fns.uniba.sk

Introduction

About 50 % of electric power is produced by nuclear power plants in Slovakia. In spite of the significant production of nuclear waste, Slovakia has not defined basic strategy of radioactive-waste isolation. However, some pilot projects and studies have been carried out. Five areas were determined as prospective sites for construction of deep geological repository (DGR). Two of them are situated in the south of Slovakia. Szecseny schlier (mixture of siltstones and claystones) of Lučenec Formation (Egerian) is one of the most prospective host rocks from lithological, structural and spatial perspective (Matejovic et al., 2006). Besides the investigation of potential host rock for DGR the studies of bentonite properties as important part of engineering barriers for radioactive waste disposals were performed (Galamboš et al., 2011). Detailed mineral and structural analyses of smectites from the bentonitic material exposed to laboratory Mock-Up test were realised (Stríček et al., 2009, Stríček, 2010). Particular interest has been focused on interaction between Fe and smectites (Osacký et al., 2009, 2010). Other field of interest is investigation of sorption of Cs and Sr on natural and modified bentonites, including irradiation (Galamboš et al., 2009a, b). Purpose of this work is to present a short review of other studies done by our group with partial focusing to interaction of organic dye (Rhodamine 6G) with smectite that is connected with changes of layer charge after treatment; possibilities to measure preferential orientation of clays after compaction by TEM and to effort to use X-ray microtomography for inner structure of sediments.

1 Gamma-irradiation effects on smectite properties

Irradiation effects on a smectite stability is one of important phenomena that is or should be interesting for safety managements of radioactive waste disposals. Therefore, two of Slovak bentonites were tested by gamma-irradiation. Samples were irradiated in dry state (JC; drying at 105°C, 24 hours), hydrated state (JB; saturated by water vapour, 24 hours) and in hydrated state with 10 % admixture of powder Fe at Slovak Technical University, using ^{60}Co source with medium dose input of 0.21 kGy/h. Maximal total absorbed dose was 1.5 MGy.

The mineralogical composition and the crystal structure of the samples were investigated by X-ray diffraction and infrared spectroscopy. The cation exchange capacity was determined using the complexes of copper (II) ion (Meier & Kahr, 1999), layer charge by the Rhodamine 6G technique: water and Rhodamine 6G solution (10^{-5} mol dm^{-3}) were added with stirring to obtain R6G-clay dispersions with final R6G and clay concentrations of 5×10^{-6} mol dm^{-3} and 5×10^{-2} g dm^{-3}, respectively. The visible spectra of R6G-clay dispersions were recorded using a UV-vis spectrophotometer (Varian Cary 100) (Bujdák et al., 2003; Czimerová et al., 2006; Šucha et al., 2009).

Mineral composition as well as the structure of the main mineral - smectite seems to be stable even under at the highest gamma-irradiation doses that were applied. Practically only one very moderate change was observed for hydrated sample after irradiation by Rhodamine 6G technique (Fig. 1). Small increase of negative intensity of absorption peak of monomers (~ 500 nm) points out decreasing of charge. If the spectra of dry and saturated samples without irradiation are compared there is also increase of area of absorbance band that relate to lower charge for dry sample (Figure 1).

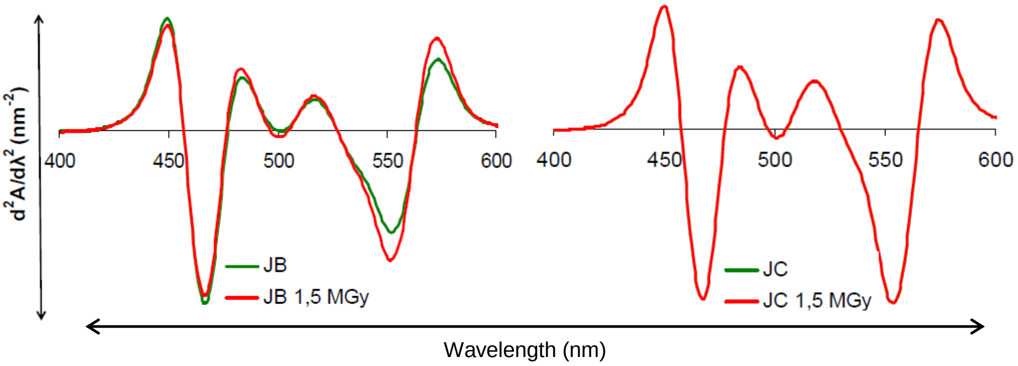

Figure 1. Second-derivate spectra of Rhodamine 6G (band position of H-aggregates: 460-470 nm– higher layer density; H-dimers: ~ 500 nm; monomers: 535-570 nm– lower layer density) measured 24 h after mixing the dye solution with the clays before and after irradiation.

2 Effect of bentonite compaction on the orientation of smectite particles

An important function of bentonite as a buffer material in a geological disposal of high-level radioactive waste is to inhibit groundwater flow and to retard the movement of radio nuclides in the region between the waste forms and surrounding rocks. It is well known from other studies that the diffusion of radio nuclides in bentonite is a function of various pore structural properties or parameters, such as porosity, dry density of bentonite, additives to bentonite, initial bentonite grain size, etc. Most of these parameters are directly connected to smectite particle orientation which may be influenced significantly during bentonite processing and compacting. Therefore study was focused on the role of compaction on the orientation of smectite particles and/or aggregates. Two different compaction techniques were applied to two Slovak bentonites. They were milled to the fractions < 250, 45 and 15 µm. A standard uniaxial technique along with an isostatic technique with pressure up to 300 MPa were used. The bentonites were compacted to dry density between 1.6 g/cm^3 and 1.9 g/cm^3. Oriented pieces were carefully sampled from pressed samples. The effect of the clay particle orientation was tested directly by transmission electron microscopy (JEOL JEM-2000 FX) of ultra thin sections observed at magnifications of 4000 – 8000x. TEM images were processed in graphical program ImageJ, used also for determination of optical porosimetry (Janega, Durmeková, 2004). Partical orientation was determined by using rose diagram software Rose (Figure 2).

Dependence of preferential orientation of particles on the compaction technique were not confirmed. The preferential orientations of smectite particles, perpendicularly to uniaxial pressure, were determined only sometimes. Randomly oriented particles were observed with same frequency as oriented.

Contradictory results were detected also for samples pressed by isostatic technique. Part of TEM images show randomly oriented and part preferred oriented samples. We assume that these phenomena could be caused by mineral and predominately partical size inhomogeneity of bentonites. Partial orientation of clay particles were observed around aggregates or larger mineral grains in bentonites pressed by both technique. The aggregates were composed of randomly oriented fine particles. Such observation allows possibility that the TEM image could represent just one large aggregate with original random orientation. Used technique is also suitable for calculation of interparticle and pore space. The technique is time consuming and involves special attention for selection of TEM images without artificial defects resulted from sample preparation.

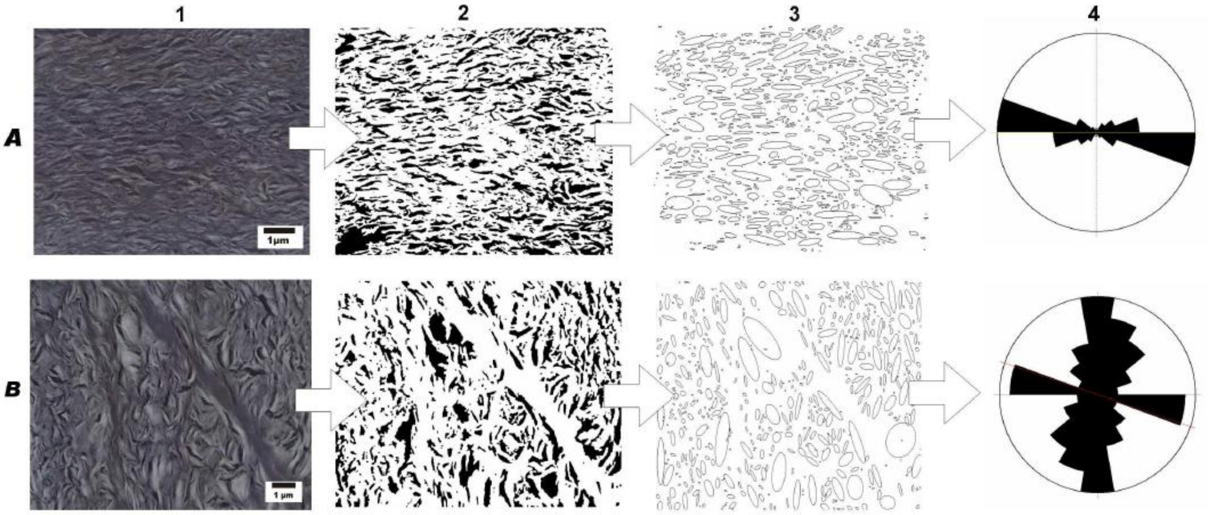

Figure 2. Example of preferential orientation (A-bentonite J, fraction <45μm, uniaxial stress) and random orientation of particles (B- bentonite J, fraction <250μm, isostatic stress) at the TEM images (1). 2- binary pictures (black area represent solid particles), 3-solid particles transformed to elipses, 4- rose diagram.

3 Lučenec Formation (Western Carpathian) – potential site for deep repository of nuclear waste

The mineral composition of Szecseny schlier was studied. XRD quantitative analysis of selected siltstones from several drill cores demonstrated their homogeneity. Major mineral phase is quartz that together with feldspars comprises half of the mineral composition. Carbonates (calcite, dolomite ± Fe carbonate) and phyllosilicates comprise approximately a quarter of siltstones composition each. The homogeneity of clay fraction was also confirmed. The presence of clay minerals is practically the same without regard to the depth of studied samples (22 to 870 m) and boreholes location. Major clay mineral is illite-smectite (75-85 % of smectite interlayers). It comprises about 60-65 % of clay fraction. Determined mineral homogeneousness of studied sediments and presence of expanding clays are next positive features of Szecseny schlier as potential geological site for nuclear waste disposal. Previous works pointed out to high dry bulk density (2.2 g/cm^3) and low porosity (14 to 20%) which relates to it. Preliminary measurements of hydraulic conductivity performed on remolded samples (i.e., samples made by recomposing and compacting samples to their *in situ* density) yield values as low as 10^{-10}m/s and even 10^{-10} m/s (Matejovic et al., 2006). An application of X-ray microtomography (David et al., 2007; Hain et al., 2011) to Szecseny schlier is testing as a possibility to determine properties of inner structure (porosity, pore size) by nondestructive three-dimensional method.

Acknowledgement

Support by Slovak grant agency (VEGA) 1/0219/10 is appreciated.

References

Bujdák J., Iyi N., Kaneko Y., Czimerová A. & Sasai R. 2003: Molecular arrangement of rhodamine 6G cations in the films of layered silicates: the effect of the layer charge. *Physical Chemistry Chemical Physics* 5, 4680—4685.

Czimerová A., Bujdák J. & Dohrmann R. 2006: Traditional and novel methods for estimating the layer charge of smectites. *AppliedClay Sci.* 34, 2—13.

David C., Robion P.. Menendez B. (2007) Anisotropy of elastic, magnetic and microstructural properties of the Callovo-Oxfordian argillite. 1983 Annual Meeting of the Southwestern Psychological Assoc., San Antonio, Physics and Chemistry of the Earth**,** 32**,** 1-7, 145-153.

Galamboš M., Kufčáková J., Rajec P. (2009a) Sorption of strontium on Slovak bentonites. J Radioanal Nucl Chem 281(3): 347–357

Galamboš M., Kufčáková J., Rajec P. (2009b) Adsorption of cesium on domestic bentonites. J Radioanal Nucl Chem 281(3): 485–492

Galamboš M., Rosskopfova O., Kufčáková J., Rajec P.(2011) Utilization of Slovak bentonites in deposition of high-level radioactive waste and spent nuclear fuel. J Radioanal Nucl Chem 288 (3), 765-777

Hain, M. Nosko, M. Simančík, F. Dvorák, T. Florek, R. X-ray microtomography and its use for non-destructive characterisation of materials. In *MEASUREMENT 2011 : Proceedings of the 8th International Conference on Measurement.* Editors: J. Maňka, V. Witkovský, M. Tyšler, I. Frollo. Bratislava : Institute of Measurement Science SAS, 2011. 123-126.

Matejovic I., Hok J., Madaras J., Slaninka I. and Pritrsky J., (2006). Status of the Deep Geological Disposal Program in the Slovak Republic. In Witherspoon P. A. and Bodvarsson G.S., ed.: Geological Challenges in Radioactive Waste Isolation. Fouth Worldwide Review, Report LBNL – 59808, 173-189.

Meier, L.P., Kahr, G. (1999): Determination of the Cation Exchange Capacity of clay minerals based on the Complexes of the Copper(II) ion with Triethylenetetramine and Tetraethylenepentamine, Clays and Clay Miner., 47, 3, 386–388.

Janega, A., Durmeková, T.(2004) Application of optical porosimetry in engineering and environmental geology. *Geológia a životné prostredie,* Štátny geologický ústav D. Štúra, 45-47, (in Slovak).

Osacký M, Honty M, Madejová J., Bakas T., Šucha V (2009) Experimental interactions of Slovak bentonites with metallic iron. Geologica Carpathica 60(6):535–543

Osacký M., Šucha V, Czimerová J., Madejová J (2010) Reaction of smectites with iron in a nitrogen atmosphere at 75 _C. Appl Clay Sci 50(2):237–244.

Stríček I. (2010) Bentonite mineral stability in barrier conditions. PhD thesis. Comenius University in Bratislava, 117p.

Stríček I, Šucha V, Uhlík P, Madejová J, Galko I. (2009) Mineral stability of Fe-rich bentonite in the Mock-Up-CZ experiment. Geologica Carpathica 60(5):431–436

Šucha V., Czimerová A., Bujdák J. 2009: Surface properties of illite-smectite minerals detected by interactions with Rhodamine 6G dye. *Clays and Clay Miner.* 57, 361—370.

LIST OF ABBREVIATIONS & GLOSSARY OF METHODS

Glossary of methods used

AFM - Is type of Scanning Probe Microscope (or Scanning Proximity Microscope) with a microscopic force sensor as a probe. By scanning the AFM force sensor (commonly flexible cantilever with the tip on the end) over a sample surface (or scanning a sample under the cantilever) and recording the deflection of the cantilever, one can measure the local height, chemical and mechanical properties of a sample (Binnig et al., 1986).

Autoradiography - A technique for visualization of radioactivity in samples by overlaying the surface with X-ray film and allowing the radiation to form an image on the film. High Resolution Digital Autoradiography is nowadays giving a spatial resolution (10–50 µm).

BIB-SEM/ BIB-cryo-SEM: Combined method of cutting/polishing a sample piece with a Broad Ion (Argon) Beam and afterwards imaging its surface at preferably high resolution, using a Scanning Electron Microscope. BIB-cryo-SEM: combination of BIB polishing embedded in SEM to produce serial high quality surfaces (mm^2) for 3D investigation of microstructures at cryogenic temperature in order to minimize the drying of clay and to track in-situ fluid-filled pores.

FFF – Field-flow fractionation is a separation technique where a field is applied to a fluid suspension or solution pumped through a long and narrow channel, perpendicular to the direction of flow, in order to cause separation of the particles present in the fluid, dependent on their differing "mobilities" under the force exerted by the field. The parabolic laminar flow field in the channel determines the velocity of a particular particle, based on its equilibrium position from the wall of the channel (Giddings, 1993).

FIB- A focused ion beam is generated by liquid metal ion sources based on gallium, gold, iridium and other metals. Ions are accelerated to 5-50 keV energies and focused into a beam of several nanometres in diameter by using electrostatic lenses. When the sample surface is affected by the FIB, ions destroy the chemical bonds and ionize it, and get implanted to a several nanometer depth. However, unlike electron beams, FIB allows for the layer-by-layer removal of atoms from the surface without damaging the deeper layers of the target. For nanoscale precision FIB operations small beam diameter (2.5-6nm) are required.
FIB- SEM is a combination of FIB polishing embedded in SEM to produce serial high quality surfaces (µm^2) for FIB-tomography, whereas FIB-cryo-SEM is the same as FIB-SEM but operating at cryogenic temperature to minimize the drying of clay and to track in-situ fluid-filled pores.

µ-EXAFS - A method by which the absorption of X-rays by a sample is measured as a function of the energy (wavelength, frequency,) of the impinging beam energy across and past a characteristic absorption edge of the element of interest. Typically, the measurements are carried out over several hundred eV past the edge at high energy resolution (< 1 eV) and require therefore considerable beam time at a synchrotron. The measured oscillations of the absorption spectrum can be modelled quantum-mechanically to derive atomic-scale short-range (< 1 nm) information (interatomic distances, coordination numbers and the identity of neighbour atoms) around the target element. The prefix µ implies that the X-ray beam is focussed to micrometer resolution.

µ-XANES - A method by which the absorption of X-rays by a sample is measured as a function of the energy (wavelength, frequency,) of the impinging beam energy across a characteristic absorption edge of the element of interest. Typically, the measurements are carried out over a few tens eV at high energy resolution (< 1 eV). The structure of the absorption edge yields depends on electronic transitions and can therefore yield information on coordination type around the target element or its oxidation state. This information can be obtained either through comparison with carefully selected compounds or by quantum-mechanical models. The prefix µ implies that the X-ray beam is focussed to micrometer resolution.

ICP-MS -Inductively coupled plasma mass spectrometry (ICP-MS) is a type of mass spectrometry that is highly sensitive and capable of the determination of a range of metals and several non-metals at concentrations below one part in 10^{12} (part per trillion). It is based on coupling together an inductively coupled plasma as a method of producing ions (ionization) with a mass spectrometer as a method of separating and detecting the ions. The ions generated within the plasma are separated on the basis of their mass-to-charge ratio and a detector receives an ion signal proportional to the concentration. ICP-MS is also capable of monitoring isotopic speciation for the ions of choice.

MIP - Mercury intrusion porosimetry is based on the premise that a non-wetting liquid (one having a contact angle greater than 90°) will only intrude capillaries under pressure. The relationship between the pressure and capillary diameter is described by the Washburn equation. Mercury must be forced using pressure into the pores of a dry material (this drying process may alter the pore structure). The pore size distribution is determined from the volume intruded at each pressure increment. Total porosity is determined from the total volume intruded.

µ-CT – Micro- computed tomography is an imaging technique that uses a computer to put a series of x-ray images to create cross-sections of a 3D-object that later can be used to recreate a virtual model without destroying the original sample. In general, there are two types of scanner setups, typically the X-ray source and detector are stationary during the scan while the sample rotates or the X-ray tube and detector rotate around the fixated sample. A contrast medium may be injected to make structures show up clearly on the x-ray images (especially in medical applications). The image produced is called a CT scan. The term micro is used to indicate that the pixel sizes of the cross-sections are in the micrometer range or nano (nano-CT) if it reaches the sub-micrometer range. These pixel sizes have also resulted in the terminology micro-computed tomography, micro-ct, micro-computer tomography, high resolution x-ray tomography, nano-CT and similar terminologies. All of these names generally represent the same class of instruments. Synchrotron-radiation-based CT (SRµCT) has the advantage over conventional x-ray sources (x-ray tubes), the unique properties (monochromatic source) of synchrotron radiation enable quantitative measurements that do not suffer from beam-hardening artifacts.

µ-FTIR – Fourier Transform-Infrared Spectroscopy (FTIR) is an analytical technique used to identify organic or inorganic materials. The prefix µ implies that the source (beam) is focussed to micrometer resolution. This technique measures the absorption of infrared radiation by the sample material versus wavelength, usually divided into three regions; the near-, mid- and far- infrared. The infrared absorption bands identify molecular components and structures. When a material is irradiated with infrared radiation, absorbed IR radiation usually excites molecules into a higher vibrational state. The wavelength of light absorbed by a particular molecule is a function of the energy difference between the at-rest and excited vibrational states. The wavelengths that are absorbed by the sample are characteristic of its molecular structure. The FTIR spectrometer uses an interferometer to modulate the wavelength from a broadband infrared source. The signal obtained from the detector is an interferogram, which must be analyzed with a computer using Fourier transforms (FT) to obtain a single-beam infrared spectrum.

µ-XAS - XAS is a generic term indicating all sorts of X-ray absorption measurements, particularly XANES and EXAFS. The prefix µ implies that the X-ray beam is focussed to micrometer resolution.

The absorption through the sample is measured either directly using ionization chambers (transmission mode) or indirectly, by measuring either the fluorescence or the secondary electrons emitted after the photon absorption with suitable detectors.

μ-XRF - A method by which the emission of X-rays after the creation of a hole in the electronic structure (e.g. via absorption of high-energy photons) is measured as a function of the emitted X-ray energy (wavelength, frequency). The fluorescence spectrum is measured either via energy dispersive detectors or tuneable crystal spectrometers. It gives information on the identity of elements present in the sample and their concentrations. In favourable cases, information on the oxidation state can be obtained. The prefix μ implies that the X-ray beam is focussed to micrometer resolution. Such a highly resolved beam can be scanned over the sample surface to generate element distribution maps.

ND - Neutron diffraction or elastic neutron scattering is the application of neutron scattering to the determination of the atomic and/or magnetic structure of a material. A sample to be examined is placed in a beam of thermal or cold neutrons to obtain a diffraction pattern that provides information of the structure of the material. The technique is similar to X-ray diffraction but due to their different scattering properties, neutrons and X-rays provide complementary information.

QENS - Quasielastic neuron scattering is a non-destructive method to measure diffusion processes on the atomic scale, averaged over a sample of typically 0.1-10g. When slow neutrons (speed ~10^5 cm/sec, compared to that of X-ray, 3×10^{10} cm/sec) impinge on liquid like water, they are scattered largely by the H atoms of the water molecules and on a time scale comparable to the time for water molecules to jump from one position to another. As a result, the scattering of the slow neutron observed contains information about the diffusive motions of the water involved.

SAXS – Small angle scattering (SAS) is the collective name given to the techniques of small angle neutron (SANS), X-ray (SAXS) and light (SALS, or just LS) scattering. In each of these techniques radiation is elastically scattered by a sample. SAXS stands for Small-angle X-ray scattering and refers to the X-Ray scattering technique where the elastic scattering of X-rays (wavelength 0.1-0.2 nm) by a sample which has inhomogeneities in the nm-range, is recorded at very low angles (typically 0.1-1). This angular range contains information about the shape and size of particles/molecules, characteristic distances of partially ordered materials, pore sizes, and other data. SAXS is capable of delivering structural information in the range of 5 and 25 nm, of repeat distances in partially ordered systems of up to 150 nm.

SEM – The scanning electron microscope (SEM) is an instrument capable of magnifying objects up to 100,000x. The SEM uses a focused beam of electrons to scan the surface of a sample, enabling to study its texture and shape in great detail. The electrons which are back scattered from the surface (SEM-BSE) are collected in a detector which generates an image of the sample that has a three-dimensional quality. Backscattered electrons usually have energies close to that of the primary electron beam. They are valuable in microanalysis because their number depends on the average atomic number of the sample. It is common for SEM instruments to have analytical devices attached to them as an energy-dispersive X-ray spectrometer (EDX).

SIMS – Secondary ion mass spectrometry uses an internally generated beam of either positive (e.g., Cs) or negative (e.g., O) ions (primary beam) focused on a sample surface to generate ions that are then transferred into a mass spectrometer across a high electrostatic potential, and are referred to as secondary ions. The interaction of the primary ion beam with the sample (under vacuum) provides sufficient energy to ionize many elements. If the primary beam is composed of positively charged ions, the resultant ionization favors production of negative ions; primary beams of negative ions favor generation of positive ions. Although most atoms and molecules removed from the sample by the interaction of the primary beam and the sample surface (referred to as sputtering) are neutral, a percentage of these are ionized. These ions are then accelerated, focused, and analyzed by a mass spectrometer.

(S)TEM-EDS - In a scanning transmission electron microscope, a high-energy electron beam is focussed on a nanometer-thick sample in an evacuated chamber and scanned over its surface. The electrons passing through the sample are detected and the signal is transformed either into an absorption-contrast image (revealing the sample morphology at the nanometer scale) or into a diffraction pattern image (if the sample is crystalline). The electron microscope can be coupled to energy dispersive detection systems measuring the secondary fluorescence induced by the electron bombardment, so that the elements in the excited volume and their abundance can be determined.

STXM – The principle of a Scanning transmission X-ray microscope (STXM) is that a zone plate focuses a X-ray beam into a small spot (dependent on the outermost zone of this zone plate ~20-40nm), a sample is raster (scanned) in the focal plane of the zone plate and the transmitted X-ray intensity is recorded as a function of the sample position. The name STXM is usually used for microscopes working in soft X-rays range (70-1200eV); a hard X-ray version is called X-ray nanoprobe or X-ray microprobe.

Diffusion – The spontaneous movement and scattering of particles (atoms and molecules) of liquids, gases and solids. The transport of mass or heat through normal thermal agitation(Parker, 2003). In experimental set-ups using this non-destructive method to measure diffusion on the macroscopic scale (> mm) in porous materials by applying radioactive isotope labeling it is differentiated between "in-diffusion", "through diffusion" and "out-diffusion".

XRD - X-ray diffraction is a method by which scattered (monochromatic) X-rays are recorded after interacting with the sample. The sample may be a randomly oriented powder or a single crystal. If the sample is crystalline, the scattered X-rays form an ordered pattern of intensity peaks (the diffraction pattern) which can be used to determine the lattice parameters or even the entire crystal structure. XRD is a widely used method in earth and material science to characterize the structure of crystalline compounds. The prefix µ implies that the X-ray beam is focussed to micrometer resolution.

List of Abbreviations

acq	acquisition
AFM	Atomic Force Microscopy
AI	Ab-initio
ALARA	As Low As Reasonably Achievable
amu	atomic mass units
BIB	Broad Ion Beam
BC	Boom Clay
BD	Brownian Dynamics
BSE	Back Scattered Electrons
BSF	Boda Siltstone Formation
CG	Coarse grained
CM	Clay matrix
COx	Callovo-Oxfordian argillite
Cryo	cryogenic
CS	cross section
D	power law exponent
DESY	Deutsches Elektronen-Synchrotron
DFT	Density Functional Theory
ED	Equivalent (pore) Diameter
EDX	Energy-dispersive X-ray Spectroscopy
EPMA	Electron probe Micro Analyzer
EZE	Edwin Zeelmaeckers
FFFF	Flow Field-Flow Fractionation
FIB	Focussed Ion Beam
FG	fine grained
FWS	Fixed Window Scans
FWHM	Full-width at half maximum
HADES	High Activity Disposal Experimental Site
HASYLAB	Hamburger Synchrotron Labor
ICP-MS	Induced Coupled Plasma-Mass Spectrometry
LB	Lattice Boltzmann
MD	Molecular Dynamics
M_{max}, M_{min}	the highest respectively lowest ion mass during one acquisition
MIP	Mercury Injection Porosimetry
MRP	mass resolving power
μ-CT	X-ray microtomography
μ-FTIR	Fourier transform infrared spectroscopy with a micrometer-scale resolution
μ-EXAFS	micro Extended X-ray Absorption Fine Structure
μ-XANES	micro X-ray Absorption Near Edge Structure
μ-XAFS	X-ray absorption fine structure with a micrometer-scale resolution
μ-XAS	micro X-ray Absorption Spectroscopy
μ-XRF	micro X-Ray Fluorescence
NCM	Non-Clay Mineral(s)
ND	Neutron diffraction
NSLS	National Synchrotron Light Source
OM	organic matter
OPA	Opalinus Clay
pdr	Pore detection resolution
PNM	Pore Network Modelling
psd	Pore-size distribution
STEM-EDS	Scanning Transmission Electron Microscopy coupled to Energy Dispersive detection System
TU	Technische Universität
QENS	Quasielastic neutron scattering
REA	Representative Elementary Area
SaF	sandy facies
SAXS	Small-Angle X-ray Scattering
ShF	shaly facies
SEM	Scanning Electron Microscope/Microscopy
SE	Secondary Electrons
SIMS	Secondary Ion Mass Spectrometry
SINQ	Swiss Spallation Neutron Source at the Paul Scherrer Institut, Villigen (CH)
STXM	Scanning transmission X-ray microscopy
TEM	Transmission Electron Microscope

To-Clay	Tournemire Clay
WD	working distance
WL	White line
WZW	Wissenschaftszentrum Weihenstephan
XRD	X-Ray Diffraction
Nano- XCT	X-ray nano computed tomography

Glossary references:

Binnig, G., Quate, C.F., Gerber, C., 1986. Atomic Force Microscope. Physical Review Letters, 56(9): 930-933.
Giddings, J.C., 1993. FIELD-FLOW FRACTIONATION - ANALYSIS OF MACROMOLECULAR, COLLOIDAL, AND PARTICULATE MATERIALS. Science, 260(5113): 1456-1465.
Parker, S.P., 2003. McGraw-Hill dictionary of scientific and technical terms. McGraw-Hill.

APPENDIX B - LIST OF PARTICIPANTS

Name	**Company**
Belgium	
DE CANNIERE, Pierre	FANC
DE CRAEN, Mieke	SCK·CEN
HONTY, Miroslav	SCK·CEN
LI, Xianling	SCK·CEN
VAES, Roland	TECNOCHEM, Beringen
VAN BAELEN, Herve	ONDRAF/NIRAS
WOUTERS, Laurent	ONDRAF/NIRAS
Canada	
AL, Tom	Univ. of Fredericton
HENDRY, Jim	Univ. of Saskatchewan
JENSEN, Mark	NWMO
Finland	
CARLSSON, Torbjörn	VTT
MATUSEWICZ, Michal	VTT
MUURINEN, Arto	VTT
France	
BOISSON, Jean-Yves	IRSN
DYMITROWSKI, M.	IRSN
GABOREAU, Stephane	BRGM
KALINICHEV, Andrey	SUBATECH
LANDAIS, Patrick	ANDRA
MARSAL, Francois	IRSN
MICHAU, Nicolas	ANDRA
PRÊT, Dimitri	HYDRASA
ROTENBERG, Benjamin	UPMC-Univ. Paris, PESCA
VIGGIANI, Cino	Univ. Grenoble (3SR)
Germany	
BANIK, Nidhu	KIT-INE
BLUM, Philipp	KIT-IAG
BOUBY, Muriel	KIT-INE
CHAGNEAU, Aurelie	KIT-INE
DENECKE, Melissa Anne	KIT-INE
DESBOIS, Guillaume	RWTH Aachen
DOHRMANN, Reiner	BGR
EMMERICH, Katja	KIT-CMM
FINCK, Nicolas	KIT-INE
GOMPPER, Klaus	KIT-INE
GÖTTLICHER, Jörg	KIT-ISS

HEMES, Susanne	RWTH Aachen
HOLLÄNDER, Hartmut	Geozentrum Hannover
HOUBEN, Maartje	RWTH Aachen
HÖSCHEN, Carmen	TU München
JOHN, Nadine	Univ. Jena (IGW)
KAPLAN, Ugras	Univ. Mainz
KAUFHOLD, Annette	Univ. Göttingen
KIENZLER, Bernhard	KIT-INE
KLAVER, Jop	RWTH Aachen
KUPCIK, Tomas	KIT-INE
LAURICH, Ben	RWTH Aachen
LIU, Tao	KIT-ISS
MARQUARDT, Christian	KIT-INE
METZ, Volker	KIT-INE
POURZARGAR, Alborz	Univ. Bochum
RÜBEL, Andre	GRS
SCHÄFER, Thorsten	KIT-INE
SCHMEIDE, Katja	HZDR
SCHUMANN, Rainer	KIT-CMM
URAI, Janos	RWTH Aachen
ZHANG, Chung-Lian	GRS
Hungary	
TÖRÖK, Szabina	KFKI, Budapest
Japan	
TAKAHASHI, Hiroaki	JAEA
SUGITA, Yutaka	JAEA
SUZUKI, Satoru	NUMO
Netherlands	
NEEFT, Erika	COVRA
SCHRÖDER, Thomas	NRG
Slovakia	
UHLIK, Peter	Univ. Bratislava
Spain	
FERNANDEZ, Raul	Univ. Madrid
RUIZ, Ana Isabel	Univ. Madrid
Sweden	
FORSLING, Willis	Swedish National Council for Nuclear Waste
FURÓ, István	KTH
Switzerland	
BECKER, Jens	NAGRA
BESTEL, Martina	PSI
BOSSART, Paul	Swisstopo

CURTI, Enzo	PSI
DOLDER, Florian	Univ. Bern
FRANK, Erik	ENSI
GAUTSCHI, Andreas	NAGRA
GIMMI, Thomas	Univ. Bern
GROLIMUND, Daniel	PSI
JURANYI, Fanni	PSI
KELLER, Lukas	EMPA
MAZUREK, Martin	Univ. Bern
MÄDER, Urs	Univ. Bern
MÜLLER, Herwig	NAGRA
NUSSBAUM, Christophe	Swisstopo
TRABER, Daniel	NAGRA
United Kingdom	
NORRIS, Simon	NDA
United States	
BEGG, James	Lawrence Livermore National Laboratory
CAPORUSCIO, Florie	Los Alamos National Laboratory
DAVIS, James	Lawrence Berkeley National Laboratory
JACOBSEN, Chris	Argonne National Laboratory, APS & North-western University
TINNACHER, Ruth	Lawrence Berkeley National Laboratory
International Organisations	
WAKASUGI, Keiichiro	OECD/NEA